Investigation, Prediction and Control of

Rubber Friction and Stick-Slip:

Experiment, Simulation, Application

Fakultät für Maschinenbau

der Gottfried Wilhelm Leibniz Universität Hannover

zur Erlangung des akademischen Grades

DOKTOR-INGENIEUR

(Dr- Ing.)

genehmigte Dissertation von

Diplom-Physiker Leif Busse

geboren am 26.10.1968, in Reinbek

(2012)

1. Referent: **Prof. Dr.-Ing. Gerhard Poll**

2. Referent: **Prof. Dr.-Ing. Jörg Wallaschek**

3. Referent: **PD Dr. rer. nat. Manfred Klüppel**

Vorsitzender: Prof. Dr.-Ing. Bernd-Arno Behrens

Tag der Promotion: 2012-07-31

Zusammenfassung

In dieser Arbeit werden neuartige Methoden zur Analyse und Beeinflussung von Gummireibung und dabei auftretendem Stick-Slip mit Hilfe von Oberflächenmodifikationen untersucht. Die Verbindung von Elastomeren, wie sie in Reifen, Schuhen, Scheiben-wischblättern oder Dichtungsringen verwendet werden, mit harten Oberflächen wie Straßen, Fußböden, Glasscheiben oder Metallbauteilen macht Verständnis, Vorhersage und Steuerung von Kontaktmechanik und Reibung unabdingbar.

Reibung zu verstehen bedeutet, die Wechselwirkung von Materialeigenschaften, Oberflächeneigenschaften und Schmierstoffen zu verstehen. Voraussetzung für eine mathematische Beschreibung der Reibphänomene ist eine fraktale Sichtweise der Substratflächen. Basierend auf einem von Klüppel & Heinrich (2000) nach der Greenwood-Williamson-Theorie aufgestellten Modell mit einer Erweiterung auf bifraktale Skalenbereiche, lassen sich sowohl Hysteresereibung als auch der adhäsive Anteil beschreiben, die für Reibung unter nassen und trockenen Bedingungen stehen. Durch Simulationsrechnungen werden neben Reibwerten noch weitere Kontaktparameter gewonnen und in dieser Arbeit vorgestellt.

Zu den Materialdaten des Modells gehören die viskoelastischen Eigenschaften der Gummisorten inklusive ihrer Relaxationszeitspektren. Da Reibung bedeutend von den systemeigenen Parametern bestimmt wird, was auch die Temperatur einschließt, spielen diese viskoelastischen Gummieigenschaften eine entscheidende Rolle bei der Beschreibung und damit auch der Simulation von Reibungssystemen. Viskoelastizität, die letztlich mittels des Zeit-Temperatur-Superpositionsprinzips von der Temperatur bestimmt wird, darf über die viskoelastischen Verschiebungsfaktoren, die man aus der dynamisch-mechanischen Analyse erhält, als mit der Reibungsgeschwindigkeit verknüpft gelten. Deshalb korrelieren hohe Frequenzen beim Verhalten des Gummis mit niedrigen Temperaturen. Dieselben Verschiebungsfaktoren werden in dieser Arbeit auf die experimentell ermittelten Reibkurven für rußgefülltes NR, S-SBR und EPDM auf nassem und trockenem Granit innerhalb eines Intervalls von Reibgeschwindigkeiten für verschiedene Temperaturen angewandt, um daraus zusammenhängende Reibmasterkurven über einen extrem großen Geschwindigkeitsintervall zu bilden. Diese gemessenen Masterkurven werden diskutiert und mit der simulierten Hysterese- und Adhäsionsreibung verglichen.

Weitere Experimente zielten darauf, Reibung zu reduzieren und in kritischen Systemen das Entstehen von unerwünschten Stick-Slip-Effekten zu verhindern. Zwei verschiedene Techniken kamen dabei zum Einsatz: Zunächst wird eine Methode präsentiert, die harte

Aluminium-/Silicananostrukturen auf der Elastomeroberfläche erzeugt. Durch geeignete Präparation werden Partikel aus hyperverzweigtem Polyalkoxysiloxan (PAOS) an der Gummioberfläche gebildet. Der Einfluss der Menge an Al_2O_3/PAOS-Dispersion, des Füllgrads von Ruß und der Temperdauer auf den Reibkoeffizienten wird über einen großen Geschwindigkeitsbereich hinweg erforscht. Experimente mit und ohne Lubrikanten wurden durchgeführt und in Hinblick auf Material- und Oberflächeneigenschaften der Proben diskutiert. Es stellt sich heraus, dass eine hinreichende Menge an PAOS eine nennenswerte Absenkung der Reibung bewirken und Stick-Slip-Phänomene unterbinden kann.

Zum anderen wurden SBR- und EPDM-Proben unterschiedlicher Oberflächenstrukturen, mit wie auch ohne Rußfüllung, mit verschiedenen Arten von Polymeren (PU, TPU, PTFE, Polysiloxan) beschichtet und untersucht, und zwar auf besonders glatten Substratflächen wie Glas, poliertem Stahl und lackierten Blechen. Es wird gezeigt, wie durch Probenbeschichtung die Reibung nennenswert abgesenkt wird, gefolgt von einer umfangreichen Analyse des Stick-Slip-Aspekts, in einem weiten Parameterraum unter besonderer Berücksichtigung der Einwirkung von Druck und Temperatur. Schließlich wird noch die Frage aufgeworfen, inwieweit das Reibmodell auf Simulationen für beschichtete Proben und beschichtete Substrate übertragen werden kann.

Schlagwörter: Gummireibung, Stick-Slip, Oberflächenmodifikation

Abstract

In this work, novel methods of analyzing and controlling rubber friction and stick-slip effects by means of surface modification shall be investigated. The interaction of elastomers like in tyres, shoes, wiper blades or seals with hard surfaces like roads, floors, glass or metal parts makes the understanding, prediction and control of contact mechanics and friction indispensible.

Understanding friction means understanding the interaction of material properties, surface properties and lubricant. A fractal point of view for the substrate surfaces becomes the prerequisite of a mathematical description of friction phenomena. Based on a model by Klüppel & Heinrich (2000) according to the Greenwood-Williamson theory and expanded to bifractal scaling ranges, hysteresis friction as well as adhesion contributions can be described, representing wet and dry lubrication conditions. Additionally to friction, other contact parameters are gained by simulations and also presented in this work.

Part of the material data for the model are the viscoelastic properties of the rubber, including relaxation time spectra. As friction strongly depends on its system parameters, including temperature, these viscoelastic properties of rubber play a major role in describing and thus simulating friction systems. Defined by temperature using the time temperature superposition principle, viscoelasticity can be assumed to be connected to friction velocity via the viscoelastic shift factors gained from dynamic mechanical analysis. Thus, high frequencies correlate with low temperatures for rubber behaviour. In this work, these shift factors are applied to experimental friction curves for carbon black filled NR, S-SBR and EPDM rubber on wet and dry granite for various temperatures in order to form continuous friction master curves over are extremely large velocity interval. These measured master curves are discussed and compared to simulated hysteresis and adhesion friction.

Further experiments were conducted to reduce friction and prevent critical systems from exhibiting unwanted stick-slip effects. Two different techniques are employed to achieve this goal: First, a method of implementing hard alumina/silica nanostructures into the elastomer surface is presented. With appropriate preparation, particles of hyperbranched polyalkoxysiloxane (PAOS) are formed on the rubber surface. The influence of variable amounts of Al_2O_3/PAOS dispersion, variable amounts of carbon black fillers and annealing time on the friction coefficient is studied for a large velocity range. Experiments were conducted with and without lubricant and discussed with respect to material and surface properties of the samples. It is found that sufficient PAOS concentrations cause a considerable decrease of friction for all systems and prevent stick-slip phenomena.

Subsequently, SBR and EPDM samples with varying surface structures, filled with and without carbon black, were coated with several kinds of polymer (PU, TPU, PTFE, polysiloxane) and tested on especially smooth substrates like glass, polished steel and varnished metal sheets. It is shown how coating the samples significantly reduces friction, and an extensive analysis of the stick-slip aspects in a wide parameter range is given, with special respect on the influence of pressure and temperature. Finally, the question is investigated whether the contact model can be transferred to simulations of coated samples and coated substrates.

Keywords: rubber friction, stick-slip, surface modification

Table of Content

Abbreviations & Variables

Abbreviations

AFM	atomic force microscopy
CB	carbon black
COF	coefficient of friction: μ
DIAS	dispersion index analysis system
DMA	dynamic mechanical analysis
EDX	energy dispersive X-ray spectroscopy
EPDM	ethylene propylene dien monomer
GW	Greenwood-Williamson
HD	height distribution
HDC	height difference correlation
MC	master curve
NR	natural rubber
NBR	nitrile butadiene rubber
PAOS	polyalkoxysiloxane
PSD	power spectral density
PTFE	polytetrafluorethylene
PU	polyurethane
RT	room temperature (20°C for TTS, 23°C for other testings)
RTS	relaxation time spectrum
SBR	styrene butadiene rubber (S-SBR: polymerized in solution)
SEM	scanning electron microscopy
SHD	summit height distribution
SSE	stick-slip effect
TPU	thermoplastic polyurethane
TTS	time temperature superposition
WLF	Williams-Landel-Ferry
XPS	X-ray photoelectron spectroscopy

Latin Variables

< >	averaged value
A_0	nominal contact area
A_c	real contact area
A_{GW}	contact area in Greenwood Williamson model
A_{Hz}	contact area in Hertz model
a_{Hz}	contact radius in Hertz model
a_T	horizontal shift factors
b	fit factor of hysteresis friction
b_0	sample width
C_1, C_2	WLF constants for horizontal shifting
C_z	height difference correlation function
d	gap distance
d_0	sample thickness
D_1	mesoscopic fractal dimension
D_2	microscopic fractal dimension
D_f	fractal dimension
E'	storage modulus (elastic modulus)
E"	loss modulus (elastic modulus)
E_0	static storage modulus
E_∞	maximal storage modulus
E_a	activation energy
E_{diss}	dissipated energy
$F_0, F_1, F_{3/2}$	Greenwood-Williamson functions
F_N	normal force on sample
F_{fric}	friction force
f	frequency
f_s	spatial frequency
f_{smin}	minimal spatial frequency
f_V	vertical shift factors
G'	storage modulus (shear modulus)
G"	loss modulus (shear modulus)
h	height of asperity
h_{Hz}	sphere distance in Hertz model
H	Hurst exponent
$H(\tau)$	relaxation time spectrum function

l_0	sample length
l_s	contact length
m	linear slope in relaxation time spectrum
M_e	average molecular weight
n	fit exponent of critical velocity
n_{GW}	number of contact points in Greenwood Williamson model
N_{GW}	number of spheres in Greenwood Williamson model
P	pressure
R_0	radius of asperity
R	gas constant
s	affine parameter of height distribution
S	power density
t	normalised distance
t_{fric}	duration of friction
T	temperature
T_g	glass transition temperature
v	sliding velocity
v_c	critical velocity of adhesion
v_p	velocity of friction peak: $v(\mu_{max})$
v_s	velocity of changing friction stability for stick-slip: $v(\mu_{min})$
V	sample volume
z	profile height
z_{max}	maximal profile height from average
z_s	transformed z for summit height distribution
$<z_p>$	averaged penetration depth

Greek Variables

α	magnification (zoom factor)
$\langle\delta\rangle$	averaged excitation depth
ε	tensile strain
γ_s	shear strain
$\Delta\gamma$	surface tension between substrate & sample
Φ	filler content
Φ_{HD} , Φ_{SHD}	height distribution, summit height distribution
Θ	contact angle
η	viscosity
λ	lateral distance between two surface points
λ_2	transition length microscopic-mesoscopic
λ_c	minimal measurable length
λ_{min}	minimal contact length
μ_{Adh}	adhesion friction coefficient
μ_{Hys}	hysteresis friction coefficient (wet friction)
μ_{max}	maximal friction (peak or plateau)
μ_{min}	minimal friction of changing friction stability for stick-slip
μ_{plat}	friction coefficient of stationary plateau
μ_{start}	friction coefficient of start peak
μ_{tot}	total friction coefficient (dry friction)
ν	Poisson number
$\xi_{\parallel}$	horizontal cut-off length
$\xi_{\perp}$	vertical cut-off length
ρ	density
σ	mechanical tension
σ_0	normal pressure on sample
σ_{HD}, σ_{SHD}	standard deviation of height distribution/ of summit height distribution
σ_L	surface tension (liquid phase)
σ_{LS}	surface tension (liquid-solid interphase)
σ_S	surface tension (solid phase)
τ	relaxation time
τ_s	shear tension
ω	angular frequency

1 Introduction

1.1 Importance of Elastomer Friction

Friction as elemental process in any mechanical system is a ubiquitous phenomenon. In some cases, there is no alternative to traction: Tyres, shoes and assembly lines simply could not work without friction, and a maximal effect is desired. On the other hand, for wiper blades, non-stationary seals, and other flexible contact systems, friction is a harassing side effect, limiting the efficiency, and has to be avoided. In addition to the pure friction coefficient, further effects like stick-slip behaviour have to be considered, too, for resonant or vibrating systems. Finally, friction is linked to mechanical exposure of the surface and thus to stability and wear of the sliding part. Obviously, there is a need to describe, understand and control contact parameters and friction. Depending on the environmental conditions, a prediction of friction is desirable for a multitude of material combinations at any given sliding speed, temperature and pressure.

Especially important are friction contacts between a soft, elastic material like rubber (= elastomer) and a hard counter surface, the substrate. Taking the huge usage of rubber parts into account, from rubber bands over rubberized fabrics to damping elements, this combination affects virtually every aspect of our world.

1.2 Motivation and Agenda of this Work

In this work, theoretical and practical aspects of the rubber friction shall be investigated, focussing on two main topics: the nature of friction curves in respect to velocity and temperature, and the possibility of reducing friction and stick-slip by surface modification. To achieve these goals, numerous configurations of elastomer systems combined with various rough and smooth substrates were considered under several environmental conditions.

Friction strongly depends on its system parameters, including velocity and temperature (Figure 1). The first topic determines the relationship between friction and its underlying material cause, namely the viscoelasticity of the sample. As described in chapter 2.1 and 2.2 there is a clearly defined identity of temperature and time induced aspects. Playing a major part in friction theory to describe and thus simulate friction systems, viscoelastic properties and thus the time temperature superposition can be expected to appear analogously also in friction curves by allocating temperature with velocity. Can friction master curves be constructed by applying the same shift factors as gained for dynamic mechanical measurements? This question is answered in chapter 4.3 by connecting friction to the shift factors to measured friction on wet and dry granite over a velocity range for various temperatures. The measurements are compared to simulated hysteresis and adhesion friction, which works moreover as a proof of theory to validate our simulation model. Further simulation results for the real contact area and other parameters complete these investigations.

Viscoelastic properties of elastomer samples change considerably when the rubber is heated or cooled. This can be investigated by measuring the storage modulus and loss modulus over a few decades of frequency in dynamic mechanical analysis (DMA) for various temperatures. According to the time temperature superposition principle, the single branches of the DMA results can be shifted to one continuous master curve by applying shift factors that obey the WLF law [1]. Thus, high frequencies correlate with low temperatures for rubber behaviour.
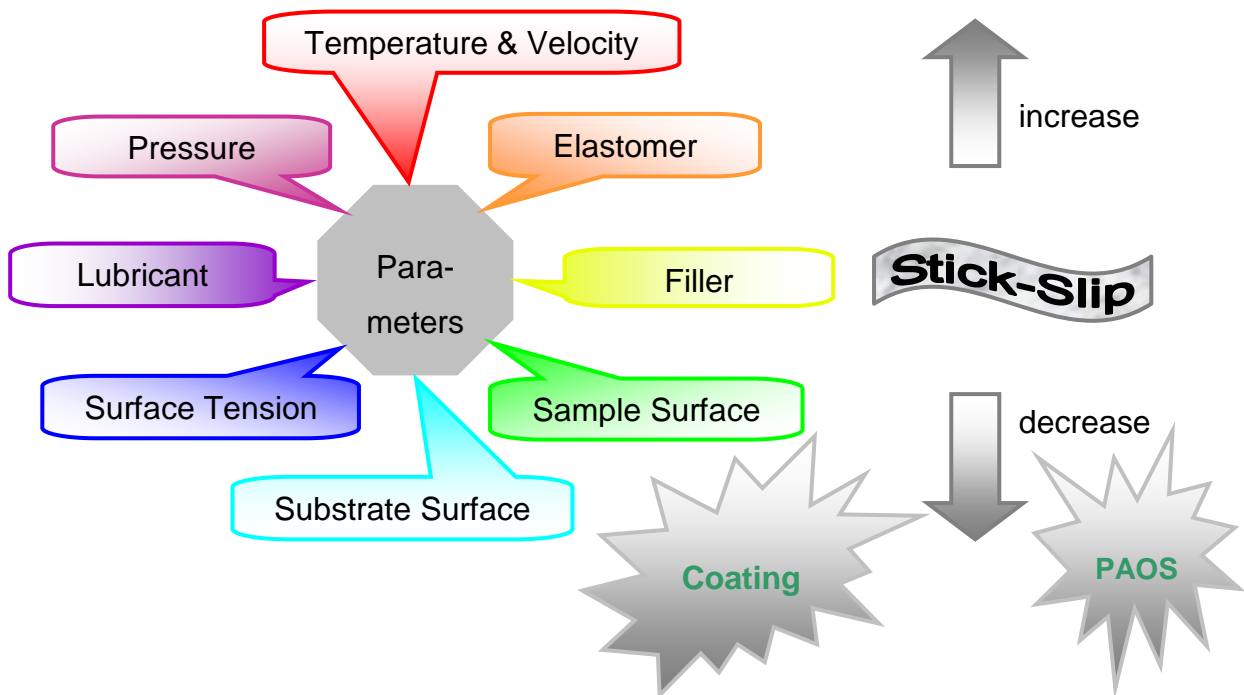
Figure 1: Friction and stick-slip are ruled by many parameters; surface modifications (coating and PAOS particles) may control it by specifically increasing and decreasing the effects.

Different types of elastomer filled with 60 phr highly active carbon black 234 (see chapter 3) were systematically investigated when sliding on rough granite in dry and lubricated state with a stationary velocity. Combining the single friction branches for each temperature by shifting with the same factors as found in DMA measurements results in friction master curves over a significantly larger velocity interval. Low temperatures can be expected to shift the friction curve to the left, high temperatures to the right on the frequency axis.

The second topic deals with the control, in this case a reduction, of friction and related effects. Two alternative solutions, an internal and an external surface modification, are presented here:

The internal method inserts sol-gel systems/ PAOS-particles surrounded by hydrophobic SiO_2 precursors into the rubber matrix, which after annealing embed nanoscopically small, hard, spherical structures on the elastomer surface. These shall reduce the number and real area of contact points and consequently adhesion friction. Similar structures are already known in biology: The sandfish demonstrates the most prominent example of a natural surface that gains an extraordinarily low friction coefficient from hard nanostructures placed on its skin.

The type and amount of PAOS is varied in order to find out a configuration of reducing friction successfully. Because of their relevance for technical applications, NBR and EPDM were chosen as rubber material. For counter surfaces, emphasis lies on granite, but other substrates were tested as well. The influence of the nanostructures on wear and their junction to the rubber matrix is also a matter of interest. Samples are characterized regarding to their surface structures and bulk properties, especially with respect to the distribution of particles and formation of surface patterns. Annealing the PAOS induced sample with appropriate parameters should build the desired structures predominantly at the sample surface.

The external method modifies the sample surface directly by depositing a polymer coating. Several kinds of polymer, with and without particles, were examined to check the influence on the friction coefficient and stick-slip, with the general goal to reduce both of them or even completely eliminate the stick-slip.

Coating was done with and without vapour deposition fluorination for bonding enhancement on SBR and EPDM rubber. To provoke stick-slip in its most intense form, extremely smooth substrates (glass, coated metal sheets, steel) were combined with the elastomers, which had been vulcanized with either smooth or rough surface – in general terms, the substrates were smoother than the samples, unlike in the cases before. The question how well the vulcanized roughness can be conserved in the coating process and whether our simulation model is still valid if the sample is too rough to enter tiny substrate cavities shall be discussed, too.

Beside the various sample/ substrate configurations, multiple temperatures and pressures as main experimental parameters were adjusted to see the effect on friction and stick-slip. Simulations supplement the experimental point of view. Properties of stick-slip like its duration and amplitude were analyzed due to their dependency on these variations. An inspection of layer stability and the changes that the exposure to friction and wear cause complete the contemplations.

1.3 State of the Art

From the beginnings of history, people were applying methods to deal with friction: Lubrication, sledges and wheels were among the earliest inventions of mankind. And from the beginnings of science, thinkers and experimenters were interested in the laws that dictate friction. Leonardo da Vinci was one of these early researchers. The first quantitative description dates from G. Amontons (1699), whose laws say

- $F_R \neq f(A)$ The friction force does not depend on the nominal sample area.

- $F_R = \mu \cdot F_N$ The friction force is proportional to the applied normal force and can be expressed by a factor μ (the coefficient of friction, COF) that correlates with the tangens of the sliding angle of an inclined plane.

Additionally it was assumed that friction is independent from sliding velocity:

$$F_R \neq f(v)$$

These empirical laws describe a number of cases more or less adequately, but not completely. They work sufficiently well for metals or low contact pressures, but fail for polymers, high pressures and extreme velocities. Obviously, a more sophisticated way of looking at things was necessary to achieve a general theory.

Later, C.A. Coulomb [2] stated that static friction, being always higher than dynamic (sliding) friction, rises with the time spent before sliding occurs:

$$F_{stat} = a + b \cdot \ln(t + t_0)$$

In 1902 R. Stribeck published his work on lubricated (hydrodynamic) friction [3] depending on velocity. Named after him, the Stribeck curve (Figure 2) splits up into several velocity intervals:

- Without any movement, only static friction appears.

- For minimal velocity the lubrication film is too thin to show a significant effect, leading to boundary friction similar to dry friction.

- Moderate velocities cause a sufficient lubrication – most parts of the sliding partners are separated by a film. In the realm of this "mixed friction", the friction coefficient, and also wear, decreases with velocity.

- After reaching a minimum, friction rises with velocity when the interface is completely covered with lubricant and hydrodynamic effects become relevant.

Most often friction in Stribeck curves is regarded as a function of lubricant layer thickness compared to subrate roughness. Sometimes the product of velocity and viscosity plotted against friction is taken into account in order to achieve a general description of lubrication influence.
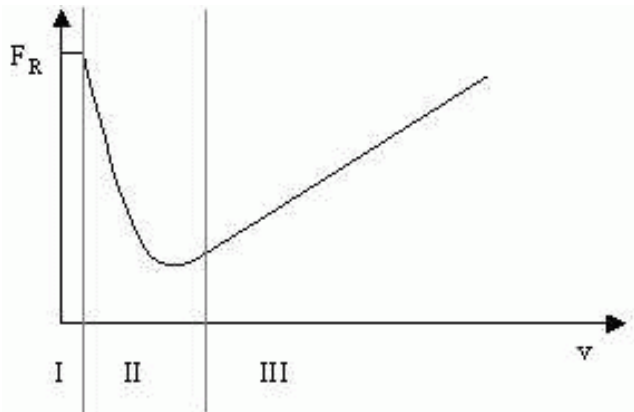

Figure 2: Stribeck curve with boundary friction (I), mixed friction (II) and fluid friction (III)

Modern tribology investigates the forces of interacting object surfaces. In literature, two main mechanisms are assumed to determine the adhesion and friction properties of elastomers on rough, solid surfaces: adhesion friction and hysteresis friction [3]-[14]. Adhesion friction is determined by molecular forces at the interface between substrate and sliding material, caused by attractive interaction of the direct contact. Thus, it is proportional to the true contact area and decreases with increasing roughness. Whereas hysteresis friction dominates on rough and wet surfaces, resulting from viscoelastic inner friction losses (chapter 2.1) due to the deforming of the rubber by asperities of the rough surface, adhesion friction becomes important on smooth and dry surfaces. Characteristical length scales of adhesion and hysteresis friction are shown in Figure 3.
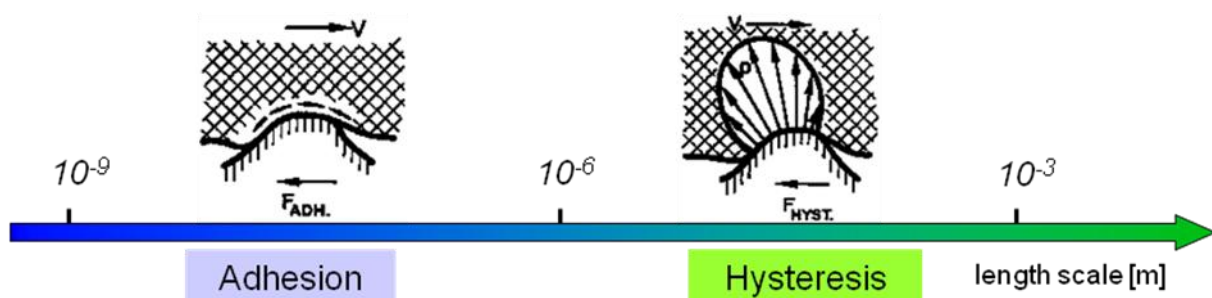

Figure 3: Rubber friction as adhesion and hysteresis on different scales [4]

The relationship between friction coefficient and its change with temperature according to viscoelastic properties had been presented first in 1963 by K. Grosch [5] for rubber systems. His investigations (Figure 4) show that velocity dependent friction at different temperatures can be merged into master curves like the TTS theory (chapter 2.2) predicts. Thus, shifting the friction curves taken at different temperatures horizontally to the velocity axis results empirically in a continuous curve. His results also reveal a maximum of friction, building a plateau for certain systems over a limited velocity/ temperature interval, before declining. Other combinations of rubber and substrate decline directly after the plateau is reached. This plateau/ peak results from a maximum in adhesion friction, correlating to the loss modulus, whereas the loss angle determines the hysteresis friction. The basic shape of the curves differs not only from elastomer to elastomer, but also from substrate to substrate.
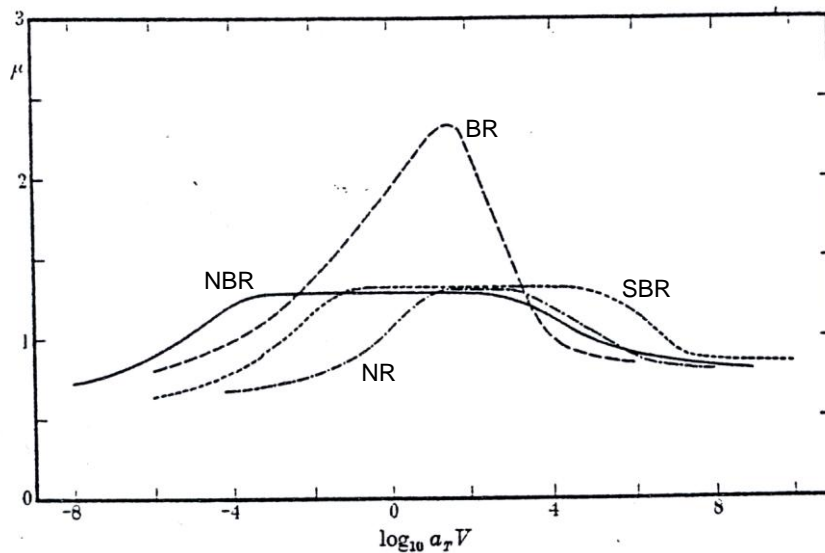

Figure 4: The friction master curves of Grosch show a maximum or ample plateaus for various elastomer types [5].

To describe the substrate, H. Hertz [15] approximated its surface 1882 with a model of equally sized half-spheres. Realistically, the real contact area of the spheres is significantly smaller than the nominal contact area, the macroscopic size of the interface. Later (1966) J. Greenwood and J. Williamson [16] expanded this classical model to randomly distributed ellipsoids ("GW model") for a more natural image. Chapter 2.4 explains these ideas.

In spite of being macroscopically flat, most surfaces display fractal structures on microscopic scales, which can be mathematically defined with the work of B. Mandelbrot [17] in 1982. Applying a fractal perspective on substrate surfaces leads to a statistical evaluation and finally to the height-difference correlation with some surface descriptors to define the surface well, taking into account only the involved asperity summits – see chapter 2.5.

Based on GW surfaces and the fractal surface descriptors, M. Klüppel and G. Heinrich [8] developed 2000 a model to describe hysteresis friction and adhesion friction for soft elastomers sliding at stationary velocity on rough rigid substrates [8],[14] with fit parameters from relaxation spectra according to P. de Gennes [18] in chapter 2.3. This friction theory is the source for the simulations done in this PhD thesis and will be described in chapter 2.6 to 2.8 in detail.

2 Theory of Elastomer Friction on Rough Surfaces

Combining soft elastomers with hard substrates evokes the need for an understanding of the elasticity of the rubber (chapters 2.1 to 2.3) on one hand and the surface geometry of the substrate (chapters 2.4 and 2.5) on the other hand. Chapters 2.6 to 2.8 apply the results to a simulation model.

2.1 Basic Elastomer Mechanics

Rubber is an elastic material. Its static tensile deformation is described by the strain ε, causing a change in the sample length l_0, and the pressure σ under a normal force F_N. Analogously, the shear deformation applies the shearing γ_s and the stress τ_s under a shearing force F parallel to the surface, shown in Figure 5.

$$\varepsilon = \frac{\Delta d}{d_0} \qquad \qquad \text{Equation 1}$$

$$\sigma = \frac{F_N}{A} \qquad \qquad \text{Equation 2}$$

$$\gamma_s = \frac{\Delta l}{d_0} \qquad \qquad \text{Equation 3}$$

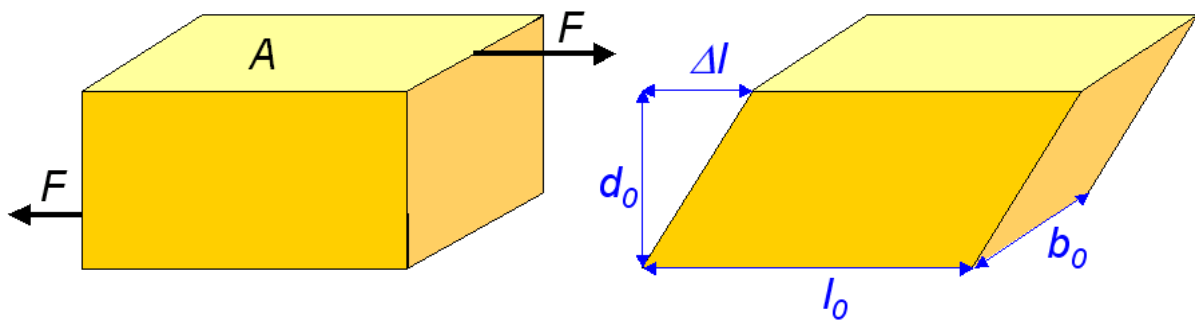$$\tau_s = \frac{F}{A} \qquad F \perp A \qquad \text{Equation 4}$$

Figure 5: Rubber geometry under shearing

The ratio between the change in thickness and length is the Poisson number ν, which becomes 0.5 for incompressible materials like rubber.

$$\nu = -\frac{\Delta d/d}{\Delta l/l} \overset{V=const}{=} \frac{1}{2} \qquad \qquad \text{Equation 5}$$

The compressive modulus E and the shear modulus G are defined as

$$E = \frac{\sigma}{\varepsilon} \qquad \qquad \text{Equation 6}$$

$$G = \frac{\tau_s}{\gamma_s}$$
Equation 7

For linear elastic, isotropic material like rubber, Equation 8 holds:

$$v = \frac{E}{2 \cdot G} - 1$$
Equation 8

In case of incompressibility (Equation 5), both moduli are linked in a simple way. For simplicity, tensile and shear dimensions may then be used analogously.

$$E = 3 \cdot G$$
Equation 9

Rubber is also a viscous material, which is explained by Newtonian behaviour of ideal fluids with viscosity η independent of the shear rate $\dot{\gamma}_s$. A viscosity falling with shear rate is called shear thinning.

$$\eta = \frac{\tau_s}{\dot{\gamma}_s}$$
Equation 10

In the dynamic case, the Equation 1 to Equation 4 become a function of time, leading for periodic treatment with sufficiently small amplitude (linear viscoelasticity) to

$$\varepsilon(\omega, t) = \varepsilon_0 \cdot \sin(\omega \cdot t)$$
Equation 11

$$\sigma(\omega, t) = \sigma_0 \cdot \sin(\omega \cdot t + \delta)$$
Equation 12

$$G^* = G' + i \cdot G'' = \frac{\sigma(\omega)}{\varepsilon(\omega)} = \frac{\sigma_0}{\varepsilon_0} \cdot e^{i\delta(\omega)}$$
Equation 13

$$G' = \frac{\sigma_0}{\varepsilon_0} \cdot \cos \delta$$
Equation 14

$$G'' = \frac{\sigma_0}{\varepsilon_0} \cdot \sin \delta$$
Equation 15

$$\tan \delta = \frac{G''}{G'}$$
Equation 16

Stress and strain are phase shifted with δ, the stress preceding the strain (Figure 6). The shear modulus becomes a complex dimension with the storage modulus G', reflecting the stored elastic energy, as real part and the loss modulus G'' as imaginary part, indicating the dissipated energy. The ratio $tan\delta$ is called loss angle.
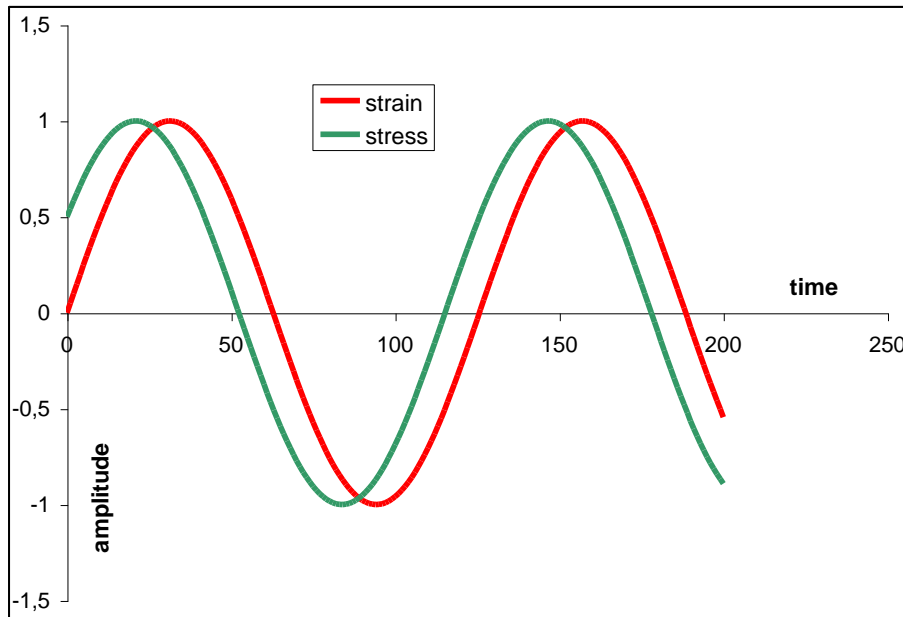
Figure 6: Stress-strain response of harmonically sheared rubber

The interaction of G' and G'' can be plotted in the function between σ and ε, which results in an ellipse as in Figure 7 with the relations

$$G' = \frac{2 \cdot \overline{E}}{\varepsilon_0^2}$$

Equation 17

$$G'' = \frac{2 \cdot \overline{P}}{\omega \cdot \varepsilon_0^2}$$

Equation 18

with the achieved power

Equation 19

$$\overline{P} = \left\langle \sigma(t) \cdot \dot{\varepsilon}(t) \right\rangle = \frac{1}{2} \cdot \omega \cdot \varepsilon_0^2 \cdot G''(\omega)$$
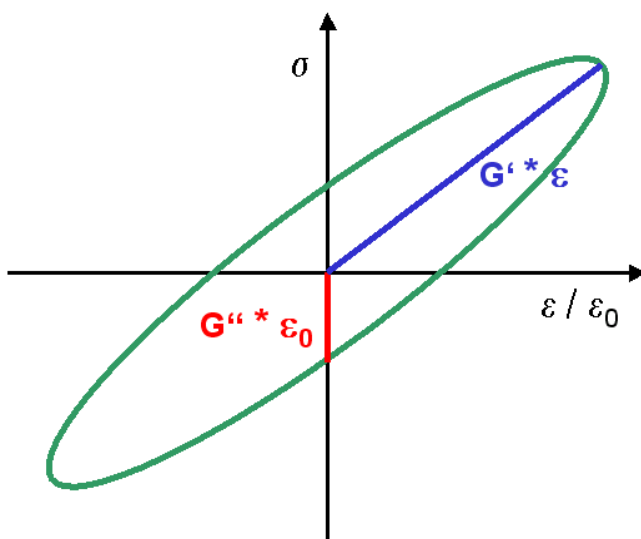

Figure 7: Stress-strain ellipse

Having both viscous and elastic properties, rubber is called *viscoelastic*. The *Maxwell model* (Figure 8) describes linear viscoelasticity as a serial connection of Hooke springs for the elastic and Newtonian dampers for the viscous part. The shear moduli (Equation 14, Equation 15) become [2]

$$G'(\omega) = G \cdot \frac{\omega^2 \cdot \tau^2}{1 + \omega^2 \cdot \tau^2}$$

Equation 20

$$G''(\omega) = G \cdot \frac{\omega \cdot \tau}{1 + \omega^2 \cdot \tau^2}$$

Equation 21

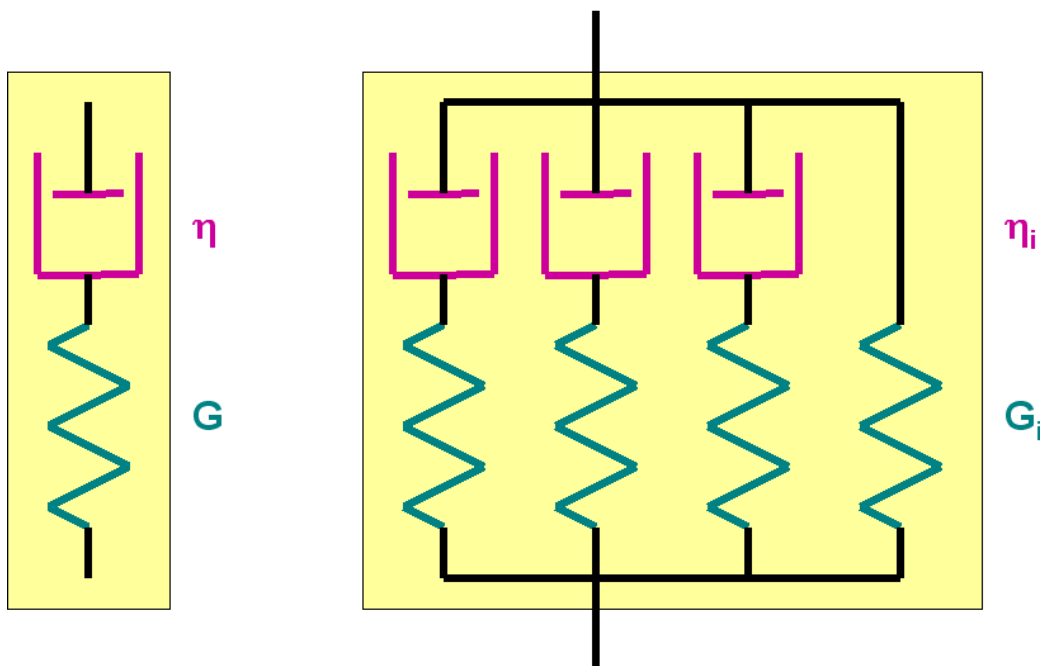$$\tau = \frac{\eta}{G}$$

Equation 22

Figure 8: Equivalent circuit diagram (left: single mode, right: multi mode) of viscoelasticity according to the Maxwell model
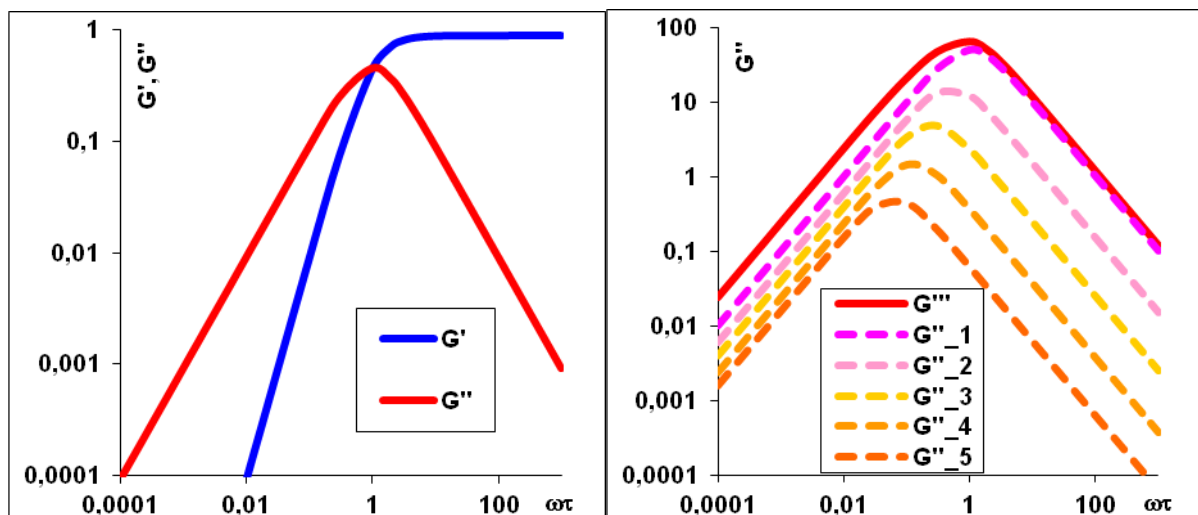

Figure 9: Shear moduli according to Maxwell model (left) and G'' for multi mode (right)

Note that τ is here not the shear stress but the relaxation time. The characteristics of this model are:

- low modulus (G' and G^*, abbreviated for this regime as G_0) and low dissipation (G'') for low frequencies ($\omega \rightarrow 0$), reflecting the softness of rubber for slow processes
- growing modulus and maximal dissipation at medium frequencies, like in a viscous fluid
- maximal modulus G_∞ and low dissipation for high frequencies ($\omega \rightarrow \infty$), which means rubber is hard for fast processes

To consider a spectrum of relaxation times (Figure 9) for a realistic material with different G_i (dashed lines) and η_i, the model can be expanded from single mode to multi mode as a parallel circuit of elements, summing up to a total (solid line):

$$G'(\omega) = G_0 + \sum_i G_i \cdot \frac{\omega^2 \cdot \tau_i^2}{1 + \omega^2 \cdot \tau_i^2}$$

Equation 23

$$G'(\omega) = G_0 + \sum_i G_i \cdot \frac{\omega \cdot \tau_i}{1 + \omega^2 \cdot \tau_i^2}$$

Equation 24

2.2 Time-Temperature-Superposition

Temperature is a paramount factor for viscoelasticity (Figure 10): Cold rubber behaves like an amorphous solid, a glass. Confined in a limited free volume, polymer chains of the elastomer are unable to exhibit position changes, resulting in a high level of energy elasticity. With rising temperature, free volume and chain mobility increase in the transition range. Above the glass transition temperature T_g, another (entropy) elastic plateau for G' appears – chains can now be disentangled and stretched into a preferential direction and will ball again in a relaxation process when the stress on them is released. Density and molecular weight determine the shear modulus at low frequencies according to the Rouse-Mooney model for entangled polymer melts [19]:

$$G' = \frac{\rho \cdot R \cdot T}{M_e}$$

Equation 25

With even higher temperatures, the entangled chain structure decomposes and the rubber will flow plastically like a viscous liquid. The loss modulus then exceeds the storage modulus:

$$\omega \to 0 \Rightarrow G' \sim \omega^2, G'' \sim \omega$$

Equation 26

The course of the temperature curve is identical with that of elasticity related to frequency, with high temperatures corresponding to low frequencies and vice versa. This phenomenon is called *time-temperature superposition* (TTS).

$$G(a(T) \cdot f_{ref}) = G(a(T_{ref}) \cdot f), \qquad G = G' \, or \, G''$$

Equation 27

It is thus possible to compare two frequency dependant elasticity curves of different temperature by shifting one of them on the frequency axis until the corresponding temperature is reached. Shifting on a logarithmic scale means multiplication of the original frequencies with a factor we will call a_T and that obeys a semi-empirical law formulated by Williams, Landel and Ferry [1]:

$$\log(a_T) = \frac{-C_1 \cdot (T - T_{ref})}{C_2 + T - T_{ref}}$$
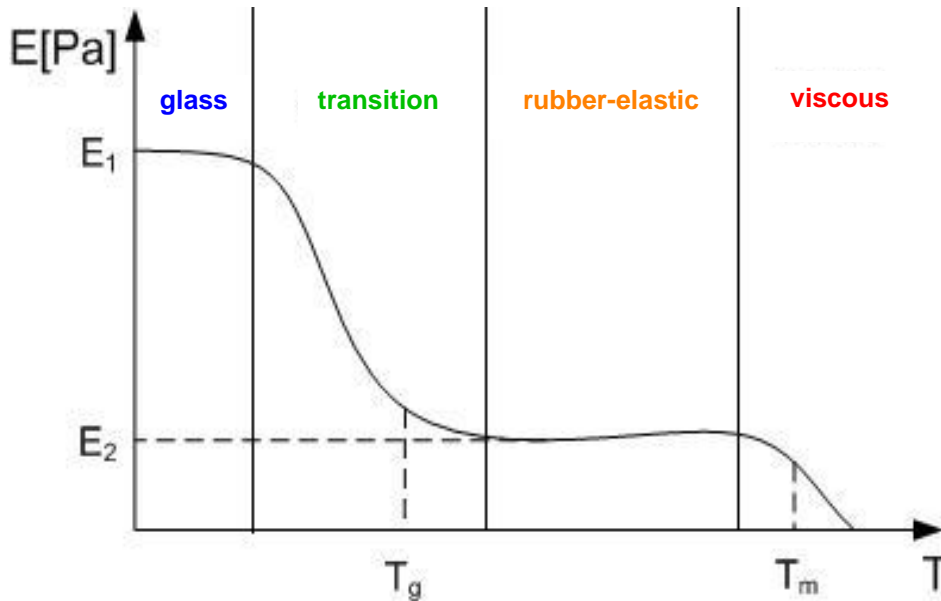
Equation 28

Figure 10: Temperature dependency of the elastic storage modulus [20]

The WLF law is valid above T_g for a limited range, empirically 100 K above glass transition with material constants C_1 and C_2. A reference temperature must be picked within this range, usually room temperature for easy comparison with experimental data. Alternatively, universal shift factors of $C_1 = 17.44$ and $C_2 = 51.6°C$ may be used when T_g is the reference temperature for most elastomers. Applied on an unfilled rubber, viscoelastic measurements of limited frequency ranges can be expanded to a wide range by measuring at various temperatures and shifting these isotherm branches according to WLF into one continuous *master curve*, as demonstrated in Figure 11. Below T_g the curves are adjusted for maximal continuity (Figure 12).
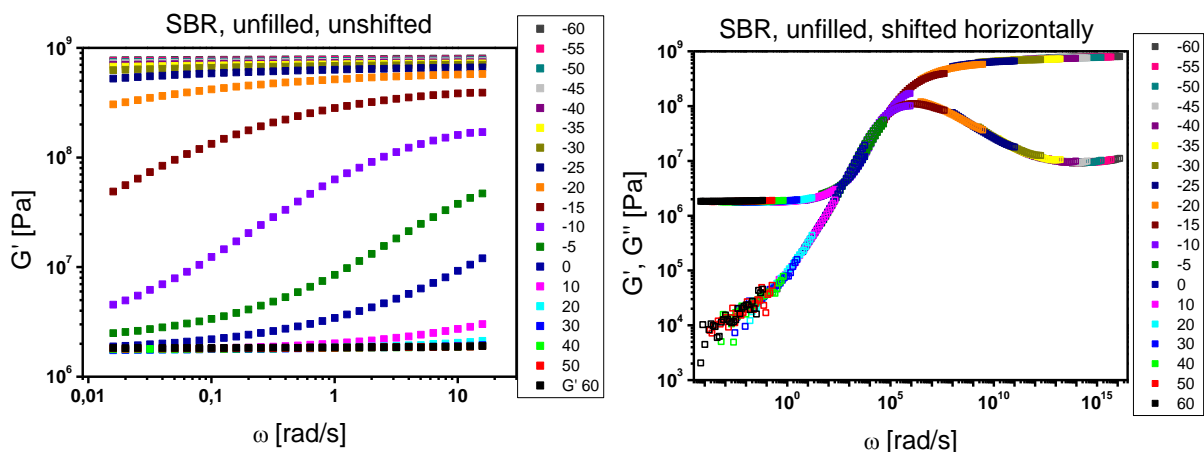

Figure 11: Single (coloured) temperature branches of unfilled rubber (left for G') can be shifted horizontally to master curves (right for G' and G" with identical shift factors).
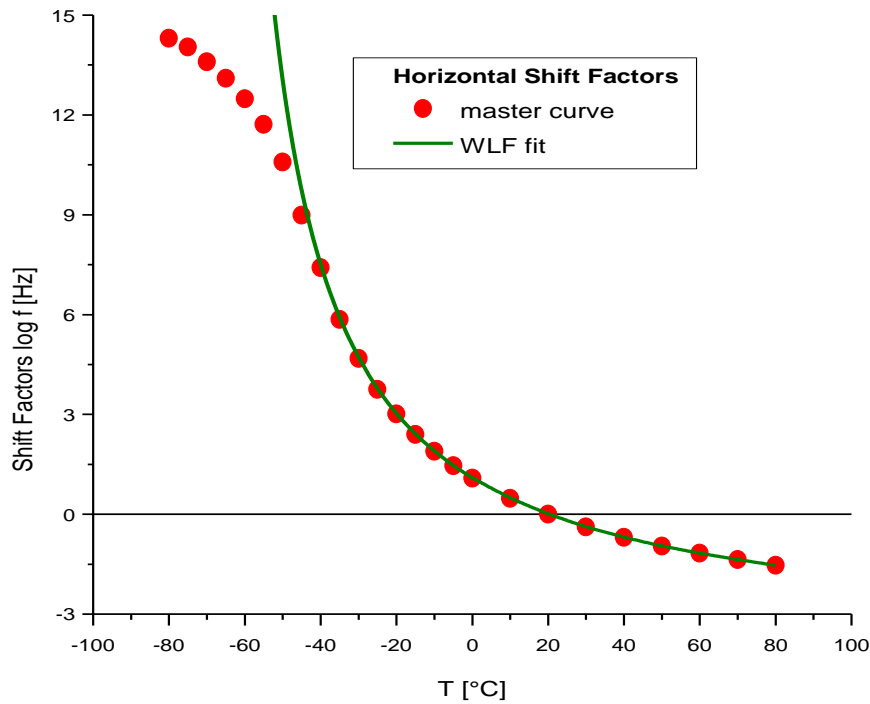
Figure 12: Horizontal shift factors of a master curve fit to the WLF law above T_g.

Difficulties arise from blending polymers, as several functions overlap each other. Using a filler in a homogenous elastomer matrix does not prevent the WLF law from working; horizontal shifting remains unchanged – glass transition with its material constant T_g is caused by the rubber matrix, independent of filler, so a frequency shift is done first with the a_T known from the unfilled sample. However, non-linear behaviour (the *Payne effect* [21]) has to be considered: The higher the amplitude, the more this effect pertains to storage and loss modulus differently. This means a vertical shift (on the elasticity scale, again logarithmically, see Figure 13) with factors f_V is necessary for both *G'* and *G''* separately: the storage modulus because the filler-filler bonds depend on the temperature, the loss modulus because high amplitudes destroy the *virgin bonds* of the clustered filler particles [22]. This can be described by the *Vogel-Fulcher* equation:

$$f = f_\infty \cdot e^{-\frac{E_a}{R \cdot (T - T_{VF})}}$$
                                                                      Equation 29

with the Vogel-Fulcher temperature $T_{VF} \approx T_g - 50°C$, the activation energy E_a and the gas

constant $R = 8{,}3144 \dfrac{\text{J}}{\text{K} \cdot \text{mol}}$.
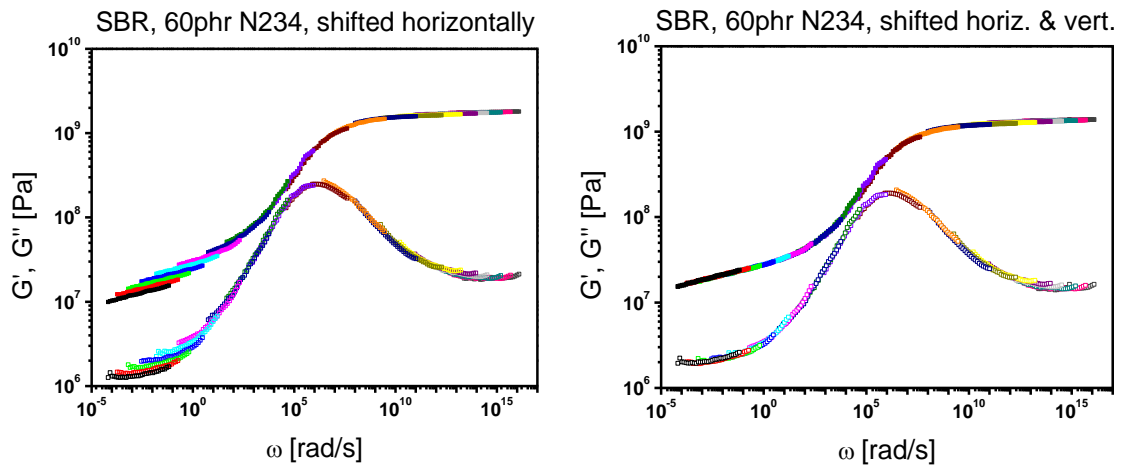
Figure 13: Vertical shift for a carbon filled rubber affects mainly the high temperature part.

In an *Arrhenius plot* (logarithmic scale against reciprocal temperature, Figure 14) the graph of the moduli become a straight line with a slope revealing the activation energy as E_a/R, related to the WLF constants by [23]

$$C_2 = T_{ref} - T_{VF}, \qquad E_a = 2{,}303 \cdot C_1 \cdot C_2 \qquad\qquad \text{Equation 30}$$

Figure 14: Vertical shift factors for *G'* and *G''* in an Arrhenius plot

2.3 Relaxation Time Spectra

As explained in chapter 2.1, a constant strain causes a stress in the elastomer that decays during time, whereas a constant stress makes the strain rise to a constant level within time. This is due to relaxation processes with a relaxation time $\tau = 1/\omega$ defined in Equation 22. The relaxation time spectrum is then [2]

$$G(t) = \int_{-\infty}^{\infty} H(\ln \tau) \cdot e^{-t/\tau} d\ln(t)$$
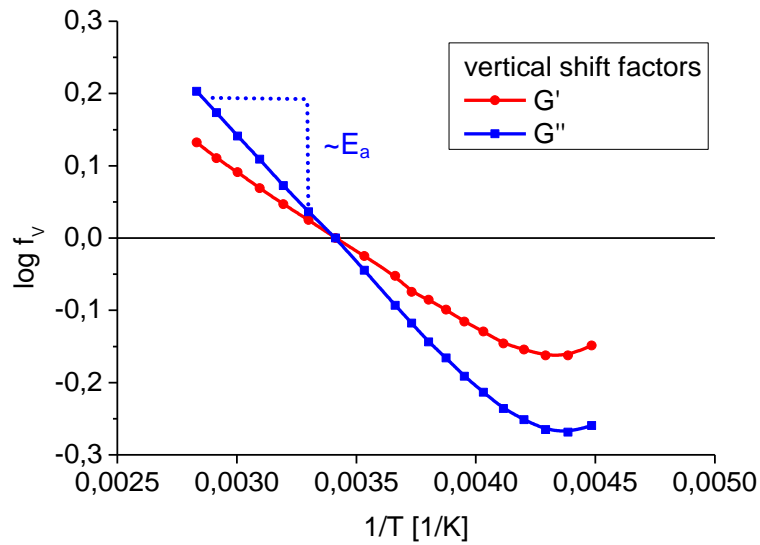
Equation 31

Several types of ansatz exist to solve this equation. The method of Ferry and Williams [1] assumes $e^{-t/\tau} = 0$ for $t < \tau$ and $e^{-t/\tau} = 1$ for $t > \tau$, which leads to

$$H(\omega) = A \cdot G' \cdot \frac{d\log(G')}{d\log(\omega)}$$

Equation 32

as iterative approximation procedure with the correction term

$$A = \frac{2 - \alpha}{2 \cdot \Gamma\left(2 - \dfrac{\alpha}{2}\right) \cdot \Gamma\left(1 + \dfrac{\alpha}{2}\right)}$$

Equation 33

α is the derivative $dH/d\omega$ from the first approximation, and Γ the gamma function. A typical example is shown in Figure 15. For the glass transition range the spectrum displays a decay

$$H(\tau) = H_0 \cdot \left(\frac{\tau}{t_0}\right)^{-m}$$

Equation 34

with a power law exponent, in double logarithmic scale as linear slope

$$m = -\frac{d\log(H)}{d\log(\tau)}$$

Equation 35

for $0 < m(\tau) < 1$, which enables us to define an exponent n we will need later to describe adhesion friction [18]:
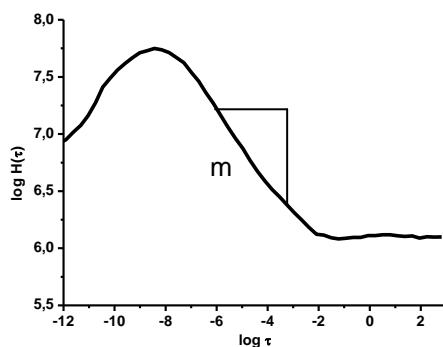
$$n = \frac{1 - m}{2 - m}$$

Equation 36

Figure 15: Typical relaxation time spectrum

2.4 Contact Theory

Understanding the interaction of two interfaces in contact requires knowledge of the surface structures. Assuming the elastomer is flexible enough to match the texture of its counterpart, we can restrict the surface description to the substrate.

A first analytical acquisition of non-adhesive contact surfaces for homogeneous, isotropic materials was raised by Hertz [24], who described simple surface geometries, as linear elastic spheres with radii R_i

$$h_{Hz} = \sqrt[3]{F_N^2 \cdot D^2 \cdot \left(\frac{1}{R_1} + \frac{1}{R_2} \right)}$$

Equation 37

generating a contact radius a_{Hz} (Figure 16)

$$a_{Hz} = \sqrt[3]{F_N \cdot D \cdot \left(\frac{R_1 \cdot R_2}{R_1 + R_2} \right)}$$

Equation 38

under a load force F_N in a distance h_{Hz} between two of such surfaces in contact. The reduced Young modulus D

$$D = \frac{3}{4} \cdot \left(\frac{1 - v_1^2}{E_1} + \frac{1 - v_2^2}{E_2} \right)$$

Equation 39

contains the elastic moduli E_i and the Poisson numbers v_i of the involved materials (1 = substrate, 2 = rubber). Incompressible materials $(v_1 = v_2 = 1/2)$ and a rubber relatively flat $(R_1 \ll R_2)$ and soft $(E_1 \gg E_2)$ compared to the substrate simplify these relations. This means the rubber counts for elasticity but not for the geometry, and vice versa does the substrate, resulting in a contact area

$$A_{Hz} = \pi \cdot R_1 \cdot h_{Hz}$$

Equation 40

Thus the indented area is proportional to $F_N^{2/3}$ for two pressed spheres, indicating an increase of total friction and a decrease of the friction coefficient. With the Hertz theory the complete surface is regarded as covered with spheres of constant size at the same level.
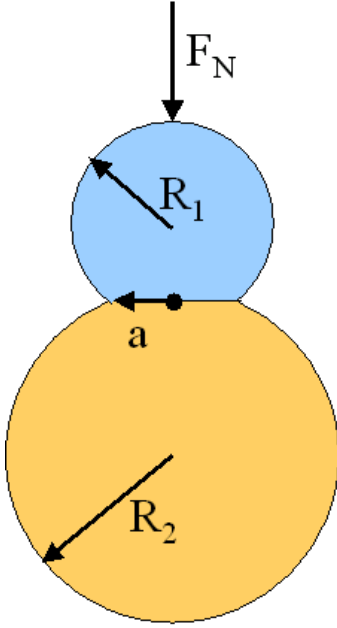
Figure 16: Two Hertz spheres in contact

Real surfaces do not consist of perfect spheres. They rather have heights z as a function of its lateral coordinates x and y, so $z(x, y)$ with a height distribution (HD) $\Phi_{HD}(z)$ of a standard deviation σ_{HD} and are not spherical but rather ellipsoids with different radii. Greenwood and Williams (GW) [16] enhanced Hertz's idea when they approximated surface asperities with spheres of Gaussian distributed heights h (Figure 17), leaving shape and size of the spheres as negligibly [25] identical. With the normalized distance t

$$t = \frac{d}{\sigma_{HD}}$$

Equation 41

from the gap distance $d := z - h$ as the space between rubber and average substrate level (Figure 18), the general *GW function* can be defined as

$$F_n = \int_t^\infty (z-t)^n \cdot \phi_{HD}(z)dz$$

Equation 42

Depending on the exponent they belong to various features of the GW surfaces:

$$n_{GW} = N_{GW} \cdot F_0 = N_{GW} \cdot \int_t^\infty \phi_{HD}(z)dz$$

Equation 43

This is the number of contact dots from the entirety N_{GW} of spheres.

The contact area can be written as

$$A_{GW} = \pi \sum_i a^2_i = N_{GW} \cdot \pi \cdot R \cdot F_1 = N_{GW} \cdot \pi \cdot R_1 \cdot \int_t^\infty (z-t) \cdot \phi_{HD}(z)dz$$

Equation 44

Finally the resulting force can be given for the assumptions made before:

$$F_N = \frac{N_{GW} \cdot \sqrt{R}}{D} \cdot F_{3/2} = \frac{16}{9} \cdot N_{GW} \cdot E_2 \cdot \sqrt{R_1} \cdot \int_{t_s}^{\infty} (z - t_s)^{\frac{3}{2}} \cdot \phi_{SHD}(z) dz \qquad \text{Equation 45}$$
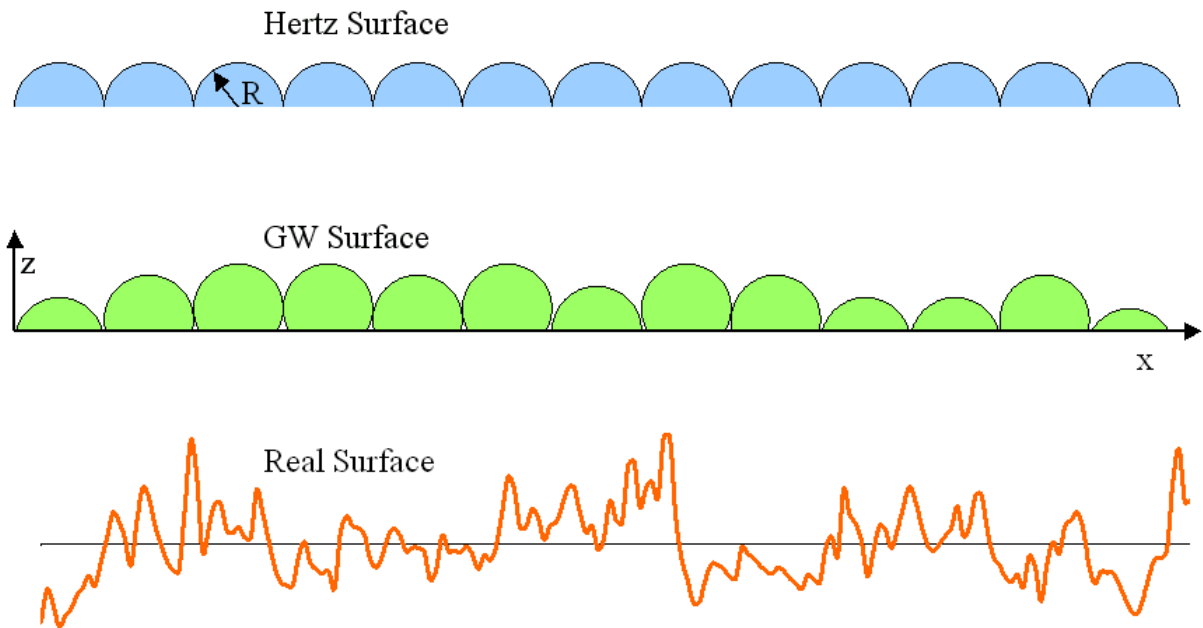
Figure 17: Hertz and Greenwood-Williams description of surface geometry
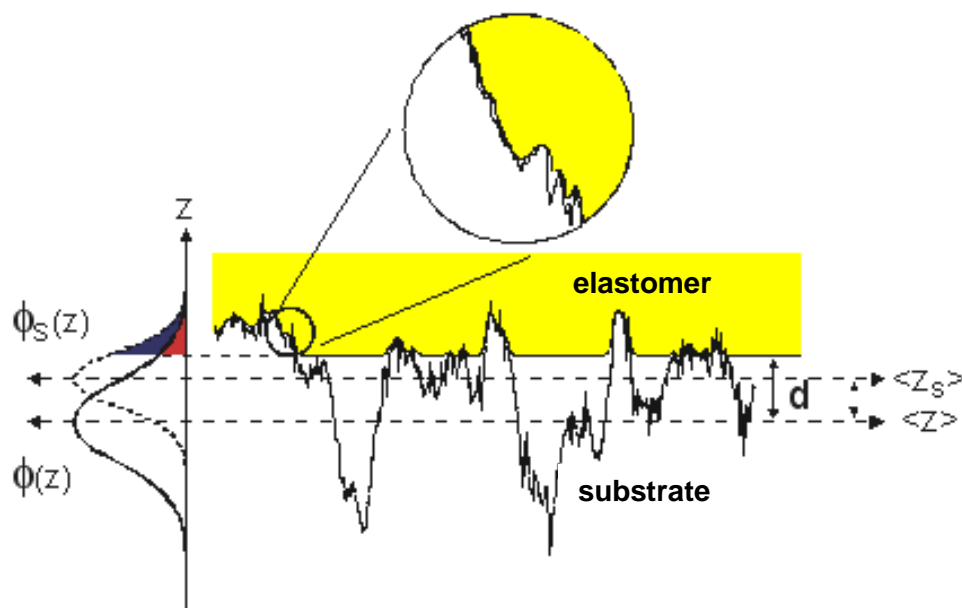
Figure 18: Surface profile of the substrate. Asperities pierce into the elastomer (yellow). Height distribution and summit height distribution are given on the left [26].

Even the GW ansatz with its clearly defined surface tips has its limitations, as the elastomer does not fill all cavities of a real surface and neither reaches all asperities, as real peaks are not independent from each other. The left part of the distribution (the valleys and deep cavities) contributes little to the contact zone and allows to regard even asymmetric distributions as Gaussian [25]. In order to neglect those asperities that are too low to indent the rubber, the relation is based not on the normal height distribution but on the summit

height distribution (SHD) Φ_{SHD}. To find this distribution, a maximal distance $\xi_{||}$ between two neighbour asperities with maximal size $\xi_{\perp}$ is postulated, see Figure 19.
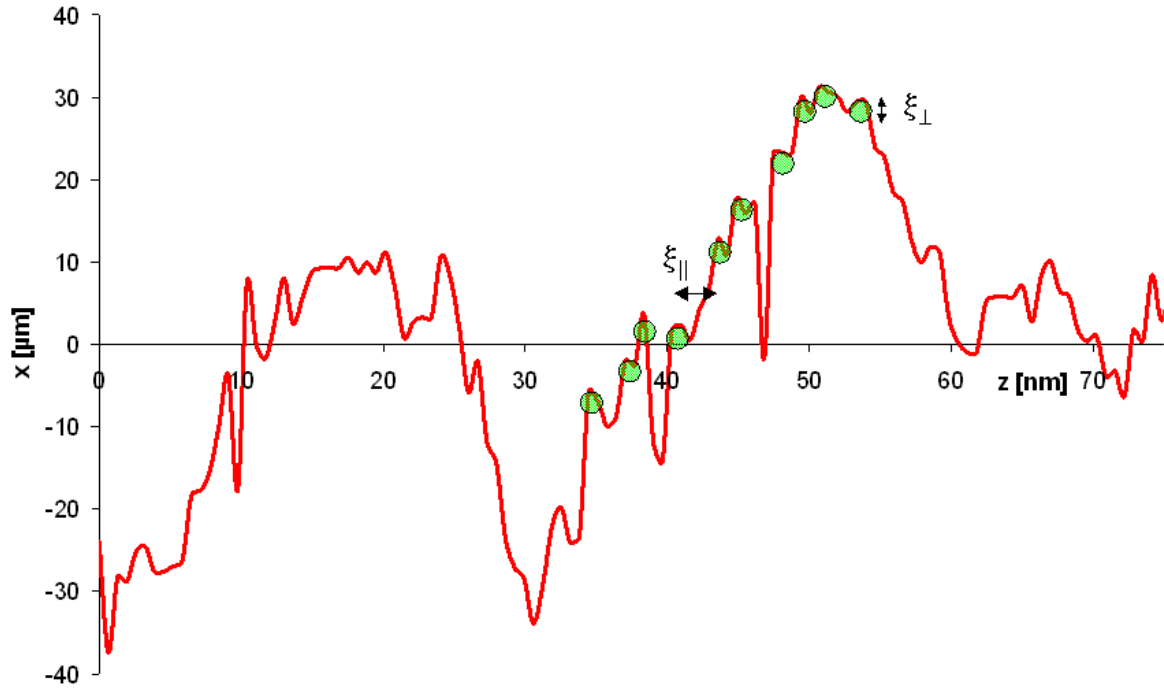
Figure 19: A height profile (red) and some of its relevant summits (green dots)

The SHD can be calculated from the height distribution $\Phi_{HD}(z)$ with the same maximum at z_{max} by an affine transformation with a parameter $s > 1$ as a surface constant:

$$z_s = \frac{(z - z_{max})}{s} + z_{max}$$

Equation 46

This s-parameter is gained by fitting the height distribution of the substrate profile to the summit height distribution which takes into account only the local maximum surface points that have direct contact to of the sample [26],[27]. The transformed distribution is shifted towards higher z-values, as shown in Figure 20. To normalize the distance we now use $t_s = d/\sigma_{SHD}$. The deviation of the SHD also transforms with this parameter, making the distribution narrower:

$$\sigma_{SHD} = \frac{\sigma_{HD}}{s}$$

Equation 47

The affine transformation connects maximal and average heights by

$$\langle z_s \rangle = z_{max} \cdot \left(1 - \frac{1}{s}\right)$$

Equation 48

Figure 20: Original height distribution (blue), transformed distribution (red) and summit height distribution (green) for the smooth vulcanization plate

2.5 Self Affinity and Surface Parameters

In order to take the properties of the rough substrate surface into account, we need to find a statistical description for its most prominent features. Many natural and technical surfaces, including the substrates used in this work, turn out to have a self-affine behaviour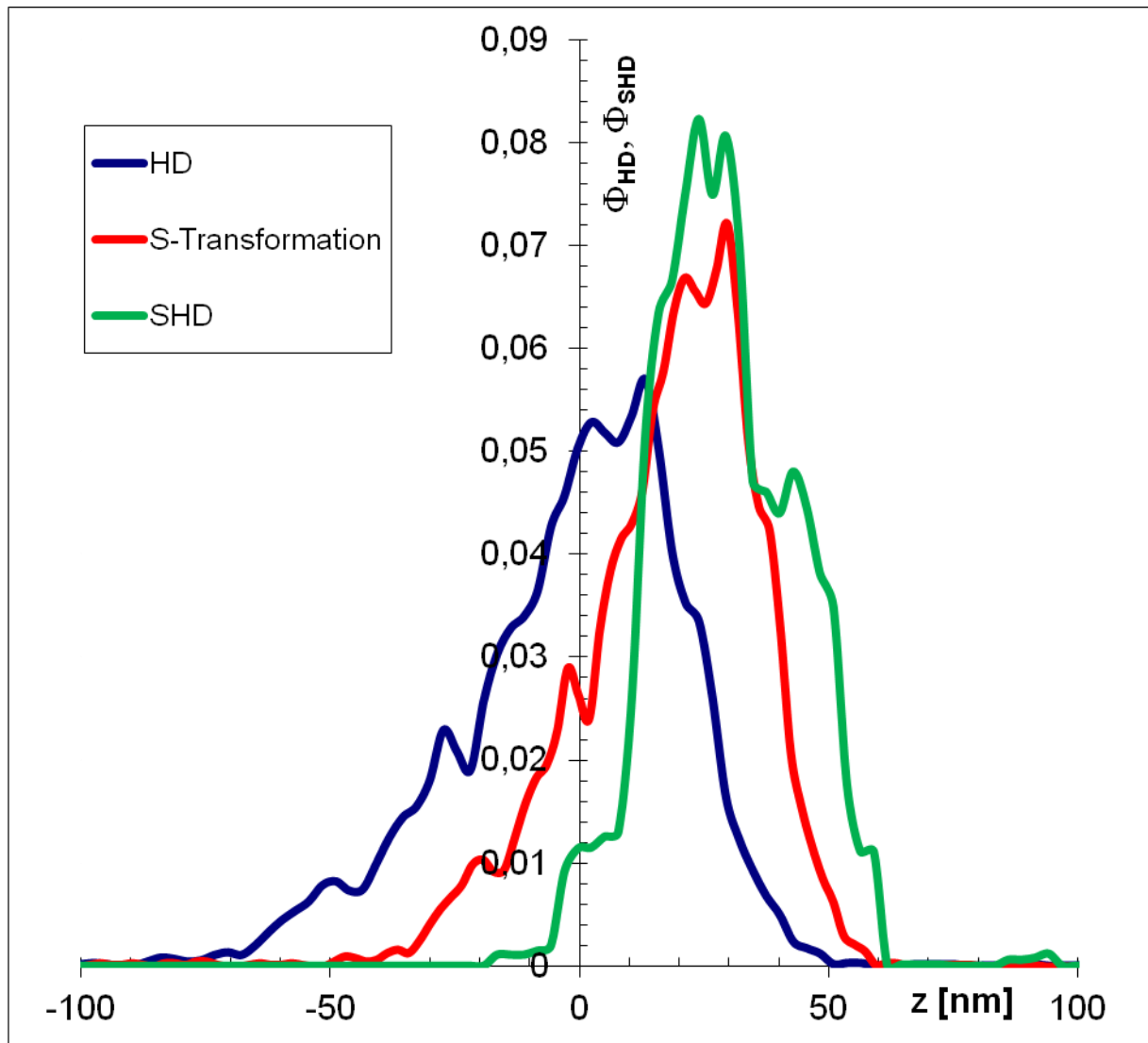 [17]. The morphology and statistical properties of self-affine surfaces stay unaffected by an anisotropic transformation: from $x \rightarrow \alpha \cdot x$ and $y \rightarrow \alpha \cdot y$ follows $z \rightarrow \alpha^H \cdot z$ with the Hurst exponent H in the range $H = [0...1]$. This means that the substrate looks qualitatively the same at different magnifications α in the xy-plane and α^H in z-direction with the Hurst coefficient (Figure 21). It is connected to the fractal dimension D by

$$D = 3 - H$$
<div align="right">Equation 49</div>

for a 3-dimensional embedding space. The fractal dimension ranges from 2 to 3 for rough three dimensional surfaces. In general, the fractal dimension is defined by the lengths of its generators g and initiators i

$$D = \frac{\log(g)}{\log(i)}$$
<div align="right">Equation 50</div>

and thus by the self-affine algorithms that underlie its geometry. The self-affine character of the surface holds up to a cut-off length which differs in a horizontal (lateral) and a vertical direction. We denote the lateral part as $\xi_{\parallel}$ and the vertical part as $\xi_{\perp}$.
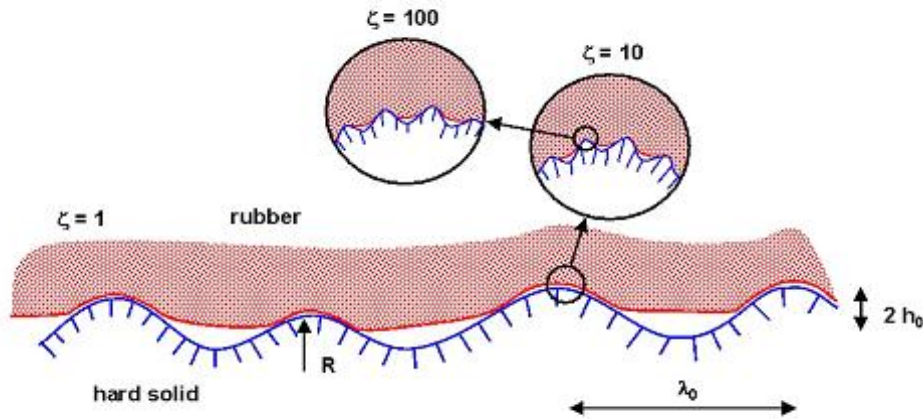
Figure 21: Schematic view of self-affinity for various magnifications [28]

In order to find out which cut-off lengths apply to a given surface and to achieve a value for the fractal dimension, we calculate the height-difference correlation (=HDC) function $C_z(\lambda)$ as

$$C_z(\lambda) = <(z(x + \lambda) - z(x))^2>$$
<div align="right">Equation 51</div>

The HDC is a measure of how strongly neighbouring points are related to each other. Assuming two points of the surface have the lateral distance λ, their heights are $z(x)$ and

z(x+λ), respectively. The squares are averaged using the "< >" stochastic average over all possible distance combinations of the rough surface. The profile does not need to be symmetric [29]. As a result, the HDC can be plotted against the distance *λ* as in Figure 22. For a surface ruled by only one fractal pattern, the graph is linear below the cut-off lengths.
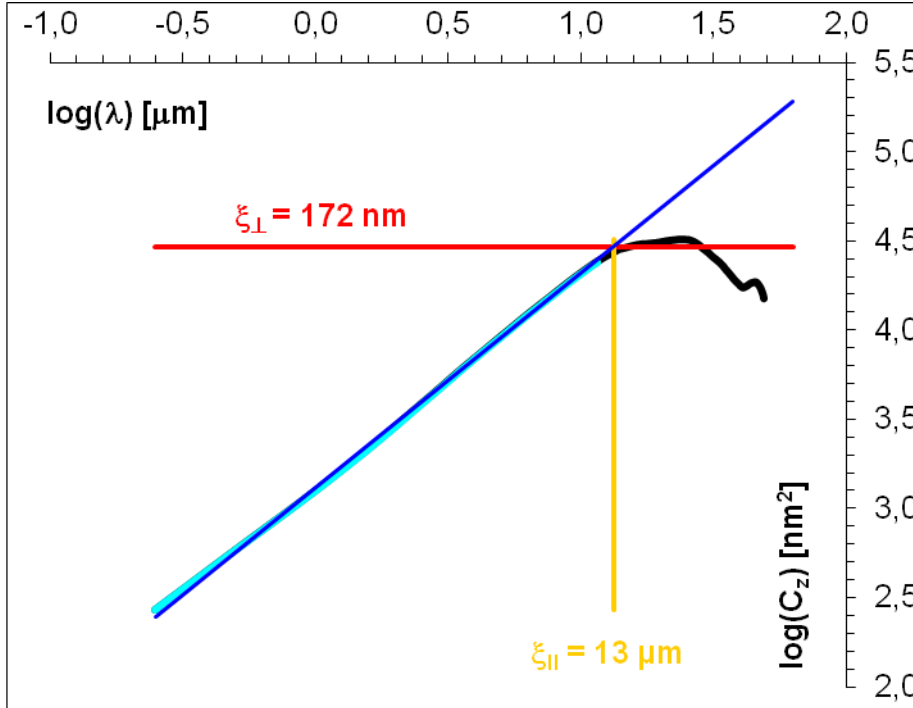
Figure 22: Example of a monofractal height-difference correlation with a linear slope (blue) until the cut-off lengths $\xi_{//}$ (lateral, yellow) and $\xi_\perp$ (vertical, red)

When more than one fractal influence coins the surface, they superpose each other and make a more sophisticated description necessary. Instead of one, two or more linear ranges are recognised. For many of the employed substrates (chapter 3.6.2) an approach of two fractal asymptotes has turned out to be appropriate. The HDC graph is then split into three regimes: Above the cut-off length $\xi_{//}$ the surface is flat, i.e. no correlation between the points can be found except for a similar common height level that determines $\xi_\perp$; this shall be called here macroscopic range. Below the $\xi_{//}$ down to the lowest measurable length λ_c the HDC can be described well by two linear functions and thus can be approximated by two scaling ranges. As a result, two different fractal dimensions D_1 and D_2 occur, meeting at the cross over length λ_2, separating the microscopic and mesoscopic range (Figure 23). The relationship between C_z and the surface parameters $\xi_\perp$, $\xi_{//}$, λ_2, D_1 and D_2, which we can extract from the HDC, is [30] for the "mesoscopic" range at $\lambda_2 < \lambda < \xi_{//}$

$$C_z(\lambda) = \xi_\perp{}^2 \cdot \left(\frac{\lambda}{\xi_{//}}\right)^{2H_1}$$

Equation 52

and for the "microscopic" range at $\lambda < \lambda_2$

$$C_Z(\lambda) = \xi_\perp^2 \cdot \left(\frac{\lambda}{\lambda_2}\right)^{2H_2} \cdot \left(\frac{\lambda_2}{\xi_\parallel}\right)^{2H_1}$$

Equation 53

If more than two scaling ranges should be necessary, the formulas can be expanded to any wanted number of multifractality [23],[26].

$$C_Z(\lambda) = \xi_\perp^2 \cdot \prod_{i=1}^{n-1}\left(\frac{\lambda_{i+1}}{\lambda_i}\right)^{2H_i} \cdot \left(\frac{\lambda}{\lambda_n}\right)^{2H_n}$$

Equation 54
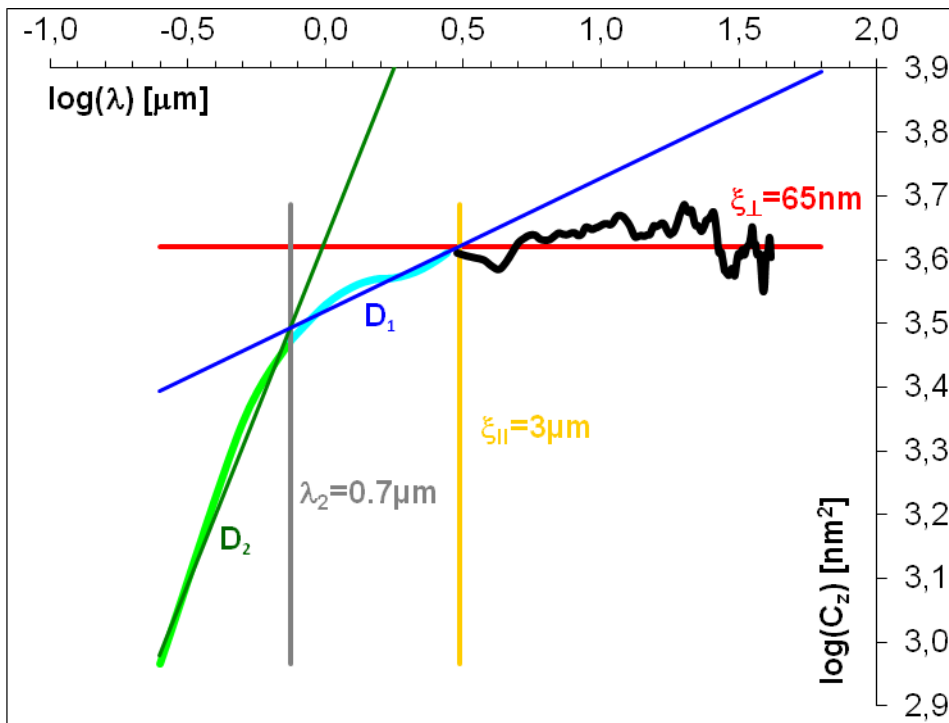
Figure 23: The HDC for a bifractal surface with a microscopic (D_2), mesoscopic (D_1) and macroscopic (almost flat) range

By Fourier transformation to the frequency space with $\omega_{min} = 2\pi v/\xi_\parallel$ and $\omega_2 = 2\pi v/\lambda_2$ where v is the sample velocity, a corresponding power spectral density $S(\omega)$ (see Figure 24) can be written for the two scaling ranges [31],[32]:
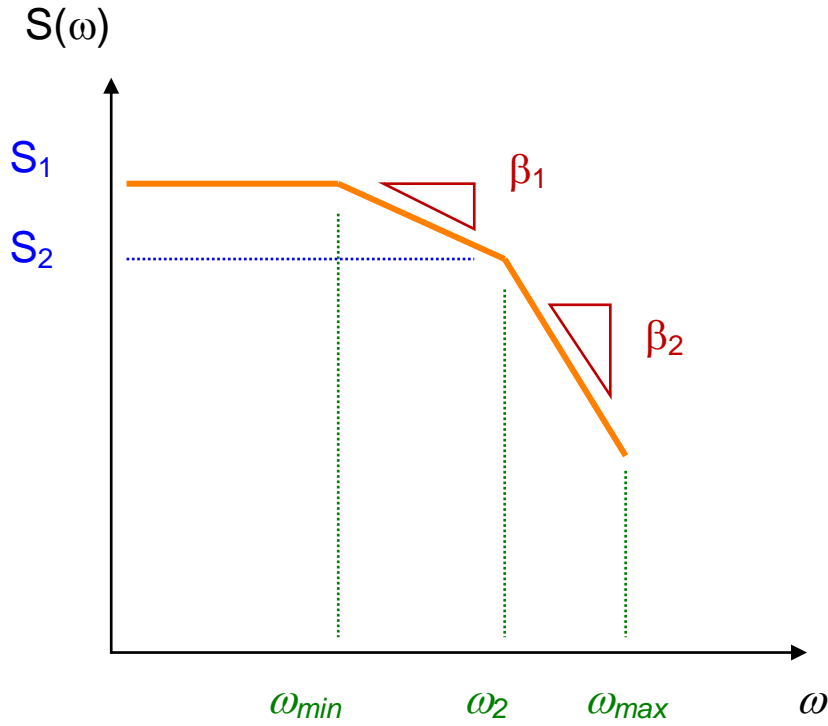
Figure 24: Bifractal power spectrum [32]

$$S_1(\omega) = \frac{(3-D_1)\cdot \xi_\perp^{\,2}}{2\pi\,v\,\xi_{ll}} \cdot \left(\frac{\omega}{\omega_{min}}\right)^{-\beta_1}$$

Equation 55

for $\omega_{min} < \omega < \omega_2$ or

$$S_2(\omega) = \frac{(3-D_1)\cdot \xi_\perp^{\,2}}{2\pi\,v\,\xi_{ll}} \cdot \left(\frac{\omega_{min}}{\omega_2}\right)^{\beta_1} \cdot \left(\frac{\omega}{\omega_2}\right)^{-\beta_2}$$

Equation 56

for $\omega_2 < \omega$ respectively, where we abbreviate the fractal dimension for $i = 1, 2$ with $\beta_i = 7-2D_i$. The frequencies are

$$\omega_{min} = 2\pi v/\xi_{ll}$$

Equation 57

$$\omega_2 = 2\pi v/\lambda_2$$

Equation 58

2.6 Hysteresis Friction

Generally speaking, friction is any force that counteracts the mechanical movement of objects that interact via a common surface by the interaction itself, resulting in a conversion of kinetic energy into heat by energy dissipation. It occurs as fluid friction when objects move through liquids or gases. This behaviour is described by the fields of hydrodynamics and aerodynamics. Other laws hold for the friction of solid bodies, depending on the type of movement, be it sliding (which means dynamic or kinetic friction as linear movement where the sample offers a constant surface part to an always new part of the substrate), rolling (a cyclically changing part of the sample is in non-sliding contact with the substrate) or static friction (no relative velocity, so movement can only start after the "sticking" is overcome). This work concentrates on the friction of two macroscopic solids in sliding contact with a clearly defined, constant ("stationary") velocity.

Sliding friction μ_{tot} as ratio of total friction force F_{fric} and normal force[1] F_N

$$F_N = \sigma_0 \cdot l_0 \cdot b_0 = \left| E(\omega_0) \right| \cdot \left\langle z_P \right\rangle \qquad \text{Equation 59}$$

determined by pressure σ_0 and geometry (or by the corresponding sliding angle α) can be divided into several superposing parts [32]: most important are the hysteresis friction μ_{Hys} and the adhesion friction μ_{Adh}, which will be treated in chapter 2.7. Two more parts will be not be considered in this work: the cohesion friction μ_{Coh} as an in our system negligible effect between sample and its own wear particles, and the viscous friction μ_{Vis} that does not occur significantly either as even with lubrication the film was rather small and of low viscosity. All friction parts are subject to parameters like velocity in their own terms.

$$\mu_{tot} \equiv \frac{F_{fric}}{F_N} = \tan \alpha = \mu_{Adh} + \mu_{Hys} + \mu_{Coh} + \mu_{Vis} \qquad \text{Equation 60}$$

This chapter deals with hysteresis friction, which is caused by the energy dissipations where the rubber sample is deformed at local asperities when sliding over a rough ground surface. The dissipated energy can be written as

$$\Delta E_{diss} = \int_0^V \int_0^{t_{fric}} \sigma \cdot \dot{\varepsilon}\, dt\, d^3x = \frac{V \cdot t_{fric}}{2} \cdot \int_{\omega_{min}}^{\omega_{max}} \omega \cdot E''(\omega) \cdot S(\omega) d\omega \qquad \text{Equation 61}$$

with the excited volume V

---

[1] We assume only positive normal forces. Though a negative force is possible as sticking via adhesion when pulling the sample vertically away, it did not appear in the experiments, and would not have led to friction anyway [39].

$$V = \langle \delta \rangle \cdot L \cdot \lambda_0 = \langle \delta \rangle \cdot A_0 \qquad \text{Equation 62}$$

from the average excitation depth

$$\langle \delta \rangle = b \cdot \langle z_p \rangle = b \cdot \sigma_{HV} \cdot F_1(t) \qquad \text{Equation 63}$$

and the sliding time t_{fric} as integration borders for the pressure σ and change of strain ε, or tension and deformation, respectively, using the *Wiener-Khintchine theorem:*

$$\langle \varepsilon(\omega) \cdot \varepsilon^*(\omega') \rangle = \frac{S(\omega) \cdot \delta(\omega - \omega')}{2} \qquad \text{Equation 64}$$

that connects the power spectral density (PSD) with the Fourier transformed autocorrelation function and thus with the squared amplitudes of the excitation by surface asperities.

$$\sigma(t) = \int \hat{\sigma}(\omega) \cdot e^{i \cdot \omega \cdot t} d\omega \qquad \text{Equation 65}$$

$$\varepsilon(t) = \int \hat{\varepsilon}^*(\omega) \cdot e^{-i \cdot \omega \cdot t} d\omega \qquad \text{Equation 66}$$

In this case Dirac's Delta function is

$$\delta(\omega - \omega') = \frac{1}{2\pi} \cdot \int e^{i \cdot (\omega - \omega') \cdot t} dt \qquad \text{Equation 67}$$

The excited frequencies, which follow the PSD as given in Equation 55 and Equation 56, can be used for the hysteresis integral [23],[33] to gain the friction force F_{Hys}

$$F_{Hys} = \frac{\Delta E_{diss}}{v \cdot t_{fric}} \qquad \text{Equation 68}$$

under a normal force F_N and thus the friction coefficient μ_{Hys} is according to our model [27]

$$\mu_{Hys}(v) \equiv \frac{F_{Hys}}{F_N} = \frac{<\delta>}{2\,\sigma_o v} \cdot \left(\int_{\omega_{min}}^{\omega_2} \omega \cdot E'(\omega) \cdot S_1(\omega) d\omega + \int_{\omega_2}^{\omega_{max}} \omega \cdot E'(\omega) \cdot S_2(\omega) d\omega \right) \qquad \text{Equation 69}$$

Again we assume a bifractal approach to suit best the nature of the HDC. Microstructures influence mainly to the lower velocities [23]. *E''* is the loss modulus of the elastomer, σ_0 is the applied pressure and $<\delta>$ is the mean excitation depth inside the rubber

$$\langle \delta \rangle = b \cdot \langle z_p \rangle \qquad \text{Equation 70}$$

with the mean penetration depth z_p of the asperities into the rubber, scaled by the factor *b*.

Further, only wave lengths above $\lambda_{min} = 2\pi v/\omega_{max}$ contribute to Equation 69. It holds [33]

$$\frac{\lambda_{min}}{\xi_{||}} \cong \left(\left(\frac{\lambda_2}{\xi_{||}} \right)^{3(D_2 - D_1)} \frac{0,09\,\pi\,\xi_\perp \cdot \left| E(2\pi v / \lambda_{min}) \right| \cdot F_0(t) \cdot 6\pi \cdot \sqrt{3}\,\lambda_c^{\,2} \cdot n_s}{s^{2/3} \cdot \xi_{||} \cdot \left| E(2\pi v / \xi_{||}) \right| \cdot F_{3/2}(t_s)} \right)^{\frac{1}{3D_2 - 6}} \qquad \text{Equation 71}$$

where $n_s \sim (3 - \beta_2) / (5 - \beta_2)$ is the summit density, *s* the affine transformation parameter (Equation 46) and

$$F_0 = \int_t^\infty \phi(z)dz \qquad\qquad \text{Equation 72}$$

$$F_1 = \int_t^\infty (z-t) \cdot \phi(z)dz \qquad\qquad \text{Equation 73}$$

$$F_{3/2} = \int_{t_s}^\infty (z-t_s)^{\frac{3}{2}} \cdot \phi(z)dz \qquad\qquad \text{Equation 74}$$

are the Greenwood-Williams functions [16] introduced in Equation 42 with the normalized distances $t = d/\sigma_{HD}$ and $t_s = d/\sigma_{SHD}$, where the gap distance d indicates the rubber distance from the mean substrate level; σ_{HD} and σ_{SHD} are the standard deviations of the height distribution or summit height distribution, respectively.

For pure hysteresis friction, λ_{min} becomes [8],[30],[32],[33]

$$\lambda_{min} \cong \sqrt{\frac{|E(\lambda_{min}) \cdot C_z(\lambda_{min})|}{\sigma(\lambda_{min})}} \qquad\qquad \text{Equation 75}$$

As seen in the Stribeck curve (Figure 2), in spite of general lubrication some spots of the interface remain in direct contact, like in Figure 25. The ratio of "true" or "real" contact A_c and the nominal contact area A_0 may be small, but these contact points are crucial for understanding the friction. The elasticity of the shortest relevant distances $\xi_{\parallel}$ on the substrate are related to those of the shortest wavelengths λ_{min}. The contact ratio is calculated with [8]

$$\frac{A_c}{A_0} = \frac{\pi}{2} \cdot \lambda_c^2 \cdot n_s \cdot F_0(t) \approx \left(\frac{F_0^2(t) \cdot F_{3/2}(t_s) \cdot \xi_{\parallel} \cdot |E(2\pi v / \xi_{\parallel})| \cdot (D-2)^2}{808\,\pi \cdot s^{3/2} \cdot \xi_{\perp} \cdot |E(2\pi v / \lambda_{min})| \cdot (D-1)^2} \right)^{\frac{1}{3}} \qquad \text{Equation 76}$$

Figure 25: Schematic sketch of contact points between substrate and sample

2.7 Adhesion Friction

While hysteresis friction is sufficient to describe tribological effects on typical wet contacts, adhesion has to be considered additionally in only partly lubricated [34], and especially on dry systems, because direct contact between rubber and substrate allows molecular interactions with the force F_{Adh}. Consequently, adhesion friction can be used (under the absence of cohesion friction) as a synonym for dry friction. It is proportional to the ratio of contact areas from Equation 76. This leads to the adhesion friction coefficient [32],[35],[36]

$$\mu_{Adh} = \frac{F_{Adh}}{F_N} = \frac{\tau_s \cdot A_c}{\sigma_0 \cdot A_0} \qquad \text{Equation 77}$$

where the load σ_0 is the applied pressure, whereas the velocity dependent interfacial shear stress τ_s produces energy dissipation by peeling effects of the rubber front side at local asperities causing crack propagation [37], and can be written [38]

$$\tau_s = \tau_0 \cdot \left(1 + \frac{E'_\infty / E'_0}{\left(1 + (v_c / v)\right)^n}\right) \qquad \text{Equation 78}$$

The shear factor

$$\tau_0 = \frac{\Delta \gamma}{l_s} \qquad \text{Equation 79}$$

relates the stress to a characteristic length scale l_s and the corresponding surface tensions γ which can be measured by contact angles, as part of the Dupré equation

$$\Delta \gamma = \gamma_1 + \gamma_2 - \gamma_{12} = \gamma_1 + \gamma_2 - 2 \cdot \sqrt{\gamma_1 \cdot \gamma_2} \qquad \text{Equation 80}$$

were γ_1 stands for the surface tension of the rubber sample, γ_2 for the substrate and γ_{12} for the disperse interaction of both, or discriminating polar tensions γ_{p2} and γ_{p2} from dispers tensions γ_{d2} and γ_{d2}, as Good's equation [39]

$$\Delta \gamma = \gamma_1 + \gamma_2 - \gamma_{12} = \gamma_1 + \gamma_2 - 2 \cdot \left(\sqrt{\gamma_{d1} \cdot \gamma_{d2}} + \sqrt{\gamma_{p1} \cdot \gamma_{p2}}\right) \qquad \text{Equation 81}$$

In Equation 78, the exponent n as a material constant is identical to the same variable found in the corresponding time relaxation spectra (Equation 36) of the elastomers. The elasticity ratio E'_∞ / E'_0 as step height for the glass transition is known from the viscoelastic properties, as found experimentally like chapter 3.4 explains. The parameters $\tau_0 = \tau_s (v=0)$ and the critical velocity v_c are subject of free fitting, to give an adequate result. The latter can be interpreted as the point where the shear stress converges to a maximum [18]: $\tau_s (v_c) \approx \tau_s (\infty)$. The dependency we find on velocity means: Contact cannot be established well when sliding speeds are high.

direction of movement

elastomer

asperity

bulge/ crack
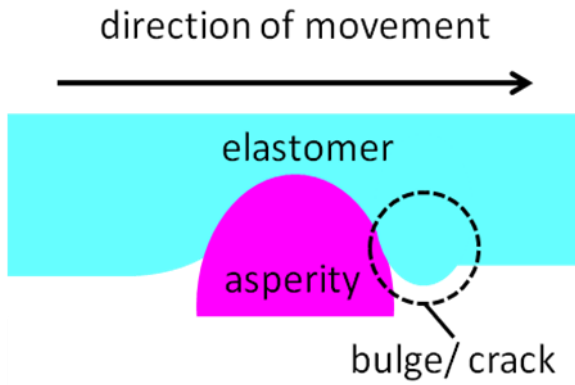
Figure 26: Movement under adhesion causes a bulge in front of asperities.

The adhesion causes an asymmetrical deformation to the rubber (Figure 26): At the leading edge, i.e. the newly arriving rubber front from point of view of the asperity, the elastomer is compressed to a bulge before passing the contact zone. Due to the deformation this bulge is the most probable area where a crack may appear. This implies, for practical reasons, the necessity to shape the border edges of the sample with flat angles to avoid exaggerated bulges and, as result, cracks and wear particles. For theoretical considerations, this peeling process, which has been analyzed by Savkoor & Briggs [40], is connected to the surface energy $\Delta\gamma$ and explains why the bulge building and shear stress depend on velocity.

2.8 Modelling

The theoretical knowledge of chapters 2.6 and 2.7 can be used to achieve a practical description of real friction systems. According to the DIK model, hysteresis as well as adhesion friction offer a quantitative description that is the base for numerical simulation. To gain a complete modelling, the results of these simulations must be compared to experimental results. Consequently, the process follows two separate steps:

First the hysteresis friction was computed. Necessary data included the statistical geometry of the substrate (s, $\xi_\perp$, $\xi_{||}$, λ_c, D_1, D_2), characterized with the tools of affine transformation and HDC, explained in chapters 2.4 and 2.5, further the viscoelastic properties of the rubber ($E'(\omega)$ and $E''(\omega)$ as functional terms (9th degree polynome, or sigmoid for G'), or their shear equivalents), completed by variables for the experimental environment (σ, A_0). Temperature, though being an important factor, had not to be considered, because most measurements were performed at room temperature, which was also the reference temperature for elastic moduli; chapter 4.3 will investigate how far the time temperature superposition of the viscoelastics can be applied to friction. Velocity was left as an independently increasing variable for the main loop. All this information was the source for a maple script that had already been proven in recent works [32] and was improved during this work. Running the script resulted in a manifold of friction information for various speeds, the most important of which are the ratio of real contact area A_c/A_0 and the average penetration depth $<z_p>$, but especially of course the friction coefficient μ. The latter is not an absolute number, for the relation of penetration depth and excitation depth is not covered by this method, so a proportional factor b is multiplied with the preliminary friction coefficient (Equation 63). To determine an appropriate value for b, the predicted friction curve was fitted to the experimentally found curve in lubricated state as best as possible. The accuracy of this operation is limited because of its strain dependency raised from mechanical-dynamical analysis. Further deviation might appear especially for extreme velocities due to the in spite of TTS shifting still confined frequency range of shear moduli. Within these restrictions, a reasonably maximal accuracy was chosen by defining the velocity steps small enough on a logarithmic scale.

The second step was to add the adhesion friction to the hysteresis curve. Some of the needed parameters (σ_0, E_0/E_∞, n and $\Delta\gamma$) had already been gained before, and the area of real contact is part of the results from hysteresis simulation. Leaving l_s and v_c as free fit parameters, hysteresis and adhesion were summed up in a spread sheet and adapted to the friction curves of tribological measurements on dry surfaces.

3 Experimental Methods & Materials

3.1 Preparation

Core of any experiment are the involved samples. For the tribological measurements, those samples consisted of various types of rubber, treated appropriately according to the experimental aim. Reproducibility and, especially for the stick-slip experiments, cleanliness is important to make sure that observed effects are caused by the laws of physics and not by contamination with dirt, grease or other unwanted chemicals. If possible, samples and substrates were cleaned residue free with isopropanol not only before the experiment as whole but also in between to remove possible abrasion particles. Those surfaces that reacted critically to solvents, like the coated sheets, were treated with distilled water only or with dry tissues. For experiments with wet surface conditions, an exposure to the lubricant is of course unavoidable.

The process of sample preparation consisted of several consecutive steps:
1. Mixing a batch of the elastomer substances including carbon black and special ingredients like PAOS
2. Vulcanization to fulfil the cross-linking
3. Annealing at various conditions, depending on experiment, for PAOS filled samples
4. Shaping the samples to fit the experimental setup
5. Coating, for those samples that were tested in the stick-slip section

Mixing, vulcanization and, if necessary, annealing was done by the DIK staff. The coating was deposited at FILK Freiberg.

After preparation or usage, the samples were enveloped in aluminium foil to protect them. Keeping the samples in a refrigerator to slow down aging effects for several months has proven to be helpful. Samples filled with PAOS on the other hand were stored in a desiccator (at room pressure and room temperature), so the low moisture would proceed further annealing only slowly and prevent further silica formation by conserving the state of annealing.

3.1.1 Mixing

The samples needed for the following experiments consisted of rubber as matrix. Depending on the type of elastomer, various materials have been made use of. The amount of rubber is the gauge to which all other components are scaled: The fraction of elastomer is always set

to 100 phr (*"per hundred rubber"*), and all other ingredients relate to this norm in weight percent compared to the rubber. Those additional substances grant quite different advantages, from increased mechanical stability for fillers like carbon black and better control of the cross-linking process to stability against aging and sun rays, plus softeners, dyes or special materials like PAOS. Chapter 3.7 explains the chemistry and the effect on the composition for the applied materials. Only pure rubber types (chapter 3.7.1) were employed, no blends.

For the mixing process an internal mixer, of the type Rheomix 3000, was used. The degree of filled volume was limited for practical reasons to 75%. To prevent the rubber from unwanted early cross-linking, temperatures were as best as possible kept constant at 40°C and rotational frequency at 50 revolutions per minute for the following tables. Components were added into the mixer in the given order.

No.	component	phr	density [g/cm3]	weight [g]	comment
1	Perbunan NT 2870F	100.00	1.000	840.2	
2	N 330	50.00	1.840	420.1	for filled
3	ZnO	5.00	5.600	42.0	
4	stearic acid	1.00	0.940	8.4	
5	sulphur	1.50		12.6	
6	CBS	2.00		6.8	
7	DPG	0.50		4.2	
8	PAOS (variable)	variable		variable	

Table 1: Mixing table for NBR samples with PAOS

No.	component	phr	density [g/cm3]	weight [g]	comment
1	Keltan 512	100.00	0.860	746.2	
2	N 550	50.00	1.840	373.1	for filled
3	ZnO	5.00	5.600	37.3	
4	stearic acid	1.50	0.940	11.2	
5	sulphur	1.50		12.6	
6	ZBEC 70	1.50		11.2	
7	MBT	0.60		4.5	
8	CBS	0.60		4.5	
9	PAOS (variable)	variable		variable	

Table 2: Mixing table for EPDM samples with PAOS

No.	component	phr
1	Keltan 512	100.00
2	N 234	60.00
3	ZnO	3.00
4	stearic acid	1.00
5	sulphur	1.70
6	CBS	2.50
7	DPG	0.60
8	IPPD	1.5

Table 3: Mixing table for EPDM samples for friction master curves

No.	component	phr
1	CV 50	100.00
2	N 234	60.00
3	ZnO	3.00
4	stearic acid	1.00
5	sulphur	1.70
6	CBS	2.50
7	IPPD	1.5

Table 4: Mixing table for NR samples for friction master curves

No.	component	phr
1	5025-0	100.00
2	N 234	60.00
3	ZnO	3.00
4	stearic acid	1.00
5	sulphur	1.70
6	CBS	2.50
7	IPPD	1.5

Table 5: Mixing table for S-SBR samples for friction master curves

Samples for investigating the effect of *coating* consisted of S-SBR 2525 instead of 5025 (i.e. 50% vinyl and 25% styrol) and EPDM with additives as given above, but both unfilled and filled with 50 phr carbon black N339 (SBR) or N550 (EPDM), respectively.

For the *silica* curves of chapter 4.2 the same recipe as in Table 5 has been used but again for S-SBR 2525 and, instead of carbon black, various amounts of silica (Ultrasil 7000 GR, Evonik) have been inserted as filler.

3.1.2 Vulcanization

The mixed batch still lacks a critical process to become a usable rubber: the cross-linking of the vulcanization. The sulphur as indispensable part of the batch links the elastomer chains in the presence of heat and pressure (typically 160°C and 280 bar). As a result, the rubber loses its purely plastic behaviour and gains elastic abilities, as the chains can be disentangled only temporarily after cross-linking, causing an increase in tensile strength and hardness. Furthermore, not only mechanical but also chemical resistance is increased by vulcanization. In any case, the sulphur links make the rubber significantly harder.

The degree of cross-linking depends on temperature, pressure and on the time during which both parameters are applied. To guarantee reproducible samples, the effect of vulcanization as a function of time is measured first with a vulcameter (in this case MDR 200E) to find out when sufficient cross-linking has occured. Similar to a rheometer (chapter 3.4) the resistance to deformation under given temperature and heat describes the elastic state and thus vulcanization of the sample. As Figure 27 shows, the measured torque of the deformation converges finally. This maximal torque strongly depends on the kind of fillers (carbon black being much more important than PAOS). The duration until the maximum is reached depends on the fillers, too. All samples were vulcanized until 90% of the maximal torque is reached by vulcanization, which is called *t90 time*. Table 6 shows some vulcanization times and the effect of cb filling.

elastomer	without carbon black	with 60phr cb 234
EPDM	11.3	11.1
NR	7.8	2.5
S-SBR	20.9	5.1

Table 6: Vulcanization times in minutes, for filled and unfilled elastomers for friction master curves in comparison, based on the t90 threshold.
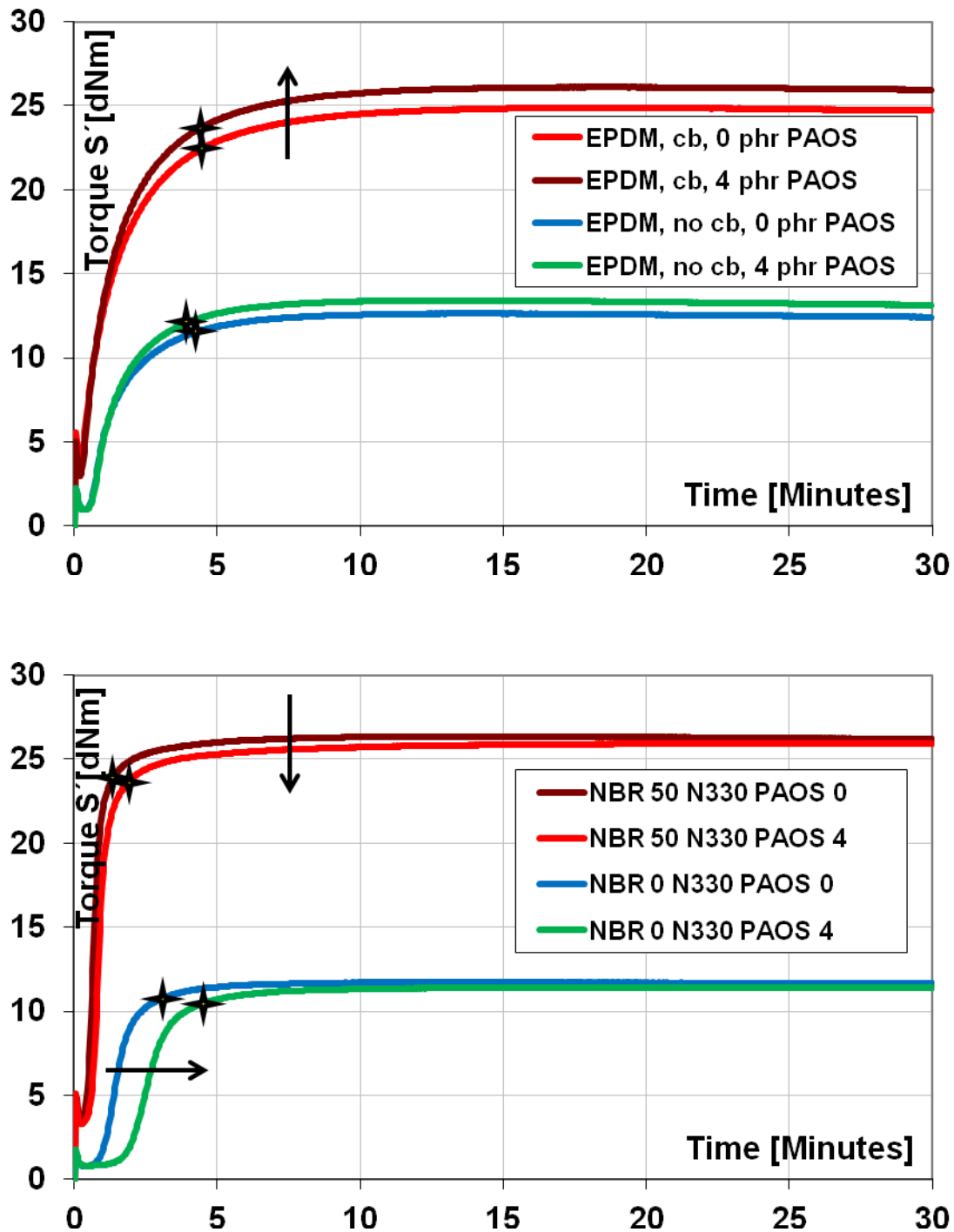
Figure 27: Example of vulcanization curves – EPDM (above) and NBR (below) filled with 50phr cb and/or 4phr PAOS. The t90-thresholds are marked with stars. PAOS influences the threshold and maximum (arrow).

3.1.3 Annealing

For most samples, no further environmental treatment is necessary beyond vulcanization. Those samples which contained PAOS, however, were additionally annealed in a climatic chamber in order to ensure a complete process of silica building on the surface. For the

PAOS reaction with water, a constant air humidity of 90% was chosen, and a temperature of 60°C accelerated the process. Apart from test series to verify the development, all samples (especially those for friction experiments) were treated this way for 24 hours. The reaction can be regarded as finished then. After this procedure the samples were stored in a desiccator, interrupted only for measurements.

3.1.4 Sample Shaping

For any standardized tribological measurement, the samples were shaped as flat hexaeders with 2 mm thickness d_0, within the vulcanization process, having square contact surfaces with lateral sizes l_0 and b_0 of 50 mm edge length each, by die cutting. A few samples had 6 mm thickness to investigate the influence of the effect on friction, or for abrasion measurements, keeping to the standard thickness for that characterization.

The leading edge (for friction measurements with the unidirectional universal tester) or both leading edges (when using the bidirectional tribometer) were ground at approximately 45°, reducing the lateral length l_0 by about 1 mm for each grinding, which had to be considered for calculating the nominal contact area $A_0 = l_0 * b_0$ and the pressure $\sigma_0 = F_N / A_0$.

Although in theory the microscopical morphology of the rubber surface should be completely ignored because the elastomer adapts to the substrate structures, this is obviously true only for rubber surfaces that are significantly flatter than the substrate and for sufficiently large pressures. A macroscopically rough rubber under a moderate weight might well have valleys that do not reach interfacial contact, especially if the substrate is extraordinarily flat like, in our case, glass, steel and coated substrates. In order to investigate this phenomenon, different types of vulcanization plates were applied:

- coarse: rough because it was grit blasted with glass pearls with heights up to 2 µm
- fine: between both extremes with heights around 300 nm
- polished: very smooth plate with heights of maximal 50 nm

For further description of the plates see Table 7.

3.1.5 Coating

On coarse substrates the structure of the rubber surface is negligible. On very smooth substrates, a smooth rubber can provoke significantly high friction values. Chapters 4.5.3 and 4.5.4 will investigate the mitigation of friction and stick-slip by coating the contact interface. The coating layers had to be sufficiently thin, or, instead of the original rubber, the coating properties would have indeed dominated the viscoelasticity of the sample. On the other hand, the coating had to be thick enough to be effective and also stable enough against abrasion (chapter 4.6.1).

The coating was sprayed as homogenously as possible onto the friction side of the sample. The chemical composition of the coating consisted of a varnish matrix in which various types of particles were embedded:

- *polysiloxane* (PTFE particles and cross-linking agent in PUR varnish)
- *PTFE* (in a 1-component PUR varnish)
- *PU* (2-component PUR varnish)
- *TPU* (pure 1-component PUR varnish without particles)

These chemicals will be discussed in chapter 3.7.4. The purpose was to confine the contact between sample and substrate to areas where particles emerge the average layer level. This should reduce friction especially for dry sliding. The particle size was of a similar order than the complete layer thickness: 10 µm for standard coatings. In order to investigate the influence of thickness, some samples were coated with a 40 µm layer, however. These exceptions are indicated when they appear. Due to spraying fluctuations and drying parameters small variations in thickness are possible.

A problem to overcome was a lack in adherence when the varnish was directly sprayed onto the sample. The system showed poor connection and the varnish peeled off easily, causing further abrasion. To solve this, vapour phase fluorination was applied to the sample before coating it. This prevented peeling for the majority of samples and allowed exploiting the parameter space to a large extent.

3.2 Surface Characterization

Being crucial for friction, the interface of the friction zone should be characterized as completely as possible. This can be done due to vertical and lateral geometrical description (profiles and morphology) of the surface, its chemical constitution and chemical bonding (surface tension) of the contact between both. Surface characterizations were done by various persons.

3.2.1 Profile Measurements

To gain information on how the height of a surface changes with lateral displacement, profiles are measured and evaluated. This can either be done with image producing methods, or with linear scanning techniques, which result in 1-dimensional lines that, if parallel, can be assembled to 2-dimesional pictures with height information as third dimension. An example of a profile is given in Figure 18. For achieving surface information like the HDC, adequate numbers of profiles have been evaluated to gain statistically reliable results. The most basic statistical information is the arithmetic average R_a of the various height values.

Mechanical Profilometer

Especially for coarse surfaces like granite or asphalt, the profilometer is a useful tool. A sensor on a stylus is moved laterally over the surface and measures mechanically the change of height. Measurements were exact to 0.5 µm laterally and 16 nm vertically, to maximal ranges of 50 mm horizontally and 1 mm vertically. Alternatively to tactile interaction, laser profilometers detect the surface without contact.

Atomic Force Microscope (AFM)

The atomic force microscopy (in this case, an FRT-AFM) is a mechanical scanning instrument. Its advantage is the high resolution, which allows measurements far below the micron scale, limited mainly by the tip radius and stability of the experimental environment, and thus is the optimal tool for smooth surfaces. On the other hand, the maximal scanning area is limited to tiny dimensions about 50 µm * 50 µm. In contrast to other scanning techniques like STM, electrical conductivity is not required for AFM – a mandatory feature for unfilled rubber and most substrates.

A small tip is fixed on a cantilever which is bent according to the movement of the tip over the sample surface, and information of the bending is transmitted with a laser beam to a photo sensor. Scanning is in lines with a small displacement to each other to build a pixel image.

The scanning range is confined to a small area. Depending on the type of interaction between tip and surface various modes can be used:

- contact mode (direct mechanical contact with constant force or constant height causes repulsion)
- non-contact mode (dynamic resonant vibration)
- intermittent contact mode (tapping mode with constant amplitude)

White Light Interferometry

The surface descriptors of some substrates have been gained with another technique, the white light interferometry. A focussed spectrum of various wavelengths (white light) from a coherent light source is reflected on the substrate's surface. The interferences caused by differences in beam lengths give information about the z-coordinate of the illuminated spot, i.e. the colour is correlated with the height. Dispersion must be considered. Resolution is in the micron range laterally and up to 10 nm vertically, and comparatively large areas of some mm can be captured with low resolution. A major advantage of this type of microscopy is the complete avoidance of mechanical contact.

3.2.2 Morphology

Similar to profile measurements, morphological investigations describe the structural geometry of the surface. However, aim of this analysis is not the height information itself, but areal structures of the 2-dimensional image in order to reveal the surface topography: patterns, artefacts and domains.

The simplest way to accomplish this is optical microscopy. A more sophisticated method is the Dispersion Index Analysis System (DIAS). It was developed especially to determine the degree of filler dispersion within the rubber. The light reflected on surface slices passes an optical microscope, and the digital image is analyzed automatically due to particle pattern recognition, allowing conclusions to the degree of dispersion and size distribution of agglomerates.

Another topographical method is scanning electron microscopy (SEM), which will be described in chapter 3.2.3 as prerequisite for EDX measurements.

Apart from this, the 2-dimensional images gained with profile methods (AFM, White Light Interferometry) as described above can be used for morphological analysis as well.

3.2.3 Chemical Analysis

Even more interesting than size and shape of surface objects are the components they consist of. Several devices were used for chemical surface analysis:

EDX

A contact free method to analyze surface chemistry is the energy dispersive X-ray spectroscopy (EDX). A conductive sample is put into a SEM device. A focused electron beam scans over the sample surface. The detected response signal becomes a pixel of the resulting image. The beam has a freely tuneable but constant energy, and excites atoms when hitting the sample as a target. Higher orbital electrons close the gap, generating x-rays. The spectrum that is produced then is characteristic for the involved chemical elements, which are discriminated from each other and the bremsstrahlung background by an included software, resulting in information about the proportional distribution of elements in the analyzed spot. Although other methods of exciting atoms for X-ray emission exist, SEM-EDX is the most common technique.

The penetration depth depends on the beam energy and normally does not significantly exceed a few microns. This means that solely surface composition and almost no bulk is given – especially important for samples with surface modifications (PAOS, coating). Being pear-shaped, lateral resolution is of a similar order, if the beam is sufficiently focused.

Infrared Spectroscopy

For this type of characterization, the surface is irradiated with a spectrum of infrared light, ranging from 700 cm^{-1} to 4000 cm^{-1} for this FTIR device. Molecular dipole excitation consists mainly of oscillation for this near IR part of the spectrum, causing absorption for the corresponding wavelength, with different molecule spectra superposing each other. With knowledge of the absorption or transmission reference spectra the amounts of chemical substances can be calculated.

XPS

The technique of X-ray photoelectron spectroscopy (XPS) uses the photoeffect for surface atoms: Each element has characteristic binding energies for its electron orbitals. According to Einstein's light quantum hypothesis, the energy of a photon is directly proportional to its frequency, and X-rays are high frequent/ energetic enough to remove electrons from their atoms. These photoelectrons are detected and, purged from secondary electron signals, correlated with elements, amounting to chemical ratios. Sensitivity for the photo effect depends on frequency and effective cross-section.
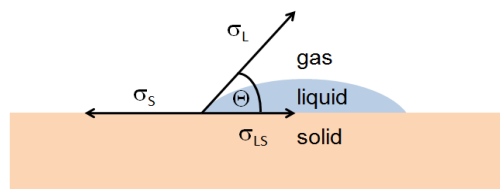
3.2.4 Surface Tension

Two techniques were used to measure the surface tension: The static sessile drop method and the dynamic Wilhelmy method.

Sessile Drop Method

A drop (volume 6 µl) of liquid is placed on a solid, horizontal sample surface (Figure 28). The type of liquid is varied with several chemicals (water, diiodmethane and ethylene glycol; more like polyethylene glycol or thiodiethanole can be used to enhance the validity of the results). In equilibrium drops minimize their energy, resulting in spheres for free fall and deformed balls on top of a surface. The angle Θ between surface plane and drop corner depends on the surface tension between the sample surface and the liquid: the smaller the interaction (e.g. hydrophobous for water), the larger the angle. It is used in Young's equation

$$cos\Theta = \frac{\sigma_S - \sigma_{LS}}{\sigma_L}$$
Equation 82

Figure 28: Surface tensions and contact angle of the sessile drop method

including the surface tensions for solid σ_S, liquid σ_L and the interface σ_{LS} of both for calculating the surface tension. The experimental setup, here with the OCA 20 instrument, is very sensitive to parameter (temperature, humidity...) changes, so reliability is gained by large numbers of tests and a maximum of liquid types. To keep changes small, a single angle measurement lasts for about 1 s, at 23°C and 25% relative humidity. According to Owens, Wendt, Rabel and Kaelble [41] the evaluations with elliptic fit for the various liquids determine the disperse and polar components of the surface tension. Evaluations assume that the sample surface is flat enough not to interfere significantly with the drop shape. According to Busscher [42] a roughness up to 0.1 µm can be neglected. Otherwise the drop must be symmetric and several times larger than the surface roughness to allow a valid evaluation. These conditions are fulfilled for the following investigations.

Wilhelmy Method

More accurate is the dynamic variant of achieving surface values, the Wilhelmy technique. The solid sample is dipped vertically into a liquid and removed again with constant velocity. The correspondence between acceding and retracting curve allows the calculation of the surface tension by averagting the advancing and receding contact angles whereas the angle hysteresis $\Delta\theta = \theta_{adv} - \theta_{rec}$ can be related to the surface roughness. As for the sessile drop, the procedure is repeated with several liquids of distinct polarities. A drawback is the limitation on small samples, for practical reasons.

3.3 Material Testing

The various possible methods for material testing are numerous and include mechanical, chemical, electrical, optical, thermal and other aspects. Unlike the surface testing described above, the techniques of this chapter characterize some bulk properties of the sample, or more precisely, mechanical bulk properties. Due to the mechanical exposure, the procedures are destructive for the sample. The properties concerning shear and torsion are explained in detail in the next chapter, as they are the key for understanding viscoelasticity.

3.3.1 Shore Hardness

A manifold of standards exist to measure the hardness as a gauge for the resistance against indentation. The most common standard for elastomers is the Shore hardness: A normed steel pen indents the sample with a fixed force at room temperature for 15 s; from the indentation depth the hardness is calculated. Deep indentations equal low hardnesses and vice versa, ranging from 0 to 100.

Large rubber hardness is an indirect hint for low elasticity and thus is important for friction. Consequently, it means that hard substances are more brittle than soft ones. Hardness is also connected to wear because soft materials are abrased by hard ones, the opposite case is negligible. To build a rubber element with good stability against wear, a hard surface with an elastic core is a helpful combination – chapter 4.5.2 makes use of this idea.

3.3.2 Rebound

Ideal elastic materials return to their a priori geometry, bouncing back objects with original momentum. Real elastic materials dissipate a part of the kinetic energy. This is measured with rebound testing: A standardized hammer hits the sample with predefined parameters; the deflection is a measure of elasticity.

3.3.3 Tensile Test

With a universal testing machine the sample can be stretched to a specified degree and the resulting force (and thus the stress tension) is measured with a load cell. The velocity can freely be chosen, and either tension or elongation can be the actuating variable.

For testing, samples of known geometry with small cross-section are stretched steadily and sufficiently slowly. As samples in general, and especially elastomers, exhibit not only a linear function (Hooke's behaviour) between tension and elongation, several characteristic parameters are defined to describe the relationship of both in the elastic and plastic regime.

For the consideration of the experiments described below, the following parameters were used:

- Tensile strength: This is the maximal tension that is reached during the complete test, regarding the original cross-section of the sample as fix (nominal tension).
- Elongation at break: This value tells the percentile ratio of how far a sample can be stretched before it breaks.
- Stress at 200%: This number gives the stress that is necessary to stretch the sample to 200% of its original length.

3.3.4 Abrasion

During friction it may happen that the structural stability of one of the interacting partners (usually the softer one) is not enough to keep the body intact: Small particles, either microscopic or macroscopic, are detached from the surface into the interface zone. This is called abrasion. Roughness and hardness determine the abrasion essentially.

To determine the abrasion, the sample (6 mm thick) is treated with a sliding surface of defined surface parameters, velocity and normal force for a certain time. The amount of abrased material is evidence for the sensibility to abrasion.

3.4 Dynamic-Mechanical Analysis (DMA)

As mentioned before, knowledge of the shear moduli of the elastic sliding partner are most important for understanding and predicting friction. Both *G'* and *G"* are revealed by dynamic-mechanical analysis (DMA). Measurements were performed with an ARES rheometer (Figure 29).
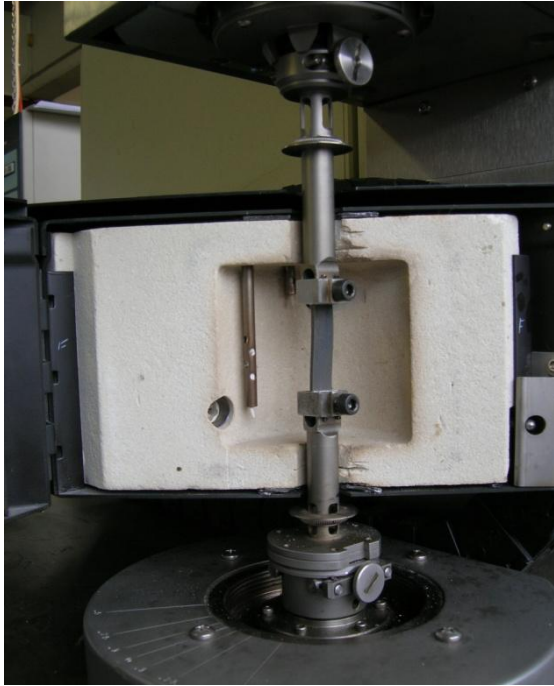
Figure 29: DMA device with open temperature chamber and a typical rubber sample

As the picture shows, a rectangular rubber ribbon (10 mm broad, 2 mm thick, length ≈30 mm) is fixed symmetrically with a clamp at either end. One attachment is pivotable in that axis and rotates cyclically in a small sinusoidal angle back and forth, evoking torsion in the sample. Typical deformation should not exceed an interval of 0.5% to 3.5%, depending on sample length and stiffness, to identify the torsion with the shear moduli for purely elastic deflection. Evaluation of the results should take this shear amplitude into account as it influences the exact master curves and thus the simulation output. Lower amplitudes were preferred for their more accurate reaction to deformation. A pre-stress of about 1 N is disposed to keep the sample in plain geometry. Technical limitations confine the rotational frequency to moderate values, i.e. about 100 Hz at maximum. On the other hand, low frequencies < 10 mHz prolong the measurements unduly. Those no more than four decades of frequency are not enough to describe the elastic properties well. To get rid of this limitation, the whole system is placed in a temperature chamber, so samples can be set to about -80°C to +100°C after thermal equilibrium is reached; reasonable values depend on the glass transition. Above +60°C most often little information is gained. Temperature can

either be run through in small steps with constant frequency *(temperature sweep)* or in coarse steps (5 K steps in the cold range, 10 K for medium range, 20 K in the hot) for a while during which the frequency exploits its own range as described above *(frequency sweep)*. Measured variables are: temperature, the shear moduli *G'* and *G''* (and thus complex *G** and *tan δ*), time, the actual sample length, the resulting torque and for frequency sweeps of course also the frequency.

Evaluation of these data makes use of the time temperature principle explained in chapter 2.2. Each temperature step gained from a frequency sweep becomes one of many isothermal branches in a diagram *G'(f)* or *G''(f)* and *tan δ (f)*, respectively. By shifting each single curve horizontally (i.e. parallel to the f-axis), a continuous *master curve* (Figure 11) is constructed from overlapping branches. The factors (or distances, for logarithmic plot) are not arbitrary, but ruled by the WLF equation (Equation 28) for unfilled samples. Filled samples lack a good overlap for hot temperature branches (Figure 13) until an additional vertical shift for the shear axis is applied, with factors in concordance to the Vogel-Fulcher equation (Equation 29). Both equations are valid above glass transition, which can well be determined by the DMA results. All master curves shown in this work refer to an unshifted temperature branch for 20°C.

3.5 Friction Measurements

Without any doubt, friction measurements are the centre of experimental testing concerning a work on investigation, prediction and control of rubber friction. They were carried out extensively and with the due accuracy. The results are both empirical findings of effects and comparison of parameter influence as well as the basement for fitting simulations.

The principle of any friction test is simple: A sample (here: rectangular 5 mm * 5 mm and 2 mm thick, with grinded edges) is pressed by a normal force on its sliding partner, the substrate. In these experiments this was achieved by putting a constant weight on the sample. Consequently, all sliding took place on horizontally levelled planes. The sample is moved parallel to this plane, and the resulting friction force is measured. To guarantee a stable friction behaviour, the sliding speed was kept constant *(stationary velocity)*; non-stationary parts of the friction curve and artefacts were neglected and not evaluated. Velocities were comparably low, so the thermal stability of the system due to frictional heat was well provided for even in dry systems. Samples and substrates were cleaned adequately, depending on their sensibility with isopropanol (normal case) or only with distilled water (coated samples and coated metal sheets), before and if required between measurements to exclude grease, abrasion particles and other unwanted materials.

To perform these experiments, two different devices were used: a special tribometer and a universal testing machine.

3.5.1 Tribometer

This tribometer is a unique machine, designed especially for the needs of this type of measurement. It was applied for the vast majority of the following experiments. Figure 30 shows its elements schematically: Any substrate (see chapter 3.6) within a lateral maximum of 10 cm * 28 cm can be fixed in a pool that is mounted on a sledge. Substrates were always levelled to set their surface horizontal.

Some measurements were performed on dry substrates. If necessary, the pool can be filled with a lubricant – this was usually a solution of 5% (volume) of commercial washing tenside with water. Rarely pure water was used for comparison; if not indicated differently, "lubricant" or "wet" always means a tenside-water mixture. Ideally the interface of the sliding partners is only thinly covered by lubricant during the whole measurement to avoid viscous friction. Adhesion friction is assumed to vanish almost completely because of this procedure.
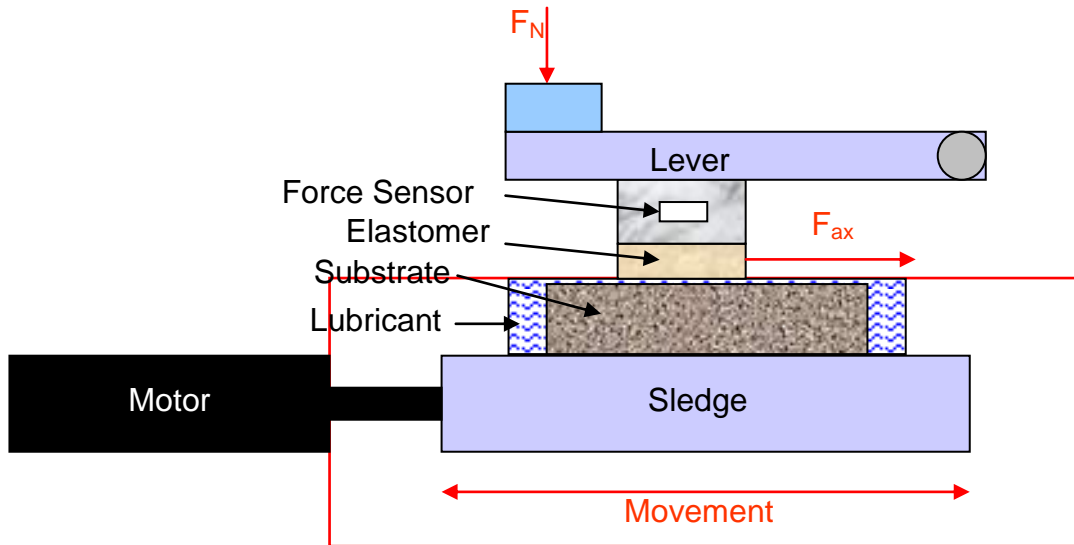
Figure 30: Schematic picture of the tribometer elements: The force sensor acts as a fixed link for the elastomer sample and the lever, which is depicted here in its down folded position. Substrate and lubricant are confined by a pool as part of the moveable sledge.

The sledge can be moved horizontally in one axis ("left-right" in Figure 31, right part) by a motor (Intellimot IM 2200) to which it is connected. The torque is powerful enough to assure continuous movement even in high friction systems. The movement is bidirectional in this axis with a constant speed and very short acceleration phases. Velocity ranges from 5 µm/s to 15 mm/s, split up into 4 steps per decade, i.e. 5 µm/s, 10 µm/s, 20 µm/s, 40 µm/s, 70 µm/s, 100 µm/s, 200 µm/s, 400 µm/s, 700 µm/s, 1 mm/s, 4 mm/s, 7 mm/s, 10 mm/s and 15 mm/s. Usually these velocity cycles were tested twice in a row from fast to slow sliding, and again twice back to high velocities, to average out fluctuations and systematic errors because of possible wear or other sample alterations.
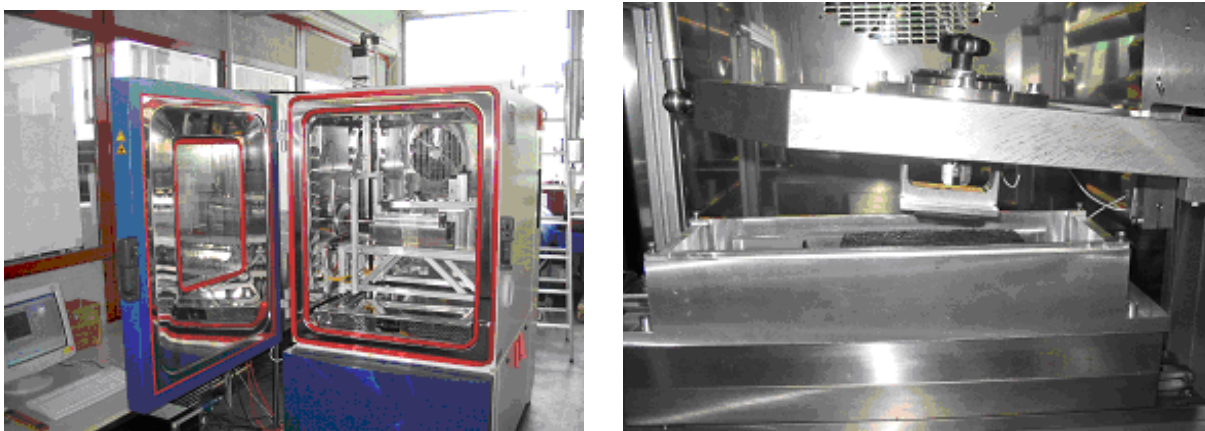
Figure 31: Tribometer in a temperature chamber (left); detailed picture (right) with lifted lever and a rubber sample fixed to the hollow shaped force sensor in between, over an asphalt substrate in the pool

As the goal is to gain reproducible data, these alterations have to be considered not only by maximizing the number of measurements. The state of the sample surface can change dramatically during the friction process, especially in the beginning when a virgin or stored sample experiences micro abrasion of its oxidized and more or less aged surface. So before starting the proper testing sequence, samples have to pass a "running-in" procedure (compare to Figure 44) of several cycles at high velocity. Friction turns out to converge to a constant level after less than 10 cycles for most cases, as Figure 44 shows. This behaviour must not be confused with the Mullins effect, which would affect only filled samples, happening already during the first stress exposures.

The other parts – sample, sensor and normal weight – are attached to a lever that can be lowered and lifted to allow or prevent friction contact and for sample exchange. The weight remains constant, at minimum the lever system weight itself, and can be increased by additional weights at the far side of the lever. If not proclaimed otherwise, all measurements with the tribometer resulted in a pressure of 25.3 kPa for the nominal contact area. The bottom of the lever holds the force sensor, which detects the shearing due to the friction force. The sample is glued beneath the sensor.

The motor activity and the sensor signals are controlled and recorded by a Labview program created for this machine. The gathered data (velocity code, friction force and temperature as a function of time) including static parameters (calibration factors, normal force, contact area...) were evaluated with a custom-made spread sheet for friction coefficient, actual distance, plateau characteristics, stick-slip effects (size, frequency, slope) and other interesting information. Figure 32 displays a plot for some of these parameters in an example. With two different types of averaged data, also two kinds of errors must be distinguished: purely statistical fluctuation from averaging the reading points of each single plateau, which was negligible for most cases, and the error bar of averaging these averaged values, which as a superposition of statistical and systematical error depended largely on the stability of elastomer.

The depicted system is surrounded by a temperature chamber. With 20°C being the reference temperature of DMA master curves, it is reasonable to investigate friction at this very condition. For assembling friction master curves, however, a broad interval of various temperatures is needed. Thus, these experiments were performed for dry contact from the coldest accessible stable environment at -35°C to a maximal temperature before the state of elastomer or glue caused superposing effects, at about +65°C. Wet contact, of course, allowed only measurements above freezing point. Prerequisite was the careful achievement

and maintenance of thermal equilibrium for elastomer, substrate, lubricant and sensor. Direct use of the temperature regulation during measurement had to be avoided because of vibrations.
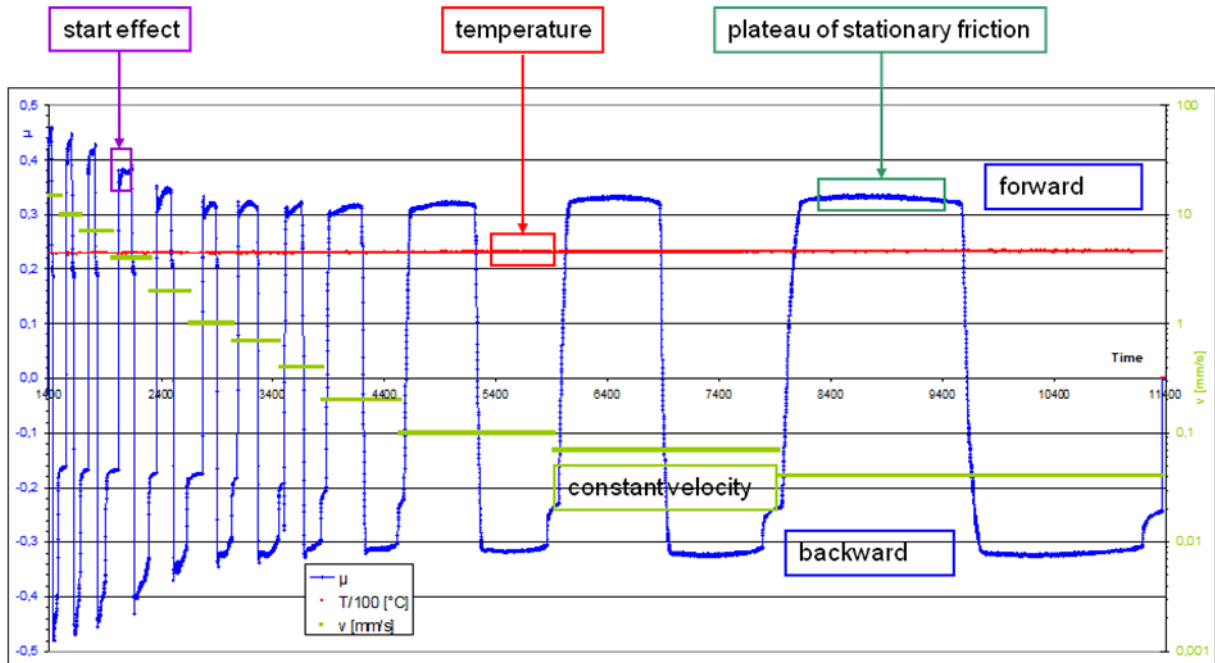

Figure 32: A friction plot from the data of a tribometer experiment. Time is the abscissa. The friction coefficient (blue) oscillates as sliding direction changes. Neglecting start effects, only the plateaus of stationary friction are evaluated. Values depend on velocity (light green), which is kept constant during one cycle. Temperature (red) remains constant all the time within a measurement series.

3.5.2 Universal Testing Machine

Similar to the tribometer, a Zwick universal testing machine (Figure 33) could be applied to perform friction measurements. This was done in times before the tribometer was available, namely for the measurements of the PAOS filled samples (chapter 4.5.1), and for some older experiments not discussed in this work. Basically, this machine has a traverse that can be moved with a chosen constant velocity over a certain distance (short for slow movement, long for fast). In contrast to the tribometer, this movement is mono-directional. A load cell measures resulting forces, which are recoded and later evaluated.
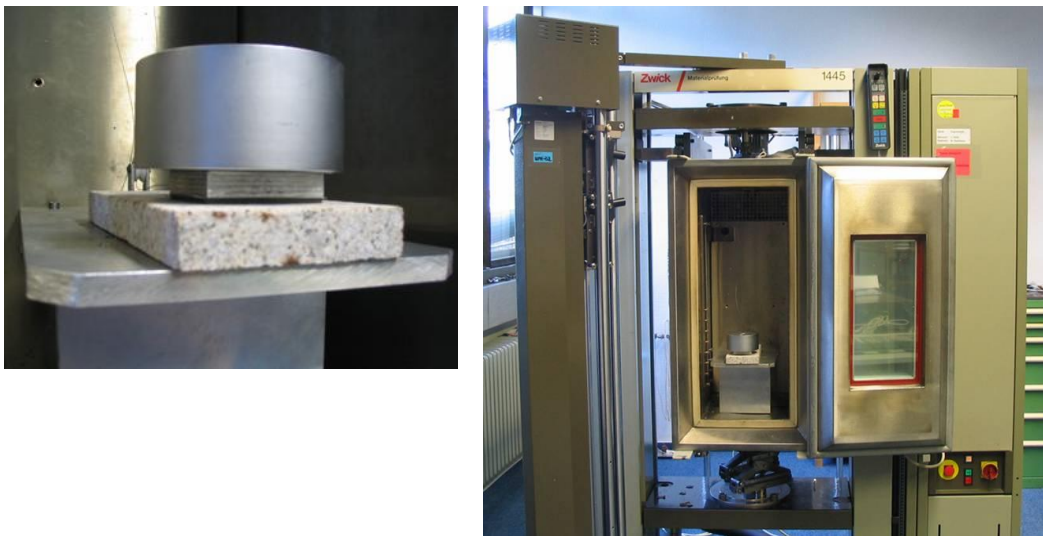
Figure 33: Universal testing machine (right) and friction system (left) with granite substrate under a sample with weight upon it

The friction setup is connected to traverse and load cell as depicted in Figure 34. Again the substrate is mounted horizontally as bottom element and for wet testing placed in a pool filled with lubricant. The sample is glued via a sample holder to the normal weight. This module is freely moveable over the surface, but linked with a flexible wire (0.54 mm diameter) over two deflection pulleys to the sensor and to the traverse, so controlled movement always appears from left to right in this scheme.
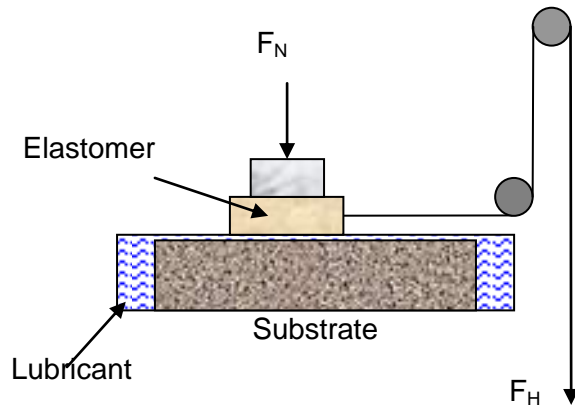
Figure 34: Principle of the sliding friction experiment for universal testing machine

The effective pressure was 12.3 kPa. Only room temperature was accessible. The stationary velocity ranged from 10 µm/s to 30 mm/s and was split up into two steps per decade (10 µm/s, 40 µm/s, 100 µm/s …), again several times for every velocity, starting from fast sliding down to slow sliding and back up to fast movement. Figure 35 shows an example of how friction force depends on selected velocities over the measured distance. As for the tribometer friction plots, only plateaus were evaluated. To achieve a tense wire in time, the sample module was pre-strained before each measurement with about 20 N. A running-in procedure was executed analogously to the tribometer.
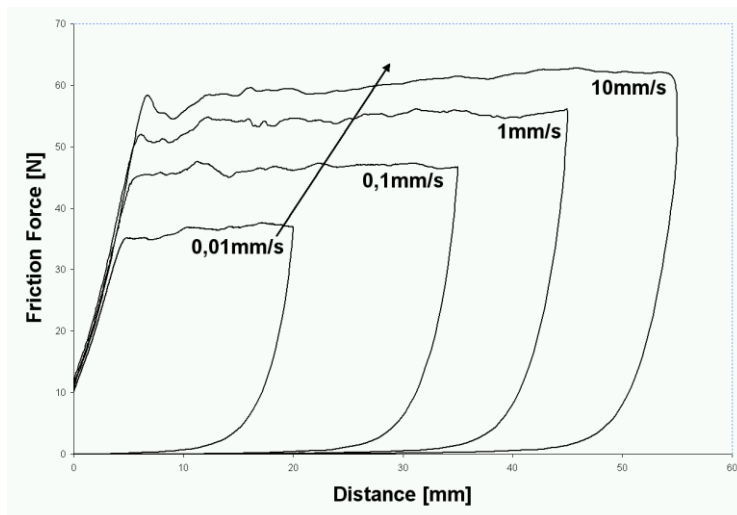
Figure 35: A friction curve compiled from experimental data of the universal testing machine for some selected sliding speeds. Friction reaches a velocity dependent plateau level over sliding distance when the wire is completely stretched.

3.6 Substrates

3.6.1 Classification

A variety of substrates has been used in conjunction with rubber samples for friction experiments. In this work, these substrates appear in the experimental setup:

- rough granite
- polished steel
- rough and fine steel, with identical values as their correspondent coarse and fine vulcanization plates (see below)
- metal sheets, coated with 2 different cross-linked lacquers ("sheet 3" and "sheet 4"), as typically used in automotive industry
- glass

Additionally, simulations have been performed within the considerations of chapter 4.4 also for other real substrates:

- tile surface
- rough asphalt

The surface structure of the elastomers was determined, if necessary, by usage of different vulcanization plates. They will be titled as

- coarse vulcanization plate
- fine vulcanization plate
- smooth vulcanization plate

All these substrates can be regarded as widespread for industrial use and thus make a "typical" friction partner for rubber in numerous applications.

3.6.2 Surface Parameters

The surfaces differ largely in their descriptive parameters. A selection of images for various surface aspects shall illustrate this: the influence of quantitative geometric parameters without qualitative effects in the comparison of substrates made from the same materials, as the coarse and smooth vulcanization plates.

Figure 36 displays some typical profiles *z(x)*, both taken as perpendicular *(x)* to the sliding direction *(y)* of friction experiments. Although the abscissa covers a similar lateral distance, the vertical heights on the ordinate reach quite different maximal values. Also, the height changes appear on a larger lateral scale for the coarse surface – already a hint of a larger

parameter declaring the beginning of either the mesoscopical or macroscopical regime. The relation between lateral and vertical parameters can be highlighted more closely with the HDC. This almost macroscopic structural appearance was caused by the production treatment of using sand-blasting with glass pearls, as can clearly be seen in Figure 37 (left side) from the AFM images. The smooth plate (right side) shows apart from true fractal microstructures also micro scratches that superpose the profile scan. Additionally two or more fractal structures may superpose each other, causing multi-fractal surface features. All profiles have been averaged to zero level and zero slope.
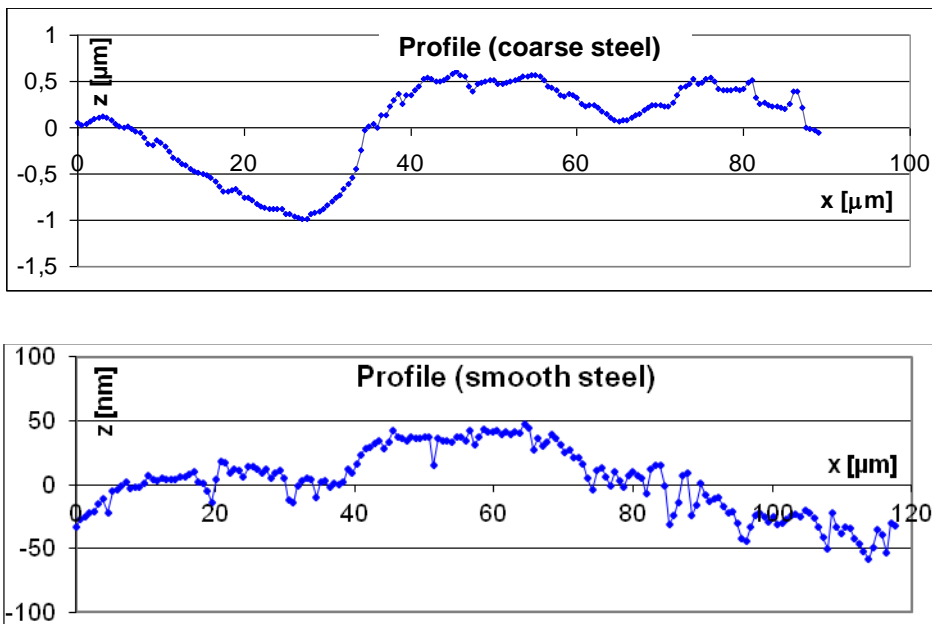
Figure 36: Profiles of vulcanization steel plates with different smoothness (coarse above, smooth below)
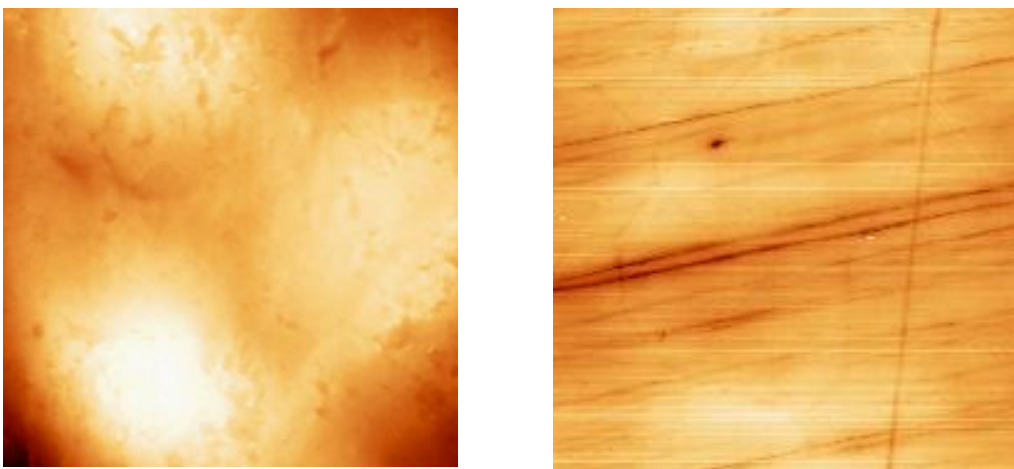
Figure 37: AFM images of coarse (left) and smooth (right) steel plates

A large amount of such profiles for each surbstrate is evaluated for its height distribution $\Phi_{HD}(z)$ as seen in Figure 38. Neither the coarse nor the smooth steel plate shows a perfect Gaussian distribution, but is biased. Especially for the coarse plate an above average number of counts adds to the upper z values, which can be interpreted by the morphology: Mainly consisting of concave spherical segments, clearly visible in Figure 37, the lower parts differ less in height, while the edges, contributing only little to the total area, emerge. The complete z-interval is of course larger for the coarse plate. Sharpness and asymmetry are important factors for traction [29].
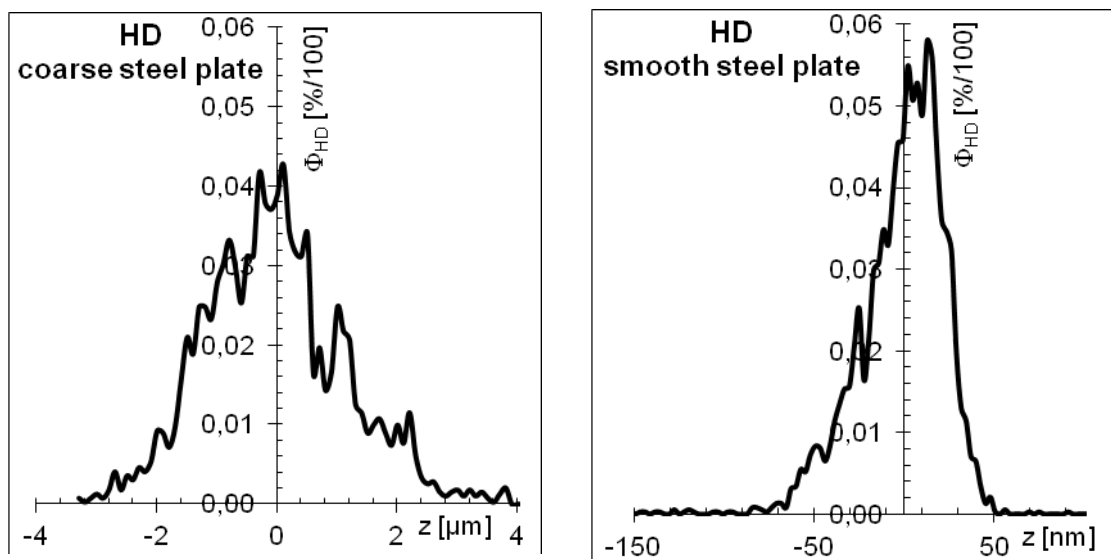
Figure 38: Height distributions of coarse (left) and smooth (right) steel plates

The relevant surface descriptors are found in the height difference correlation, which again derives from a sufficient number of profiles. Figure 39 shows the HDC for the plates. In both cases a bifractal classification seems appropriate. As already supposed from the profiles, the crossover λ_c from microscopic to mesoscopic fractality is much higher for the coarse surface (grey lines). The borders to macroscopic flatness $\xi_{||}$ (yellow lines) on the other hand are almost identical for both. In accordance to the maxima of the profile heights, the corresponding orthogonal cut-off parameters $\xi_{\perp}$ reach commensurate values (red lines) at the intersection point. Fractal dimensions D are derived from the linear fractal slopes (green and blue, extrapolated a linear fit lines). A wide lateral measured range is prerequisite for a reliable value, as limited intervals falsify the fractal dimension. As expected D is minimal for the flat part of the coarse plate. Note that coordinate scales are chosen the same laterally in this figure images but differently vertically (in [mm^2] and [nm^2], respectively).
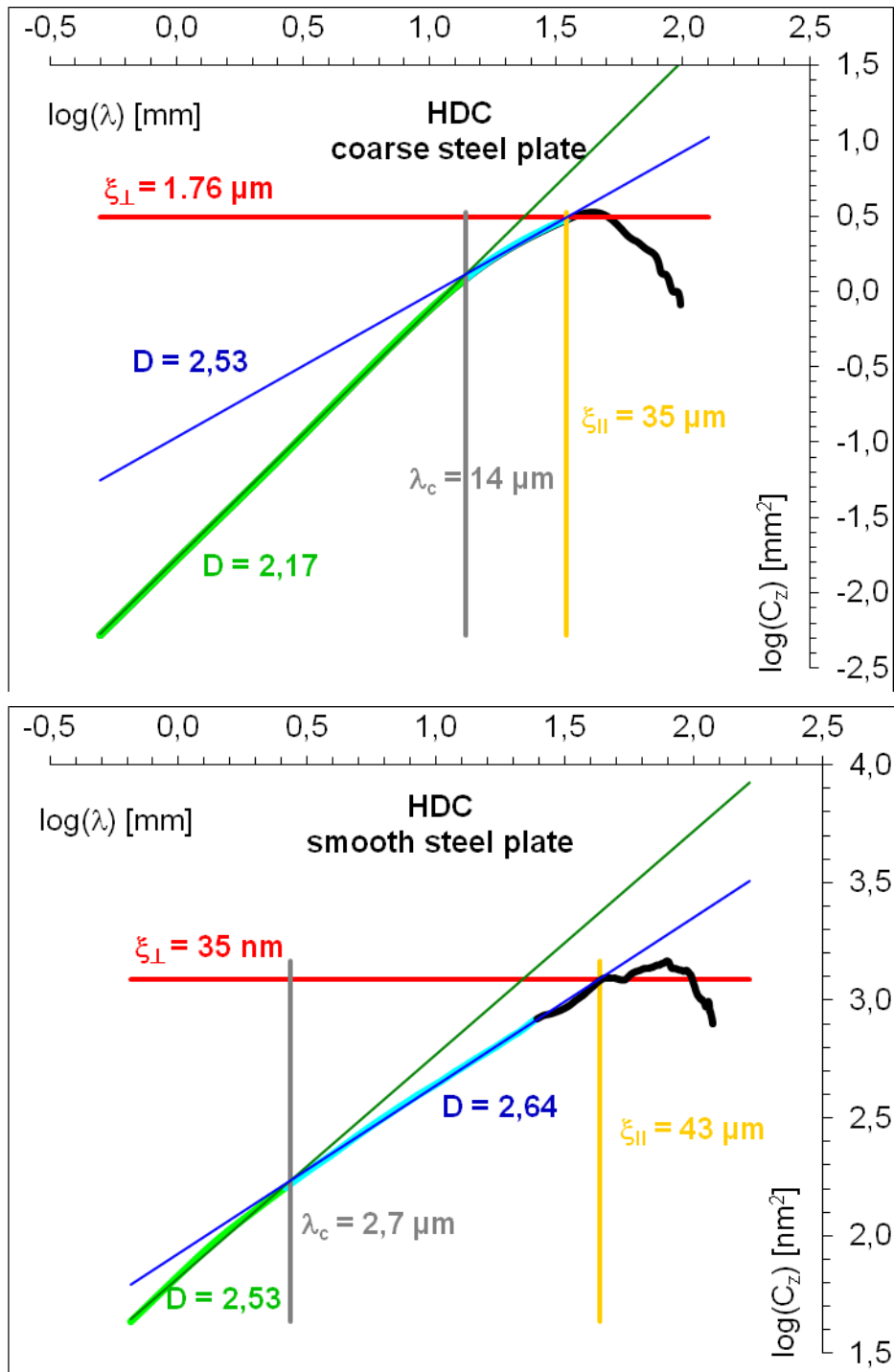
Figure 39: Height difference correlation of coarse (above) and smooth (below) steel/ vulcanization plates

A general survey of the most important surface descriptors is given in Table 7 for all substrates that appear in the presented experiments and simulations.

Asphalt and granite are the coarsest materials, both in maximal heights and orthogonal descriptors, which correlate with the vertical standard deviation. Polished steel, glass and coated substrates on the other side are exceptionally smooth. Lateral descriptors tend to

follow this classification from microscopic to macroscopic, and Figure 40 displays this relationship. There is no exact proportionality, however, and the ratio of lateral and vertical cut-off lengths tells if the structures are rather sharp or yet blunt. Asphalt for example is in spite of similar roughness sharper than granite, as the ratio in the table tells. Glass is extraordinarily blunt.

Substrate	z_{max} [µm]	$\xi_\perp$ [µm]	$\xi_\parallel$ [µm]	λ_2 [µm]	D_{mak} -	D_{mik} -	$\xi_\parallel / \xi_\perp$ -	s -
Asphalt	800	430	1440	332	2.39	2.09	3	1.25
Granit	550	313	2490	93	2.37	2.13	8	1.25
Tile	26	13	270	-	2.31	-	21	1.25
Polished Steel	0.845	0.313	1.89	-	2.32	-	6	1.25
Coated Sheets	0.02	0.017	18	2.6	2.45	2.80	1059	1.61
Glass	0.005	0.0033	37	-	2.84	-	11212	1.37
Smooth Vul. Plate	0.05	0.035	43	2.7	2.64	2.53	1229	1.31
Fine Vul. Plate	0.3	0.172	13.3	1.0	2.39	2.45	77	1.54
Coarse Vul. Plate	2	1.76	35	14	2.53	2.17	20	1.26

Table 7: Surface descriptors of relevant substrates, in some cases as bifractal approximation
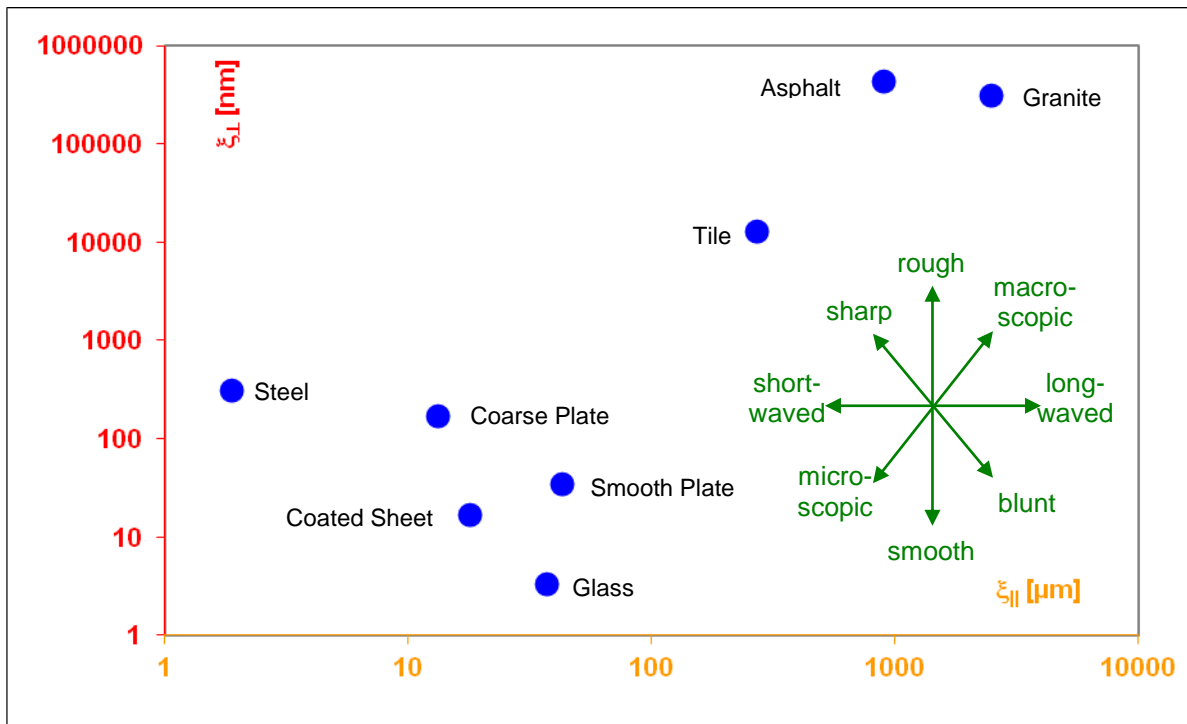
Figure 40: Orthogonal versus parallel cut-off lengths, showing a relation between vertical and lateral structures on fractal surfaces. The green arrows indicate the denotations of the directions.

Of course the substrates not only differ in their geometry but also in their chemistry (important for adhesion and considered in their surface tension) and hardness. Except for the coated sheets all substrates are very hard compared to the rubber samples.

3.7 Elastomer Samples

For our tribological considerations, elastomers play the part of the soft friction partner. This is also the case in typical applications beyond lab experiments. Their adhesive and flexible nature makes them a paramount choice in contact systems. But the interface is not necessarily ruled by the elastomer bulk – surfaces can rather consist of coatings, structure educing particles, wear debris or lubricant. The search for novel materials and investigation of sliding systems should take this into account.

3.7.1 Chosen Types of Elastomers

Elastomers [43],[44] are defined as polymers with an extraordinarily low elasticity modulus. Being well above glass transition at room temperature, stress or pressure will only deform them temporarily, because the coiled polymer chains are stretched and retract again as soon as stress is released *(relaxation)*. This process is almost purely entropic elastic for elastomers. The chains are strengthened by cross-linking them with sulphur during vulcanization.

Although all elastomers share common features – elasticity with high deformability, softness, incompressibility – they differ not only in the quantity of these attributes but also in other properties like glass temperature or stability against thermal, chemical and photonic (ultraviolet radiation) influences. A manifold of elastomers has been developed since the discovery of natural rubber to suit all kinds of applications. The following experiments focus on some wide spread elastomer species that shall be introduced now.

EPDM

Ethylene-Propylene-Dien-Monomer (EPDM) is a synthetic copolymer, i.e. the polymer consists of different monomer types within each single chain (in contrast to a blend, when different kinds of chains mix to build the material). It stands out for a high resistance against heat and cold, sunlight, moisture and ozone and is thus an excellent choice for outdoor applications. Due to the chemical stability it is furthermore predominantly employed for hoses, gaskets and other seals in contact with hot or aggressive environments. The good flexibility of EPDM becomes an important advantage then.

NBR

Nitrile-Butadiene-Rubber (NBR) is another synthetic copolymer. Its stability against oil, grease and hydrocarbons as well as against heat and abrasion offers a broad usage as gaskets, hoses and rubberized fabric with small friction coefficients. An important application are laboratory gloves.

NR

Natural rubber (NR) is mainly gained from the latex of the rubber tree *Hevea Brasiliensis*. Chemically it consists of isoprene. A reversible strengthening through shear induced crystallization under mechanical exposure makes NR robust for friction and rolling on rough interfaces. However, it is sensitive to oil and sunlight. Applications are tyres, gloves, rubber foams and many others.

SBR

A very common synthetic elastomer is *Styrol-Butadiene-Rubber* (SBR) as copolymer of styrol and butadiene (being the larger part). The variant used here is a material from solution polymerization, called *S-SBR*. It has a good chemical resistance against inorganic liquids and a sufficient thermal stability for outdoor usage. SBR is the main contributor for tyre production but also used for gaskets and conveyor belts.

3.7.2 Reinforcing Fillers

Being a soft material, pure elastomers suffer strong abrasion in sliding situations. Without reinforcement, devices made for inducing friction like tyres would rather become disposable products instead of long term machine parts. To overcome this limitation, reinforcing fillers are added already during the mixing process. They make the rubber harder and significantly less abrasive. Modern compoundings often make use of silica or even CNT to achieve special reinforcement, which shall not be treated here as not being part of the utilized samples.

Carbon Black

The classical reinforcing filler, and the main one used for the experiments of this work, however, is *carbon black* (cb).It consists almost completely of the element carbon. In spite of their chemical identity, various types of cb exist due to structural differences, conditioned by the parameters of their fabrication (soot from incomplete burning). On the nanometer scale amorphous cb forms more or less spherical *primary particles*, surrounded by an envelop of stiff glassy rubber, the *bound rubber*, on a nanometer scale [29]. The particles stick together via glassy bonds and form chain shaped *aggregates* [45],[46]. When many aggregates cluster they build *agglomerates* with a multitude of sterical branches as shown in Figure 41 [47]. It is the breaking of those filler-filler bonds that softens the rubber when exposed to deformation *(Mullins effect)* [48],[49].
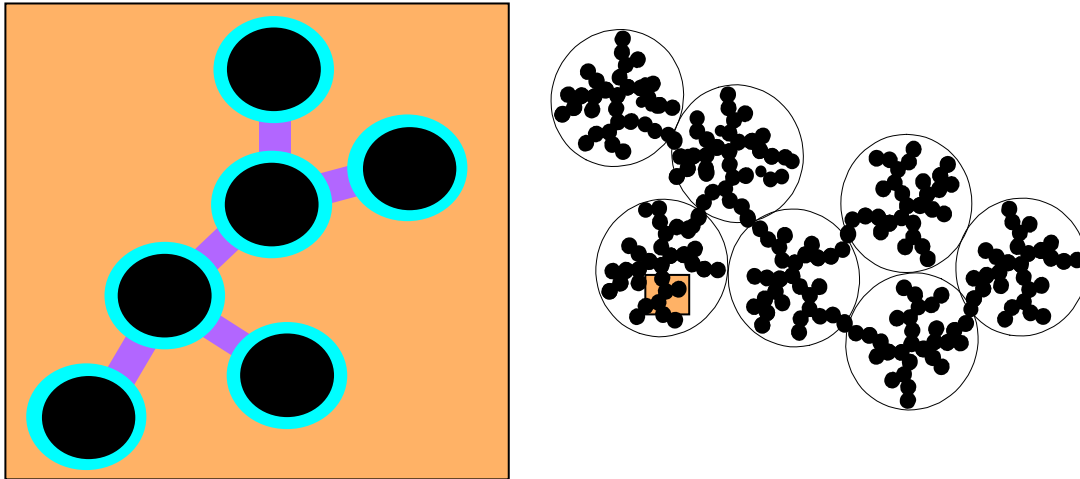
Figure 41: Carbon black aggregates (black) have glassy envelopes (blue) and bonds (purple, left).
They form agglomerates (right, aggregates in orange zoom).

Crucial for the mechanical stability of the cb within the elastomer matrix is the *percolation*. It describes to what degree the clusters (in this case: agglomerates) that fill part of the space are cross-linked. The percolation threshold is reached when a single agglomerate connects the complete matrix. The probability of achieving this threshold for a given amount of cluster material can be calculated for several types of cluster shapes for the particular dimension. All samples contain enough cb to be well percolated.

Percolation makes the rubber conductive as carbon is a good electrical conductor. Apart from mechanical and electrical behaviour also optical and thermal properties depend on the nanostructure of cb.

Structural features are surface activity (effects chemistry), aggregate size (important for percolation), porosity (decreases density) and size of the primary particles (small particles have higher reinforcement and abrasion resistance). To classify the various types of cb, the structure is encoded with an ASTM norm, with low numbers for a high surface area, i.e. fine cb. The samples contain cb of the following classes:

- N 234: highly active cb (high wear resistance, high reinforcement, 112 m^2/g)
- N 330: cb for high abrasion resistance and high tensile strength (75 m^2/g)
- N 550: medium active cb made for fast mechanical reaction (high tear resistance, 39 m^2/g)

Silica

Silica is a catch-all term for the acids of silicon. As material ingredient, it denotes its own anhydride: silicon dioxide. In amorphous form, it builds a colloidal suspension, the silica sol,

which consists of spheroid particles of nanoscale size. Stabilization leads to cross-linking of these particles to a silica gel.

The most important application is elastomer reinforcement combined with increased wet traction and low rolling resistance, especially in tyres ("green tyre"), but many others appear in chemistry, biology and technology from fire extinguisher powder to food industrial usage to aerogels and as ingredients of cements, coatings or varnishes. Silica can also be found in natural organisms.

The silica used for these experiments, Ultrasil 7000 GR, is a highly dispersible white powder (a granulate) with a bifunctional silane as coupling agent for tyre optimization and a specific surface of 170 m^2/g.

3.7.3 PAOS

Many possible ingredients of rubber already exist. Most of them affect the bulk rather than the surface. A novel way in order to build a certain surface structures shall be described now. The goal is to establish hard spherical nanoparticles that act as concentrated contact point and thus minimize the total real contact area resulting in lower friction especially for dry interfaces (see Figure 42 for the principle). As base material silica was chosen, which arises from the silica liquid precursor hyperbranched *polyalkoxysiloxane* (PAOS) in an in situ sol-gel process and aluminium oxide.
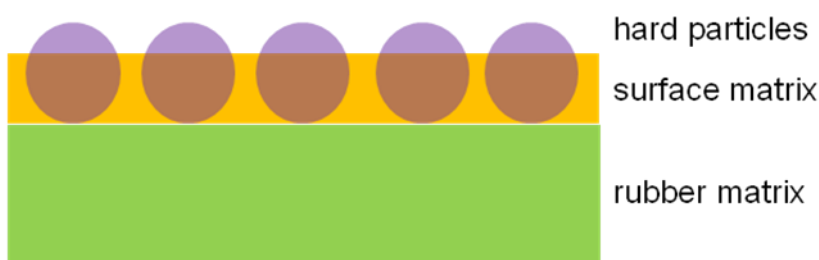
Figure 42: Nanoparticles embedded on the rubber surface minimize contact area and friction

Figure 43 shows the chemical structure of the PAOS. It functions as a precursor polymer in sol-gel processes, is hydrophobic and resists hydrolysis but is soluble in organic solvents [50],[51]. Various modifications of PAOS are possible. All PAOS variants used in these experiments have been produced at the Deutsche Wollinstitut (DWI), Aachen. Furthermore PAOS allows dispersing other nanoparticles like alumina in the continuum. Though various types of PAOS with different particle sizes in the micrometer range were tested in the experimental phase, the results shown here were performed with hexadecyl modified PAOS including a 10 % (weight) of dispersed hydrophobically modified Al_2O_3 particles.
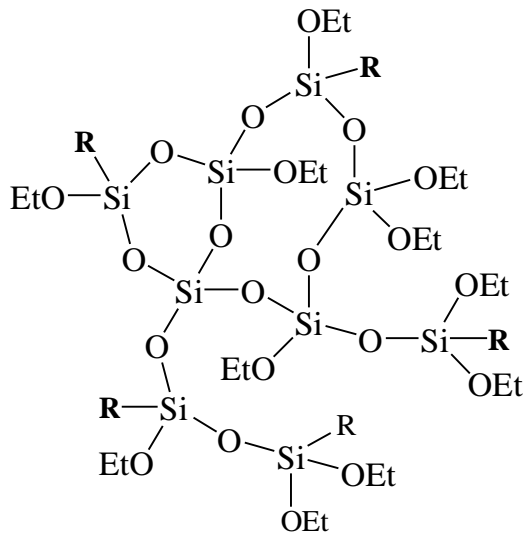
Figure 43: Formula structure of PAOS; *R* stands for -$C_{16}H_{33}$ [52].

Exposing the PAOS to humidity converts it to form silica particles. This process happens faster under increased temperatures (this *annealing* is described in chapter 3.1.3).

3.7.4 Types of Coating

For some experiments it was necessary to coat the sample surface in order to show its effect on friction compared to the uncoated surface. All coatings consist of a polymer matrix in which, for some combinations, particles of a similar size as the coating thickness (10 µm) are embedded to act as spacer when exposed to friction (the structure is similar to the one used with PAOS particles, so see Figure 42 for the principle). The coatings will be abbreviated as followed.

- *natural:* pure elastomer surface without any coating
- *PTFE*
- *PU*
- *TPU*
- *Siloxane*

The features of these classes will be explained below. However, the names do not mean that the coatings consist purely of the given material. It is rather the main component and additional substances are part of the polymer matrix or particles. Chapter 4.1.1 illuminates the details of the surface properties for the various coatings.

Of course it is crucial for the coating layer to adhere stronger to the elastomer sample than to the opposing substrate. Imperfections in adherence lead to abrasion, crimpings at the edges and finally to dissolution of macroscopic coating spots, completely falsifying the measurement. Simply spraying the coating material onto the clean elastomer turns out to be

not enough to guarantee this for such low adhesive materials as were used. Except for some early batches the samples were fluorinated in the gas phase, which allowed good adherence in most cases. This and the coating processes were accomplished at FILK (Forschungsinstitut für Leder und Kunststoffbahnen GmbH, Freiberg).

PTFE

This is a 1-component coating based on a PUR polymer matrix with PTFE (*Polytetrafluorethylene*) particles. Properties of the thermoplastic PTFE are, besides thermal and chemical stability, an extraordinarily low surface tension, so minimal friction can be expected at the contact points. For pure PTFE, static friction is even as low a dynamic friction.

Polysiloxane

As "siloxane coating" we denote a cross-linked PUR based coating with particles of polysiloxane and PTFE. *Polysiloxane* (silicone) combines the inorganic silicon with a polymeric structure. It is hydrophobic and possesses good thermal stability and low surface tension. Most important, it becomes a lubricant in liquid state at room temperature. Thus the avoided but never completely excludable abrasion of particles is expected to support friction minimization by a self-lubrication effect of this coating type.

PU

The coating WF-13-419 is a cross-linked *polyurethane* (PU) with two components, specially designed for elastomers like EPDM. It shall minimize friction, abrasion and squeaking while staying elastic. PU consists of at least two different kinds of monomers and features good coating adherence, chemical and thermal resistance. This coating does not contain particles.

TPU

Only one component is used for the WF13-462 coating. It is based on a non-cross-linked PU polymer with high elasticity. TPU is an abbreviation for *thermoplastic elastomers* (TPE) on urethane base. They show distinct plastic behaviour at high temperatures (in this case about 40°C) by dissolving bonds in the polymer network.

4 Results of Measurements and Simulations

The experimental results can be divided into three groups: the detailed description of the state the sample displays depending on its preparation and experimental exposure (chapter 4.1), the connection of the theory of friction (chapters 4.2, 4.3 and 4.4) and the friction in experimental investigations, and the effect of various systematic modifications (chapters 4.5 and 4.6) on the control of friction and stick-slip. The following sub-chapters specify these topics.

4.1 Elastomer Characteristics

The interpretation of experimental data relies on the knowledge of the material constitution of the samples. Preparation defines the original state for the sample, but the experiment itself modifies the sample unintentionally. This is superposed by aging effects, even without exposure to tribological stress. Figure 44 illustrates how the friction values develop during the running-in phase for each cycle, until friction reaches a constant level. Normal force (62 N) and velocity (10 mm/s) as typical but wear intense experimental configuration remain unchanged for the running-in, which is performed by default every time before the real measurement starts. A new running-in can even mitigate the effect of surface aging to a certain degree.
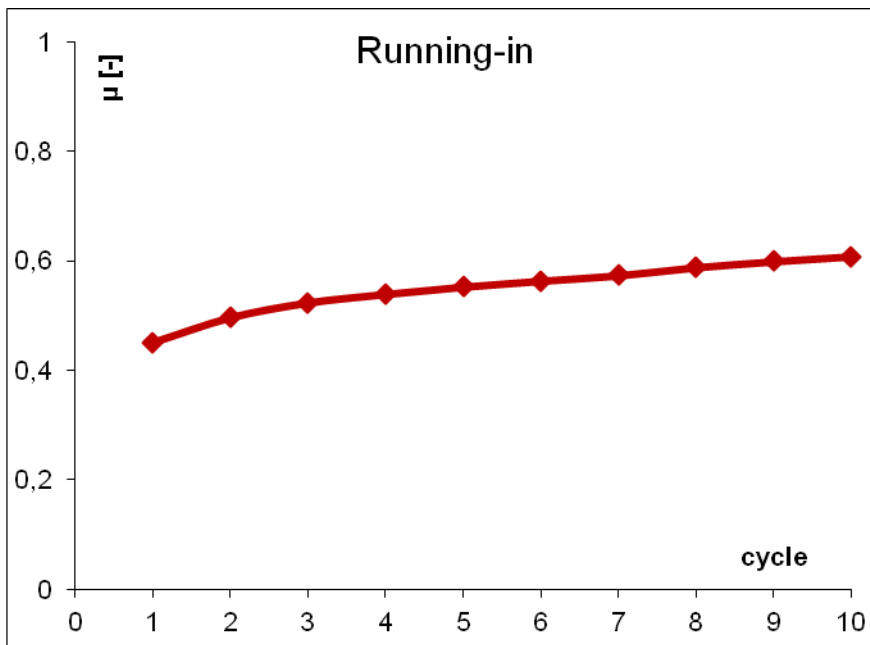
Figure 44: Friction values are not stable from the beginning, but experience a running-in development (filled EPDM, smooth with TPU coating, on dry coated sheet).

Sample characteristics are surface morphology, mechanical bulk properties and especially viscoelastic properties. Most important is the characterization of modified samples.

4.1.1 Surface Properties

Two sample modifications – those samples treated with PAOS and those coated with various lacquers – aim on the surface enhancement and thus deserve special attention in regard to their surface properties.

Samples with PAOS

The most obvious way to look at the surface is optically. The DIAS images (Figure 45) of annealed samples with rising PAOS amounts show island shaped particles near the surface. The number of particles clearly increases with PAOS amount (from left to right), with only small decreases in size – a first sign that PAOS manifests not only in the bulk but also on the surface. Of course filling the samples with carbon black (upper row) increases the number of detectable particles even more. All particles are sized between 10 µm and 50 µm.
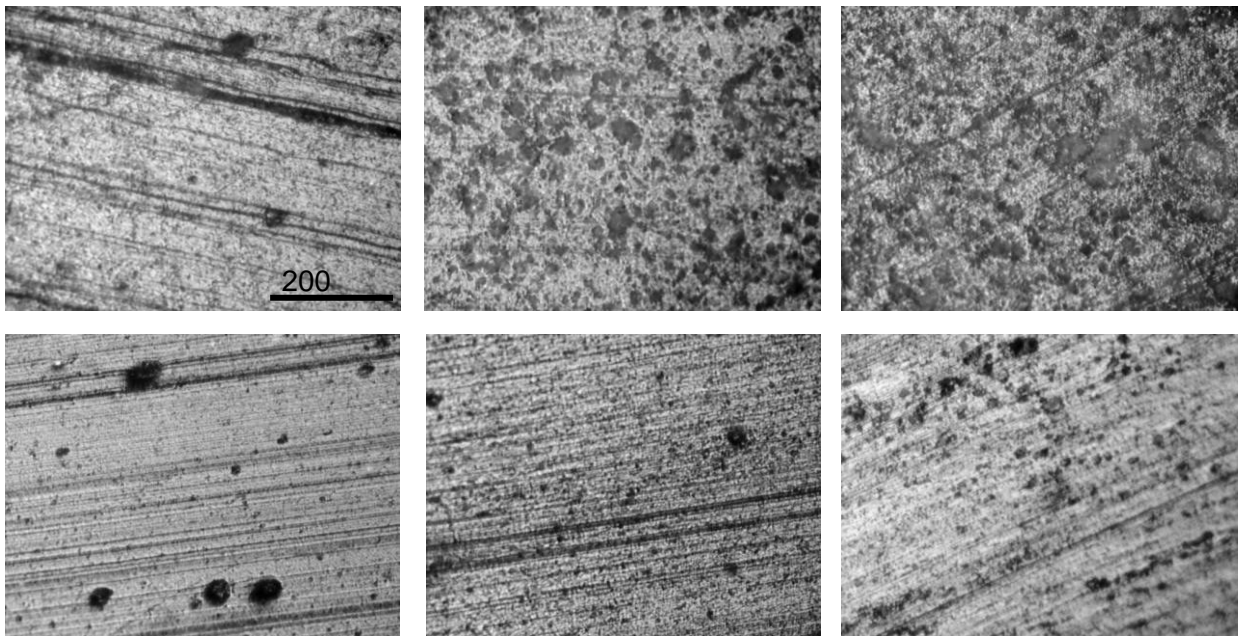
Figure 45: Light microscopic images (DIAS) for 0phr (left), 10phr (middle), 20phr (right) PAOS, with carbon black (upper row) and without (lower row), image size 640*460 µm [52]

Surface structures can be observed with AFM measurements. Apart from the pure existence and particle size, also the alteration of the particles is of interest. In Figure 46 both annealing and abrasion can be compared. Even without annealing some particles are present in these cb filled EPDM samples with 4 phr PAOS. Annealing for 24 hours (lower row) spreads the dots to larger areas, resulting in a higher degree of PAOS coverage, as more alumina/silica particles are clustered on the surface.
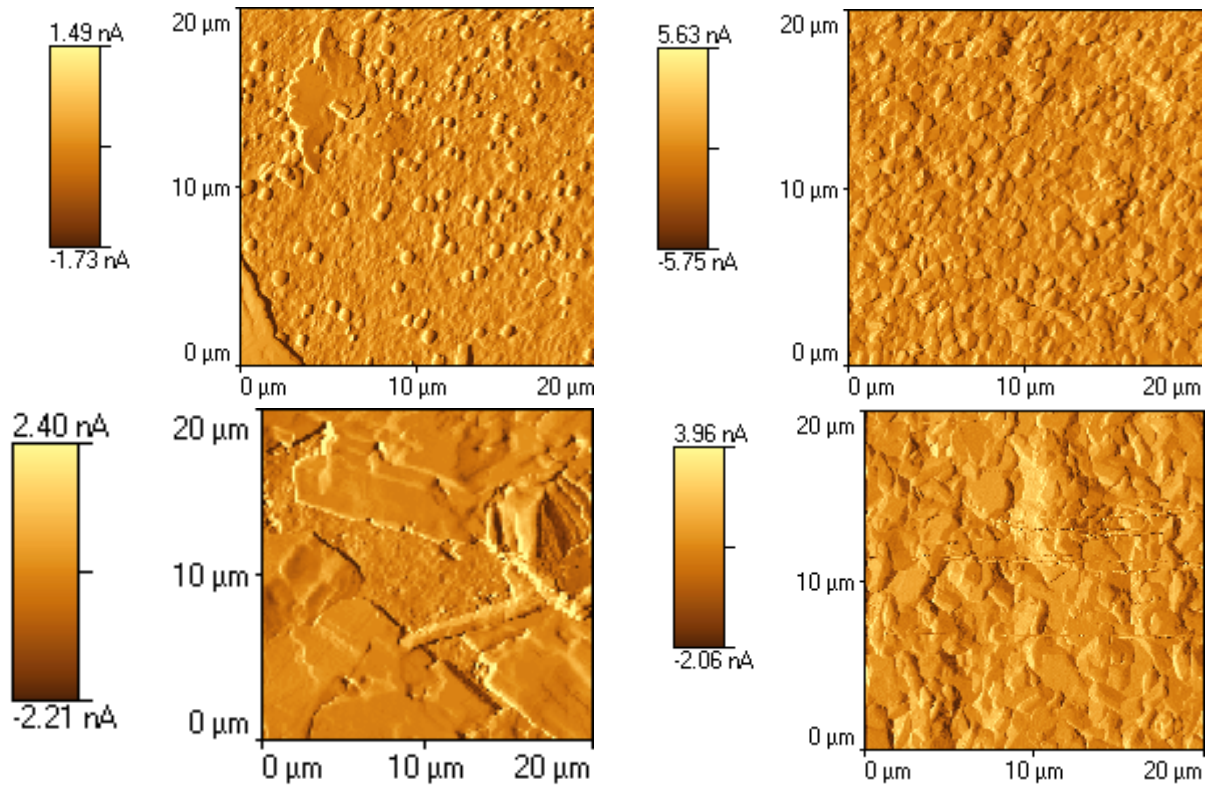
Figure 46: Influence of annealing (top row not annealed, bottom row 24 h annealed) and abrasion (left side fresh, right side abrased) on EPDM samples with 4phr PAOS
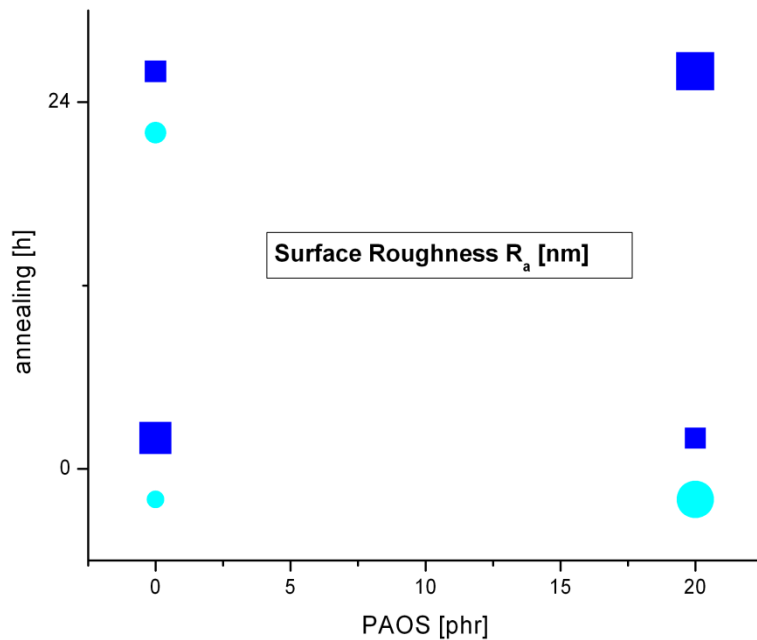
Figure 47: Graphical overview of roughness for PAOS amount versus annealing time. Neighbouring symbols (dark blue square with 50phr cb, light blue circle without) indicate the same annealing.

After friction experiments (right column) both samples display the structural corners are less accented, which explains changes in friction for longer sample usage. The silica domains have not only become flatter but also less deviating in their size distribution, so they built islands rather than dots or cumulated ledges. If PAOS has recently appeared on this surface, it has not built original structures yet.

Although the influence is not always as clear as in these images, further AFM measurements with varying amounts and types of PAOS confirm that annealing leads to agglomeration of PAOS clusters and abrasion flattens the structures. Adding carbon black sharpens the structures, and removing PAOS lets no large structures appear. Roughness analysis shows that both PAOS and carbon black are well diffused in filled samples, and cleaning with isopropanol does not affect it. The arithmetic roughness R_a is given in Table 8 and Figure 47 for various sample parameters. The presence of PAOS and carbon black have a tendency to increase roughness, while annealing has a minor effect on it. For EPDM the results are similar as for NBR.

Obviously the visible silica particles emerge partly out of the matrix. Their lateral distribution is more or less homogeneous, but their heights can differ significantly, which can be confirmed by SEM images. Concentrating the contact to a small amount of points should result in smaller friction coefficients (as wanted) but also in amplified abrasion (unwanted) around the affected particles in contact. This presumption will show that it is true in chapter 4.5.1 for the friction experiments.

How completely has PAOS been transformed into silica, and how homogenously? In the ideal case, PAOS diffuses to the surface and silica dots are only generated there exclusively for maximized effectiveness. Infrared spectroscopy (Figure 48) reveals for both NBR and EPDM that a silica peak actually can be found on the surface but appears not less pronounced in the bulk of the sample. For samples without any PAOS, the silica peak vanishes completely, so no other silica contents contaminate this evidence. Although the transformation from PAOS to silica is directed to happen on the surface during annealing, an early start of this process already during vulcanization and storage cannot be ruled out. This problem was minimized by using PAOS with large hydrophobicity.
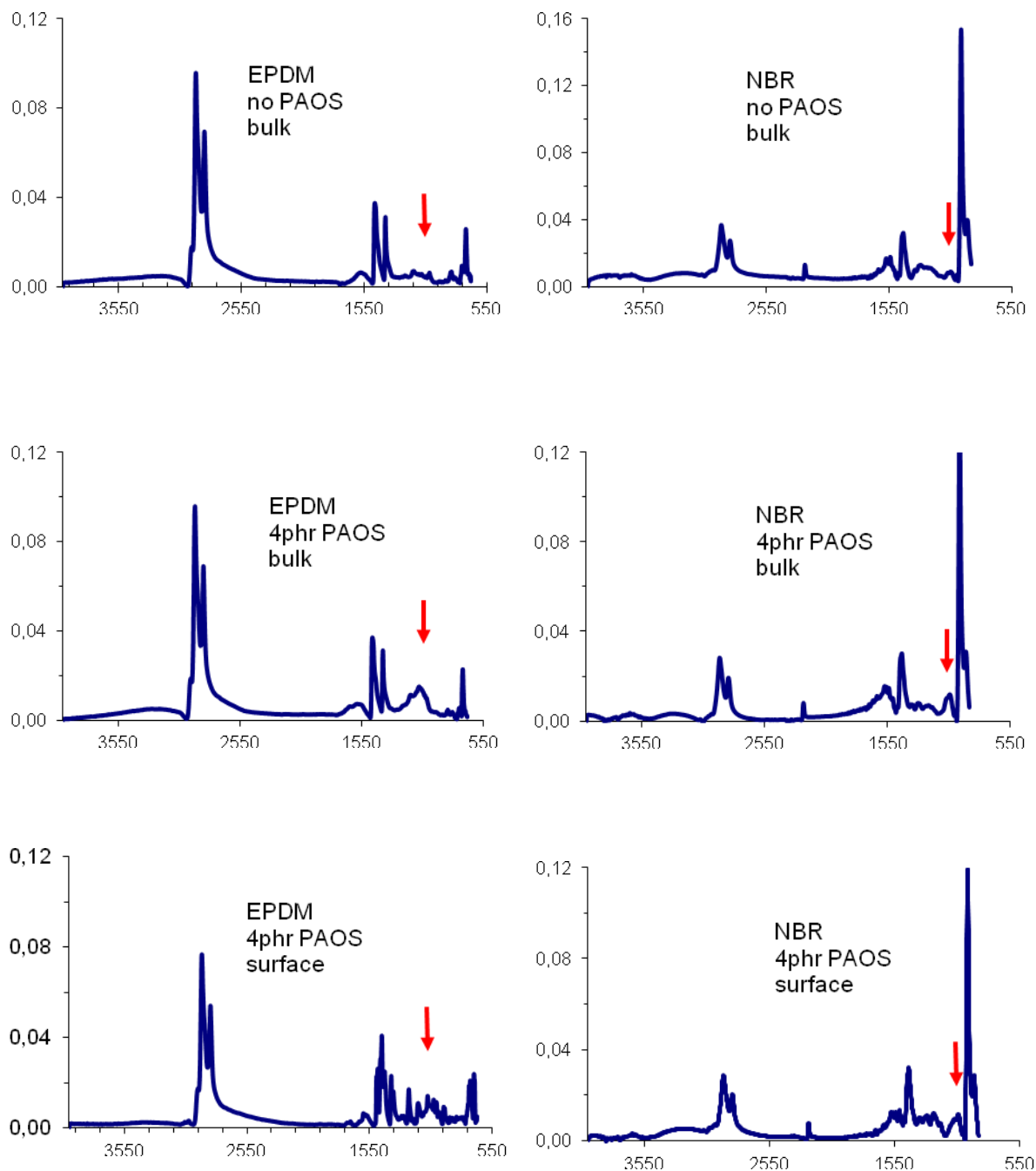
Figure 48: IR spectra of EPDM and NBR filled with 50phr cb reveal the existence of annealed PAOS
(red arrow over peak/ flat)

To determine the presence and amount of chemical elements on the surface, XPS
measurements were performed at the DWI (Figure 49). All analyzed samples contain PAOS
and were annealed for 24 hours. Carbon as the by far most strongly present element is not
indicated here. The other elements, including silicon, differ significantly for varying lateral
positions (visible in the error bars) and thus indicate an inhomogeneous, insular distribution
on the surface. This inhomogeneity however is superposed by the local agglomerations of
carbon black. PAOS is less soluble in NBR than in EPDM and should concentrate more on

the surface – the XPS data for silicon indeed turns out to be slightly higher on NBR surfaces. A tendency for smaller friction might be the consequence.
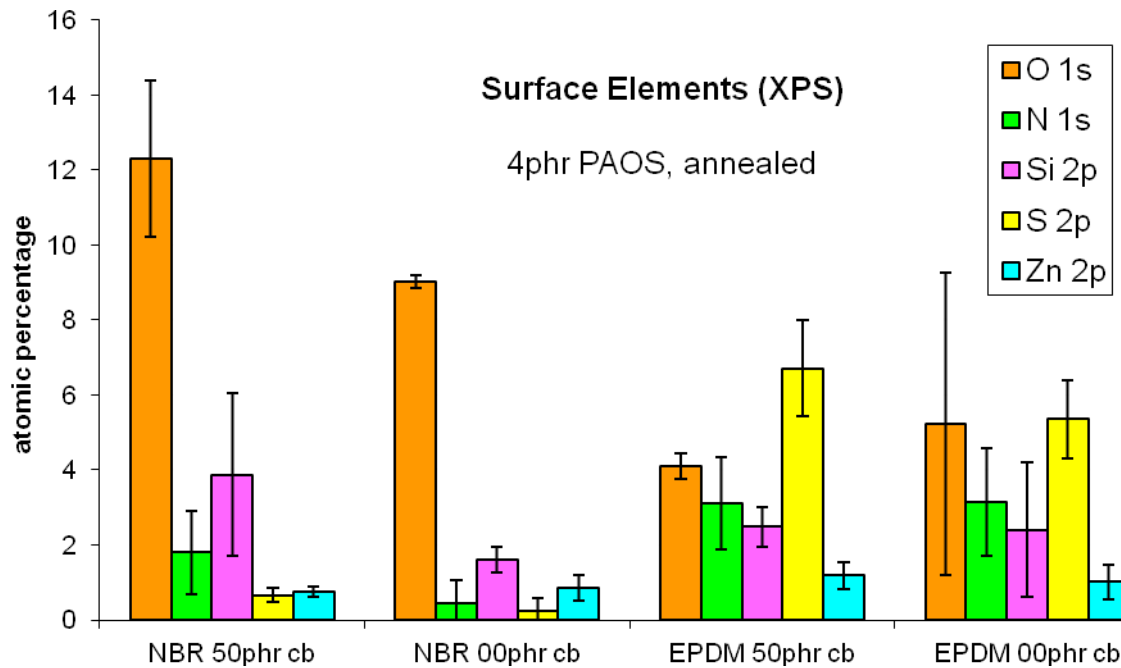
Figure 49: XPS results for surface elements (apart from carbon) on PAOS induced NBR and EPDM samples [52]

carbon black	PAOS	annealing	R_a	surface tension [mN/m]		
[phr]	[phr]	24 h	[nm]	total	polar	disperse
0	0	before	154 ± 17	16.6	2.0	14.6
0	20	before	667 ± 181	11.3	0.3	11.0
0	*0*	*after*	*215 ± 42*	*16.4*	*1.9*	*14.5*
0	*20*	*after*	*-*	*15.1*	*0.2*	*14.9*
50	0	before	644 ± 187	17.3	1.7	15.6
50	20	before	260 ± 77	18.8	0.6	18.3
50	*0*	*after*	*289 ± 157*	*17.1*	*1.9*	*15.2*
50	*20*	*after*	*883 ± 161*	*19.9*	*1.0*	*19.0*

Table 8: Surface tension and roughness for PAOS filled samples. Figure 50 corresponds to this table.

The surface tension (sessile drop, in Figure 50 and Table 8) may give further information about what to expect for friction modification. Analysis of NBR samples containing PAOS with hydrophobic Al_2O_3 particles was done due to the parameters PAOS amount (none and 20 phr), carbon black amount (none and 50 phr) and annealing time (none and 24 hours). Adding PAOS significantly decreases the polar part in any case, and slightly the total tension without carbon black. In cb filled samples however, the disperse part is increased by more

PAOS. Furthermore, the total tension is increased by adding carbon black itself. Annealing increases the total tension for PAOS filled samples but, as expected, has little effect on samples without PAOS. In contrast to NBR, annealing seems to minimize the polar part strongly for EPDM with PAOS and cb. The high surface tension on EPDM is also more sensitive to usage of isopropanol, which reduces it to almost the level of NBR.
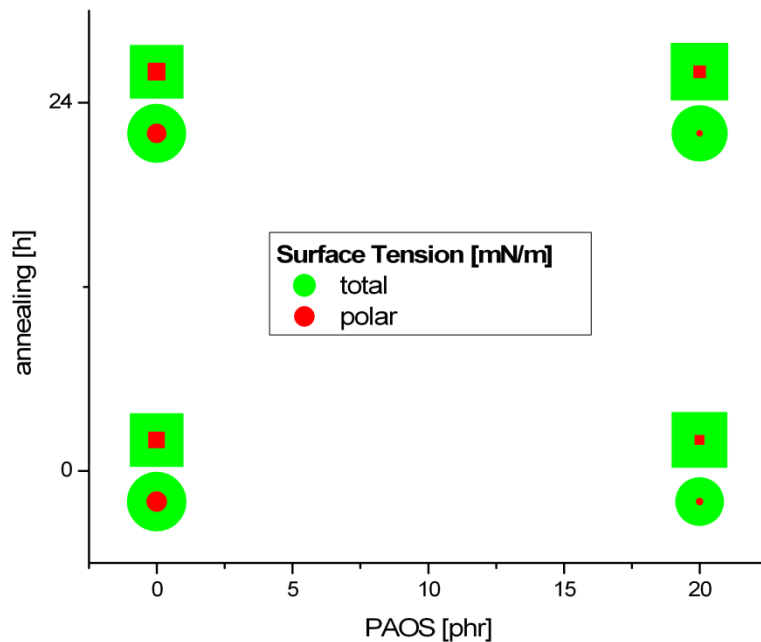
Figure 50: Graphical overview of surface tensions for PAOS amount versus annealing time. Neighbouring symbols (square with 50phr cb, circle without) indicate the same annealing. Total and polar parts scale with the covered area.

Samples with Surface Coating

The surface properties of coated samples can be focused on two pivotal aspects: the change in roughness, which superposed the natural surface structure imprinted during the vulcanization, and the individual surface tension [53] of each coating. Both are likely to affect friction on a large scale.

The intended coating thickness of 10 µm was indeed exceeded by the coating process. Cross sections reveal the true typical thickness for each coating type [54]:

- PTFE: 16 µm
- PU: 11 µm
- TPU: 26 µm
- Siloxane: 19 µm
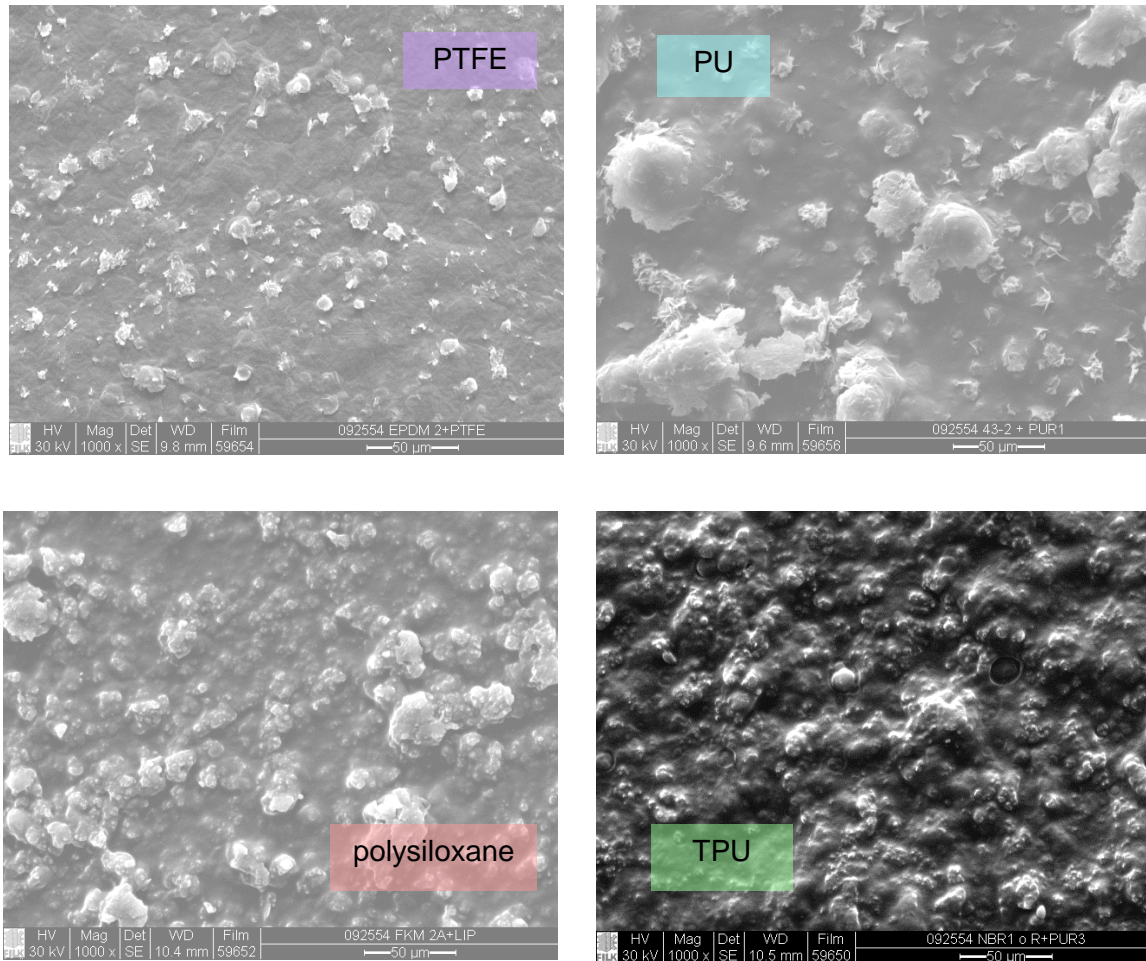
Figure 51: The surface morphology of SEM images (1000* magnification) varies with the coating type [55]

Those values suffer little lateral variation, except for PU, which is constricted inhomogenously while drying. The embedded particles of the varnish are, with peculiar sizes of 8 to 15 µm, similar as or slightly smaller than the thickness of the complete coating. Figure 51 shows the morphology of the coatings in SEM images with the same magnification. The morphologies differ qualitatively and quantitatively: Whereas TPU is a smooth resin, PU is structured, and clusters have formed in different sizes depending on the coating. The large formations on PU indicate to maturing processes, possibly related to the drying constriction. Sizes of lateral structures tend to rise with the sample roughness [56].

Analyzing the SEM images with EDX and ATR-IR for their elemental composition exhibits fluor concentrated in spots from PTFE both in the PTFE and also in the siloxane coating but not for PU and TPU, which are dominated by carbon, silicon and oxygen.

coating	elastomer	filler	structure	roughness R_a		[nm]
PU	S-SBR	with cb	smooth	1300	±	360
TPU	S-SBR	with cb	smooth	1100	±	150
Siloxane	S-SBR	with cb	smooth	680	±	200
PTFE	S-SBR	with cb	smooth	500	±	60
natural	S-SBR	with cb	smooth	44	±	27
natural	S-SBR	with cb	fine	490	±	110
natural	S-SBR	with cb	coarse	790	±	200
natural	S-SBR	without cb	smooth	66	±	29
natural	EPDM	with cb	smooth	42	±	12
natural	EPDM	without cb	smooth	71	±	12

Table 9: Roughness values R_a taken from AFM measurements for various surfaces modifications. The root combination of parameters is highlighted [57].

How does roughness change with elastomer, filler, surface structure and coating? Table 9 gives an answer to this question. Based on cb filled S-SBR 2525 with a smooth, uncoated surface as reference (marked bold in the table), parameters are varied. All mean arithmetic roughnesses R_a were gained from AFM profiles. Structuring the sample with coarse vulcanization plates instead of smooth ones makes the surface, as intended, considerably rougher. The differences between SBR and EPDM are negligible. Samples without carbon black are a little rougher than filled ones. Structures of the natural sample surfaces are superposed by the unavoidable roughness of the coating films, rendering the structural influence of elastomer and filling obsolete. PTFE and siloxane coatings bring even smooth elastomers to almost "coarse" level, PU and TPU convert all samples to "very coarse", regardless of other parameters.

The results of the AFM roughness can be correlated with the full width at half maximum σ of histograms from white light interferometry, which also incorporate information about the roughness, but rather on a macroscopic scale whereas the AFM measures microscopic structures. So both R_a and σ have been rescaled to compare them in Figure 52, and in fact, the values show a proportionality for coated samples. The same prevails for the averaged contact angle hysteresis ΔΘ gained from Wilhelmy measurements. This method, however, combines the effect of roughness with strong information about surface tension, so coated samples have not as high values as the uncoated, natural surface might suggest. The presence of fluor lets the moderately rough siloxane and PTFE coatings reach similar values as the considerably rougher PU and TPU.
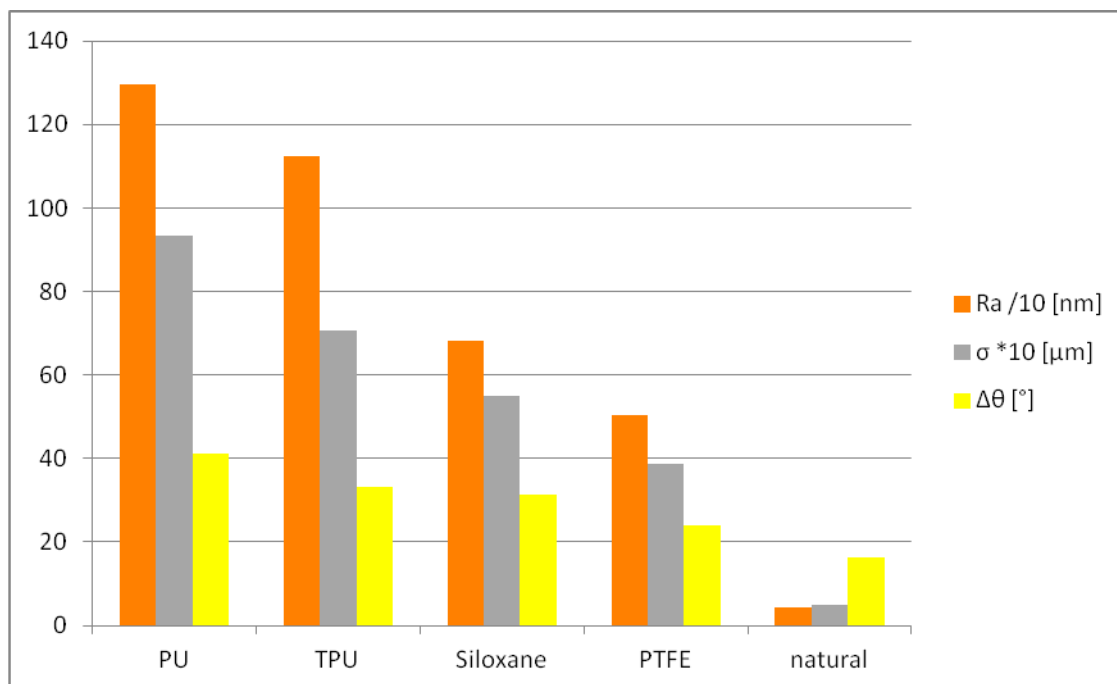
Figure 52: On smooth S-SBR 2525 filled with cb, coatings increase roughness as indicated both from AFM measurements (R_a /10 [nm] orange) and white light interferometry (σ *10 [µm] grey) while the contact angle hysteresis (ΔΘ [°] averaged over several liquids, yellow) rises significantly less [56].

4.1.2 Mechanical Properties

Many parameters determine the mechanical behaviour of the samples. Table 10 shows how the amount of carbon black, PAOS and the annealing time influence various mechanical aspects. "Elongation at break", "Stress at 200% strain" and "Density" are self-explanatory; all other are described in chapter 3.3.

The combination of annealing and addition of Al_2O_3/PAOS dispersion increases hardness and rebound, whereas tensile strength, elongation at break and the stress at 200% strain drop considerably for high PAOS contents. Some of these property changes (hardness, elongation) are typical for inactive fillers, comparable to the effect of the carbon black, which has been well studied [26]. Others are rather connected to softeners, distinguishing PAOS from carbon black. Density rises with filler, too, but partly replacing the total percentage of carbon black by PAOS leaves density constant. Remarkable is the drastical augmentation of abrasion, especially without carbon black and after annealing, due to a lack of cross-linking. PAOS can be detected even on abrased surfaces. The effect of carbon black on the sample is as expected: The material becomes more solid, hard and inelastic. For EPDM the elastic rebound is higher; the elastomer is softer and less tear-resistant.

carbon black [phr]	PAOS [phr]	anneal time [h]	IRHD hard-ness	re-bound [%]	tensile strength [MPa]	elongation at break [%]	stress 200% [MPa]	DIN ab-rasion [mm^3]	density [g/cm^3]
0	0	0	54	53	5.0	340	2.3	65	1.01
0	10	0	55	53	3.8	350	2.2	100	1.02
0	20	0	56	54	2.2	340	1.4	145	1.03
0	*0*	*24*	*54*	*55*	*4.3*	*360*	*2.2*	*65*	*1.01*
0	*10*	*24*	*58*	*56*	*5.7*	*380*	*2.5*	*150*	*1.02*
0	*20*	*24*	*64*	*56*	*2.7*	*390*	*1.7*	*265*	*1.03*
50	0	0	75	33	27.9	290	16.8	70	1.17
50	10	0	76	36	23.3	270	14.9	85	1.17
50	20	0	75	39	18.6	250	13.4	140	1.16
50	*0*	*24*	*74*	*33*	*24.7*	*260*	*16.7*	*75*	*1.17*
50	*10*	*24*	*78*	*36*	*24.7*	*270*	*16.1*	*105*	*1.17*
50	*20*	*24*	*80*	*38*	*17.8*	*230*	*14.4*	*175*	*1.17*

Table 10: Mechanical properties of NBR in respect of PAOS amount [52]

4.1.3 Viscoelastic Properties and Shift Factors

PAOS Induced Samples

The effect of filler material and thermal treatment on the viscoelasticity of elastomer samples is pictured in the DMA temperature sweeps of Figure 53 with 0.5% amplitude. With its influence on magnitude and speed of vulcanization, the presence of PAOS can be expected to affect the material after finished cross-linking, too. Indeed, a rising amount of PAOS increases the shear moduli *G'* and *G''* in the high temperature range and thus a lower step size of the G_∞/G_0 ratio. Consequently, the maximum of the loss angle *tanδ = G''/G'* , which is strongly correlated to friction, is diminished without changing the associated temperature of the angle – PAOS behaves like a non-active filler without coupling to the polymer. Carbon black filled samples, however, show a much higher, well known increase of the shear moduli with a decreased maximum of *tanδ*. As for PAOS, the corresponding glass transition temperature remains unchanged. Annealing has only minor effects on the viscoelasticity.

Samples for Friction Master Curves

While fillers modify the general stress sensibility to strain, the thermal course, or due to the TTS, the frequency dependency belongs to the elastomer bulk. In Figure 54 the three cb filled rubbers of the friction master curve experiments are compared in viscoelastic master

curves from DMA frequency sweeps: As usual, the curves were left unshifted for the reference temperature of 20°C.

The shear storage modulus *G′* rises with frequency and finally enters a maximum, with EPDM as softest and NR as stiffest material at high frequency/ low temperature. As all these rubbers behave almost identical for low frequencies, this means a low step size or low temperature dependency for EPDM. For SBR, the rising starts significantly "earlier" (= lower frequent) because this material has an especially low glass transition temperature. This is even better observable for the loss modulus *G″* and the loss angle *tanδ*, visible in the peak of the curves. The maximum of the loss angle depends strongly on the elastomer type.
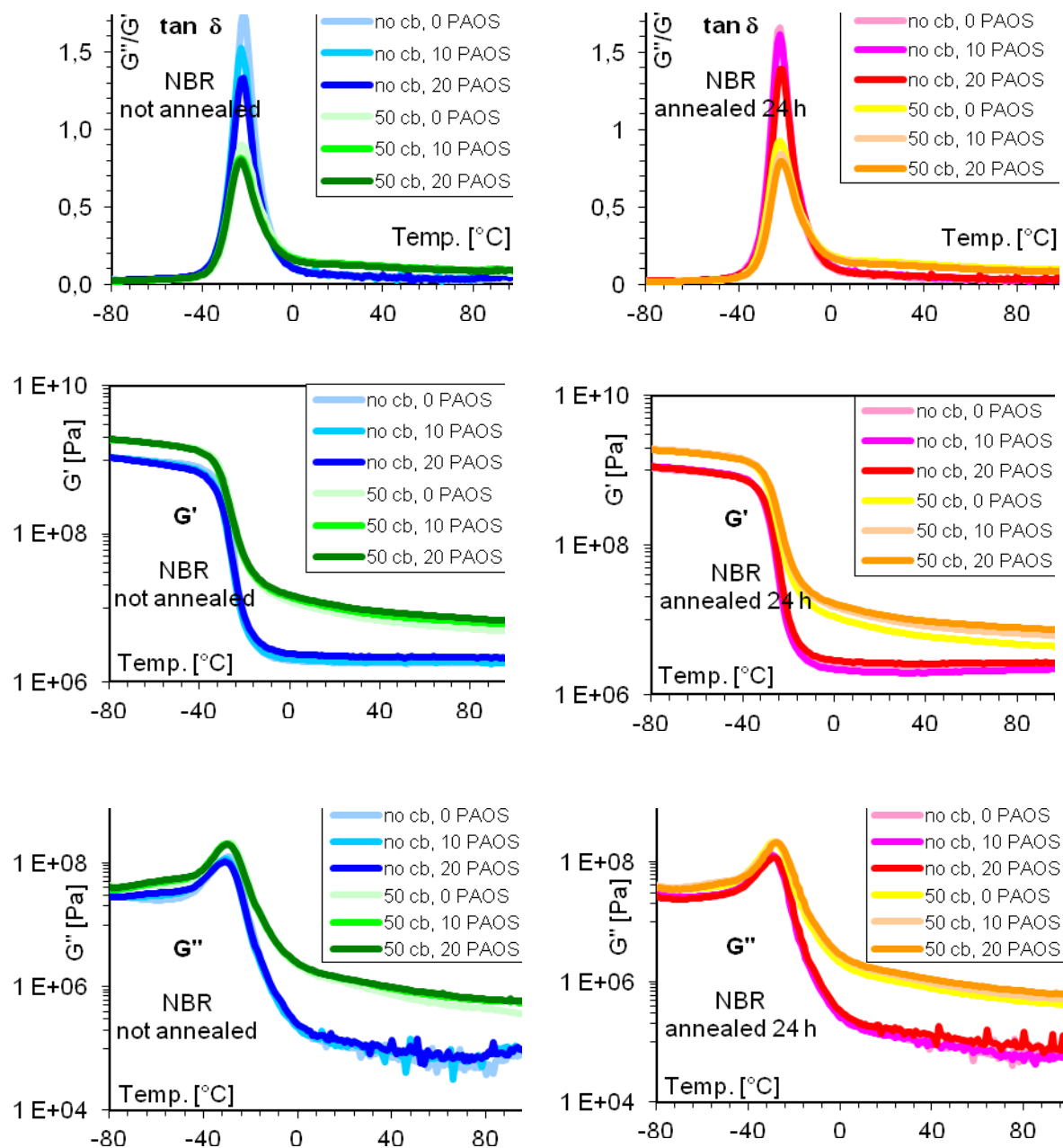
Figure 53: Viscoelastic properties as temperature sweeps of NBR with various PAOS degrees [phr] before (left) and after (right) annealing, either with 50 phr cb and without.
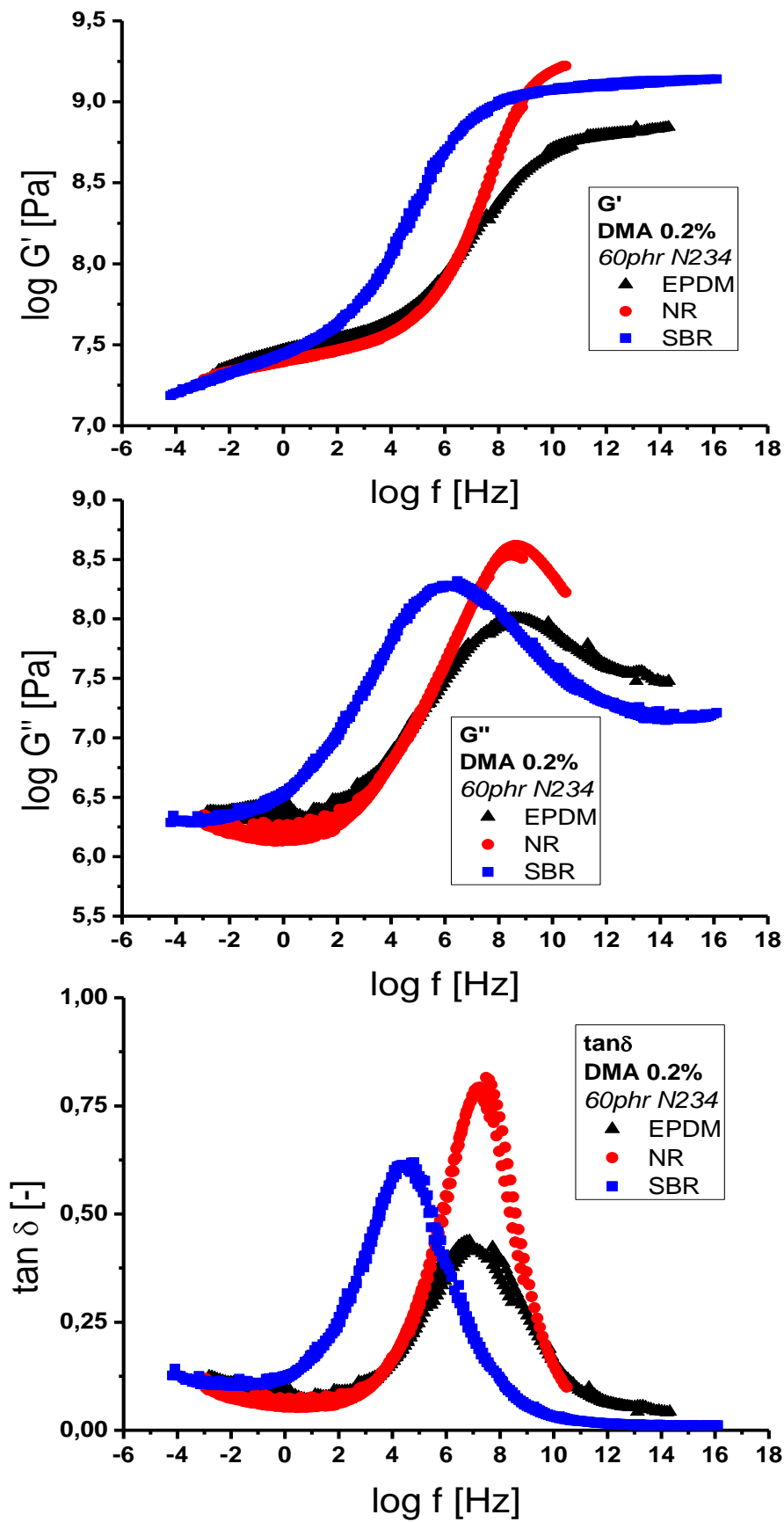
Figure 54: Viscoelastic storage modulus, loss modulus and loss angle for various filled rubbers of the friction master curves experiments. SBR is of the 5025 type.

To gain the DMA master curves, horizontal and vertical shifting as depicted in Figure 55 has been applied on the frequency branches. All fit to the WLF equation with constants as given in the box down to the glass transition.
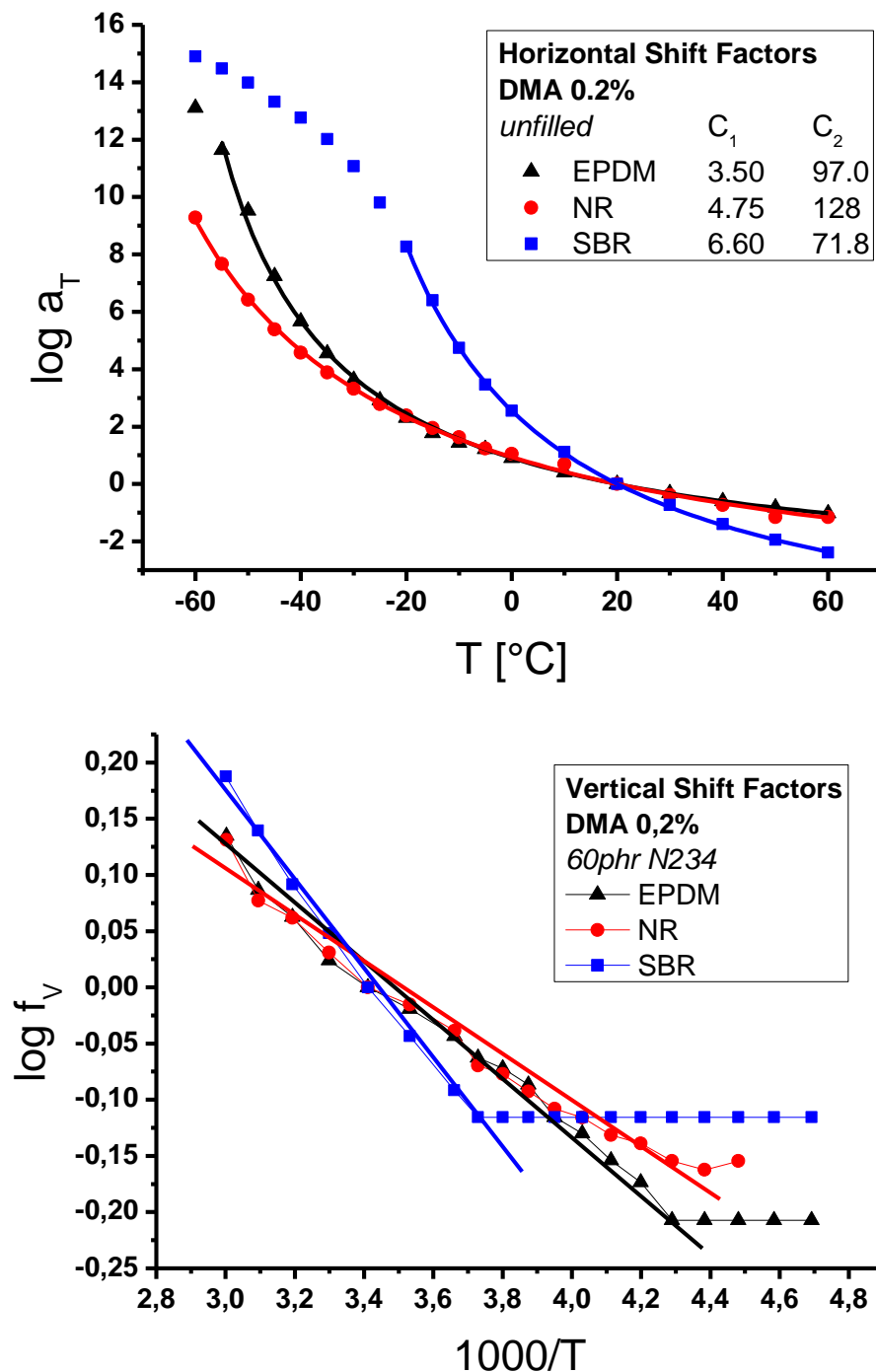
Figure 55: Horizontal (above) and vertical (below) shift factors for the master curves of Figure 54

Coated Samples

The factors above belong to the rubber samples used for the friction master curve tests. For the variant mixture of the S-SBR 2525 used as base material for coating (Figure 56)

however, the WLF constants (Figure 57) account for $C_1 = 4,3$ und $C_2 = 94°C$ with a glass transition temperature at -33°C as maximal loss angle and -42°C as maximal loss modulus. Not surprisingly the addition of carbon black lifts the moduli for low frequencies and reduces the maximal loss angle; the storage/ loss modulus ratio drops from 620 to 275 by filling. As a bulk effect the viscoelastic behaviour should not be bothered by surface structures: Direct DMA comparison of samples with smooth and rough surface indeed confirm this assumption perfectly.
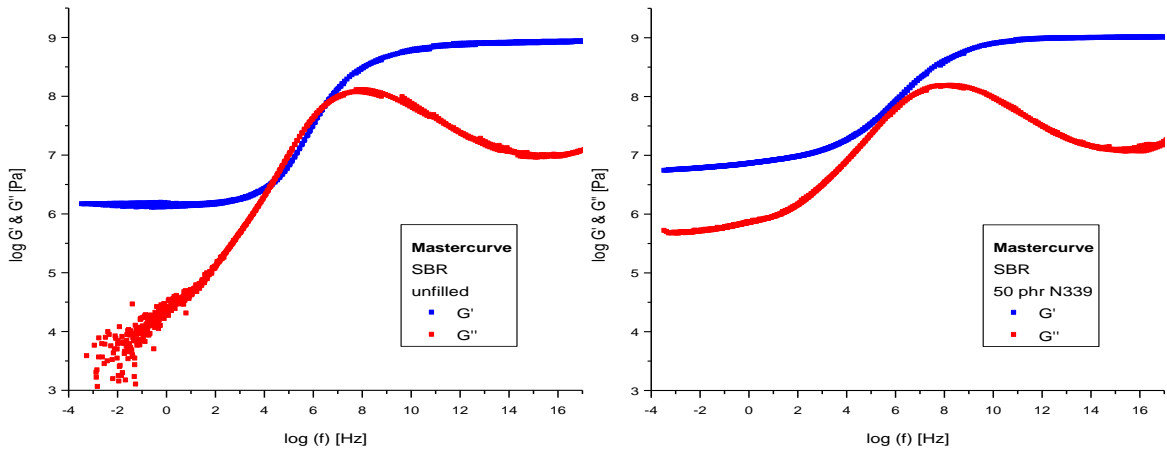
Figure 56: Master curves for S-SBR 2525 from DMA measurements with 0.5% amplitude filled with carbon black (right) and unfilled (left)
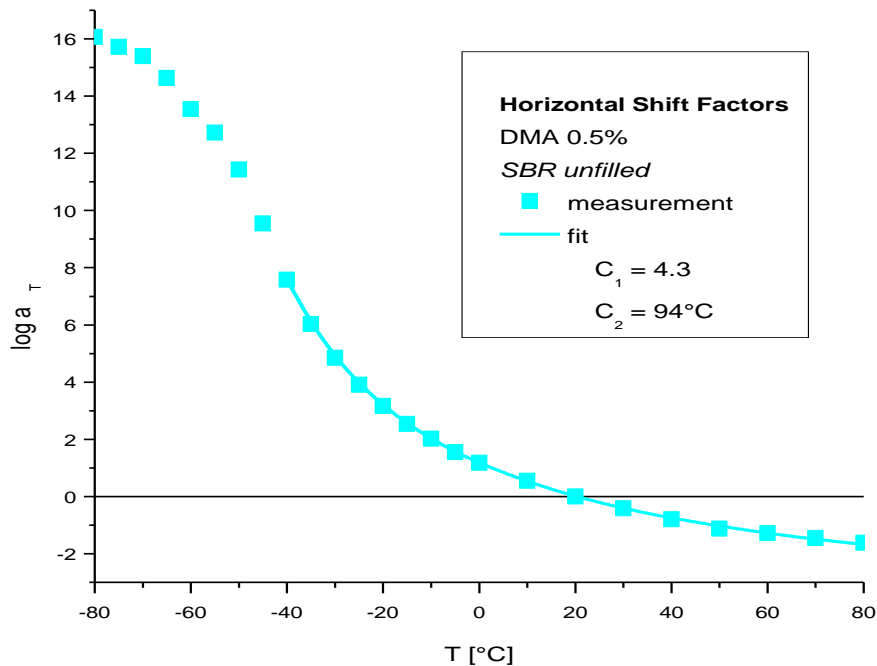
Figure 57: Horizontal shift factors for the unfilled S-SBR 2525

Silica Filled Samples

With the same SBR material the influence of silica has been tested. DMA measurements were again performed with 0.5% amplitude. Figure 58 reveals how the viscoelastic properties depend on the filler content: The filler increases the moduli of the master curves monotonously, especially for high temperatures, without changing values in the glass matrix dominated high frequency range, so the ratio $E'_\infty/E'_0 = G'_\infty/G'_0$ decreases (see Table 11 for values). The effect grows disproportionately high with the amount of silica.
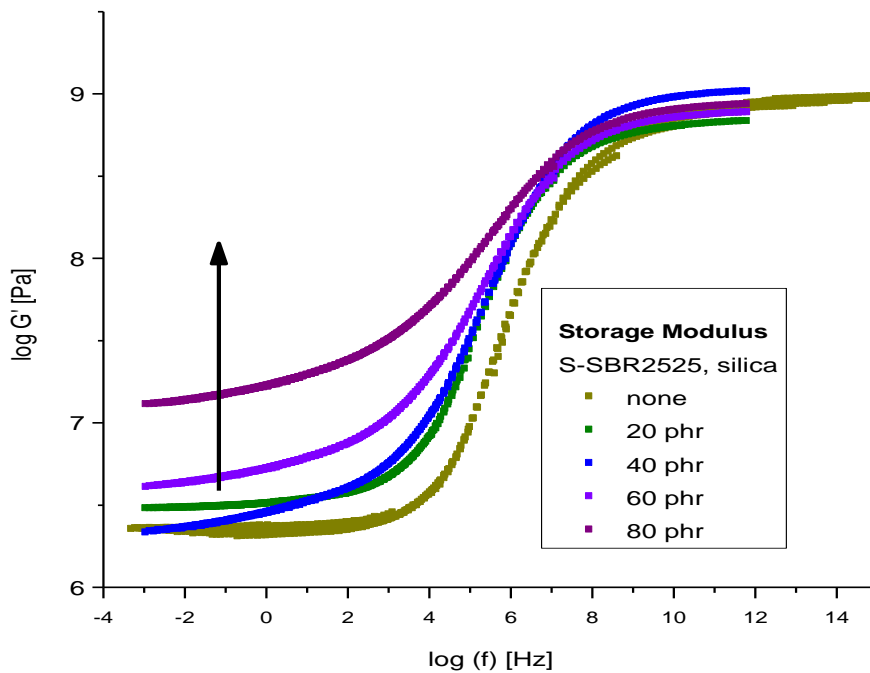
Figure 58: The master curves (0.5%) for the storage modulus show a strong increase for low frequencies when silica is added to the sample (arrow).

This also means the glass transition is broadened considerably compared to that of unfilled sample, because chain mobility is reduced in the presence of filler, as can be seen in the curves of storage modulus. The effect is minimal for weakly filled samples (20 phr silica), moderate for medium filled ones (40 to 60 phr) and dominant for highly filled sample 80 phr.

Looking at the loss modulus G'' in Figure 59, the increase with filler content is obvious, too, but more proportional to the filler amount than for the storage modulus. In both cases, the increase is smaller for low temperatures, as chain mobility is limited anyway under these circumstances. This stability is already reached for the frequency of maximal loss moduli at glass transition, so the curves meet in a single point that differs neither in frequency nor in modulus for any filler degree.
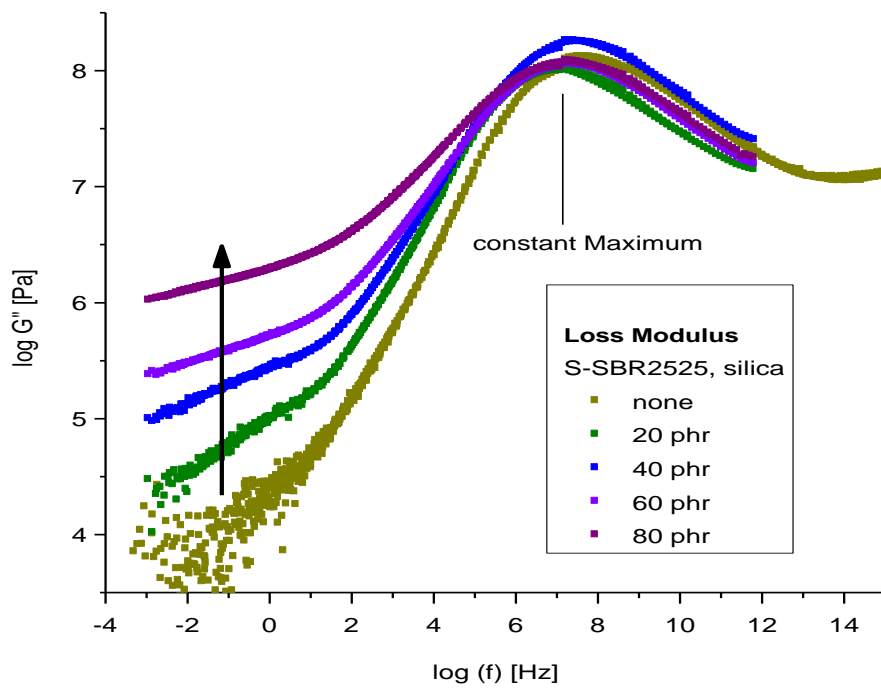
Figure 59: Also the loss modulus is affected in the low frequency range while the peak remains unchanged.
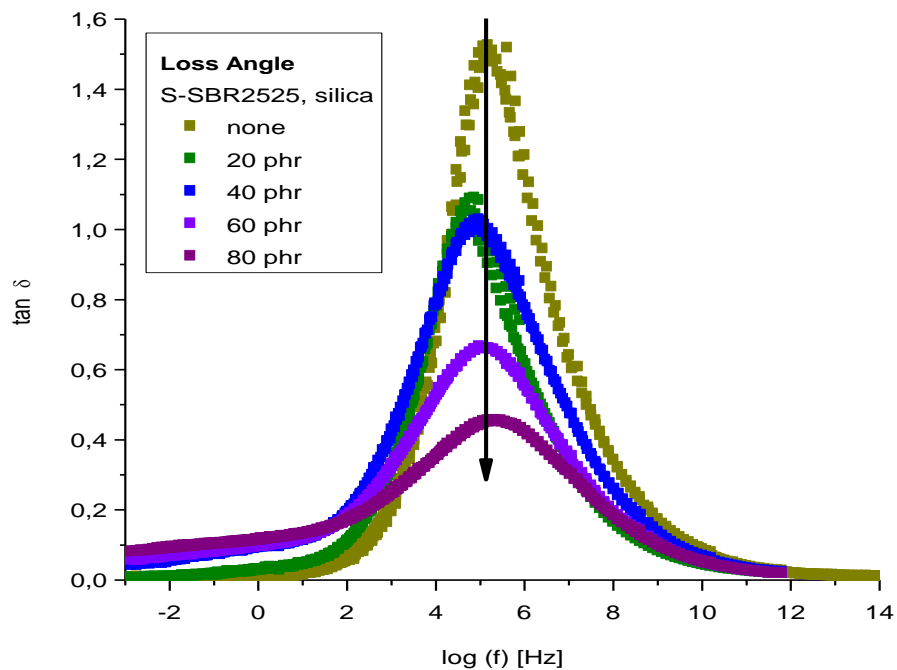
Figure 60: Resulting from the moduli behaviour, silica drastically decreases the loss angle but not its frequency.

As a result, the frequency of the maximum for $\tan\delta = G''/G'$ does not change either with filler content, but as G'' stays the same while G' increases, the value of the maximum decreases strongly when filler is added (Figure 60). The frequency dependency of G' and G'' becomes not only smaller but also more similar with rising filler amount.

Horizontal shift factors for SBR 2525 have already been described above and they have been confirmed by dielectrical measurements [58] over a range from -100°C to +100°C in discrete steps of 5°C, while varying the frequency. While horizontal shifting is valid either for unfilled as well as for filled samples, vertical shifting becomes a need after silica filling independently for G' and G''. Figure 61 shows the Arrhenius plot for 60 and 80 phr silica, with higher shift factors for a higher filler degree, and larger shift factors for the loss modulus than for the storage modulus.
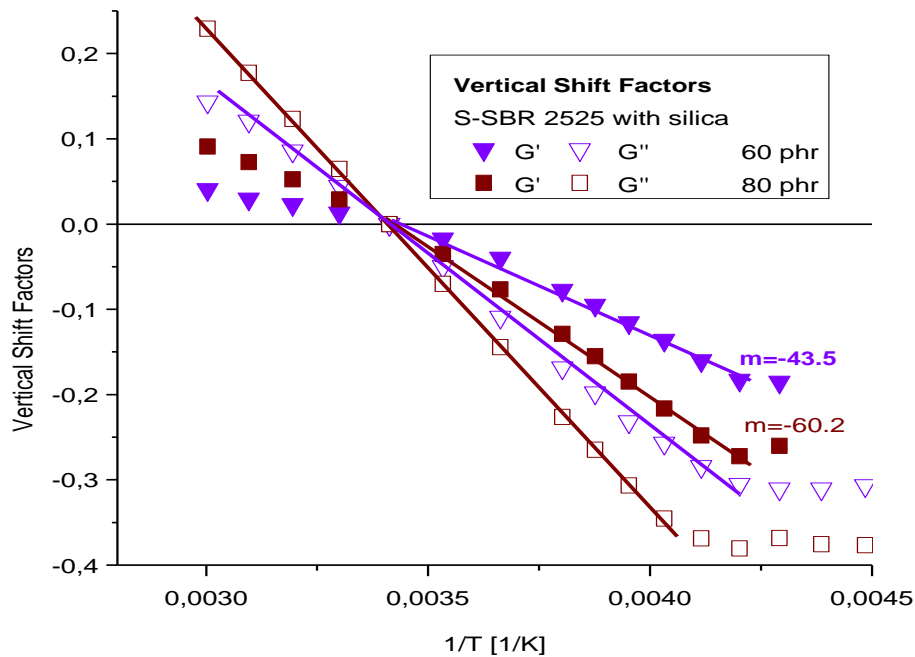
Figure 61: The presence of silica makes vertical shifting necessary. For both G' and G'' factors increase separately with silica amount.

4.1.4 Relaxation Time Spectra

The relaxation time spectra can be calculated from the viscoelastic response of the DMA measurements as explained in chapter 2.2 and result in Figure 62 for several cb filled types of elastomers. Evaluation of the linear slope m provides the exponent n according to Equation 36. The high glass transition temperature of SBR shifts the curve to the right on the time axis but does not affect the slope itself.
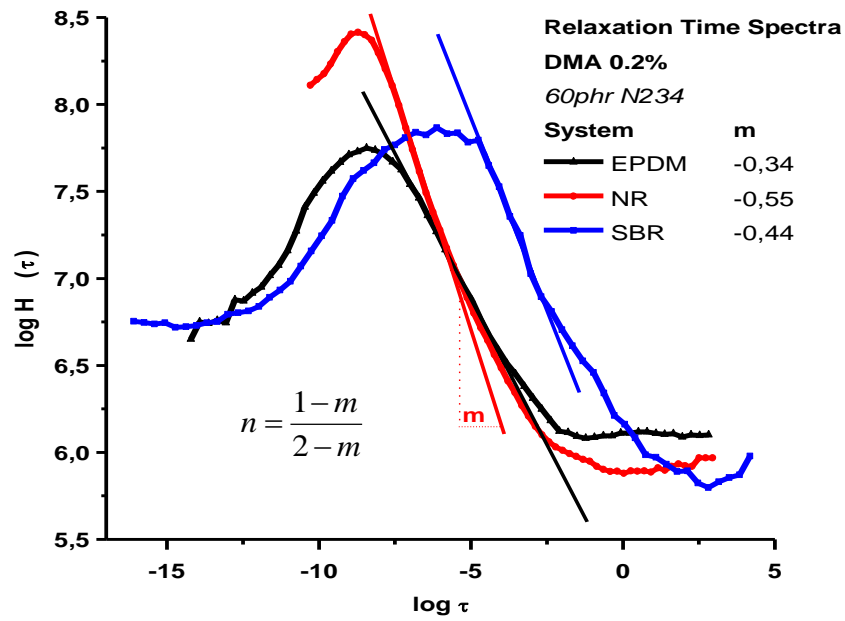
Figure 62: Relaxation time spectra of the corresponding viscoelastic data from Figure 54 and their resulting slopes *m*
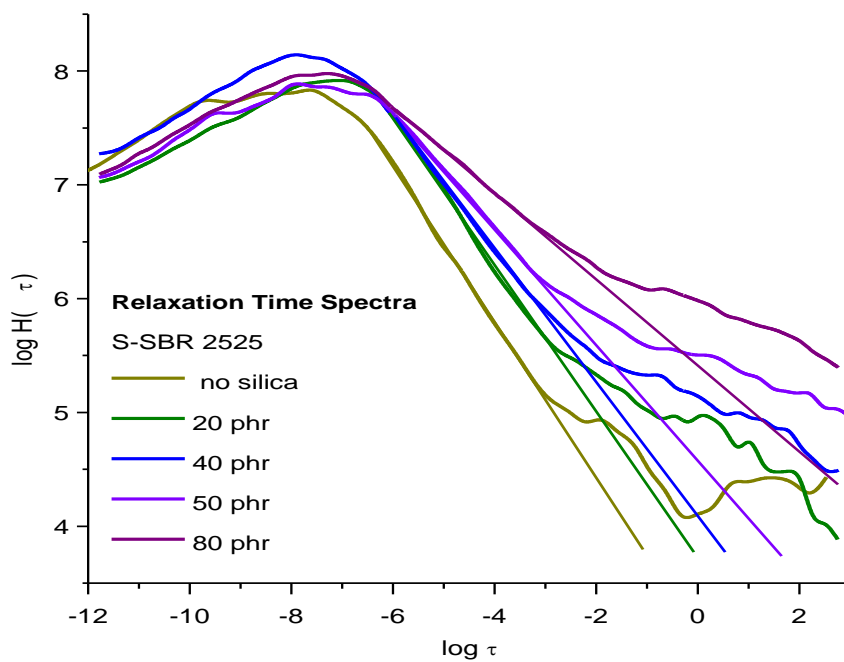
Figure 63: Relaxation time spectra of S-SBR 2525 with variable silica amount

The relaxation time spectra not only depend on the rubber itself but of course also on the filler. Figure 63 gives the spectra of SBR 2525 for a number of silica filling degrees. The linear slope of the falling flank flattens more and more by increasing the filler, resulting in increasing *n*. Again, the effect rises especially for large filler amounts. Values for the parameters that rule viscoelastic behaviour of these samples are noted in Table 11.

phr silica	E_∞/E_0	Slope *m*	Exponent *n*
0	473	0.714	0.209
20	298	0.711	0.211
40	541	0.594	0.283
60	389	0.441	0.357
80	178	0.358	0.390

Table 11: Viscoelastic parameters (DMA 0.5%) depend on the amount of silica in SBR 2525.

4.2 Friction Plateaus of Silica Filled Systems

In this chapter the influence of strengthening filler on friction will be analyzed systematically. A series of SBR samples filled with various amounts Φ of silica (from none to 80 phr in steps of 20 phr) has been investigated tribologically on rough granite and asphalt [59],[60]. Simulation of hysteresis and adhesion friction are compared to the wet and dry measurements and give results that will prove helpful in the understanding of general friction dependence on velocity as it is surveyed from a larger view point in chapter 4.3.

4.2.1 From Wet Friction to the Silica Plateaus of Dry Friction

As prerequisite of understanding the total friction and its correlated adhesion simulation, the measurement of wet friction and simulation of hysteresis friction are the logical first steps. The results of the wet measurements on granite are shown in Figure 64, and on asphalt in Figure 65.

On both granite and asphalt surfaces, friction clearly increases with velocity, which means lubrication is effective especially at lower speeds. On asphalt the slope remains nearly the same over all measured velocities – temperature effects can largely be ruled out when using a lubricant – whereas granite displays but a softly increased slope at higher sliding speeds. Simulations emulate the curves, including their increase, even more pronounced for extrapolating into the fast range.

The absolute amount of friction is quite similar for both substrates. In general, friction on granite tends to be only slightly higher than on asphalt. The exact behaviour strongly depends on the filler amount: For asphalt, the friction increases monotonously with the degree of filler in the complete velocity range. On granite, this is true only when disregarding weakly filled samples (the measured friction coefficients of 20 phr silica are hardly discriminable from those of the unfilled sample), corresponding to the small effect that marginal silica fillings provoke on the viscoelastic response. 80 phr silica show in any case the definitely largest effect; a desired result especially for tyre construction. The increase of friction with velocity can be explained by the increased stiffness and thus hysteresis of filled elastomers.
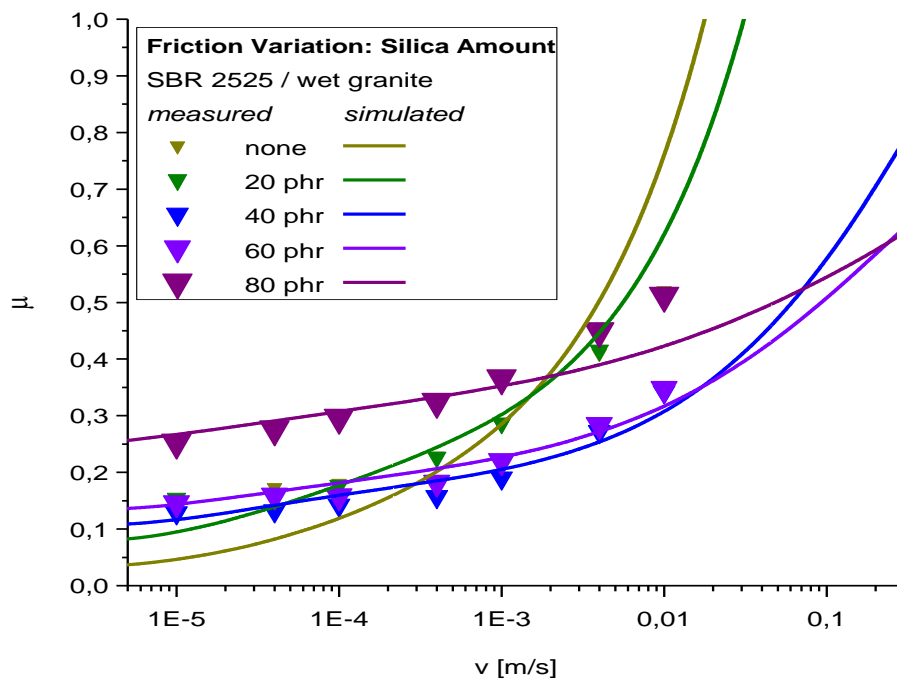
Figure 64: Inducing silica flattens the hysteresis friction curve on wet granite.
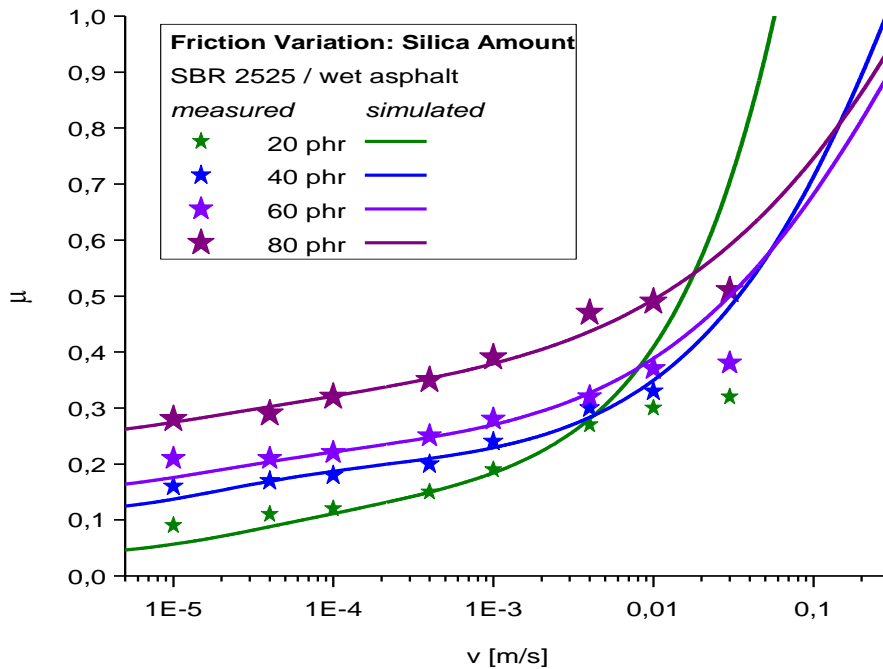

Figure 65: Also on asphalt, silica makes wet friction depend less on velocity. The rise of hysteresis friction is pronounced more clearly on this substrate.

The total friction μ_{tot} (Figure 66 for granite and Figure 67 for asphalt) in the dry systems is drastically increased by the presence of adhesion. This is true for all measured velocities, and especially strong in the range of a few mm/s, when the curves run into plateaus – a more or less constant level of friction over a distinct velocity range. The velocity of the start of the plateau is not significantly influenced by the silica amount, but the shape of the plateaus is: Generally spoken, the higher the fraction of silica, the more explicit is the plateau and the longer it extends into high velocities (at least for simulation, as the experiment is limited in this aspect). The arrow in Figure 66 follows the magnitude of silica from none to 80 phr on granite.
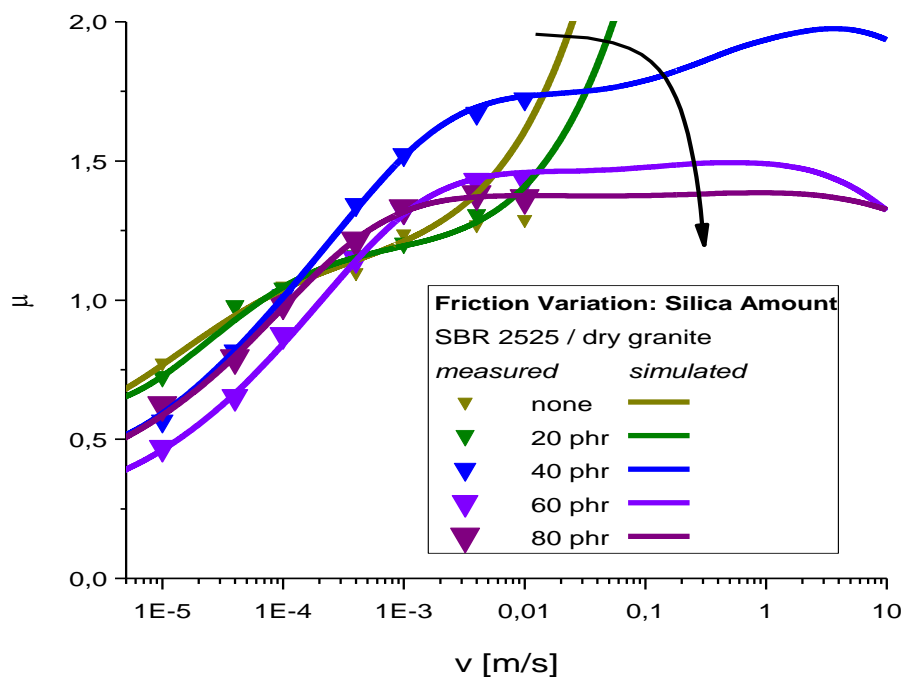
Figure 66: Dry friction on granite runs into a plateau that is lower and reaches to higher velocities with increasing silica amount. Simulation reproduces the measurement.

Not only the total friction displays a local maximum, but also the pure adhesion friction exhibit an absolute maximum because the true area of contact, which plays a vital role for adhesion, decreases with velocity.

Filler does not influence the amount of friction as much as in the hysteresis case. Apart from high velocities, where weakly filled samples display an almost constant plateau that is only slightly diminished by more filler, adhesion friction decreases generally with filler amount in all systems, also for low velocities. This can be explained by the higher hardness of filled elastomers, which prevents the rubber from intense contact and thus from reaching large

true contact areas. Summing up, the dry friction is as well decreased with filler, though not as strictly as for pure adhesion. Again, both substrates own similar friction curves.

Friction coefficients are almost identical for low filler samples and rather similar for high filler samples at low velocities, which are increasing less with velocity for measurements on asphalt, making the curves more strictly related directly to filler amount. With a larger $\xi_{\parallel}/\xi_{\perp}$ ratio (see Table 7), granite offers larger gripping even for filled samples at high velocities, which is confirmed when regarding the true contact areas. This explains why highly filled samples have a bit higher friction at fast sliding. Not only the maximal friction coefficient, but also the peak velocity v_p are influenced by the lateral scaling parameter $\xi_{\parallel}$: Asphalt, which is laterally smoother than granite, exhibits the beginning of the plateau area at lower velocities. The effect of temperature might play a role for high velocities, especially without lubricant [28].
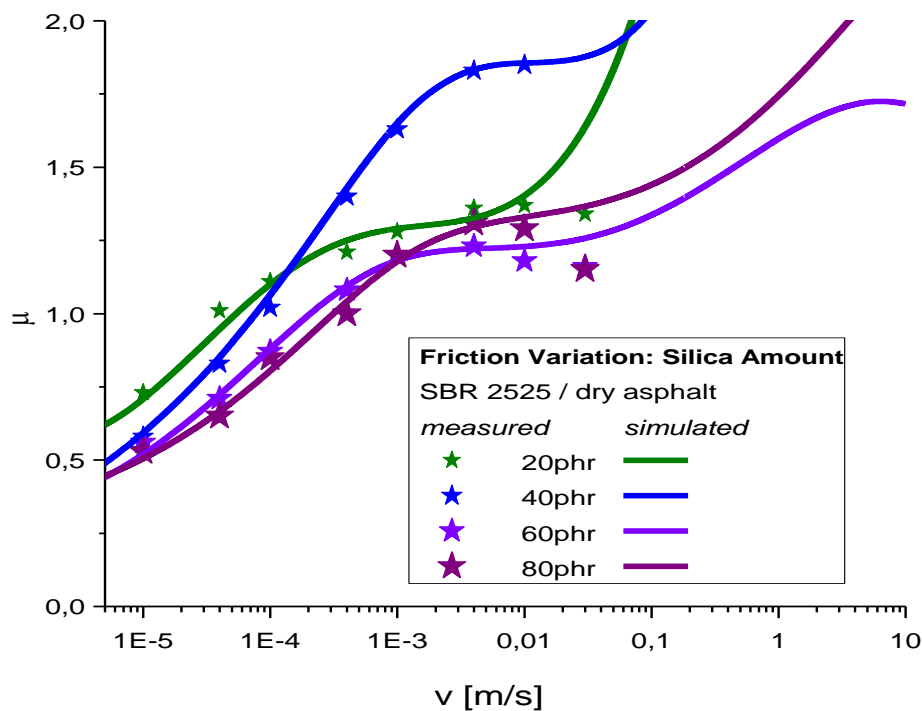
Figure 67: On asphalt the plateau is established for an even smaller amount of silica already, and again experiment matches the simulation. The rise at 40 phr is more pronounced than for granite.

4.2.2 Fit Parameters and Contact Simulation

The simulation of total friction (drawn lines in the figurers above) as sum of hysteresis friction and adhesion friction works well and reflects the data points of measurement (triangles for

granite, stars for asphalt) nicely. Trusting the extrapolated simulation curve thus seems appropriate. We will now discuss the parameters that led to this result.

Some parameters (E_∞/E_0, $n...$) of the modellation (see chapters 2.6, 2.7 and 2.8) are given by the material background of the investigated system. Table 12 summarizes the complementary, free fit parameters b, τ_0 and v_c.

First we compare the simulated hysteresis friction scaled with factor b to the data of wet friction measurements. The values for b start at high numbers for unfilled samples, then quickly decrease with filler amount and stay almost constant above the percolation threshold at 40 phr silica. On granite, b is higher than on asphalt. This means that the effect penetrating asperities propagates more deeply in the unfilled samples up to 40 phr. Obviously, the measured curves can be reproduced fairly well with simulation for low and moderate velocities, but is less accurate when sliding faster than a few mm/s: Then the simulations are much steeper than measurements for low fillings (up to 20 phr), match to a large extent for medium fillings (40 and 60 phr) and are not steep enough for high fillings (80 phr), on a granite surface. For asphalt, simulations behave the same way but are slightly steeper than on granite in comparison to the measurements, and fit the measurements still at higher velocity. The answer can be found in the surface: As $\xi_{||}$ indicates, granite is rougher than asphalt on the lateral scale, so the simulations are valid at higher velocities. The highly filled simulated curves are less steep and thus less dependent on velocity because their elasticity depends less on temperature and thus less on frequency than the weakly filled samples.

The second step is to add an adhesion term to the hysteresis fit. The shear stress rises with filler amount for both granite and asphalt, especially for highest filler content. Simulation range and accuracy of the simulation are only limited by knowledge of the regarded viscoelastic and surface properties. The critical velocity v_c displays a maximum at a silica content of 40 phr for both substrates.

The fit is excellent for most points, even at higher velocities. While temperature effects by friction heating could be assumed to be negligible on wet surfaces, they may indeed play a role on dry substrates when the sliding speed is high enough. The heating results in an increasing elasticity, which means the hysteresis part for dry friction is lower than for wet friction. Hysteresis friction is still increasing with velocity, but its steepness is reduced by filler amount already on wet surfaces. Combined with the decreasing real area of contact at high velocities, dry friction may be reduced in effect, as seen for asphalt when sliding fast. As a

result of these two contrary effects, dry friction enters a plateau for velocities above some mm/s, as the wet part is still increasing. This behaviour has already been found by Grosch [5] as master curves of samples filled with 50 phr highly active carbon blacks (N220, N330) sliding on dry clean silicone and in [23] for carbon black filled S-SBR 5025 on rough granite. In our case, the same behaviour is found for the simulations of highly silica filled systems: On granite, dry friction follows clearly this plateau shape for the filled samples. On asphalt, the effect is present but less accentuated. The effect is confirmed by simulation and well visible on the extended velocity scale.

	Granite			*Asphalt*		
	b	τ_0	v_c	b	τ_0	v_c
phr silica	-	kPa	mm/s	-	kPa	mm/s
0	70	5.91	0.020	-	-	-
20	27	6.56	0.045	10	64	0.62
40	7	15.4	1.90	4.5	150	9.00
60	6,8	18.8	0.90	5.5	110	0.60
80	7.5	48.8	0.33	7	420	1.00

Table 12: Free fit parameters for hysteresis and adhesion simulation of silica filled samples

4.2.3 Simulation Functions

Looking at the true contact area in Figure 68 we find a decrease of contact with an increase of filler content, and with velocity. This is caused by the vanishing ability of rubber to fill the gaps and thus get in contact with its interface when either the elasticity or the contact time, at high velocities, is diminished. Though still in the per mille range, granite offers a larger contact than asphalt. To understand this, it is useful to regard not only the vertical, but also lateral surface descriptors: The larger the ratio $\xi_{//}/\xi_{\perp}$, the flatter and easier to access are the surface structures, and the more contact is possible. Granite surface is more long-waved (see Figure 40), explaining the phenomenon. Additionally, this ratio makes microscopic contact on granite easier than on asphalt even for high velocities, so the curves for asphalt decrease faster than those for granite.
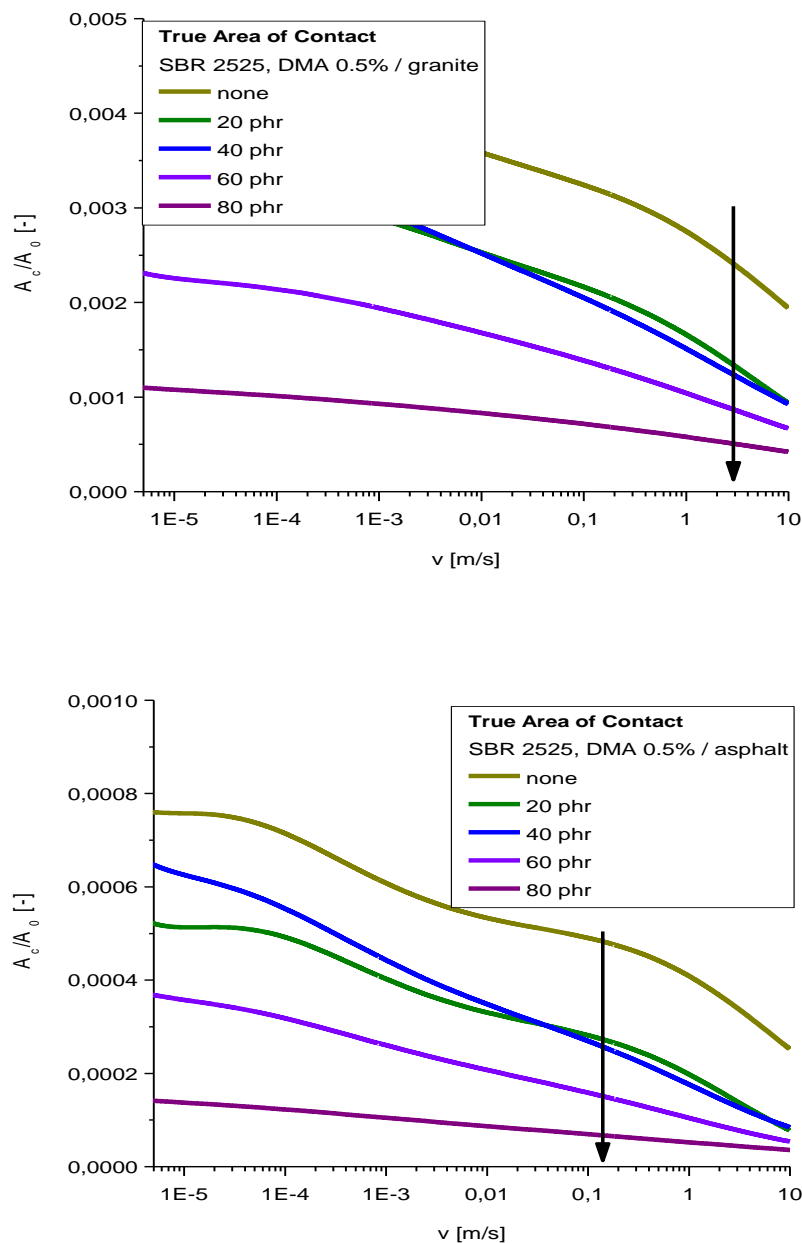
Figure 68: Simulated true contact area for silica filled granite (top) and asphalt (bottom)

The curves of the shear stress τ_s(v) are displayed in Figure 69 and show how the stress rises with velocity and converges to a plateau of the value $\tau_s(\infty) = \tau_0*(1+E_\infty/E_0)$. For very small velocities (not visible in this graph), τ_s becomes the fit parameter τ_0, which is connected to the surface tension γ_0 by a characteristic length scale l_s with $\tau_0 = \gamma_0/l_s$. As τ_0 increases at about one decade, γ_0 increases slightly with filler amount.

The increase of τ_0 is even large enough to compensate for the decreasing ratio E_∞/E_0, so the values for τ_s are also rising with filler content – which is understandable because filler

decreases the elasticity of the samples – and is significantly higher on asphalt, assumingly due to differences in surface polarity. Again, the filler amounts put the curves into groups of low, moderate and high filler contents.
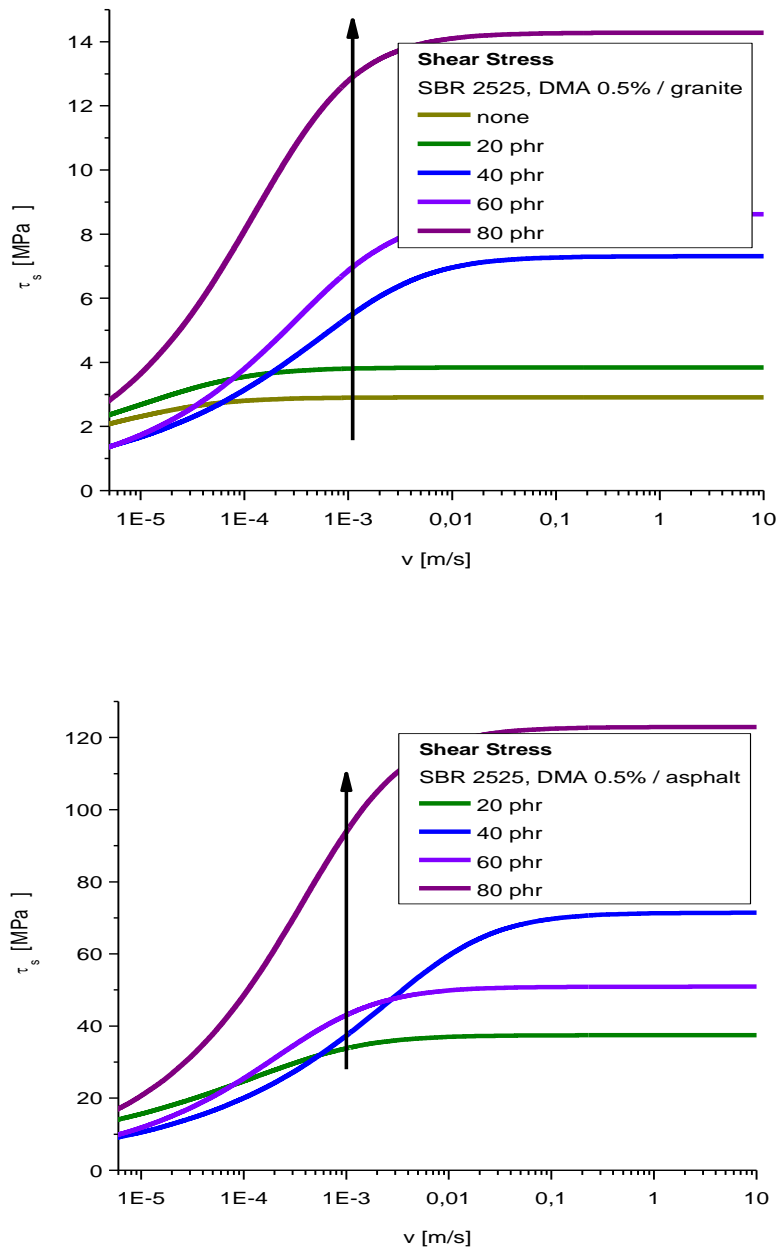
Figure 69: Best fitted shear stress for silica filled granite (top) and asphalt (bottom)

Large filler amounts also shift the beginning of the plateau to different velocities that reflect the critical velocities $v_c(\Phi)$, reaching a maximal value already at moderate velocities. The rise of shear stress starts about one decade higher in velocity on asphalt than on granite. The increasing relaxation exponent n makes the curves more distorted with rising filler amount. This increasing distortion, together with the decreasing E_∞/E_0 and increasing τ_0 are responsible for v_c reaching its maximum at 40 phr.

The *minimal contact length* λ_{min} in the lateral direction is also a simulated function, but not shown here. Higher velocities result in a strongly increasing minimal contact length, which means that at high velocities only large structures contribute to the friction process as fewer small asperities become accessible for the fast sliding rubber.

Higher filler contents also result in higher minimal length, too, because the poorly elastic filled sample cannot enter the cavities deeply to establish a laterally broad contact. For asphalt, this is true only at a second glance: As the highly filled samples have a weaker slope in minimal wave length, curves reverse for high velocities. Looking at smaller velocities reveals the same behaviour as on granite, but on smaller values, as the ratio $\xi_{||} / \xi_{\perp}$ is also smaller on asphalt. The slope is explainable by the fact that at high velocities high frequencies are excited, and the master curves show that elasticity depends less on frequency for filled samples.

 The *gap distance d* increases with velocity, as the time for the elastomer to enter the cavities of the substrate is reduced. It also increases with filler amount : This can be explained by the lower elasticity of filled samples, preventing the rubber from filling the cavities deeply. On asphalt the distance is a bit higher than on granite due to the slightly higher $\xi_{\perp}$. It is easy to notice the analogy of the filler influence here and in the storage modulus: 20 phr and 40 phr silica content are almost indiscriminable in this aspect, whereas highly filled samples (80 phr) display clearly different values for all velocities and the curve of the unfilled sample drifts apart only for high velocity.This can be interpreted as being caused by the considerably different glass transition due to filler. Again, high frequencies correspond to large sliding velocities.

4.3 Verifying the Friction Model by Friction Master Curves

The DIK model describes the course of the friction coefficient at different velocities and is thus connected to the frequency within the excited elastomer. As explained in chapter 2.2 concerning the time temperature superposition, frequency and temperature behave antisymmetrically and one can be calculated into the other. Since the model takes frequency dependency for the sample into account, it should be able to predict an extrapolation of the friction curve using the TTS principle – and match the experiment [61] [62]. This demand assumes that friction obeys the same laws as viscoelasticity. Whether this is true, shall be investigated in this chapter.

Friction experiments have been conducted for this task with the tribometer for a set of temperatures: Naturally, lubricated surfaces were restricted to a temperature above 0°C, and experimental setup suggested a limitation of moderate heat up to 65°C. Dry measurements were performed down to maximally cold environments. To represent a dense overlap, the temperature was split into discrete steps of about 10 K each, completed with an additional step (-30°C) to close the gap for very cold rubber. NR, S-SBR and EPDM as bulk material filled with 60 phr carbon black N234 served as samples. Rough granite was chosen as substrate.

The resulting temperature branches were shifted the same way and with the same horizontal shift factors that are known for these materials from DMA measurements with 0.2% amplitude, now to transform velocities rather than frequencies, resulting in a stretched v-axis. No vertical shifting was applied. The temperatures assigned to the branches in the figure legend are given as rounded, but exact values were used for the shifting process. A consistent colour code was used to identify the branches with temperatures. In all cases, the base temperature for calculation was 20°C, and the speeds given in the graphs are related to this.

4.3.1 Measurement with Lubricant and Simulation of the Hysteresis Friction

Typically the friction increases with velocity at room temperature. This classical behaviour holds for the samples of this investigation, too. Figure 70 (left) shows the temperature branches of the friction coefficient over the measured velocity range for the natural rubber sample on wet granite. The right part of the figure combines all branches to a continuous master curve. Obviously this operation produces a fairly recognizable master curve: Friction coefficients offer a tolerable scattering, and the slope rises in concert with the branches. Even with a temperature range of only 40 K in the medium warm temperature regime, the applicable velocity argument is prolonged from 3.5 to now 4.7 decades.
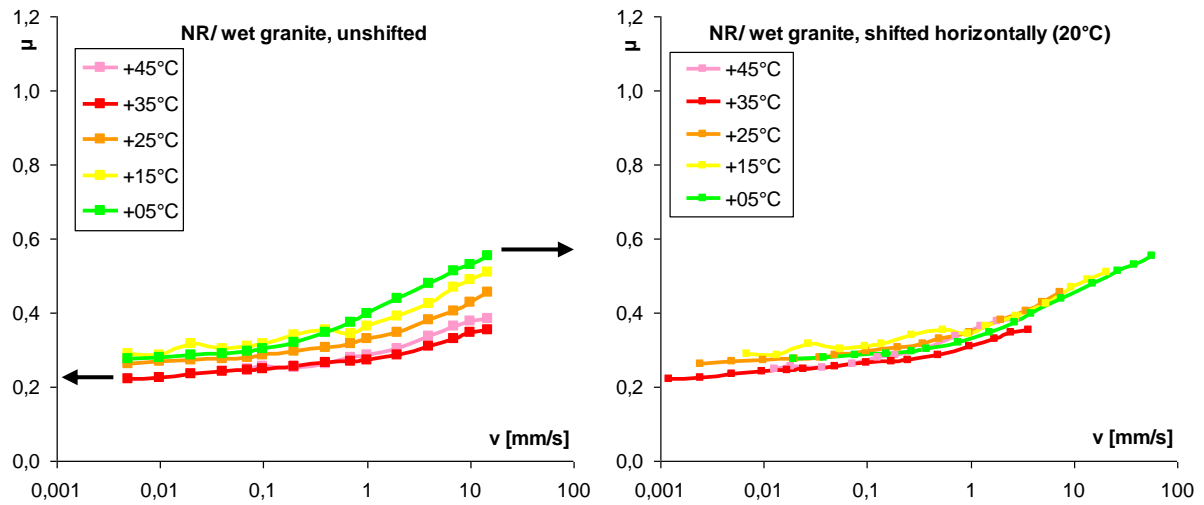
Figure 70: A bunch of isotherm branches (left) is shifted (right) with the DMA factors for NR on wet granite.

From the viscoelastic point of view (chapter 4.1.3), EPDM is closely related to NR, so temperature shifting on friction should be similar as well. Indeed the general course of the master curve in Figure 71 looks comparable, with good overlap of the branches. Then the velocity spans an interval of 4.8 decades. Starting from an almost constant level only slightly lower than NR, friction again rises above 1 mm/s (all given velocities for friction master curves are related to RT) and becomes at high sliding speed a bit lower than for NR.
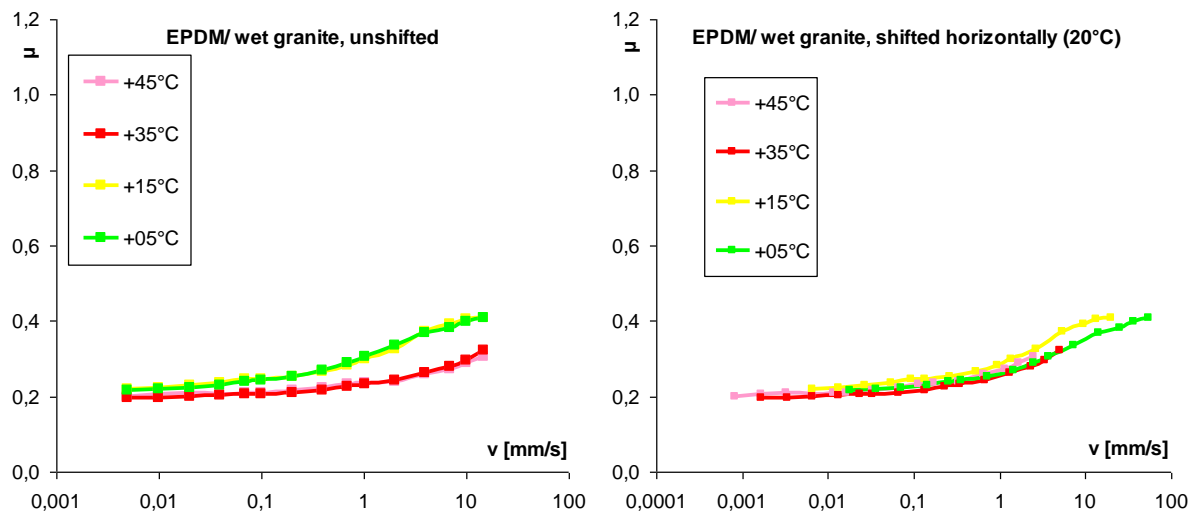
Figure 71: The shifting procedure done for EPDM on wet granite

For S-SBR the branches and master curve are shown in Figure 72. The high T_g of this material (chapter 4.1.3) lets us predict a significantly different scaling than for NR and EPDM. The constant level for low velocities is essentially skipped, friction rises fast above 10 µm/s and the low temperature branches indicate a stagnation for high velocities. Overlap is less

accurate than for other samples. A simulation in the figure matches the basic shape of the master curve. The given velocity stretches over 6.9 decades for 50 K.
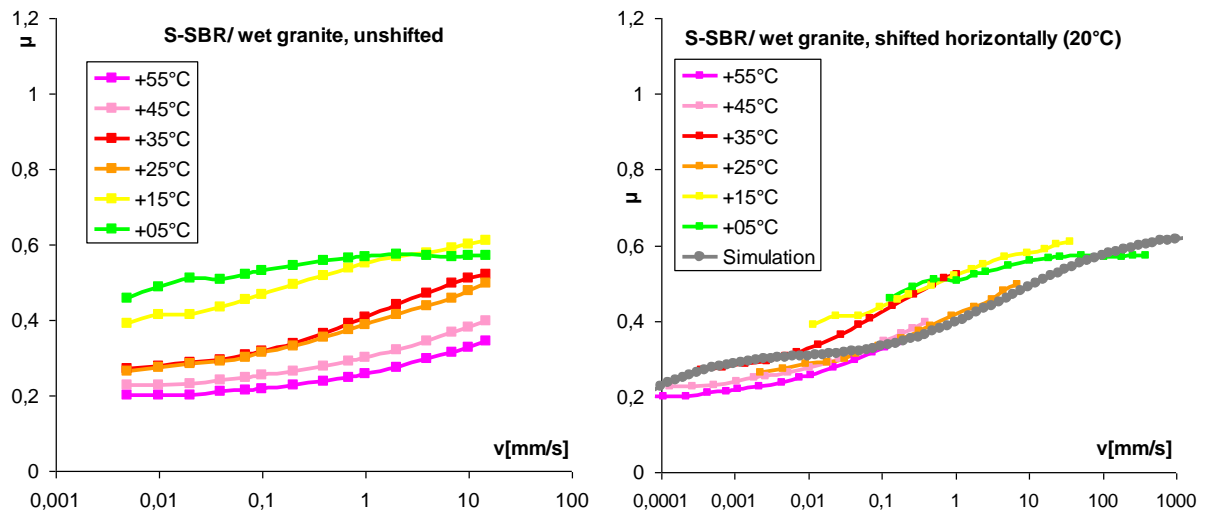
Figure 72: Temperature master curve of S-SBR on wet granite compared with simulation ($b = 1.57$)

4.3.2 Friction Measurements on Dry Substrate and Adhesion Simulation

Dry interfaces allow measurements at temperatures below the freezing point and hence grant a considerably wider velocity interval after shifting. Besides, extreme cooling turns out to cause the largest effect on the rubber – which is comprehensible because the slope of the WLF function is highest just above the T_g.
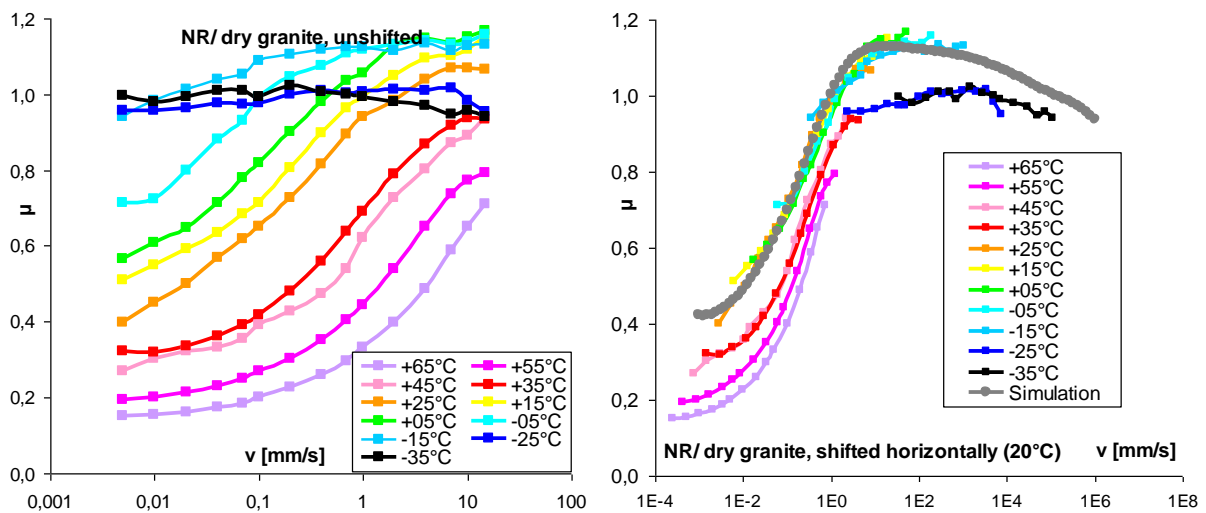
Figure 73: NR on dry granite (left) and the master curve with simulation (right). $b = 2.18$, $v_c = 980$ mm/s, $l_s = 2.63$ µm

The branches now build a master curve that rises with velocity, reaches a maximum μ_{max} at the peak velocity v_p and declines after a short plateau slowly at higher sliding speeds, which is similar to the shape of empirical friction curves that display a plateau behaviour because of novel fillings, as described in chapter 4.2.

This plateau with μ_{max} = 1.15 is most pronounced for NR (Figure 73), ranging from about 10 to 100 mm/s, with a softly rising slope and a very slow decay afterwards. Simulation verifies the experiment. The single branches become continuous by shifting mainly for moderate temperatures (-15 to 25°C), but experimental friction drops for heat and extreme cold. A wider spread mastering procedure caused by a larger C_1 seems to promise a better result. The velocity is expanded to 8.6 decades over 100 K.
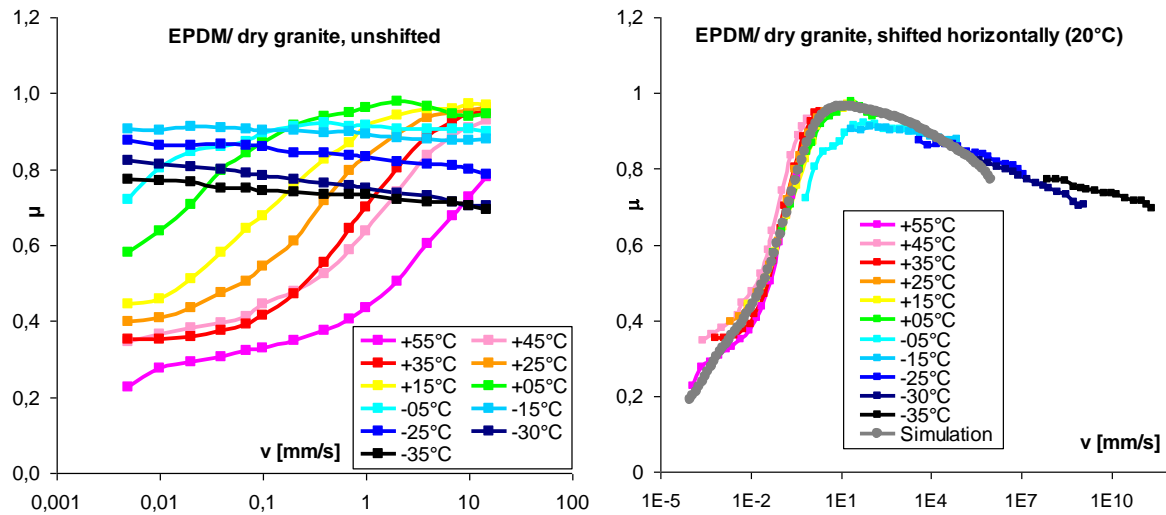
Figure 74: Branches (left) and master curve with simulation (right) of EPDM on dry granite. b = 1.70, v_c = 530 mm/s, l_s = 2.32 µm
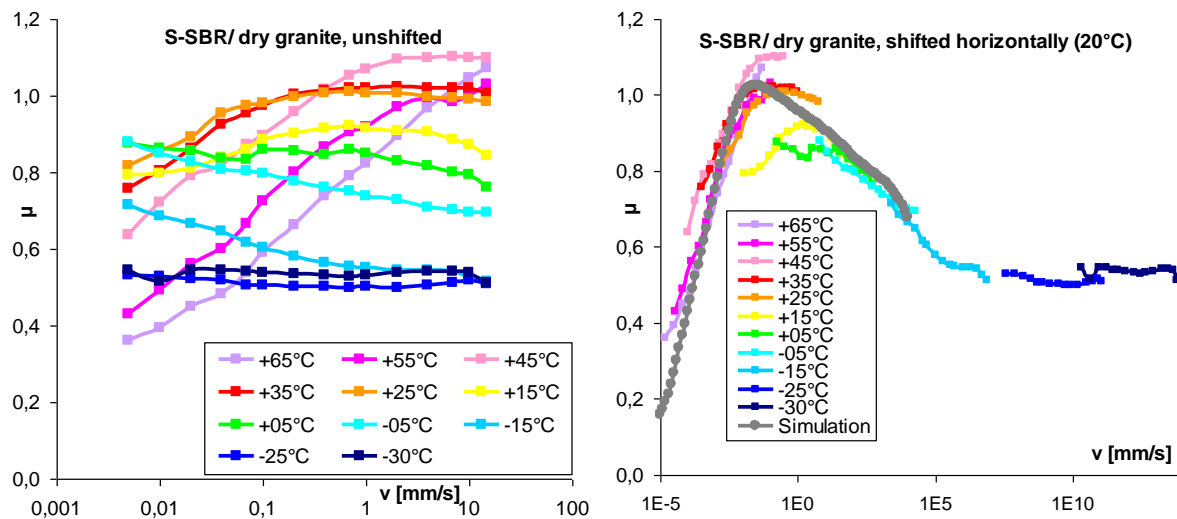
Figure 75: Isotherm measurements with S-SBR on dry granite (left), simulation and master curve (right). b = 1.57, v_c = 5.2 mm/s, l_s = 2.23 µm

As expected, similar behaviour is found for EPDM on dry granite, Figure 74: The curve rises more sharply and decays without plateau when sliding faster than v_p = 8 mm/s at maximum friction μ_{max} = 0.96. Experimental curves overlap very well and can be reproduced nicely by

simulation for all but the coldest branches. A 90 K temperature interval is enough to give the velocity for 15.3 decades. In general, friction is slightly lower than NR, like it was also for the lubricated system.

Finally Figure 75 shows dry granite in combination with S-SBR. The rising slope is steeper than for other materials and the maximum at 40 µm/s appears much earlier because of the high T_g. The decay for growing velocity above $v_p = 100$ µm/s with $\mu_{max} = 1.03$, without any high plateau, is also stronger but runs into a low level plateau for sliding faster than 500 m/s. This shape is comparable to friction curves published in [5]. A velocity interval of 18.6 decades is achieved by shifting over 95 K. The amount of friction is comparable to EPDM.

For the investigated systems, the branches could be shifted to a master curve with the DMA factors. This is an empirical verification that taking viscoelastic shift factors into account, as predicted by theory, is justified for these materials. Furthermore, simulation predicts total friction correctly. The practical use of transfering DMA master curves to friction master curves will be discussed in chapter 5.1.

4.3.3 Simulation Parameters for Friction Master Curves

As explained in chapter 2.6 the total friction is a combination of hysteresis friction and adhesion friction. While hysteresis is calculated directly from the interaction of surface structure and viscoelasticity, adhesion is gained as a second step from the shear stress and the real contact area. The latter is only a small amount of the nominal contact area, which is shown in Figure 76. The contact decreases with velocity as the rubber has less time to enter the cavities of the substrate. The decay is largest for the SBR, again explainable with the glass transition: NR and EPDM start with a slow decay and gain a slope comparable to SBR only for higher velocities. The real contact area is a direct result of the hysteresis simulation.
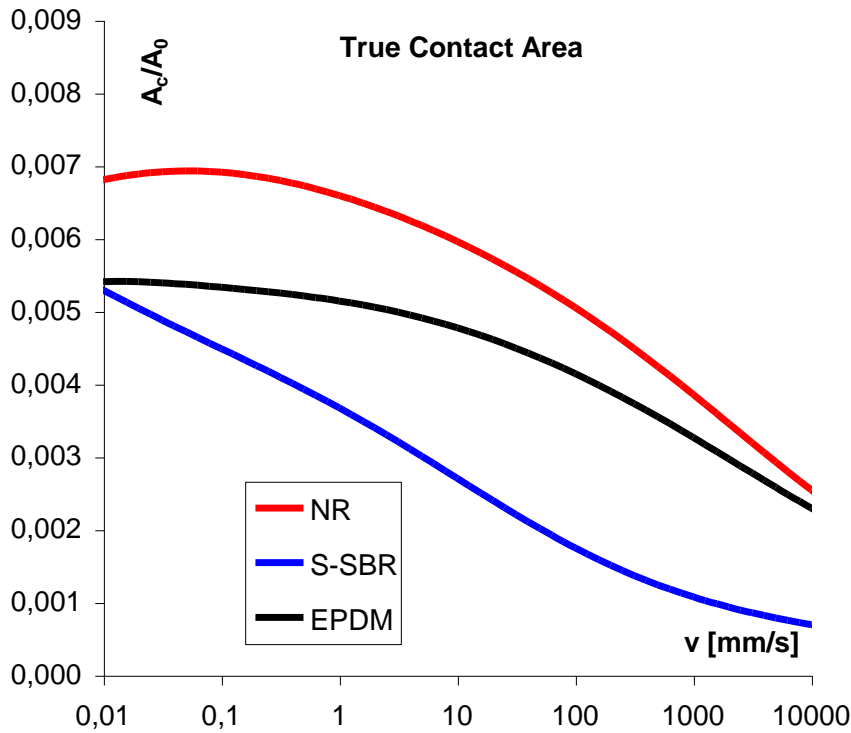
Figure 76: The true contact area is considerably smaller than the nominal contact area.

In contrast to this, the shear stress is fitted with two parameters, v_c and τ_s via l_s, as given in the figure captures in chapter 4.3.2. Being small for lowest velocities the shear stress experiences an increase until the critical velocity v_c when the step reaches its plateau in Figure 77, representing the maximum shear τ_s. Not surprisingly this happens already at slow sliding for SBR, while NR and EPDM have almost the same critical velocities. The values of v_c for all materials are about 50 times larger than the velocity of the maximal total friction v_p. The contact length l_s is very similar for all three samples; differences in shear stress are due to their individual surface tension as material constant.

This results in the pure adhesion component of the friction, Figure 78. All curves display a comparable shape of similar size, but of course the SBR curve is shifted towards lower velocities. Small differences between NR and EPDM in real contact area and shear stress compensate each other, resulting in nearly identical adhesion curves. The maxima of adhesion friction ($\mu = 0.75$, 0.69 and 0.71 for NR, EPDM and SBR, respectively), are related to velocities (6.3, 5.0 and 0.025 mm/s) that are roughly twice as high as the velocity when 90% of the maximal shear stress is reached (3.1, 1.9 and 0.016 mm/s), for all three sample materials.
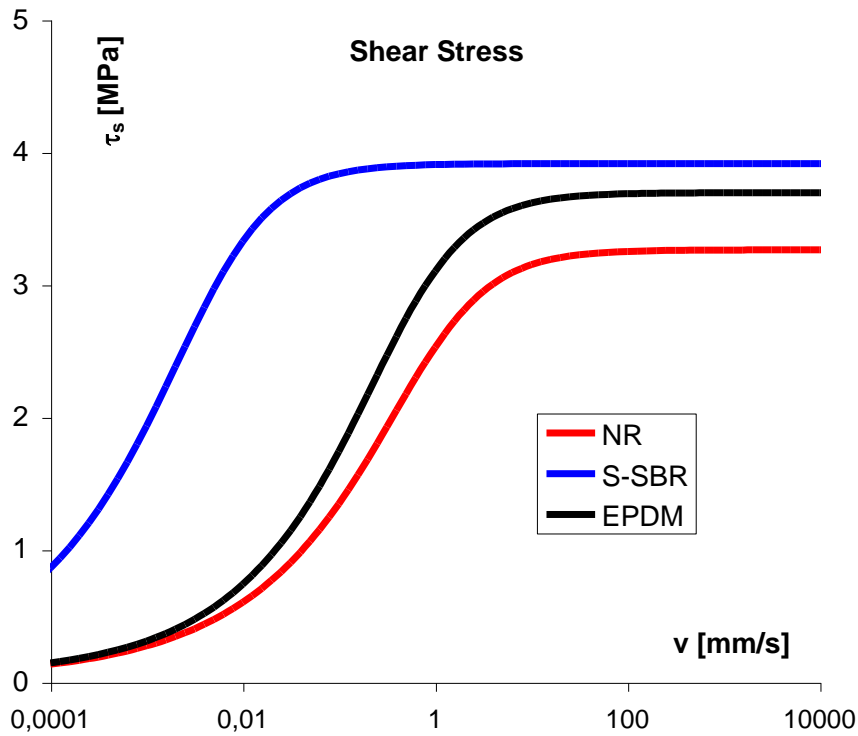
Figure 77: The adhesive shear stress reaches a plateau just above the critical velocity.
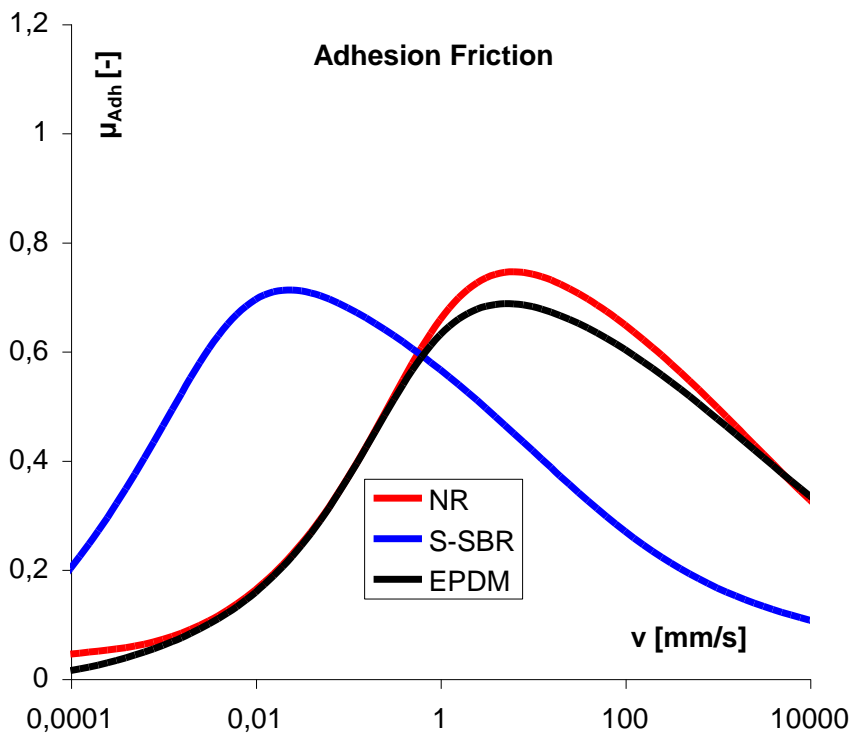
Figure 78: The simulated adhesion friction of the investigated materials

4.4 Parameter Dependence of the Simulation of Contact Variables

The previous chapter demonstrates that the influence of pressure on the friction is not trivial but depends on the interaction of elastomer and substrate in a complex way. Experiments allow only a limited variation of contact pressures by applying different weights – less than factor 4 in our case. The pressure range could be expanded by diminished nominal contact areas, but stable friction mechanics with negligible edge effects demand a minimum sample size. That raises the question how the meaning of pressure can be investigated adequately. The answer is simulation.

The following computational outputs for contact the most important variables (true contact area, gap distance, penetration depth, GW ratio and of course hysteresis friction) were performed for isothermal systems. In real situations the effect of temperature cannot be ignored under huge pressure, but here, neglecting thermal influence allows to compare the results of a large number of simulations that cover an extremely high pressure interval: 9 decades, with $P \equiv \sigma_0$ from 3 Pa to 3 GPa, subdivided into 2 steps per decade. Due to the good continuity of the curves only every second simulated pressure is displayed in the following diagrams. In this chapter each pressure in the array of curves is encoded with its own colour, and the plots with fixed velocity follow the colour code of chapter 4.3.3: Each colour stands for an elastomer type. As in the canonical code of chapter 4.5.1, carbon black filling is given by filling symbols, but in difference to the graphs before, symbol shapes are used solely to distinguish samples for better clarity, as no more than one substrate appears in each single diagram.

The considered substrates are two very rough surfaces (asphalt and granite both in bifractal approximation) as well as two significantly smoother types (polished steel and a ceramic tile). They all have comparable fractal dimensions, and except for tile, similar bluntness. The surface descriptors of these substrates can be found in Table 7. Four types of rubber have been chosen for these simulations: EPDM, NR and SBR 5025 in the same configurations as used for the friction master curves of chapter 4.3, all both unfilled and filled with 60 phr N234, plus SBR 2525 both unfilled and filled with 60 phr silica (DMA 0.5%). Thus a broad and representative number of friction systems is covered. In the following a representative selection of these simulation groups is presented.
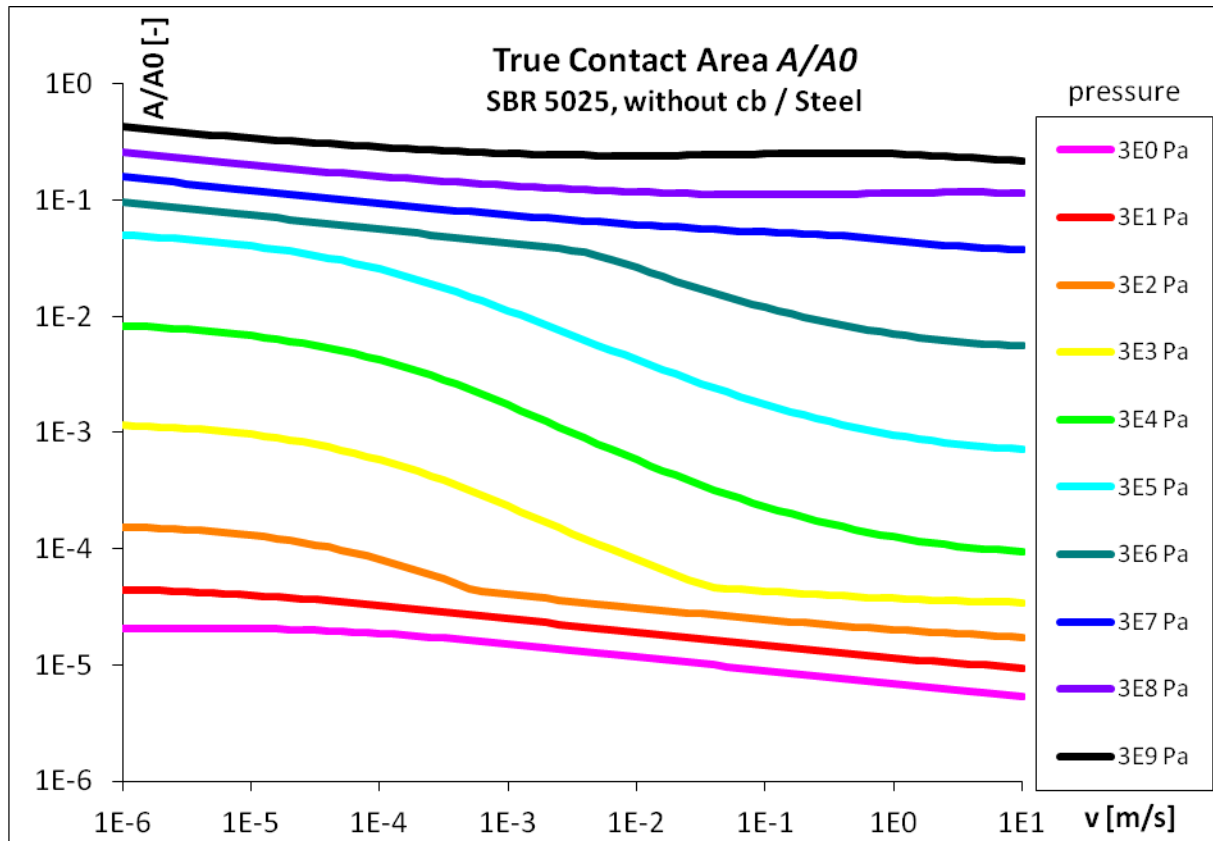
4.4.1 True Contact Area

Figure 79: Simulated true contact area of unfilled SBR 5025 on steel for a multitude of pressures. Colours in this array of curves stand for rising pressure in Pa.

Increasing pressure deforms the rubber and forces it to fill cavities of the substrate surface with increasingly more volume. This also increases the real contact area between the two partners. A non-existent force of two barely touching materials would be effectively zero, as only three points that define a mathematical plane could come into contact. Pressure causes a finite contact area, and for a perfectly fractal substrate (chapter 2.5) combined with a perfect continuum elastic material, an increase of pressure would always further increase the real contact area, though convergence is possible. Practical reasons will confine this ideal behaviour: lacks in fractality, inhomogeneities of the rubber and, as the final border, the end of continuum mechanics on the atomic scale. A true contact area A_c larger than the nominal contact area A_0 would not make sense anyway. As a result, we expect a maximal true area to be reached at high pressures. The simulations should reflect this within the limitations of the underlying model and the computation.

In Figure 79 at the example of unfilled SBR sliding on steel, the real contact area starts as a tiny part of the nominal contact area (about 1/1000 percent) for the very low pressure of 3 Pa, rising heavily until converging when coming close to the GPa range, at almost nominal contact area. This behaviour additionally depends on velocity, most important for moderate

pressures. The elastomer needs time to enter the cavities, so the decrease of true contact is unavoidable and not surprising for higher sliding speeds. Simulations covered the interval from 1 µm/s to 10 m/s, which is larger than experiments allowed.
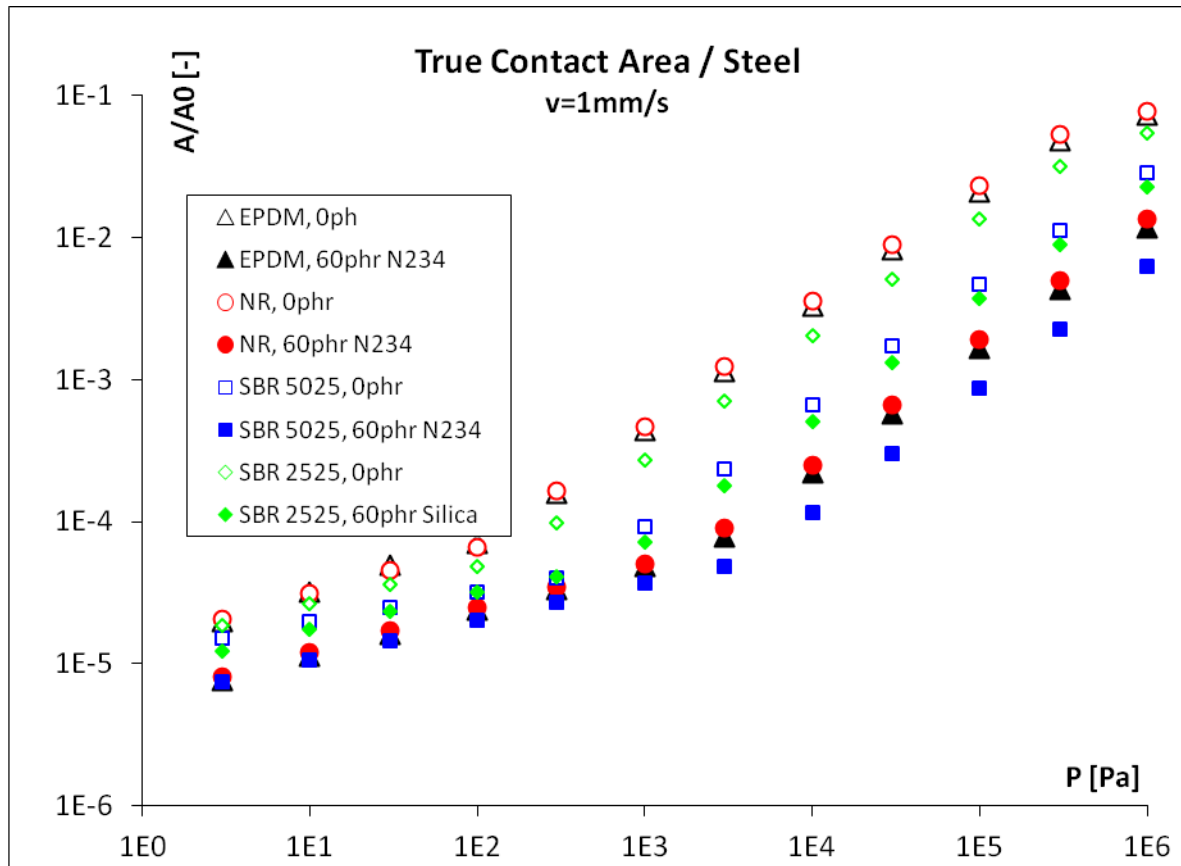
Figure 80: The simulated true contact area of several rubbers for a fixed velocity rises with pressure.

In order to compare the various systems of rubbers and substrates, a plot that embodies all arrays of all curves in one single diagram is not helpful. Instead the velocity aspect is reduced to one significant value, chosen as 1 mm/s for comparability to experiment. This does not cause problems, as the curves for computed real contact are qualitatively quite similar for other substrates than steel and other rubbers than unfilled SBR 5025 – this velocity is always a meaningful choice for any of these simulations. This holds also for the following functions discussed below.

The true contact area rises with pressure for all kinds of elastomers on steel (Figure 80); and the rubbers behave comparably on other substrates (not illustrated here). Filled samples, of course, always have lower A_c/A_0 ratios than their unfilled analogons. EPDM and NR have rather connatural values, and obviously adapt better to the hard surface than SBR. In filled state the difference becomes smaller. Interesting is the sharp bend (i.e. transition to steeper slopes) in the kPa range for all slopes, a kind of critical contact level, increases more effectively, especially for hard samples, where this bend appears at higher pressures. Steel

and tile display this feature, whereas the rougher substrates employ nearly straight lines instead.

4.4.2 Gap Distance
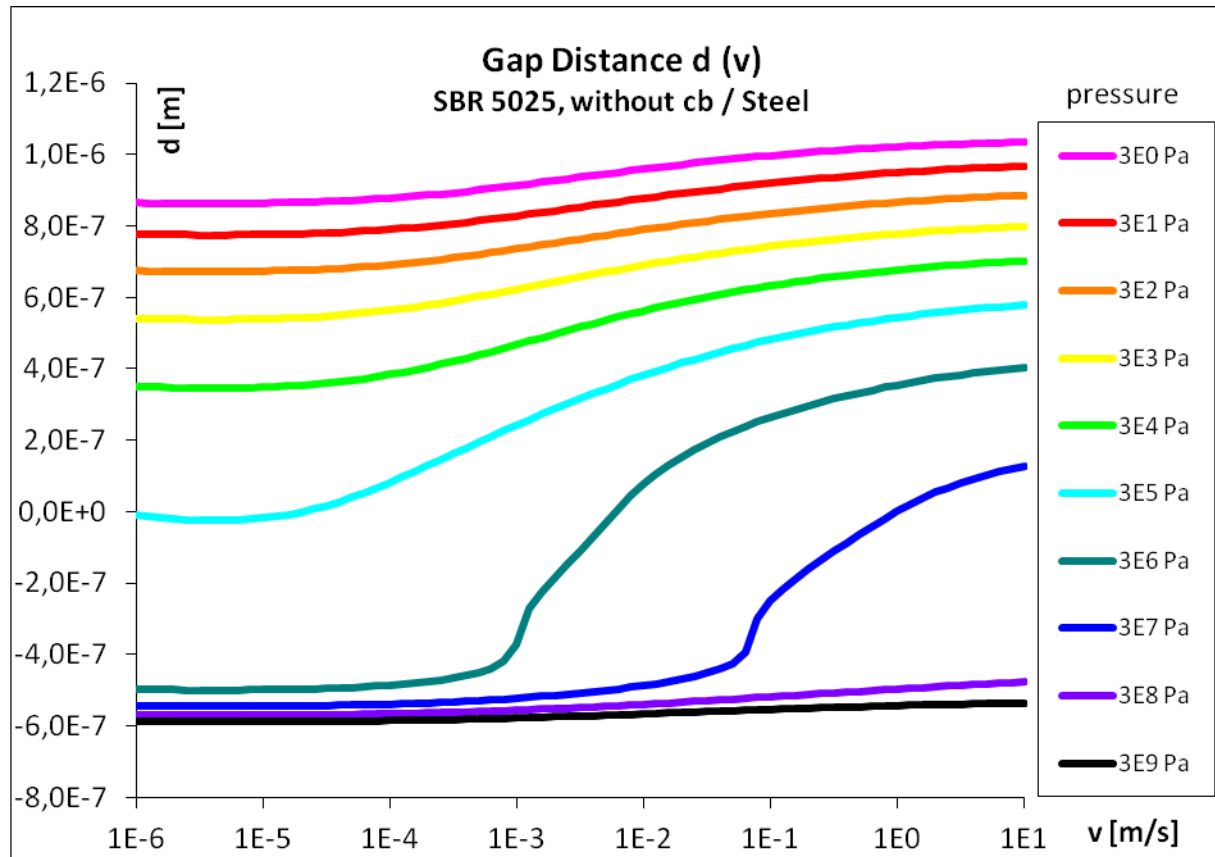
Figure 81: The array of curves for the gap distance of the same sample decreases to minimum level when pressure is high enough.

The gap distance *d* should follow comparable tendencies, but inversely: Lower gaps caused by higher pressures and rising gaps with increasing speed. This is found true in Figure 81, again for unfilled SBR 5025 on steel. As before, changes in pressure intensity are most relevant atmoderate values. The comparison of gap distances for all simulated pressure series (Figure 82), here on tile, concentrates on displaying the low pressure range with its maximal gradient at about 100 kPa. Elastomer type does not seem to matter much for this aspect, but filled samples can clearly be discriminated from unfilled ones. Carbon black filling with its higher storage modulus helps helps to maintain a higher gap distance than silica does. There is no bending point within this range in either curve, just a continuous change in slope. This change is lowest on granite, highest on tile. On all substrates but steel, gap distances differ little from sample to sample for low pressures and much for high pressures.
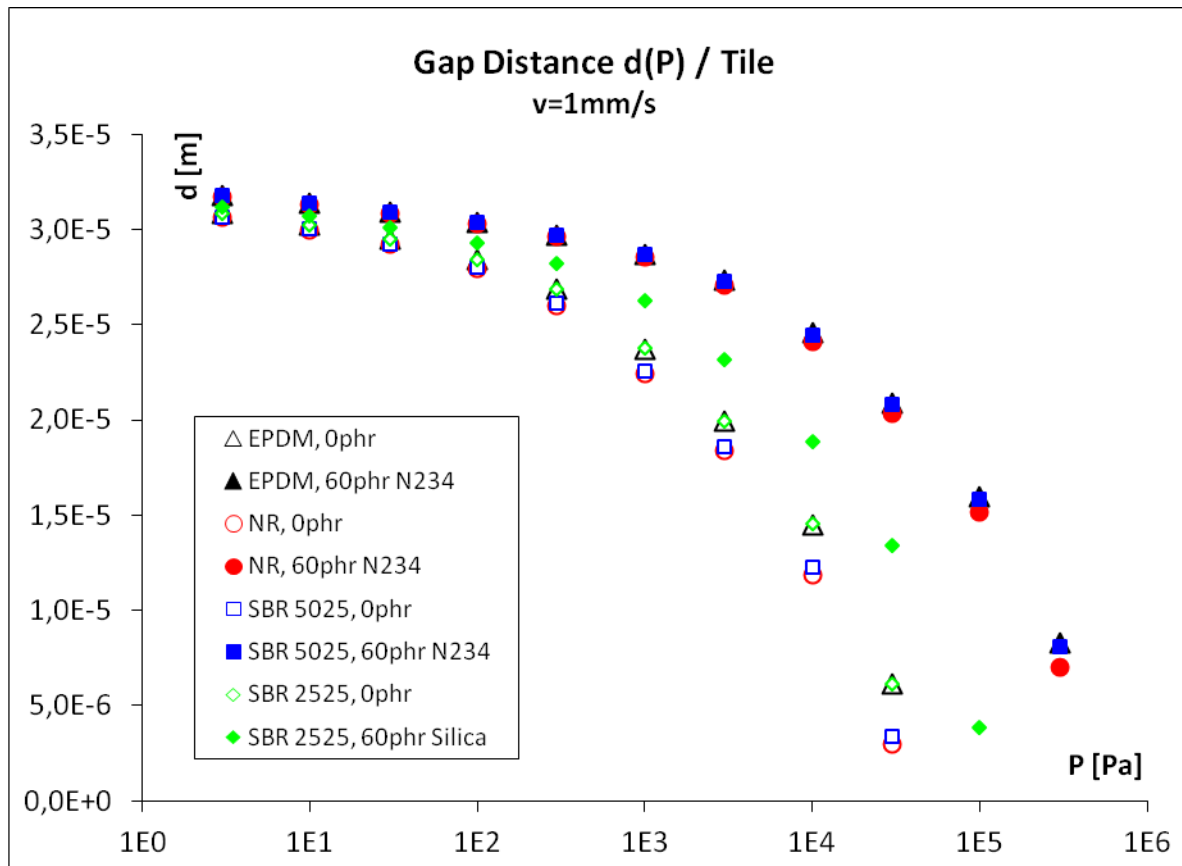
Figure 82: On tile the gap distance as a function of the computed pressures is falling at 1 mm/s.

4.4.3 Penetration Depth

As expected, the penetration depth z_p decreases with speed and rises directly with pressure. The influence of elastomer and filler matches the result for the gap distance analogously, as general statements for all systems. As with the contact area, only granite (Figure 83) and asphalt have a constant slope. Tile and steel show similar slopes not before approximately 1 kPa is reached. For low pressures the computed penetration depths are very exiguous and even below vertical heights, and therefore probably beyond the range of valid simulation.

Remember that no absolute spatial values can be given, but the results must be fitted to the experiment with the *b* factor, in order to gain the relevant excitation depth.
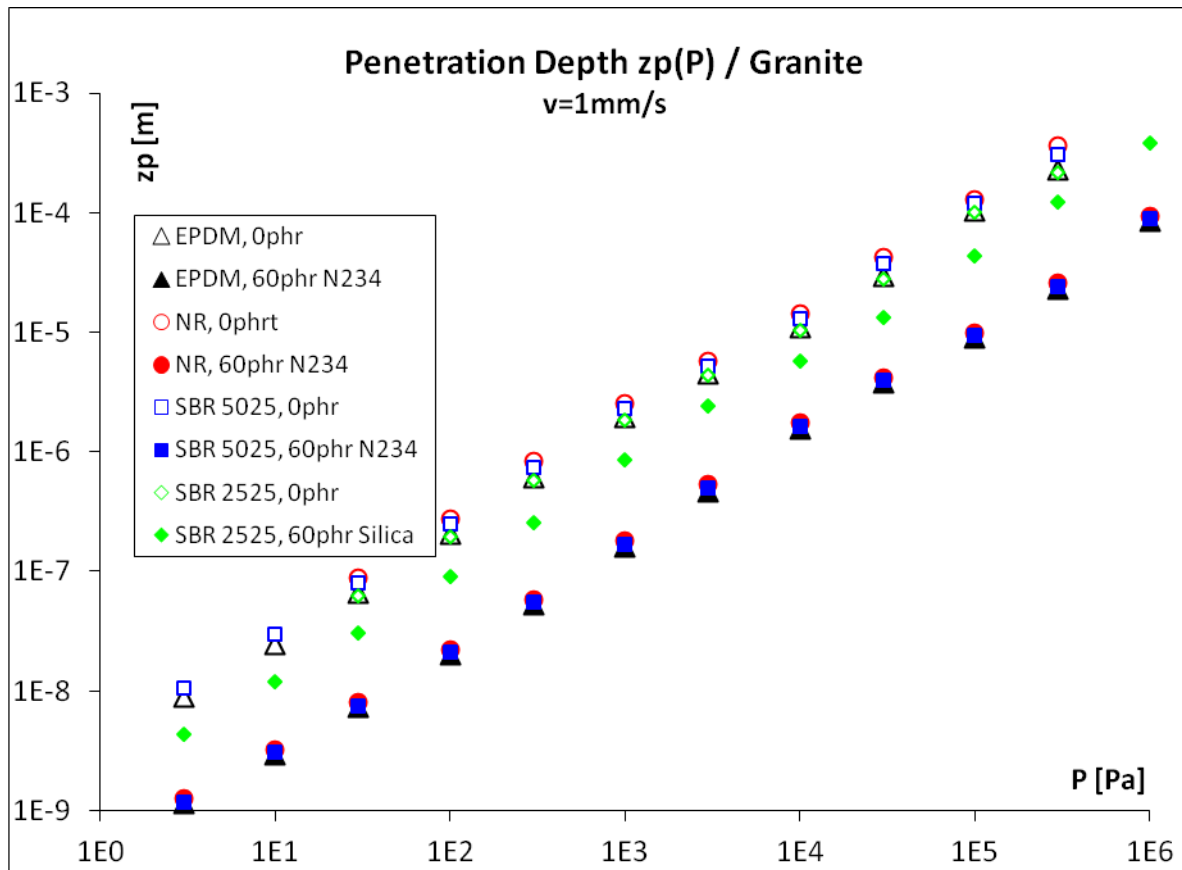
Figure 83: The penetration depths rises steadily with pressure on granite.

4.4.4 GW Ratio

All the contact aspects shown above, be it the vertical aspects or the ratio of real and nominal contact, represent the result of a force and the affected area. As defined in chapter 2.4, the Greenwood-Williamson functions are linked to the contact area and the resulting force: Disregarding the friction integral, the ratio of F_1 and $F_{3/2}$ is proportional to hysteresis friction. Figure 84 illustrates the trend of $F_1/F_{3/2}$ on asphalt: It rises with velocity. The strict seperation of the curves for unfilled, cb filled and silica filled samples persists also in this case. Values drop sharply in the low pressure range and rise gradually for high pressures on rough substrates. On smoother surfaces the ratio is several decades higher for low pressures, because a marginal force can still cause a wider contact than for rough substrates, followed by a more or less constant level at high pressures. On granite, the pressure influence is less significant than on asphalt, probably due to the higher ratio of vertical and horizontal surface descriptors. Note that the corresponding normalized t values at fixed speed $v = 1$ mm/s still depend substantially on the applied pressure but differ only marginally form one combination of substrate and elastomer to another, so direct comparison between the systems is possible.
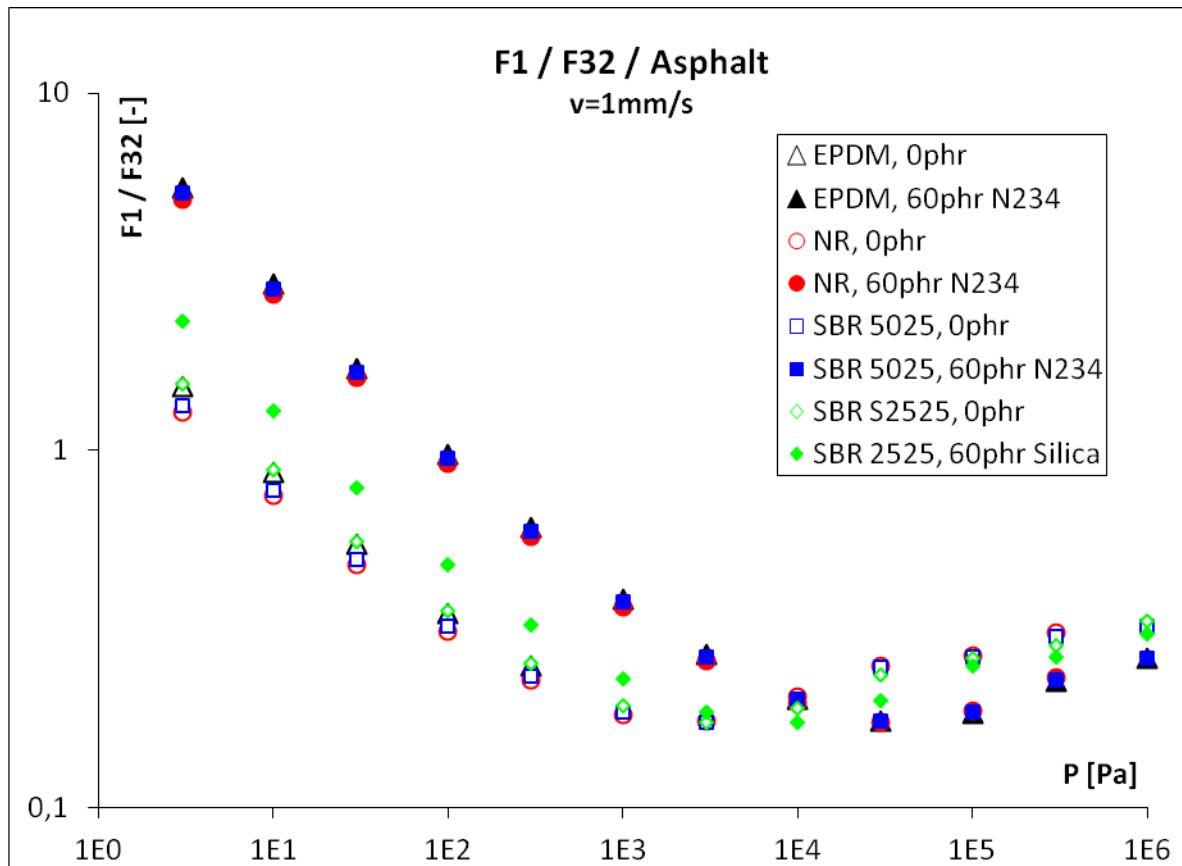
Figure 84: The ratio of two GW functions on asphalt

4.4.5 Hysteresis Friction

A large number of variables is allocated to the simulation and leads to the most complex aspect of the simulations: the friction force itself, or, more exactly, the hysteresis friction. The systems display major differences not only from one rubber to the next, but between the substrates, too. To accommodate this fact, the complete friction results for all combinations of elastomer and substrate are given in Figure 85 and Figure 86.

Neither a consistent reaction on pressure nor on velocity can be observed – friction force increases with normal force, but not proportionally. Instead, the results must be interpreted individually. Friction mainly ascends with velocity, but especially SBR reaches a friction maximum easily which may also appear for other rubbers on steel. Slightly higher pressures shift this maximum to higher maximum friction values as well as to higher velocity; for higher pressures the friction curve becomes flatter again. Results for velocities significantly higher than v_p may be unreliable.
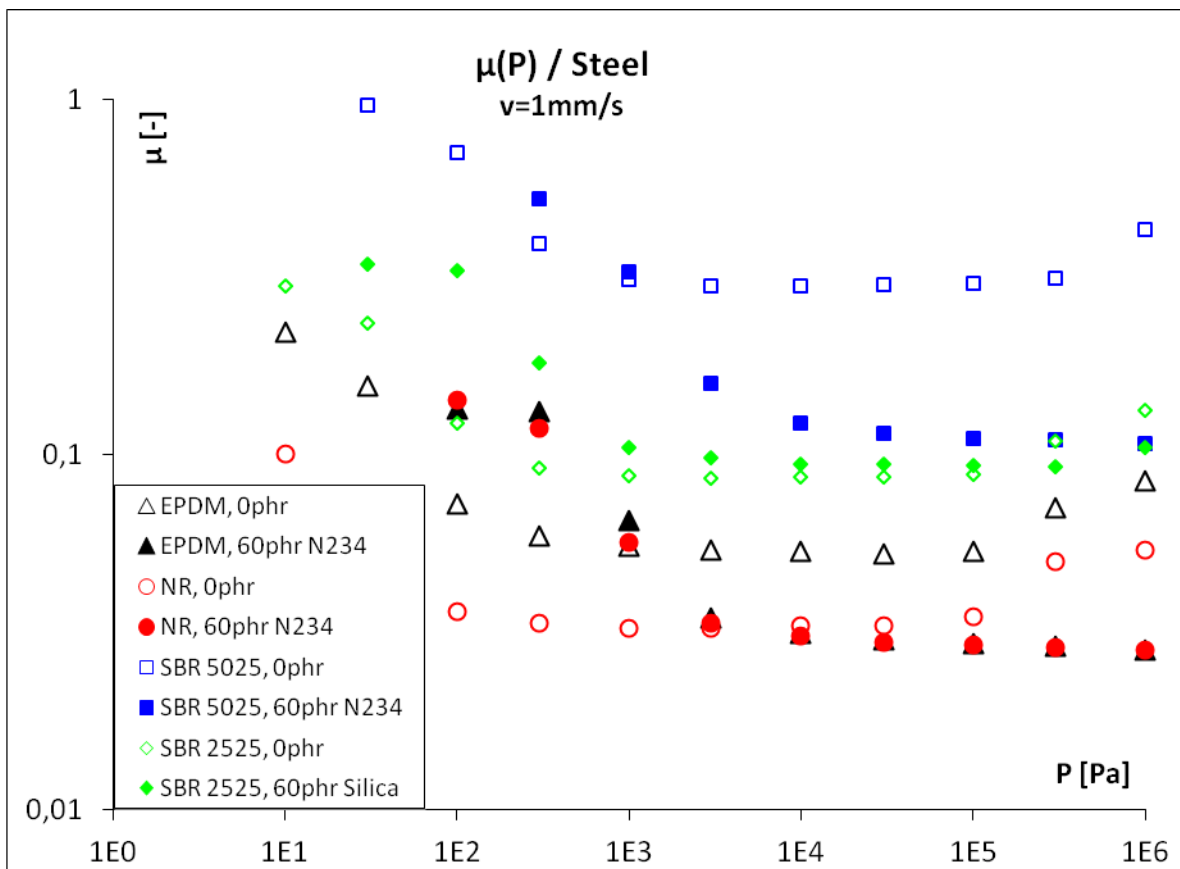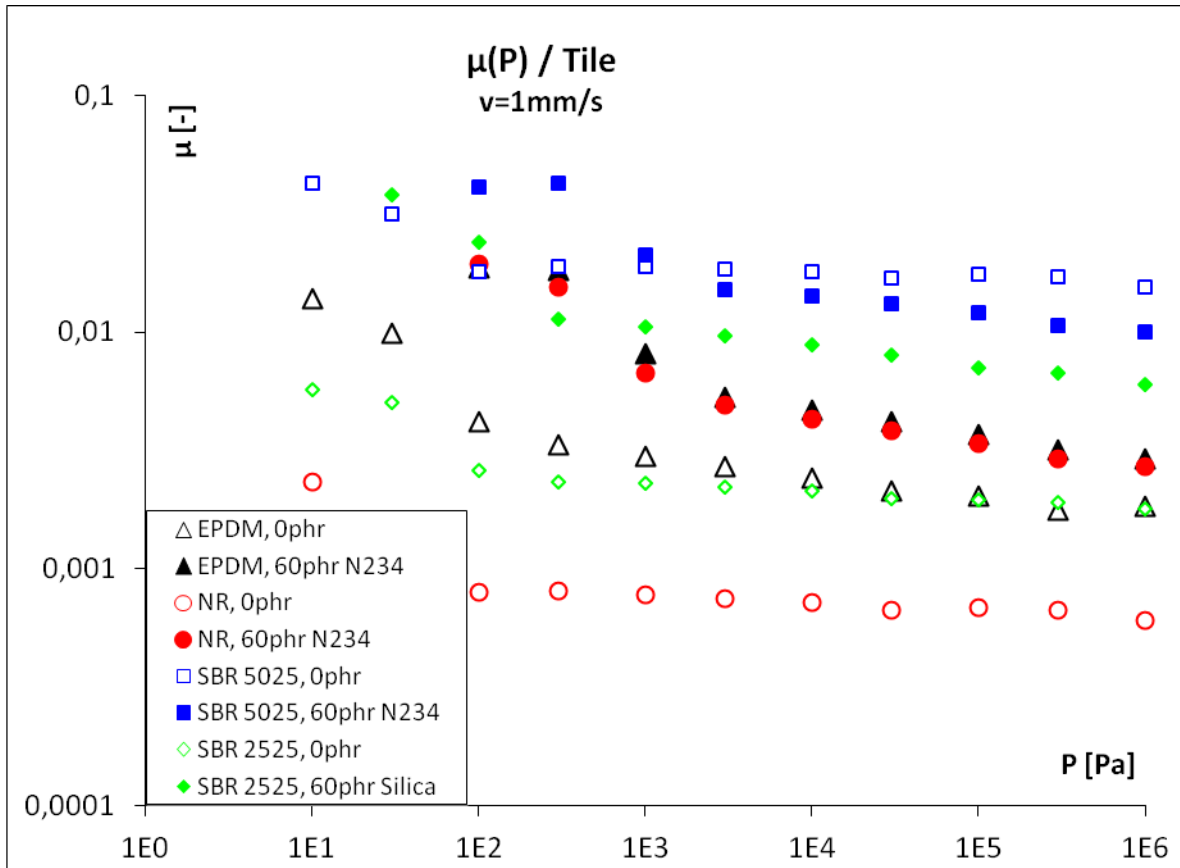
Figure 85: The simulated hysteresis frictions of the considered elastomers on flat substrates show a tendency to decline gradually with pressure.

On the smooth substrates (steel and tile), friction in general decreases clearly with velocity when low pressure is applied, and only little for pressures higher than moderate. This matched basically experimental observations reported previously in this thesis. This "critical pressure" again depends on the hardness, i.e. filler of the sample, in combination with the substrate. The sporadic rise in friction for highest pressures might well be an artefact. Filled samples have a higher friction than unfilled – not unusual, due to the resistance a hard elastomer poses to deformation.

The elastomers definitely differ in their friction curves, even with the same filler. SBR reaches the highest friction values, followed by EPDM and at last NR. This holds for all substrates, with comparably small differences within each substrate for filled samples. Qualitatively it is also essentially the same order as in experimental measurements on wet surfaces at 1 mm/s. The absolute values of the friction coefficient, however, are not predictable without the properly fitted b factor. So, the accuracy of comparing the friction of different rubbers is limited, and a fortiori comparing different substrates, explaining the noticeably different friction maxima of tile and steel.

The interdependencies are more complicated on the rough substrates: On asphalt, friction drops within a limited interval at moderate pressures. On granite this pressure dependency is less pronounced and shifted to higher pressures. Beyond the borders of this interval, friction ascends with pressure. It is noticeable as well that some values did not converge to results. This is a serious hint that simulation should be regarded with caution for extreme parameters, especially for the combination of rough substrates with extraordinarily low or high pressures. Fortunately the pressures that can be applied in the experiment are in the moderate range where computations are reliable. The difference between filled and unfilled samples tends to be slightly more distinct than on smooth substrates, as a rough surface allows even hard materials to fill cavities, maximizing resistance against deformation and friction.
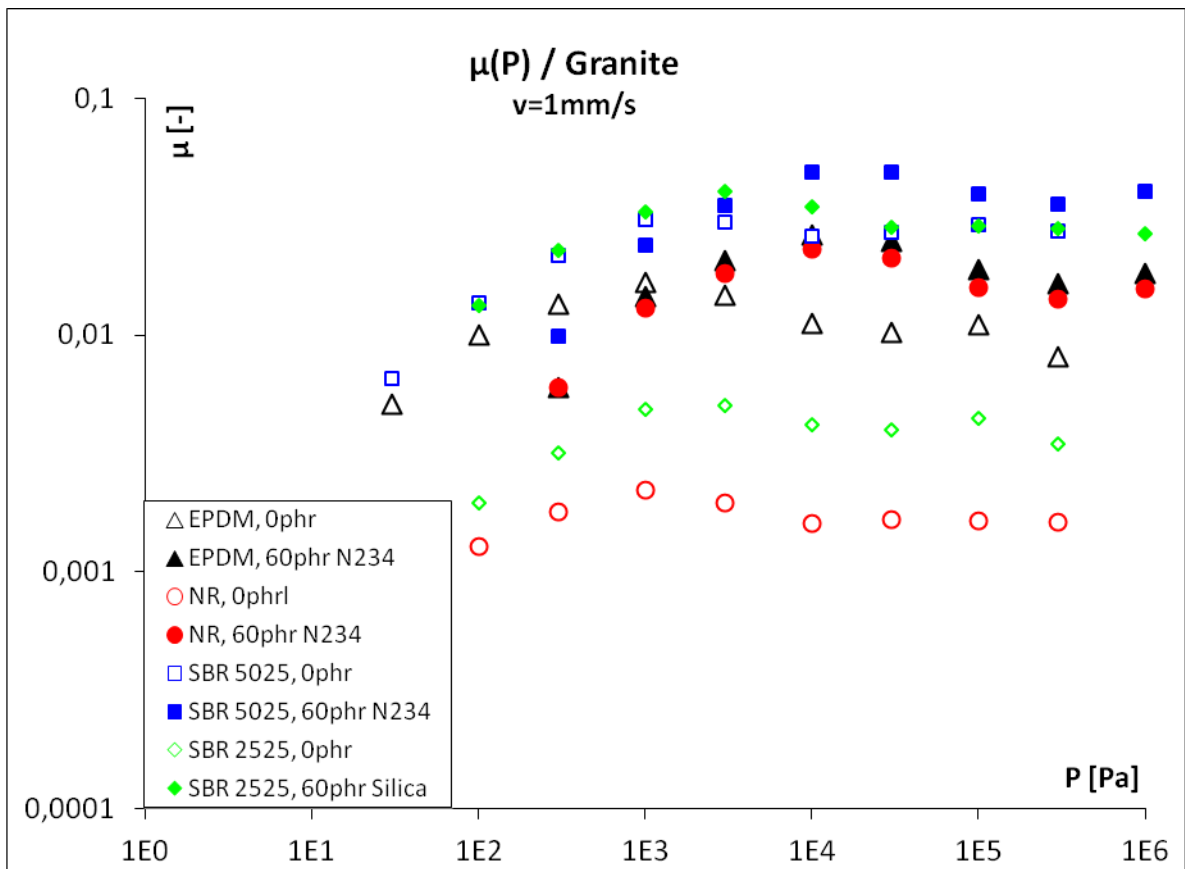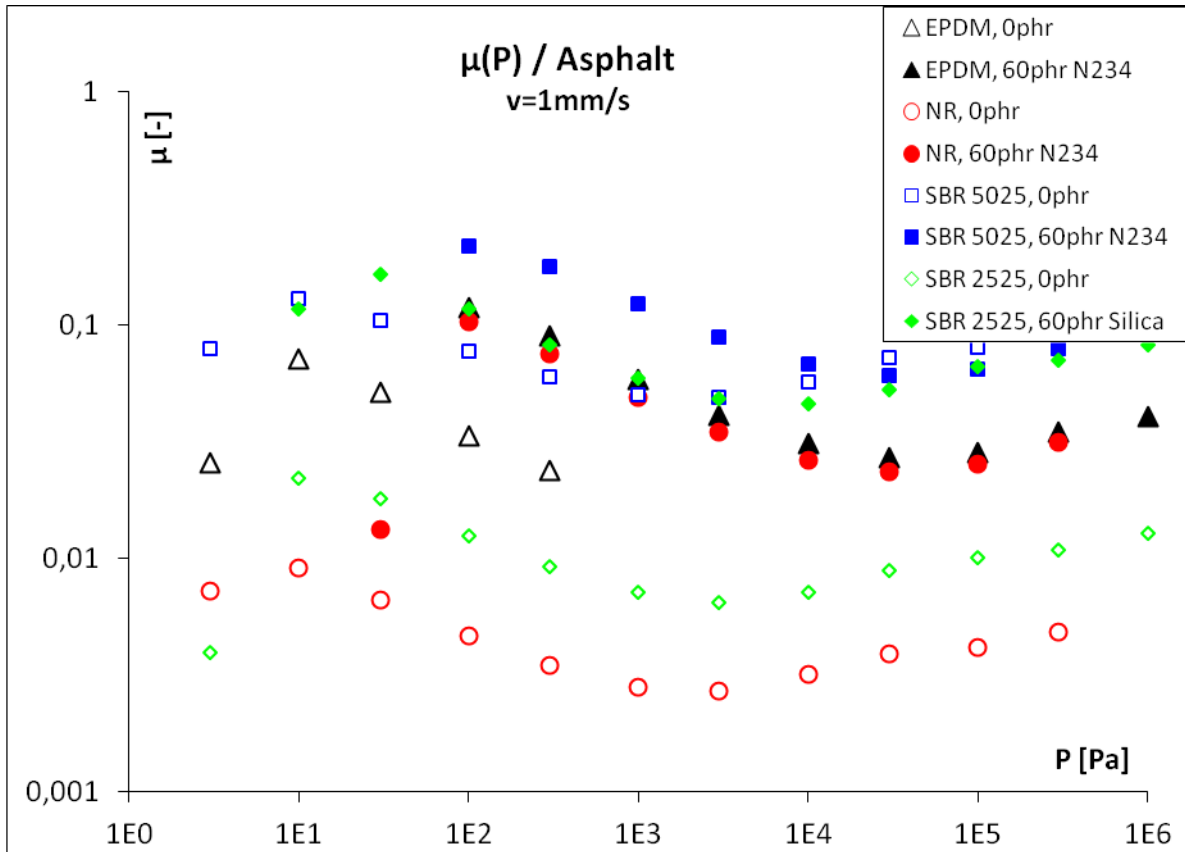
Figure 86: The simulated hysteresis friction on rough substrates differs not only quantitatively but also qualitatively from smooth surfaces.

4.5 Reduction of Friction by Surface Modification

The last chapter explained how friction curves, either experimental or simulated, can be described even beyond the usual scale. But how can the values of the friction actually be modified? In the following chapter we concentrate on methods to reduce friction. Two techniques will be compared: the modification of the sample surfaces with hard particles from the bulk, and the coating of surfaces with and without particles. Friction analysis will be completed by investigation of environmental effects, simulation and stick-slip effects.

4.5.1 General Explanations on Graphical Friction Results

In the figures showing friction curves within this chapter, it is necessary to employ a large variety of parameters. In order to show these parameters without confusing them between one graph to another, it is helpful to use a uniform system of parameter encoding. The following features will be applied consistently for the investigation of PAOS "*(p)*" and of coating "*(c)*":

Bulk Properties

- **Elastomer type:**   EPDM   light colours

                           NBR *(p)*   dark colours

                           SBR *(c)*   dark colours

- **Carbon black filler:**   without   □ empty symbols

                           with 50 phr   ■ filled symbols, black frame if needed

- **Silica filler:**   0…80 phr   symbol size & colours ■ ■ ■ ■ ■

- **PAOS filler *(p)*:**   0 phr   ▪ small symbols

                           10 phr   ■ medium symbols

                           20 phr   ■ large symbols

Surface Treatment

- **Roughness *(c)*:**   smooth bulk   ⎯⎯ continuous line

                           rough bulk   – – dashed line

- **Gas phase fluor. *(c)*:** with   ■ straight symbol

                           without   ■ symbol shadow

- **Annealing time *(p)*:**   0 h   ■ yellow (EPDM)   ■ dark yellow (NBR)

                           24 h   ■ magenta (EPDM)   ■ pink (NBR)

- **Coating type *(c)*:**   **none (**natural) ■ grey (EPDM)   ■ black (SBR)

                           PTFE   ■ indigo (EPDM)   ■ purple (SBR)

                           PU   ■ cyan (EPDM)   ■ dark blue (SBR)

	TPU	■ lgt. green (EPDM) ■ dark green (SBR)
	Siloxane	■ orange (EPDM) ■ red (SBR)
• **Coating thickness** *(c)*:	10 µm	■ small symbols
	40 µm	■ large symbols

Environmental Conditions

• **Substrate:**	asphalt	★ star
	granite	▼ triangle, tip down
	coated sheet 3	▲ triangle, tip up
	coated sheet 4	◆ diamond
	glass	● circle
	fine steel *(c)*	■ square
	polished steel *(p)*	■ square
	rough steel	▬ bar
• **Lubricant:**	dry	▬ thick line
	wet	— thin line
• **Pressure** *(c)*:	normal	— uniform line
	higher	= patterned line (various types)
• **Temperature:**	hot	■ purple
	…	spectral colours ■ ■ ■ ■ ■
	cold	■ blue

For plots that combine various temperature graphs, a temperature spectrum as described above replaces the normal colour code; this proceeding has also been applied to the master curves of the previous chapter. All other colours signify a combination of rubber type and either coating type or annealing time. Coding explanation is repeated in every single graph in the legend for the appropriate parameters only. In order to achieve compatibility, values employ the same range on the v-axis, and a limited set of different values for the μ-axis. The plotted lines have been splined.

4.5.2 Tribology and Diminished Friction by Sample Induction with PAOS

The friction coefficient µ generally increases with velocity for all friction systems investigated in this chapter. Friction of a measurement fluctuates below one percent in the evaluated range. At high velocities the dry friction in some cases becomes almost constant. This plateau behaviour has already been observed for other systems [5],[60],[61] and is explained as a superposition of an increasing hysteresis friction and a decreasing adhesion friction, as defined in chapter 2.7. Consequently, elastic samples without carbon black display higher friction values (direct comparison between Figure 87 and Figure 88), especially on dry substrates, because they can enter the cavities more deeply and cover a higher area of real contact. This concerns predominantly the fast sliding. PAOS is expected to establish a similar effect but without making the sample harder.

As presumed, the presence of PAOS lowers the friction on dry granite. This is true without (Figure 87, effect symbolized by arrow) as well as with (Figure 88) carbon black fillers and fits well to the observed reduction of surface tension. In contrast to carbon black, which reduces friction mainly because of making the samples harder (a bulk effect), PAOS keeps the sample soft (even softer than without it) and still reduces friction because of minimizing the real contact area (a surface effect).

The friction reduction is generally amplified by annealing.Thereby friction becomes also less dependent on velocity even without any PAOS, so after annealing PAOS is efficient for fast sliding (more than 20% less friction for 20 phr) but not at low velocities. The flattening of friction curves by annealing is a feature often observable in the investigated systems. The averaged (velocity independent) friction may either be slightly increased or decreased after annealing. Note that natural annealing for non-laboratory samples, components and parts is unavoidable in a humid, normally pressured environment, so full PAOS establishment is only a matter of time. Friction measurements and material testing for samples with different annealing times indicate that a full effect is reached after about 20 hours annealing.
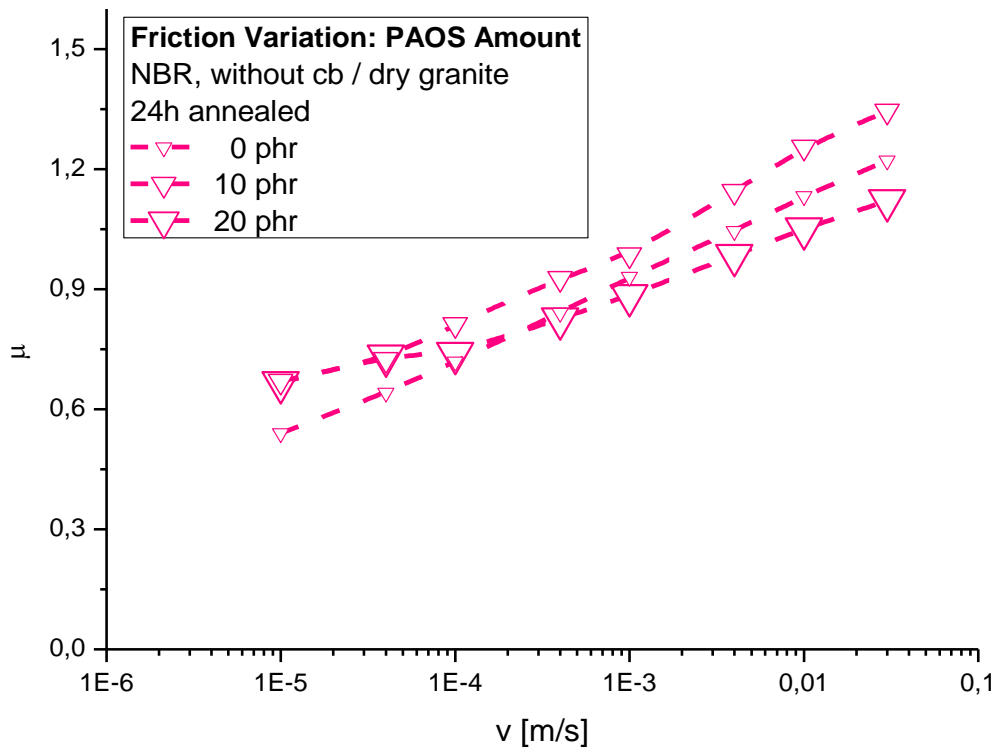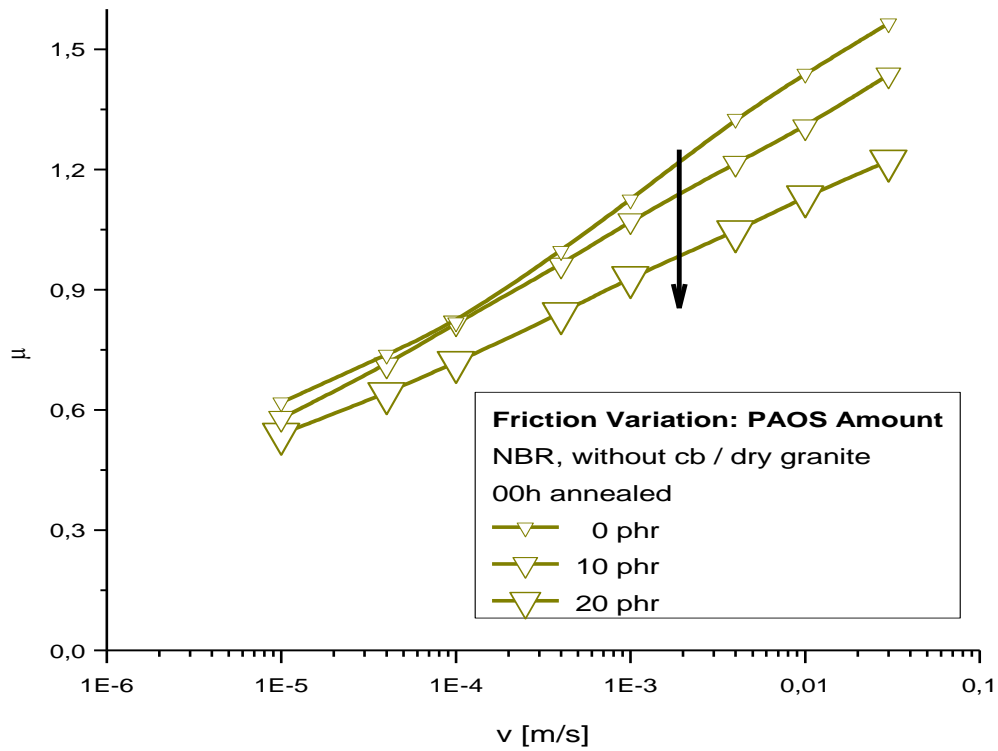
Figure 87: Friction of samples without carbon black before (above) and after annealing (below) on dry granite
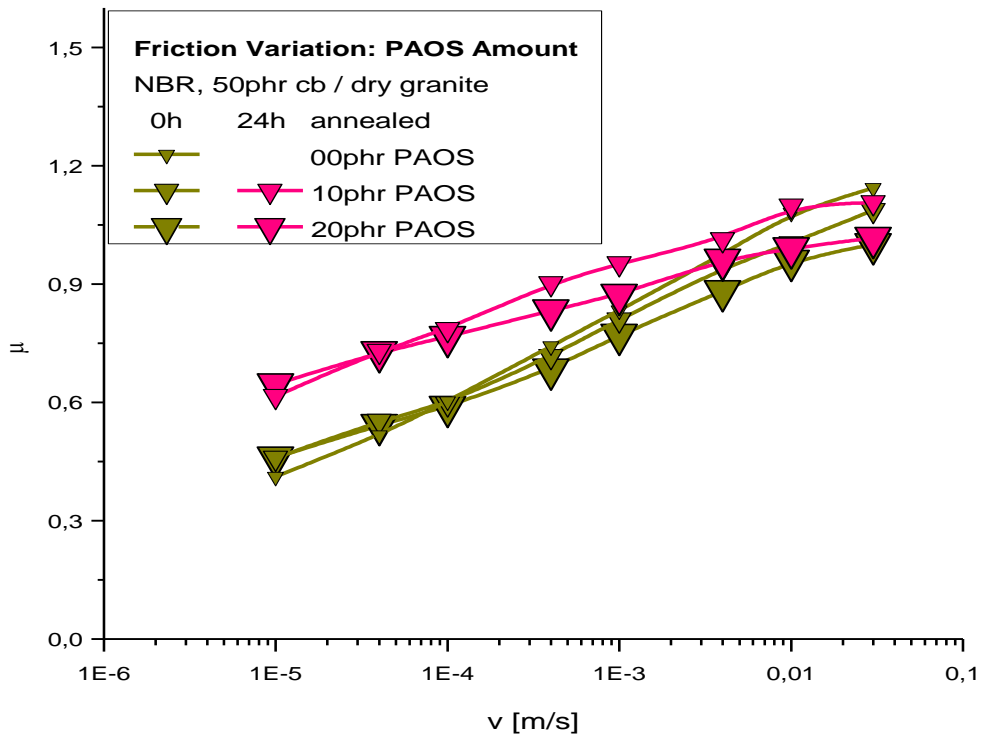
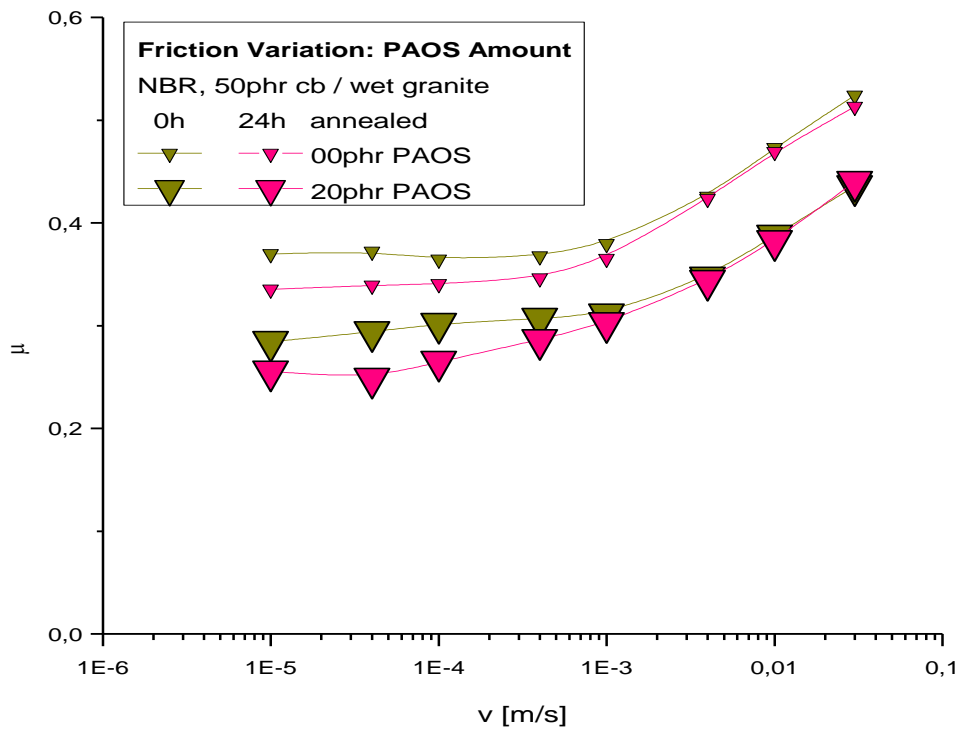Figure 88: Friction of samples with carbon black before and after annealing on dry granite

Figure 89: Friction on samples with carbon black on wet granite

The increase of high velocity friction is caused by hysteresis effects (present both for dry and wet surfaces), so this behaviour should apply even more with lubricated sliding and also for lower velocities, which is confirmed in Figure 89. Apart from PAOS influence, friction is considerably lower on lubricated substrates, especially for carbon black filled samples (again up to 20% for 20 phr PAOS). Annealing enhances the effect of PAOS and lowers friction especially for small velocities for any degree of PAOS.

On rough substrates like granite the differences of cb filled and unfilled samples are moderate. Smoother substrates are known to induce higher friction and also stick-slip on soft, smooth materials like these rubber samples. Especially unfilled samples are prone to this (for dry interfaces, whereas wet conditions always showed lower friction and no stick-slip). So the effect of PAOS filling was tested for elastomers without cb on two smoother counterparts: polished steel and glass.

PAOS reduces friction not only on granite but also on polished steel, as depicted in Figure 90. The originally very high friction coefficient can be drastically reduced by PAOS. Contrary to granite, the reduction factor depends on the velocity in a non-linear way. Another difference, a slight increase of friction after annealing, is also found in the data for surface tension. For highest velocities, stick-slip behaviour is observed in absence of PAOS, so the periodical sliding and resting [63] of the sample makes it difficult to determine well defined friction coefficients in this case. On the other hand, most parts of the friction graph are not influenced by stick-slip and remain qualitatively the same. Presence, amplitude and frequency of stick-slip depend hardly on material parameters like rubber type, cb filling or annealing time for these samples, but predominantly on velocity – and can be prevented by lubricant or PAOS.
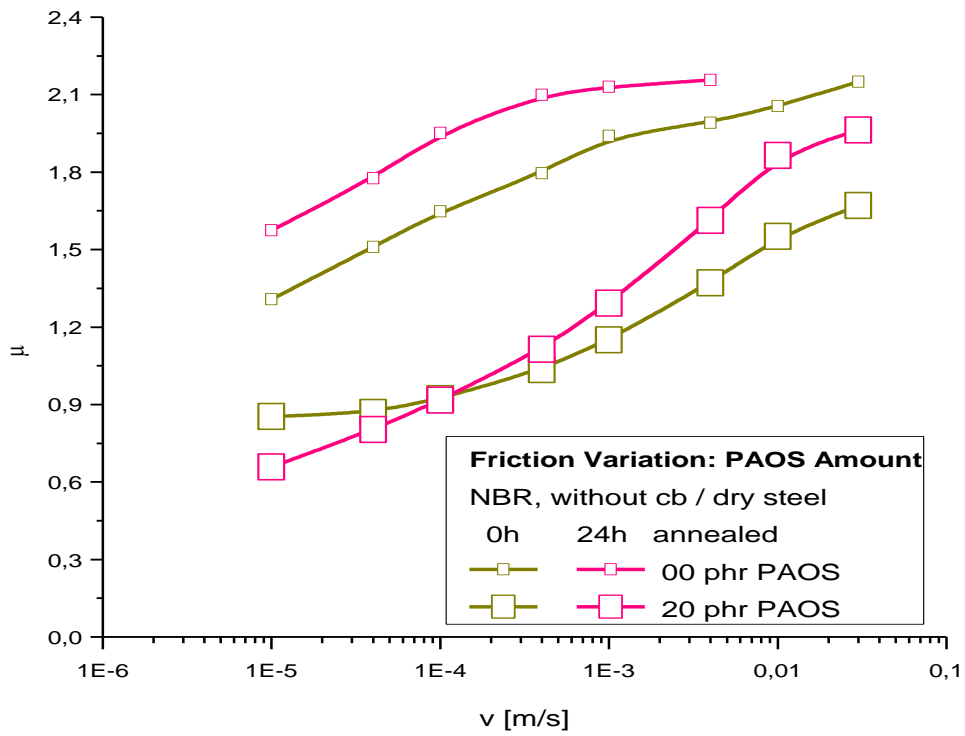
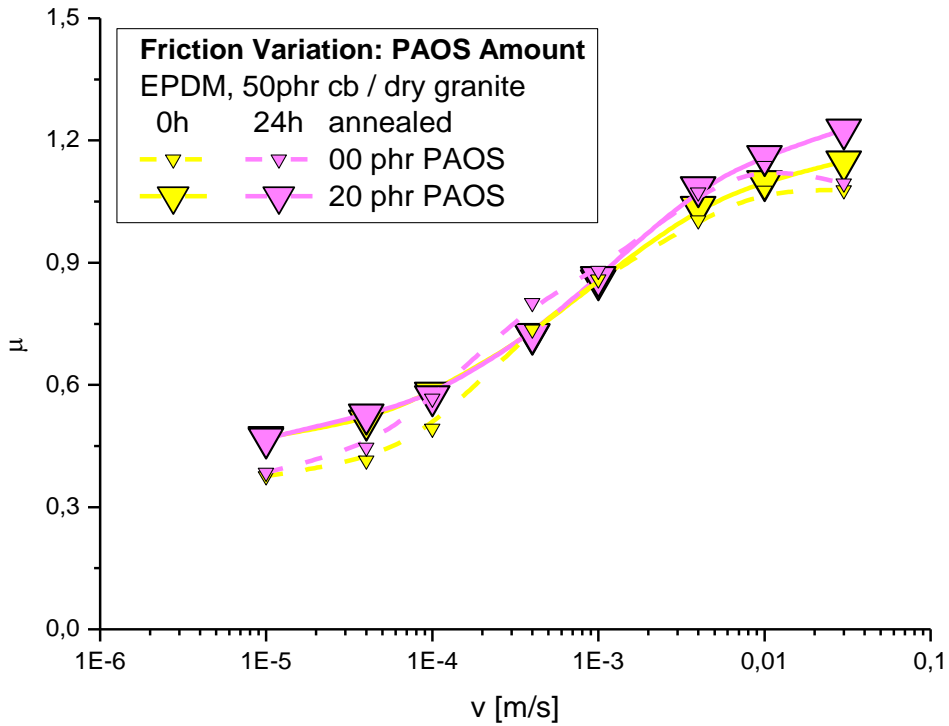Figure 90: Effect of PAOS filling of NBR on dry polished steel

Figure 91: Effect of PAOS filling of EPDM on dry granite

Friction on glass (not shown here) is even higher than on steel since the extraordinarily flat surface results in a large real contact area between the friction partners. On this substrate, stick-slip is extremely pronounced for systems without PAOS above a critical velocity (0.1 mm/s), though not for the whole friction curve, i.e. self excited vibration needs to establish over the sliding distance. The drop of friction above that velocity is a characteristic effect for these stick-slip systems, as contact is temporarily lost. Adding 20 phr PAOS reduces friction by approximately 50% in the low velocity range and completely removes stick-slip in the high velocity range. This offers a significant advantage as stick-slip is usually regarded as unfavourable in many applications. As a side effect from avoiding stick-slip, the qualitative behaviour of the friction curve becomes more regular: a stable friction slope which rises monotonously with velocity.

So the application of PAOS does significantly reduce friction for the investigated parameters (filler degree, substrate, lubricant, annealing) and has as such proven successful for NBR rubber. Enhancing an EPDM based friction system, however, is obviously not possible, as Figure 91 demonstrates. All curves, with and without PAOS just like with or without annealing display effectively the same friction, although annealing provokes the mentioned friction flattening by lifting the low velocity end. The marginally higher friction of EPDM compared to NBR results mainly from its adhesion component, so affecting the system with surface particles like PAOS appears promising.

According to Figure 49 the silicon amount of cb filled EPDM is lower than of cb filled NBR: A clue for a less perfect accumulation of PAOS on the surface. It is thus imaginable that for EPDM a different set of production parameters is needed to achieve the desired effect. First experiments with less hydrophobic PAOS types or smaller amounts (4 phr PAOS) did not display the expected behaviour for NBR either, and for some combinations even increased friction. All this is superposed by the inevitable progression in natural annealing and further aging.

4.5.3 Decreasing Friction and Stick-Slip by Coating

Most relevant properties that rubber provides in its applications are caused by the bulk. Friction, on the other hand, is caused by a combination of a pure surface effect (adhesion) and a near-surface effect, the hysteresis part. The consequent approach is to separate the materials for bulk and surface: an elastomer coated with friction tailored varnish. The following considerations will analyze the influence of the aspects that emerge from a parameter variation for coated samples.

Natural Sample Surface (without Coating)

Before examining how friction affects tribological systems, it is appropriate to take a look at the natural samples without coating: On glass and coated sheets as smooth substrates the friction for smooth– and especially unfilled – elastomer samples is far too high and irregular to give conclusive results. Even for rough samples (Figure 92), friction is extraordinarily high and suffers from stick-slip, so a complete curve is not measureable, e.g. for sheet 3.
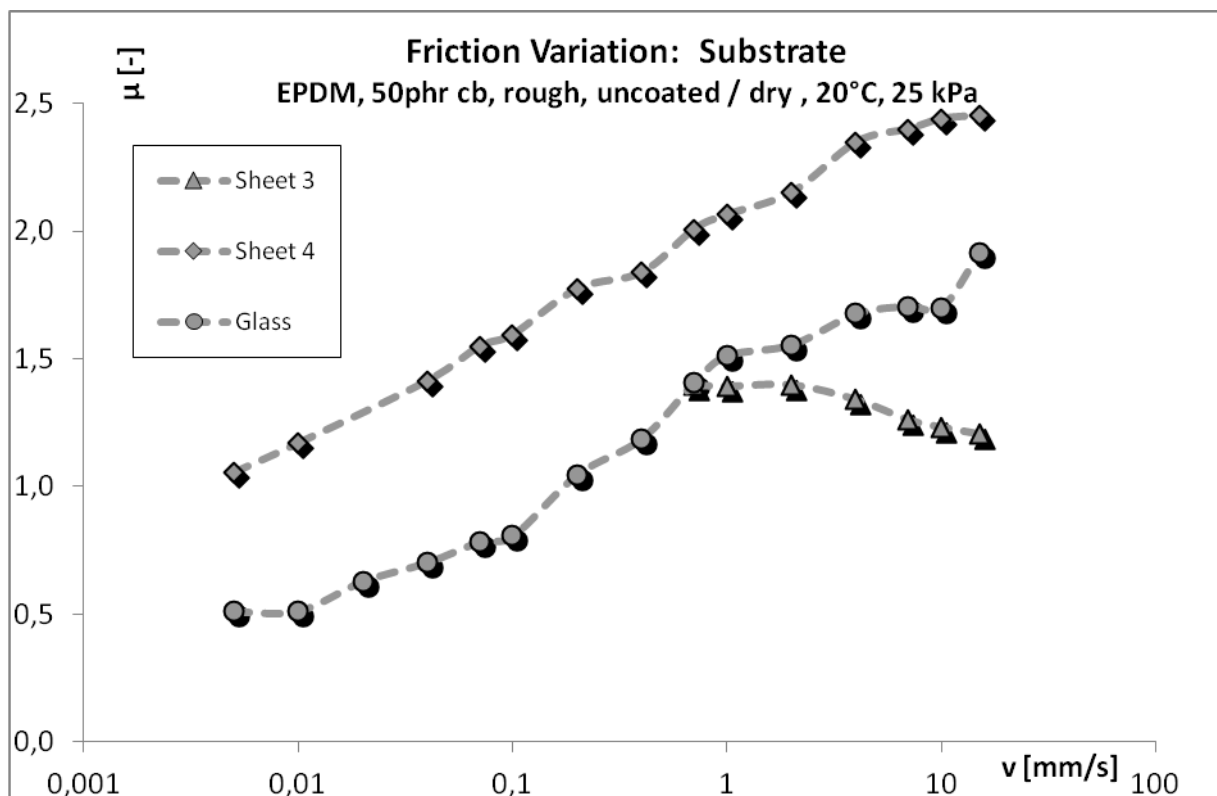

Figure 92: Uncoated samples exhibit extraordinary high friction on smooth substrates.

However, on rough steel friction becomes more moderate and regular. On the question how the elastomer type defines friction, the result is clear, as Figure 93 demonstrates: SBR elastomers experience higher friction than EPDM rubber, for both smooth and rough sample surfaces. This is most pronounced for high slidings speeds, whereas for slow velocities the difference becomes small or even non-existent. Viscoelastic properties provide an

explanation: EPDM is slightly harder than SBR 2525 and thus cannot establish contact (adhesion friction) as easily as SBR, and at the same time has a lower glass transition temperature. Additionally, the surface tension of each rubber interacts with the substrate. The general shape of the curve is quite typical for a stick-slip free friction slope in the moderate velocity range.
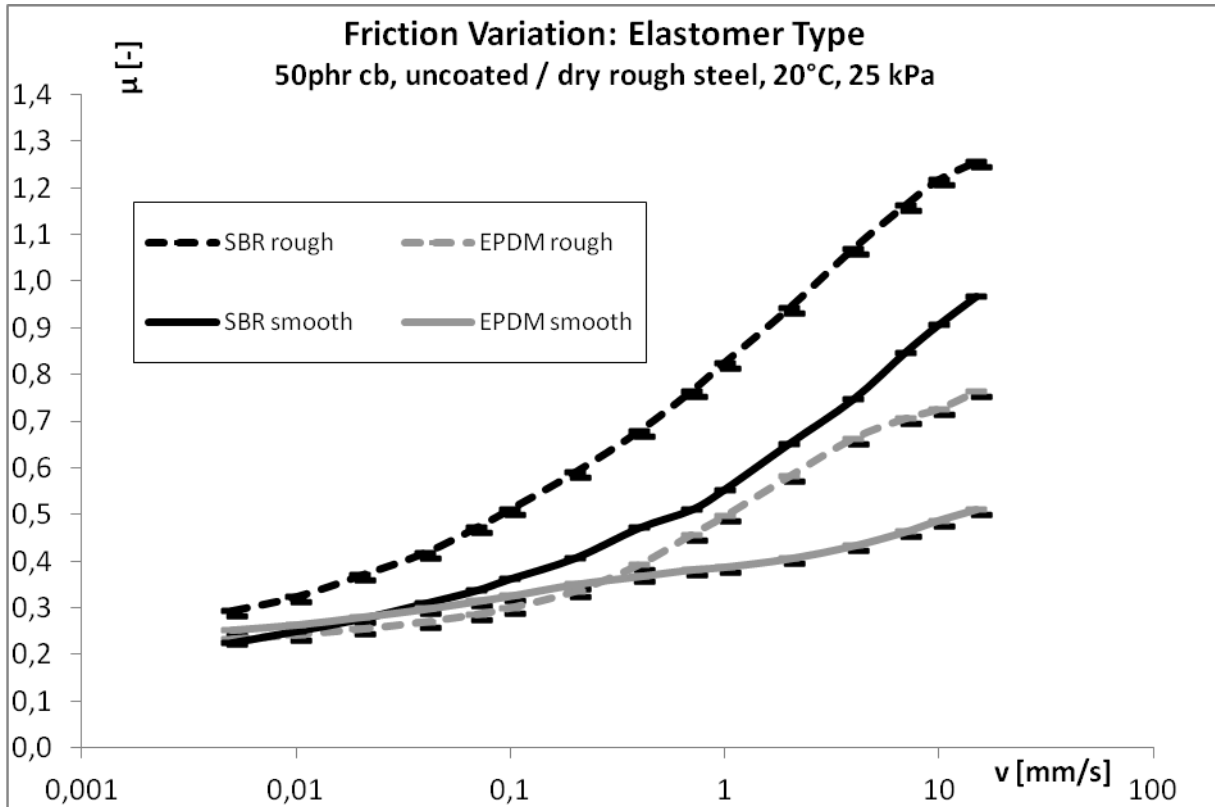

Figure 93: In uncoated state the friction of SBR clearly exceeds that of EPDM.

The situation changes when a coating interrupts the direct contact between rubber and substrate: Surface tension of the elastomers no longer matters, and the slightly harder EPDM is expected to lead to increased friction as now its hysteresis friction is dominant. As Figure 94 to Figure 97 prove that for coated samples EPDM has higher friction than SBR– coating has a stronger effect on SBR than on EPDM. Both elastomer frictions, however, become quite similar on steel and glass while the effect is better visible on coated sheets for rough than for smooth samples because the surface energies of the coatings modify the friction maximal for coating–coating contact. Tension is also different for each coating, so PTFE with its low surface tension does not fit the scheme.

Elastomer Type

The most important effect of coating is the drastic reduction in friction: For all velocities, "coated friction" is only a fraction (COF rarely larger than 0.7) of "uncoated friction" which can easily reach values of 2 or more, and the effect is maximal for fast speed, reducing the slope

of friction. Too flat slopes are, on the other side, susceptible to stick-slip. Chapter 4.6.2 will investigate this effect.
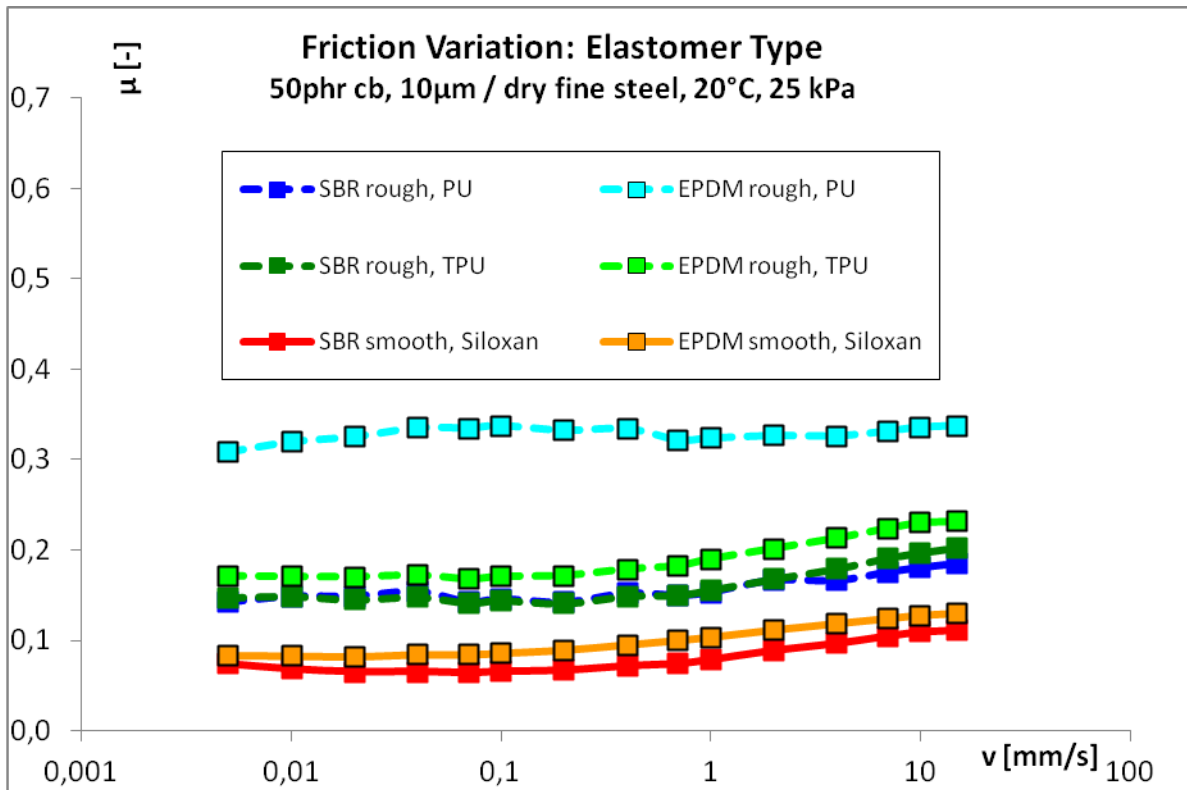

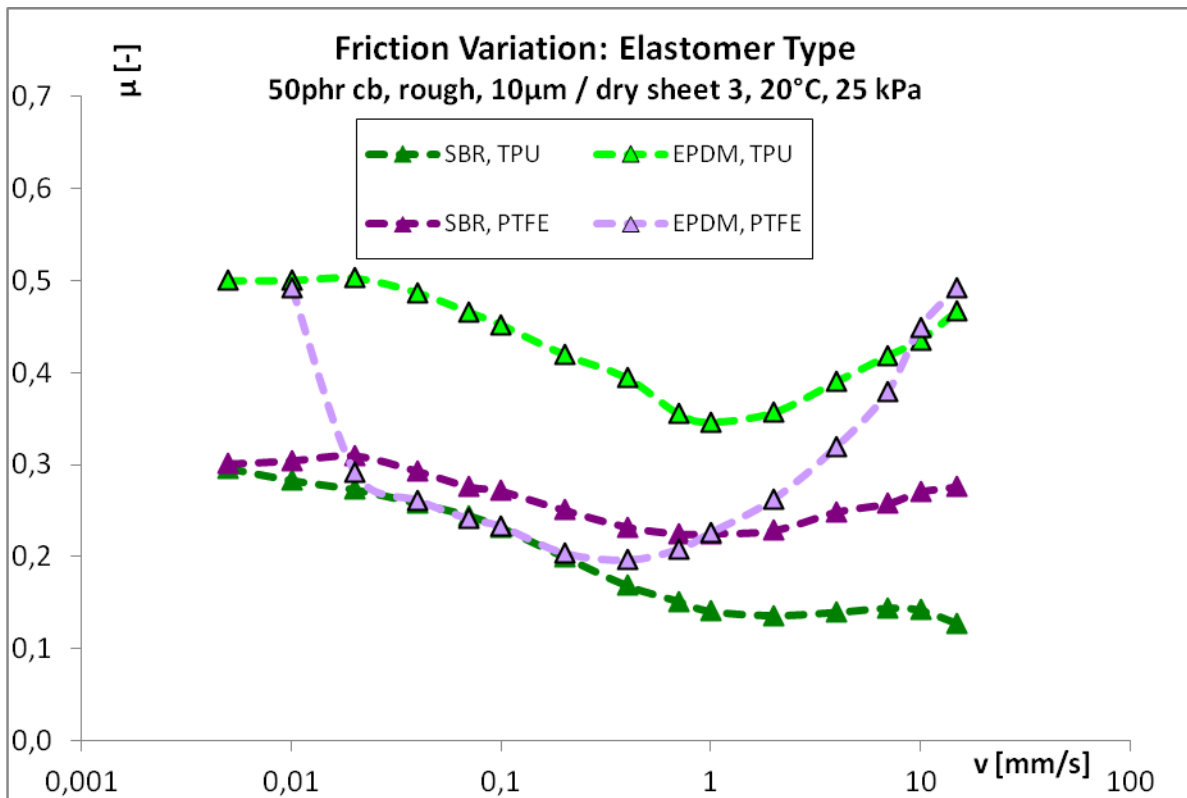Figure 94: Coated SBR and EPDM in comparison on steel

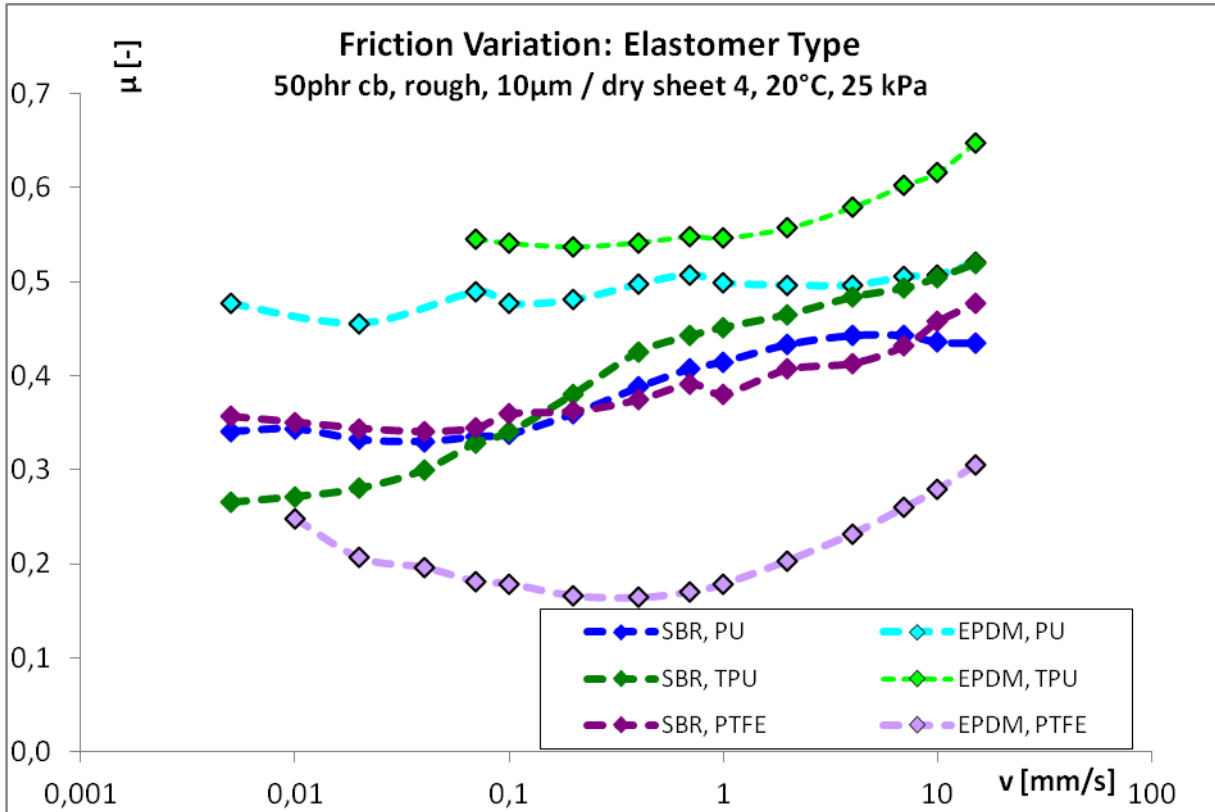Figure 95: Coated SBR and EPDM in comparison on coated sheet 3

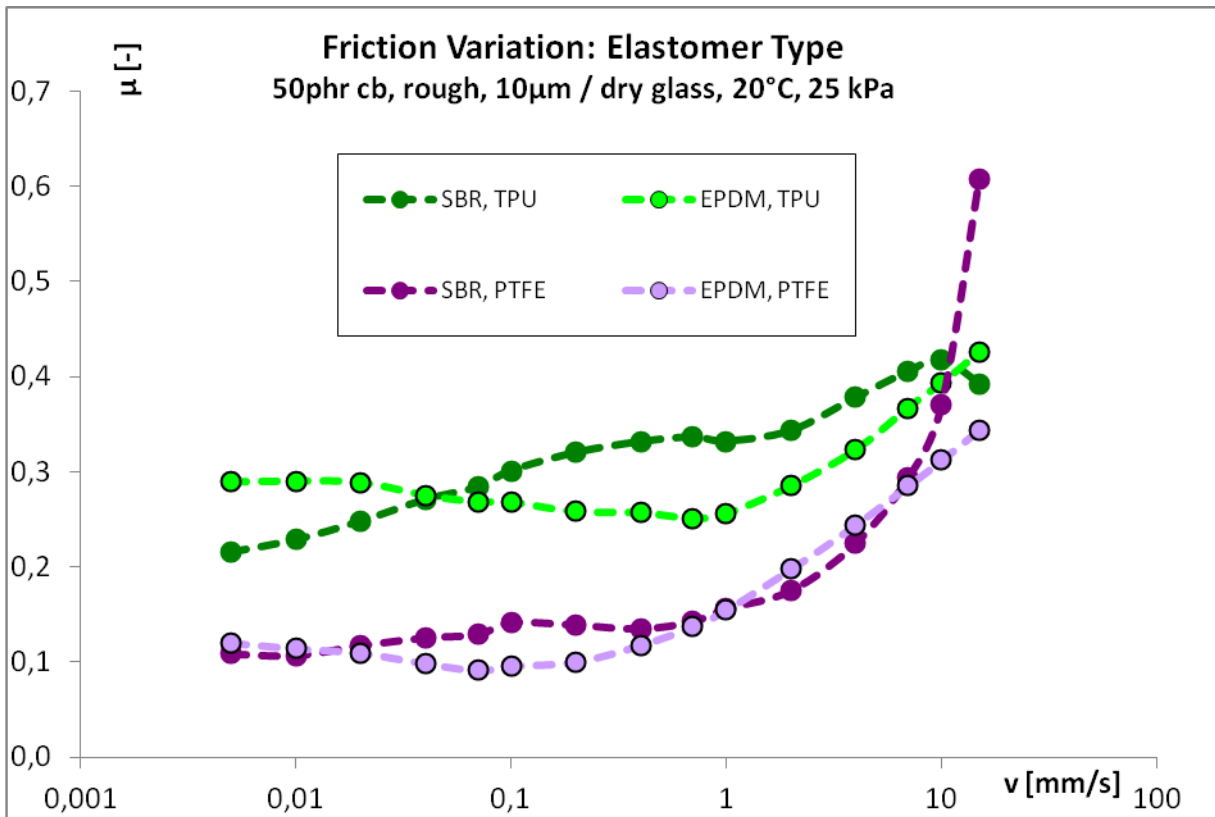Figure 96: Coated SBR and EPDM in comparison on coated sheet 4

Figure 97: Coated SBR and EPDM in comparison on glass

Carbon Black Filler

A very effective way to make samples harder and more stable is the employment of carbon black filler. Figure 98 shows how filled, stiffer SBR samples can create more friction almost independently from the coating type, although the effect is minimum for siloxane – a hint that siloxane samples are less dominated by the bulk. The result cannot simply be transferred to EPDM, which produces considerable stick-slip on siloxane.
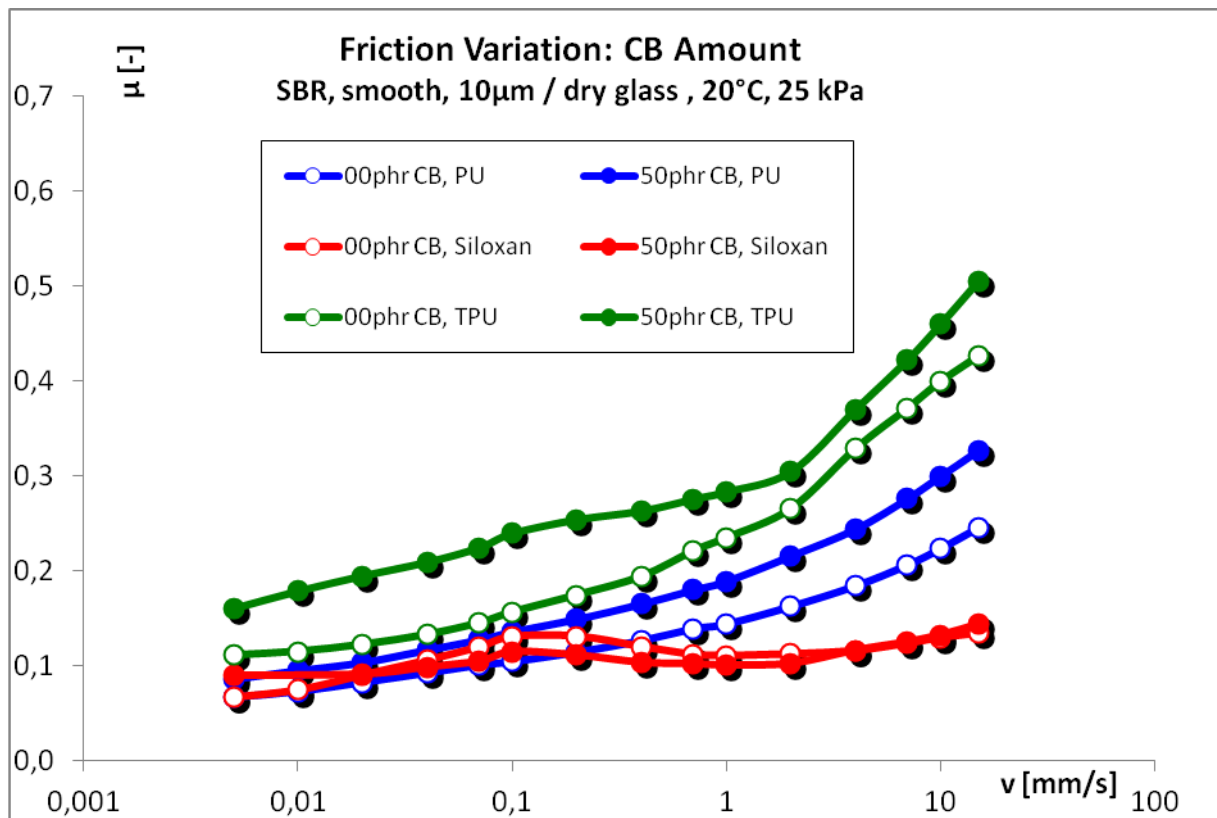

Figure 98: Filling SBR with cb increases friction.

Roughness

The next aspect switches from bulk properties to surface structure: As can be seen in Figure 93, a rough rubber can cause more friction than a smooth one. This is not surprising on rough steel, as the relatively coarse asperities can interlock with their counterparts and induce high hysteresis as a large volume is deformed. But on smooth substrates, friction originates mainly from adhesion, so a smooth rubber should cause much higher friction on glass or coated sheets than a rough rubber. This is indeed the case, as Figure 99 demonstrates high friction on glass for rough and even higher friction for smooth samples. Coating probably mitigates the effectiveness of surface structures on the sample, but still gives a formidable drop in friction with rough sample structures. The same is generally true for all coating types on all substrates, though not always as pronounced as in this example. Smooth substrates have large friction anyway and are more sensitive to sample roughness

to reach low friction coefficients. Also, it is easier to gain a positive friction slope with rough samples than with smooth ones, even on rough counterparts like steel.

These observations rely on the reduction of true interfacial contact in dry state, but are not valid when a lubricant prohibits contact anyway. Allowing a more homogeneous lubrication coverage, samples on wet interfaces tend to have less friction with a smooth than with a rough surface.
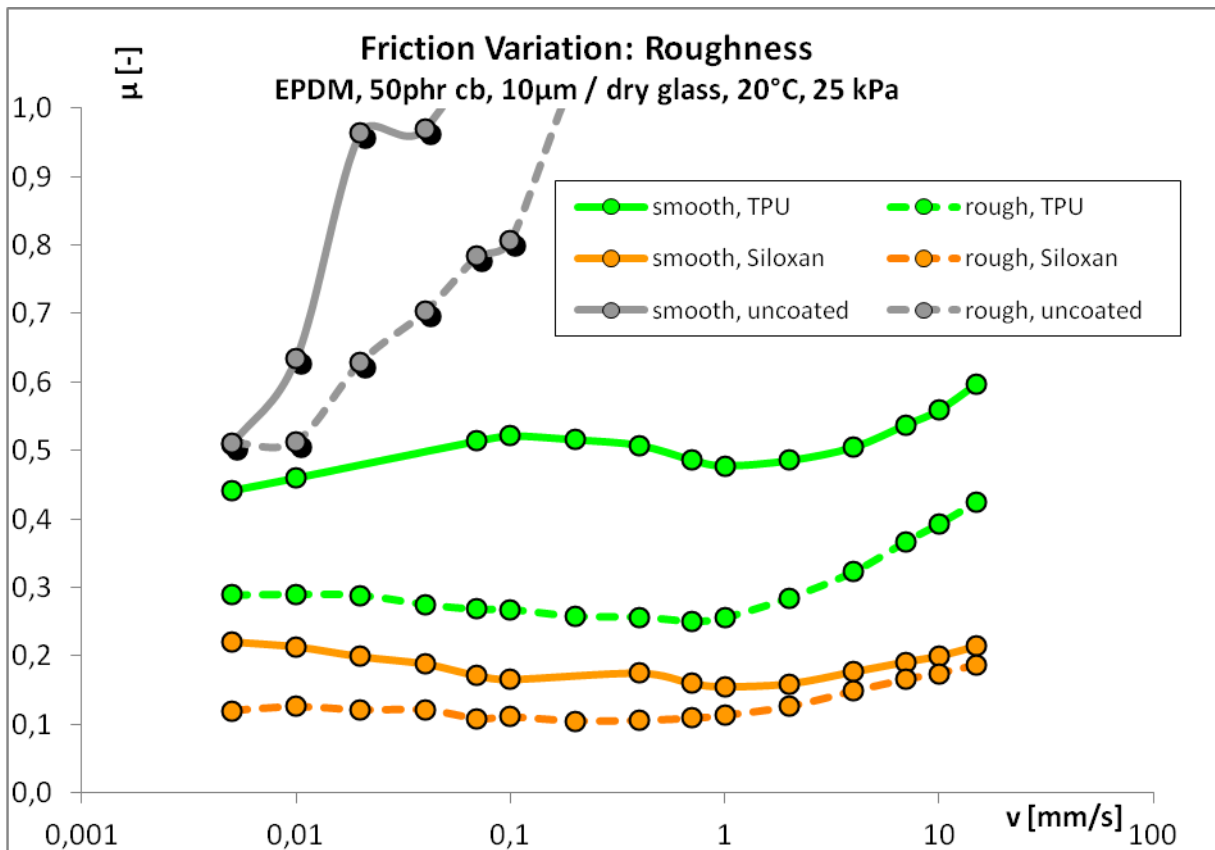

Figure 99: Rough samples have less friction than smooth samples on glass.

Coating Type

Basically all observed effects in these systems are a superposition of elastomer and coating behaviour. Which coating is the best in order to reduce friction, and which for reducing stick-slip? Although a correlation can be expected, these two questions must be considered separately. In almost every possible combination of parameters, the various coating types queue up in a fix order of friction coefficients – Figure 100 and Figure 101 are typical examples. The uncoated sample is always highest (beyond the scale in the following figures). Among the coatings, TPU usually exhibits the least effect, followed by PU. Siloxane and PTFE tend to sojourn in the same, lowest range of friction; the first certainly due to microscopic wear particles acting as solid lubricant, the latter because of low surface tension. From this point of view, these two are the best choice for reducing friction. Optimal success

is gained at high velocities. But for slower sliding, the difference to PU and TPU is in most cases considerably smaller and often linked to a negative slope, which is likely to provoke stick-slip. The stability of sliding must be taken into account, just like the mechanical stability – see chapters 4.6.1 and 4.6.3 for details. The effectiveness of coatings tends to differ more largely on EPDM than on SBR, especially for slow velocities.

Figure 102 shows an exception to the rule: Deviating from other substrates, TPU becomes on steel more powerful in friction reduction than PU, supposedly due to surface tension effects.
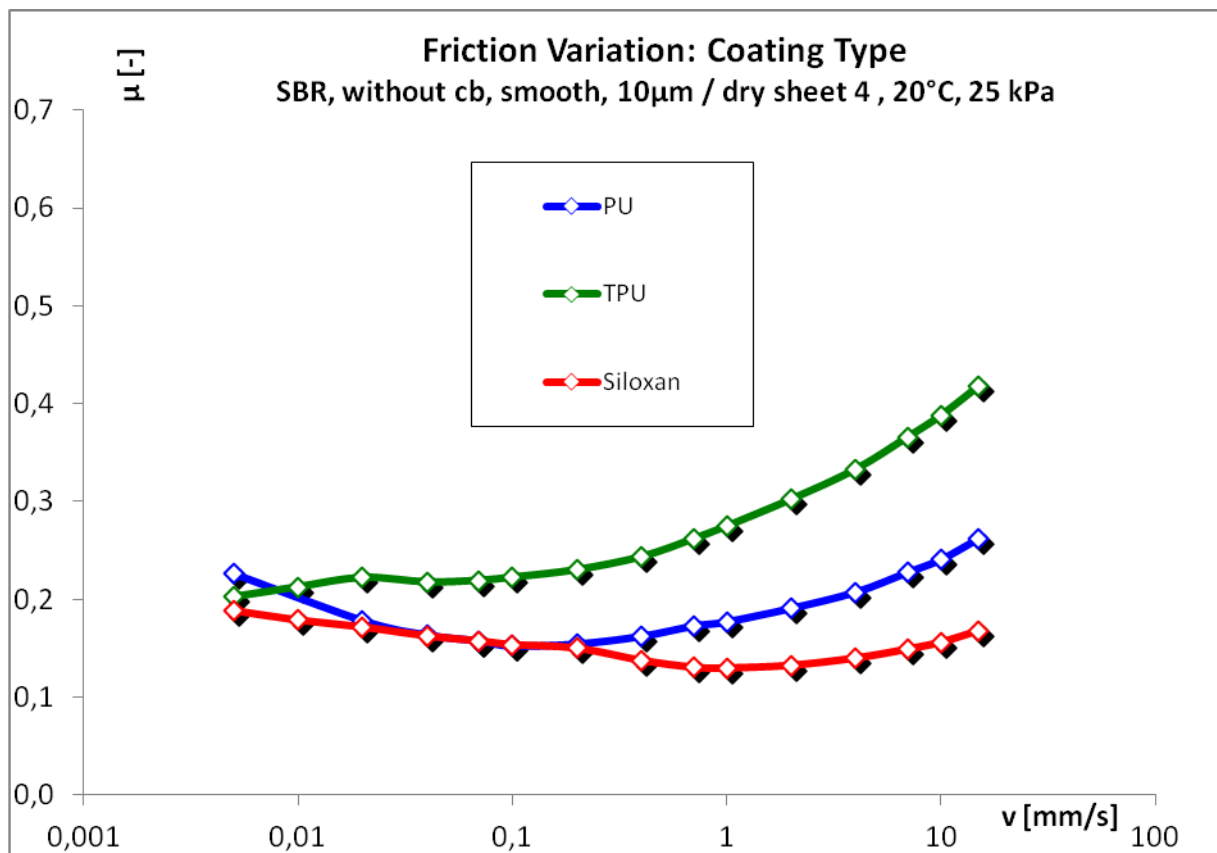

Figure 100: Different kinds of coating decrease friction to a different degree.
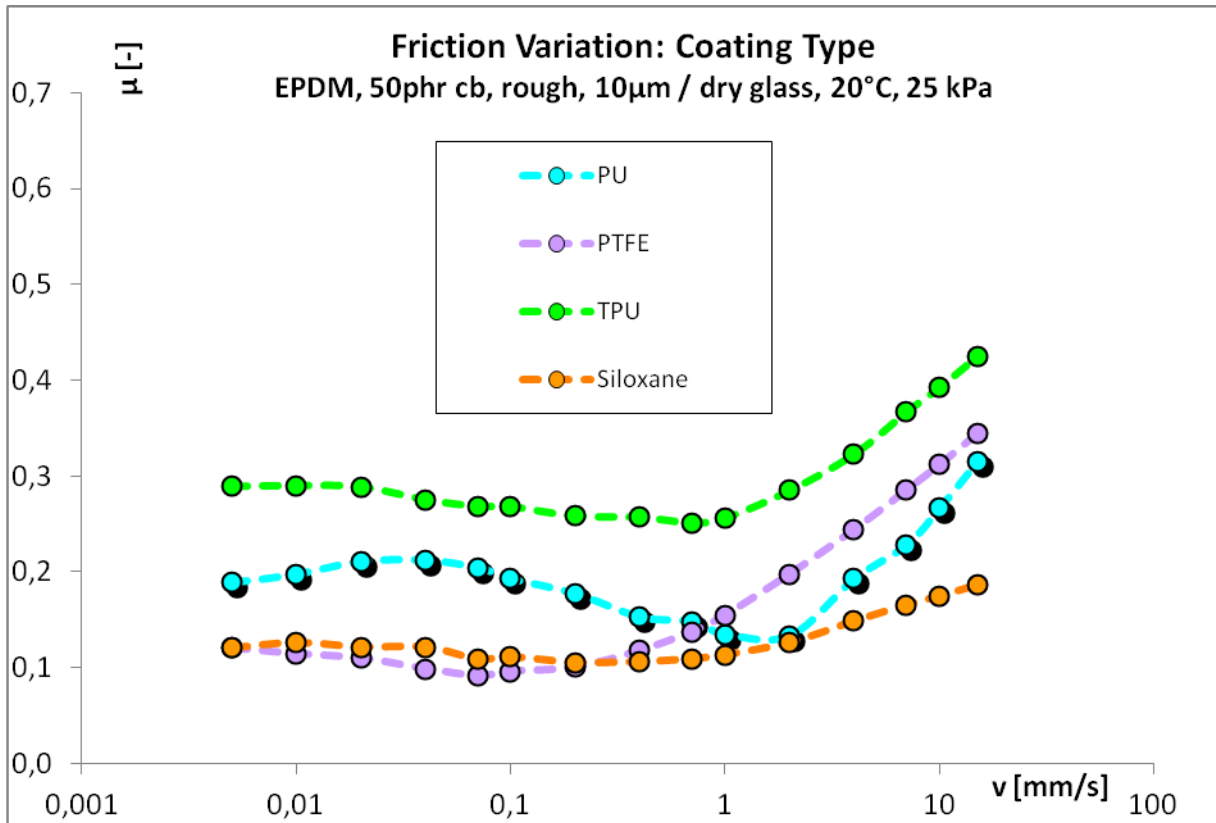
Figure 101: The dependence on the coating type is identical for glass, even when elastomer, filler and roughness changes compared to Figure 100.
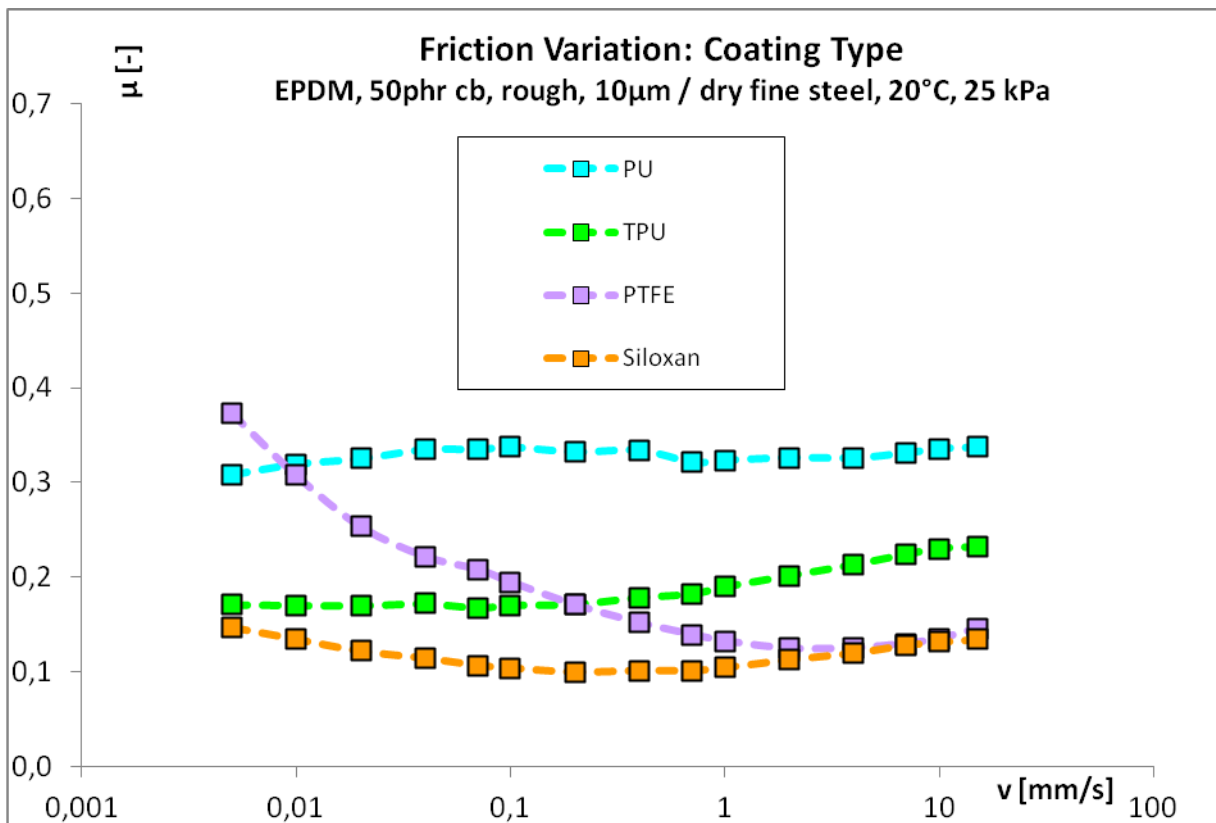

Figure 102: On steel the relative effectiveness of coating is different from that on coated sheet.

Layer Thickness

The type of coating is important because of its surface tension, but also because of its own viscoelastic deformation which is superposed to the bulk viscoelasticity of the rubber. The thicker the layer, the more relevant become viscoelastic effects within it. This should better be visible in comparison with the asperity of the substrate: Flat substrates gain according to chapter 2.4 a smaller penetration depth, so broadening the layer thickness beyond a certain value does not further enhance the minimation of friction. This can be observed in Figure 103 for the example of fine steel. On rough steel (Figure 104), in contrast, the maximal effectiveness of PU coating is not reached with 10 µm and can be optimized when coating is set to 40 µm instead. In a system consisting of two components with different hardnesses, the major part of deformation will affect the softer material, so unfilled elastomers are supposed to be less susceptible to a resulting friction decrease by coating. Indeed a reduced friction occurs in cb filled SBR on coated sheet when the sample PU coating is increased from 10 to 40 µm, but fails to work better in unfilled SBR. On glass as an extremely flat substrate coating thickness does not matter either. For EPDM the results have been verified on rough steel.
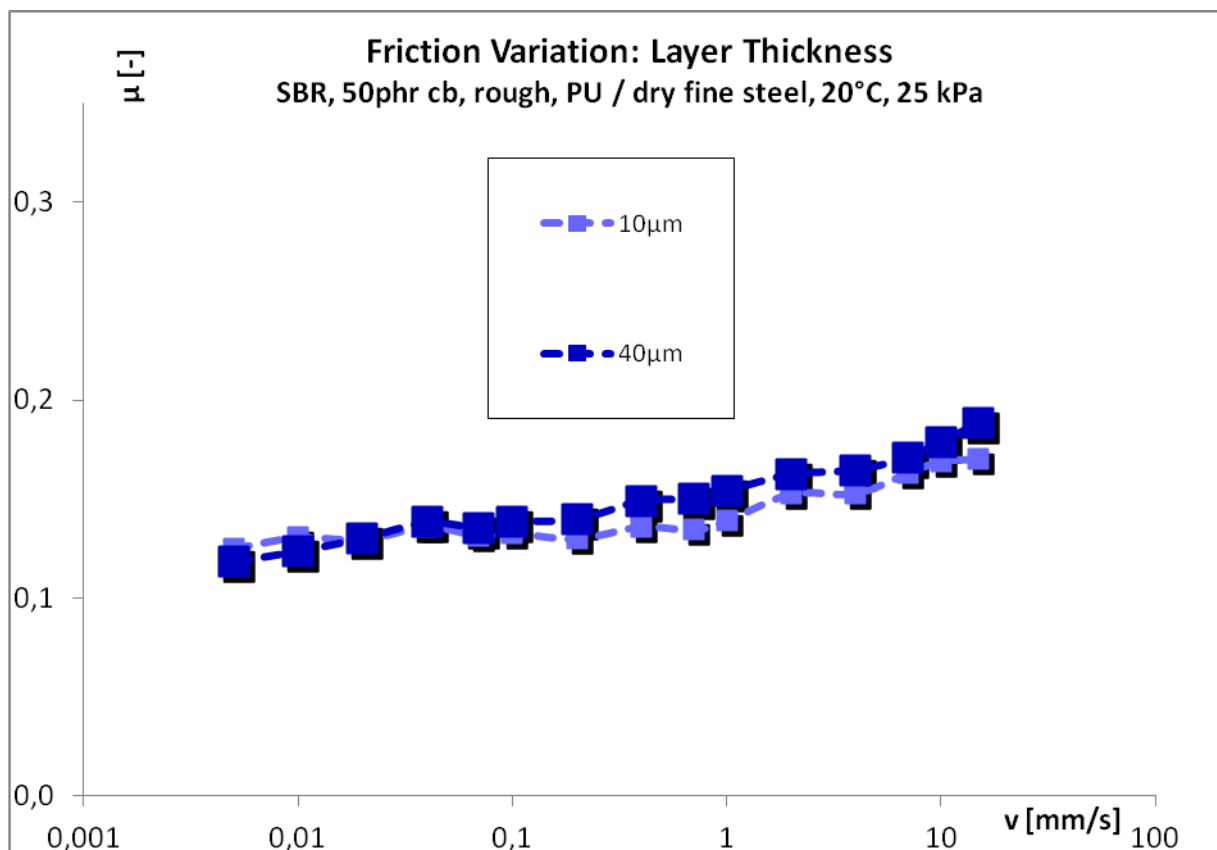

Figure 103: On fine steel an augmentation in thickness of coating layer provokes no effect.
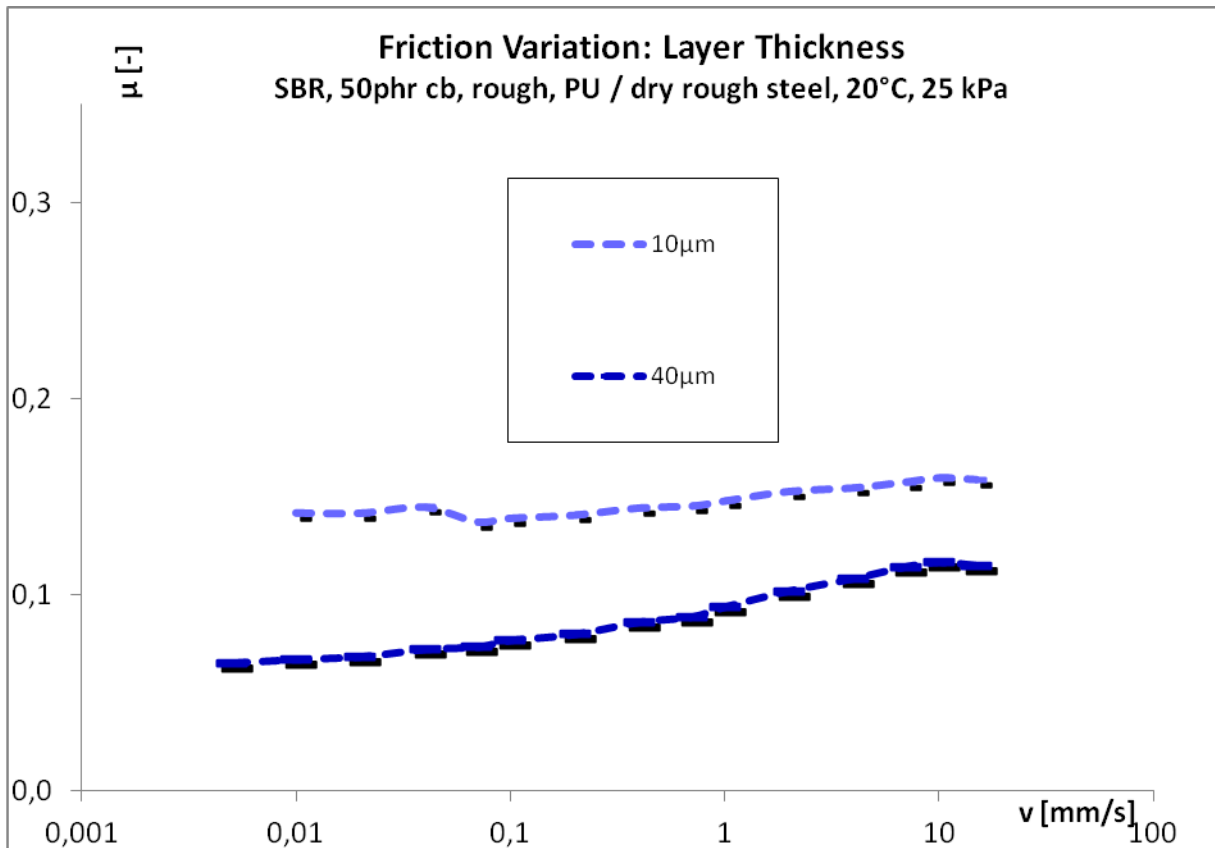
Figure 104: On rough steel thicker coatings have less friction than thin coatings.

Substrates

For the substrates a clear order is found concerning the friction coefficient. The tendency is already visible for the uncoated samples (Figure 92 and Figure 93) and remains the same after coating, although on a much lower friction level: Rough steel with its minimal true contact area has always the smallest friction coefficient, and the fine steel is almost as effective in reducing friction. Glass offers an even smoother contact interface, resulting in mediocre friction above that of steel. Coated sheets combine this smooth surface with its surface tension, so these sticky flat substrates end up with highest adhesion and frictions. A supplementary effect that aggravates this behaviour is the flexibility of the sheet surfaces: Unlike the rigid steel or glass substrates, the sheet coating can adapt to its counterpart, filling asperities, thus further increasing the contact zone. Which of the latter two substrates produces highest sticking depends on the corresponding sample coating as relation of the involved surface tensions: On PTFE sheet 4 reaches maximal friction, whereas on siloxane and uncoated samples sheet 3 produces the highest resistance to sliding. On PU and TPU no definite order between the two is established. From Figure 105 to Figure 108 some typical examples are given to reflect this order.
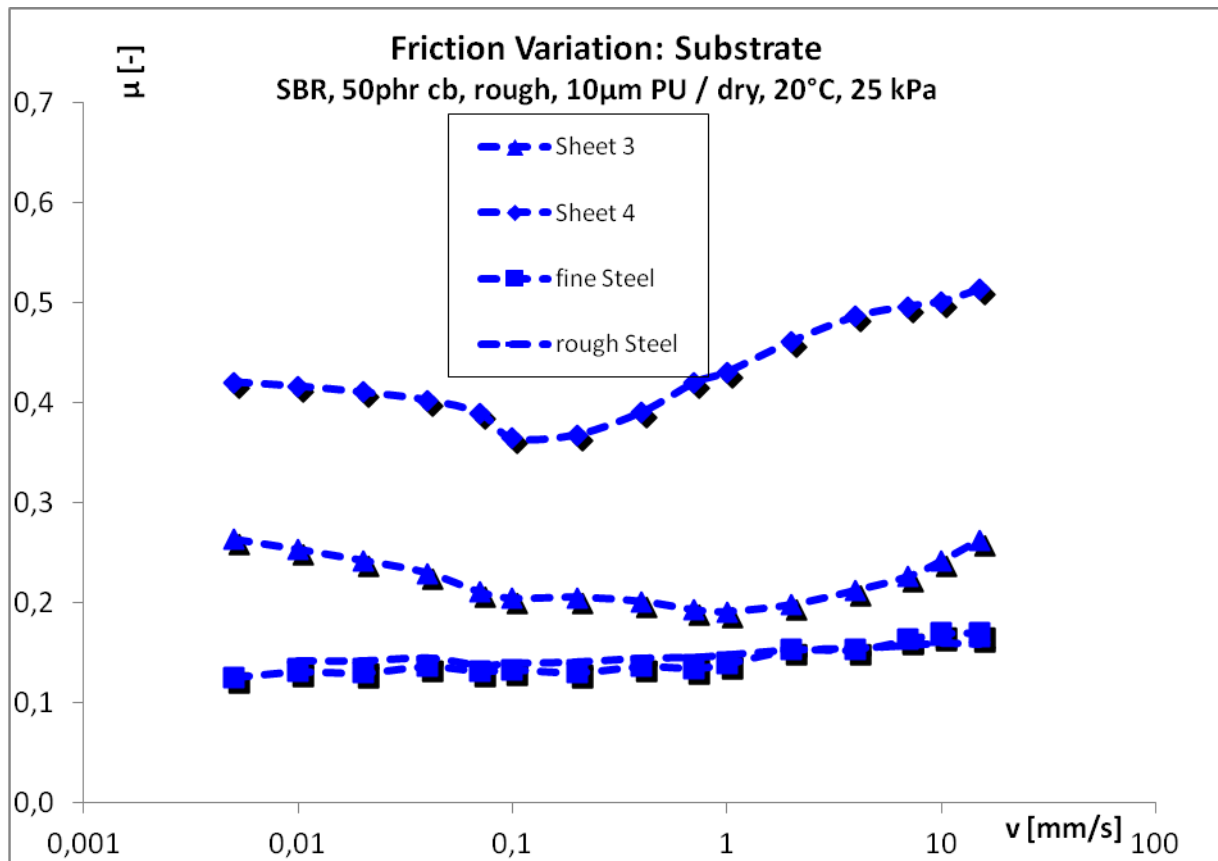
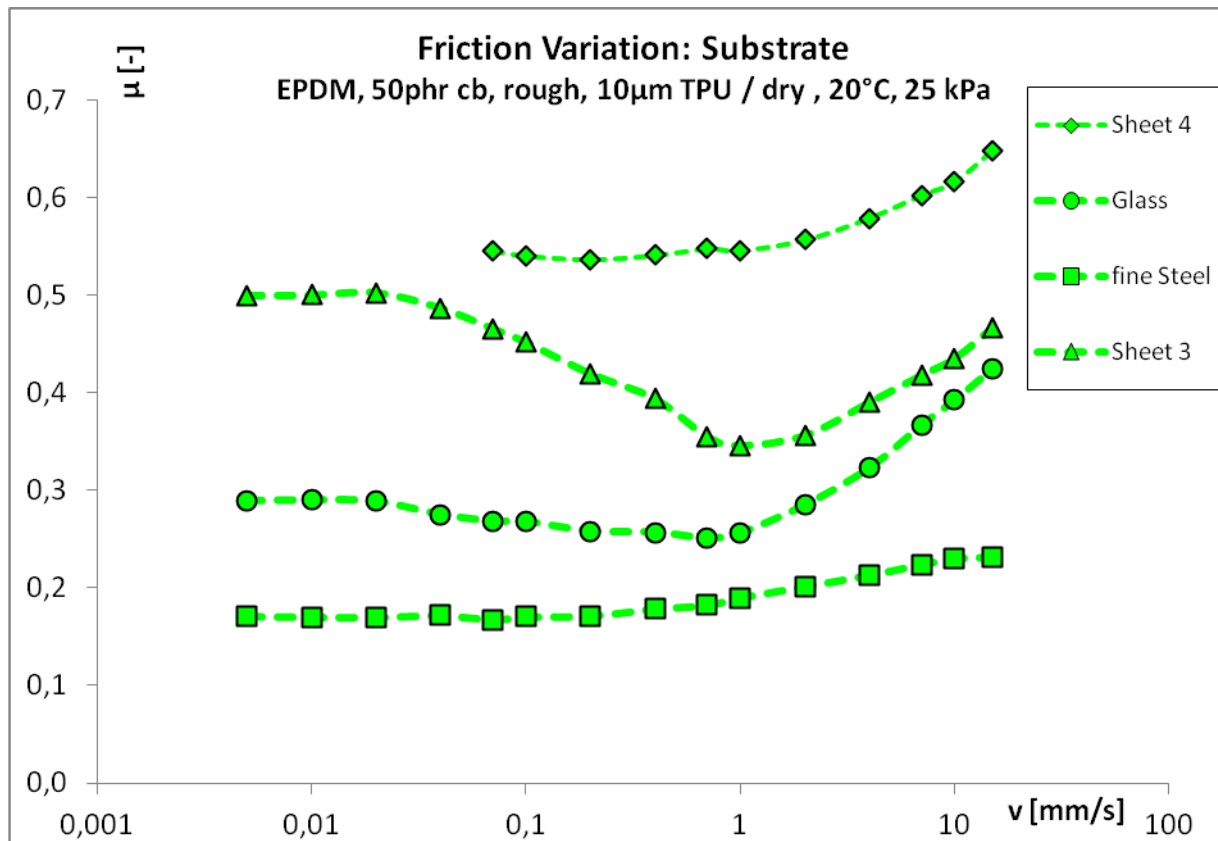Figure 105: PU coated samples on different substrates

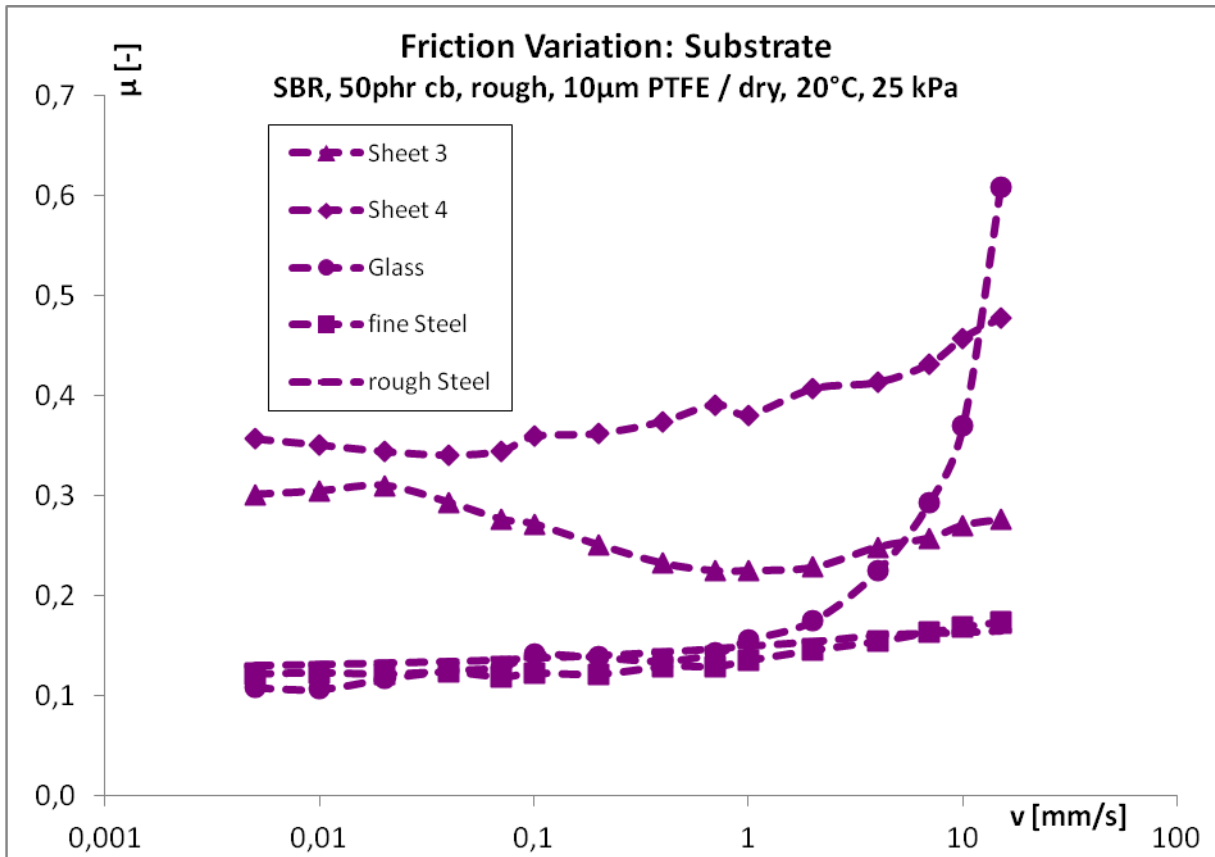Figure 106: TPU coated samples on different substrates

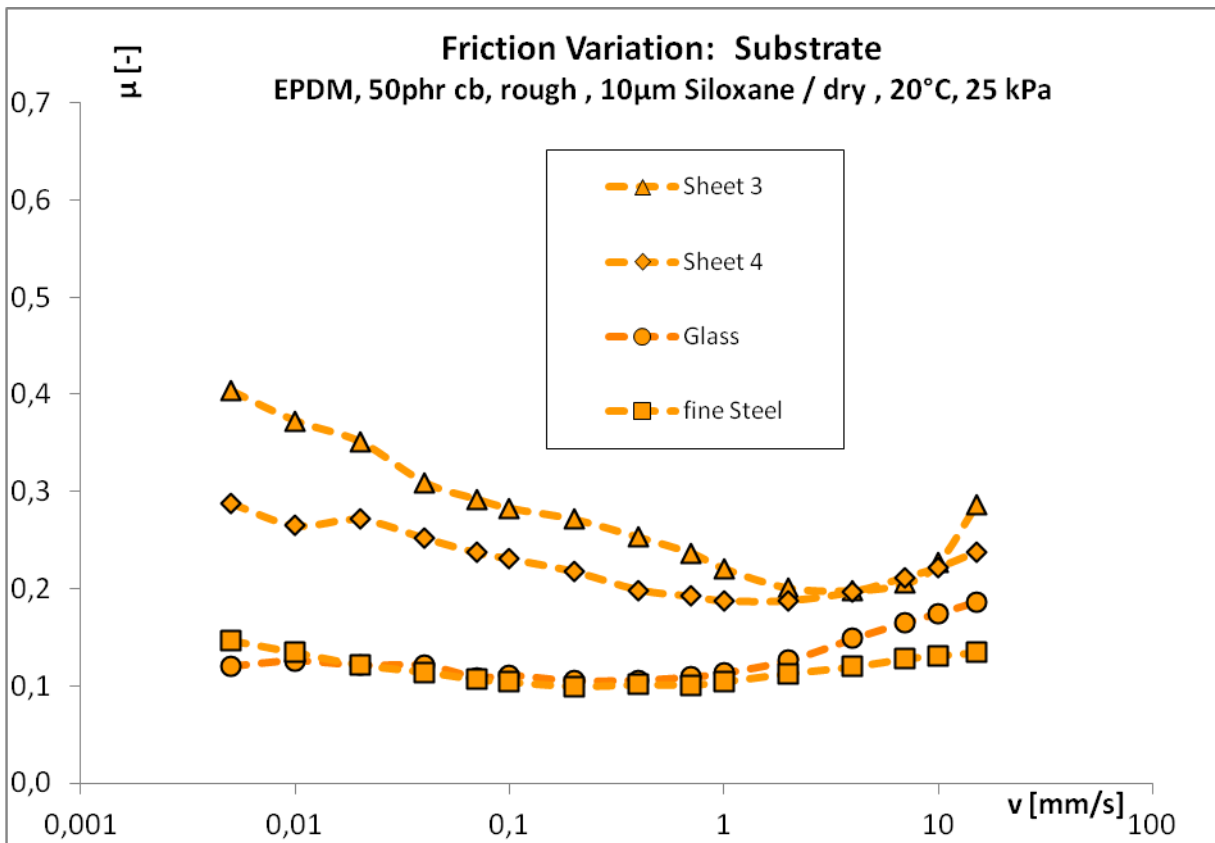Figure 107: PTFE coated samples on different substrates

Figure 108: Siloxane coated samples on different substrates

Surface roughness of the sample and filling with carbon black do not interfere with the substrate order, neither does it matter if SBR or EPDM is the bulk rubber. It is interesting that on every system shown here and in the vast majority of investigated systems a negative slope appears predominantly when sliding slowly on one of the coated sheets. This behaviour is especially distinctive for siloxane. Because of material properties siloxane tends to establish self-lubrication, which seems to be triggered especially on substrates with high surface tension.

4.5.4 Influence of Environmental Parameters on the Friction of Coated Samples

The previous chapter dealt with the influence of the "local material" parameters: the inner and outer state that the sample and the substrate contribute to the friction process. Apart from these local parameters, friction depends substantially from global environmental parameters: the pressure that is applied on both friction partners and the temperature they have.

Pressure

As stated in chapter 1.2, Amontons' laws predict a friction coefficient that links friction force proportionally to normal force, no matter how large the contact area is. This (macroscopic) nominal area must be strictly discriminated from the (microscopic) true contact area, which amounts to only a small part of the nominal area's value, but increases more and more when pressure rises. The increase of the true contact area is neither linear nor unlimited, but can be approximated as linear function for small pressures. Consequently, Amontons' law can be presumed to be correct for small up to moderate pressures but fail for high nominal pressures. Carbone & Bottiglione [64],[65] predict the friction to drop with sufficiently high pressures. Roughness plays a role, too [66]. The exact correlation depends on the parametrical circumstances.

In order not to superpose this question with a pressure induced deformation of sample microstructures, smooth sample surfaces are preferable for experiments. When put to the test, the result differs indeed depending on what set of parameters applies to the system. Figure 109 shows the friction for several values of pressure for a carbon black filled EPDM sample on steel: The influence of pressure is not visible, and the curve replicates within usual deviation. The standard pressure of 25.3 kPa can be regarded as low or moderate, and even 97.3 kPa is not an extreme value. Obviously the border of Amontons' description are not reached yet in this case.
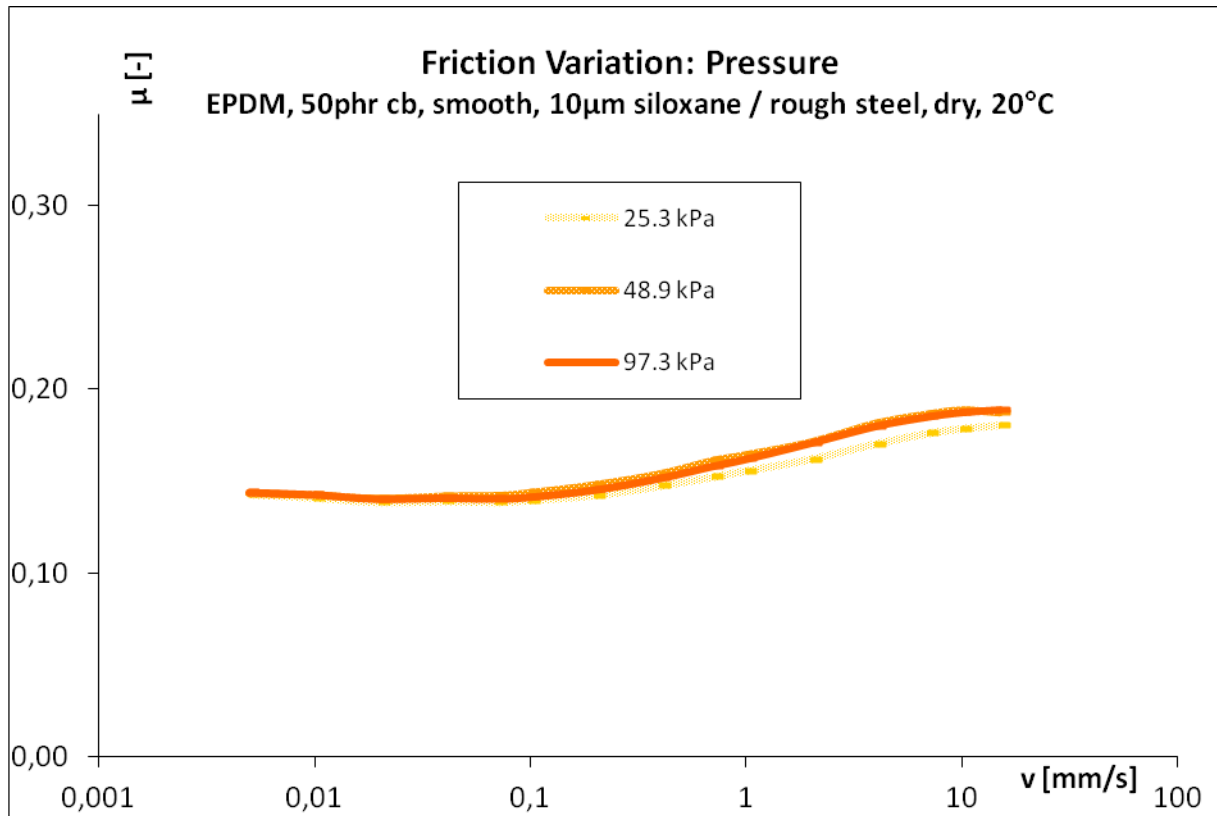
Figure 109: On rough steel increased pressures have little effect.
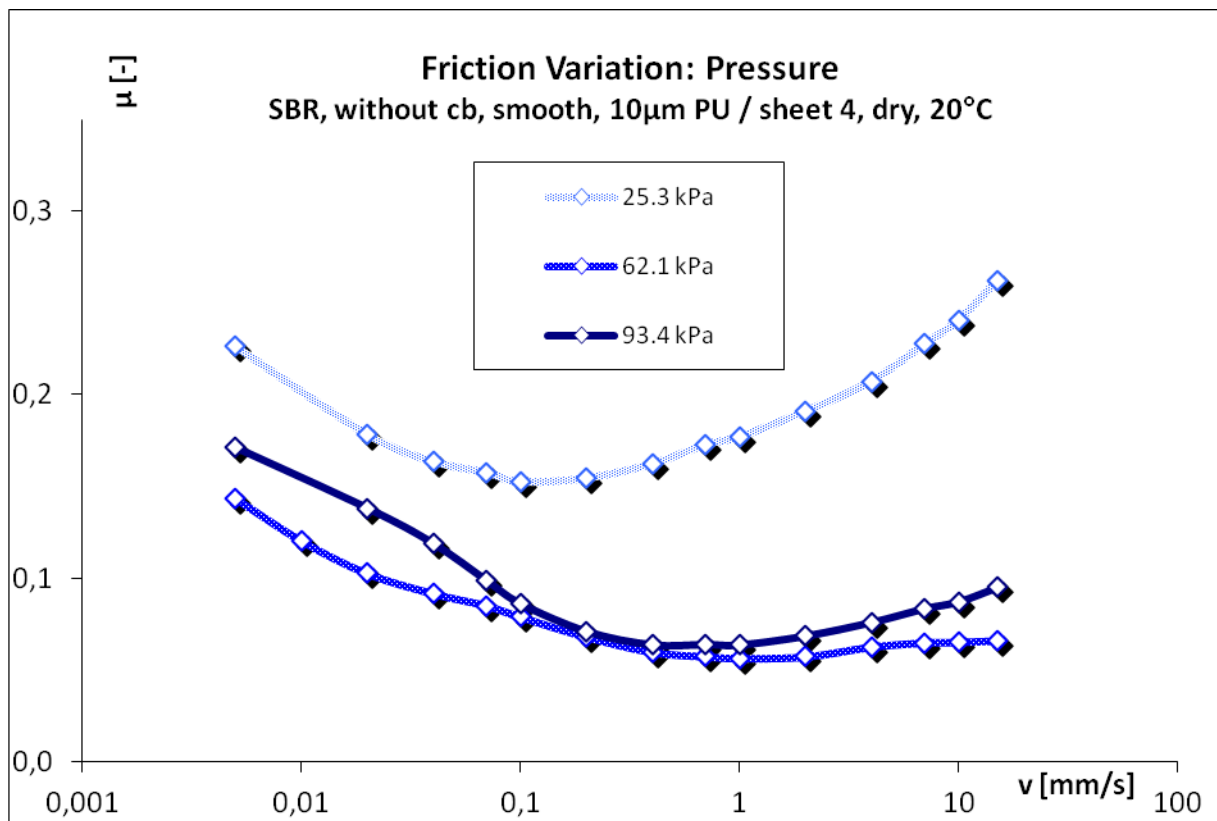

Figure 110: Modifying experimental parameters causes decreasing friction with rising pressure.

A quite different situation emerges when an unfilled and thus significantly softer elastomer is used for the experiment: The increased pressure causes friction to decrease extensively (Figure 110). This, of course, refers only to the friction coefficient, while the friction force is still increased. The effect is largest in the range of positive friction slope. This indicates that the cause of the negative slope – the soft coating of the metal sheet in adhesion contact with the sample – plays its own role in this system. It is imaginable that the combination of two soft interfaces enhances the possibilities of increasing the true contact area by pressure forced interlocking of microscopic structures, resulting in a cumulated friction drop according to the described predictions.

Temperature

Another important environmental feature is temperature: It affects the elastomer bulk, its coating, lubricant where applicable and, for the sheets, also the substrate coating. All uncoated substrates can be regarded as thermally inactive. Furthermore, a thermal equilibrium can only be established for velocities as small as in these tribological experiments, but in many real, hardly defined applications friction heat complicates the situation.

How does temperature modify the friction of coated samples? As seen in chapter 4.3, a temperature change is equivalent to a frequency shift for uncoated rubber on hard substrates. As the coating is only a small layer which consists, like the rubber, at least of partly viscoelastic material, a similar behaviour can be expected on hard substrates, in this case fine steel. This has been investigated for carbon black filled EPDM with a PTFE coating. Just like in the considerations of the friction master curves, a huge variety of curves is recorded (Figure 111) in friction measurements with a set of temperatures. The step size is 15°C from one temperature to the next. Again, horizontal shifting combines these branches to a clearly shaped friction master curve, expanding the velocity range to about 11 decades. The negative slope, already well known from friction measurements at room temperature for almost all PTFE coated systems, is extremely distinctive for temperatures at RT and above. With its excellent thermal conduction steel allows for measurements nearly unaffected of friction heat.
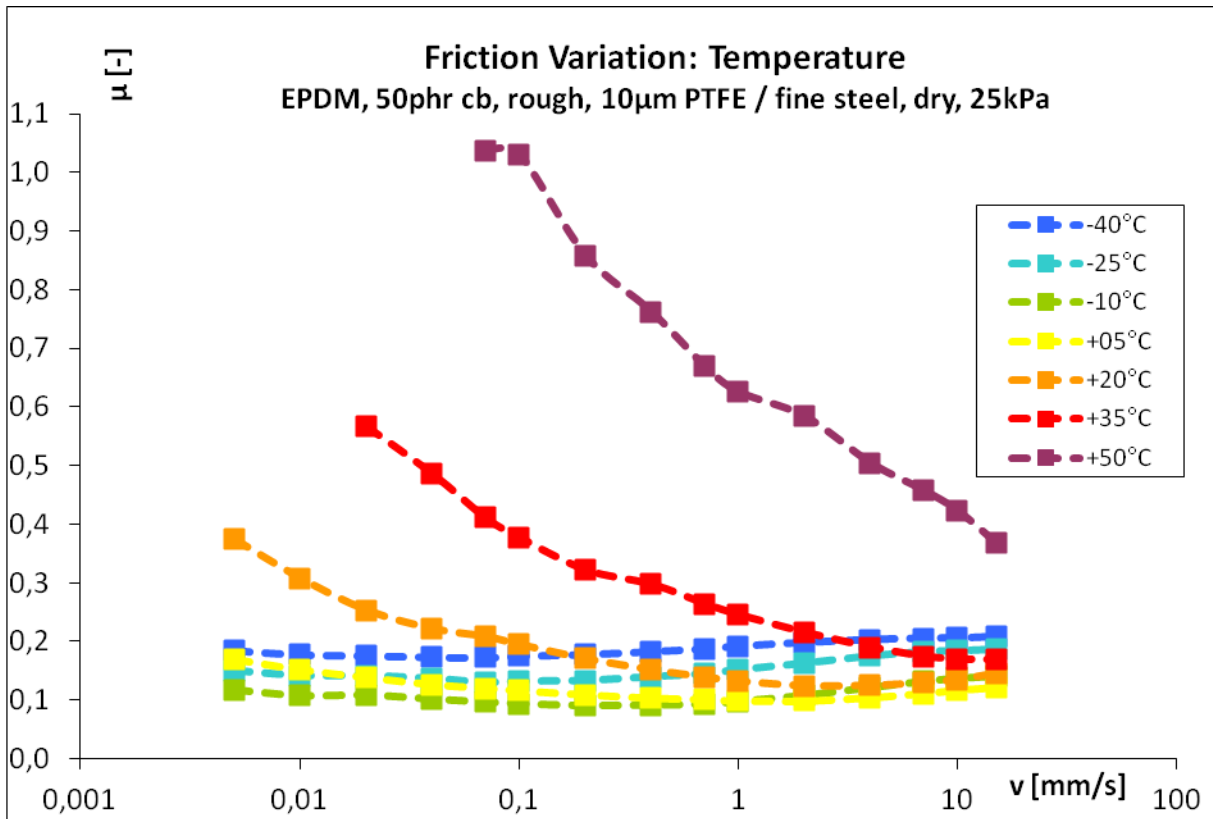
Figure 111: On fine steel the variation of temperature causes friction to split up into distinct temperature branches.
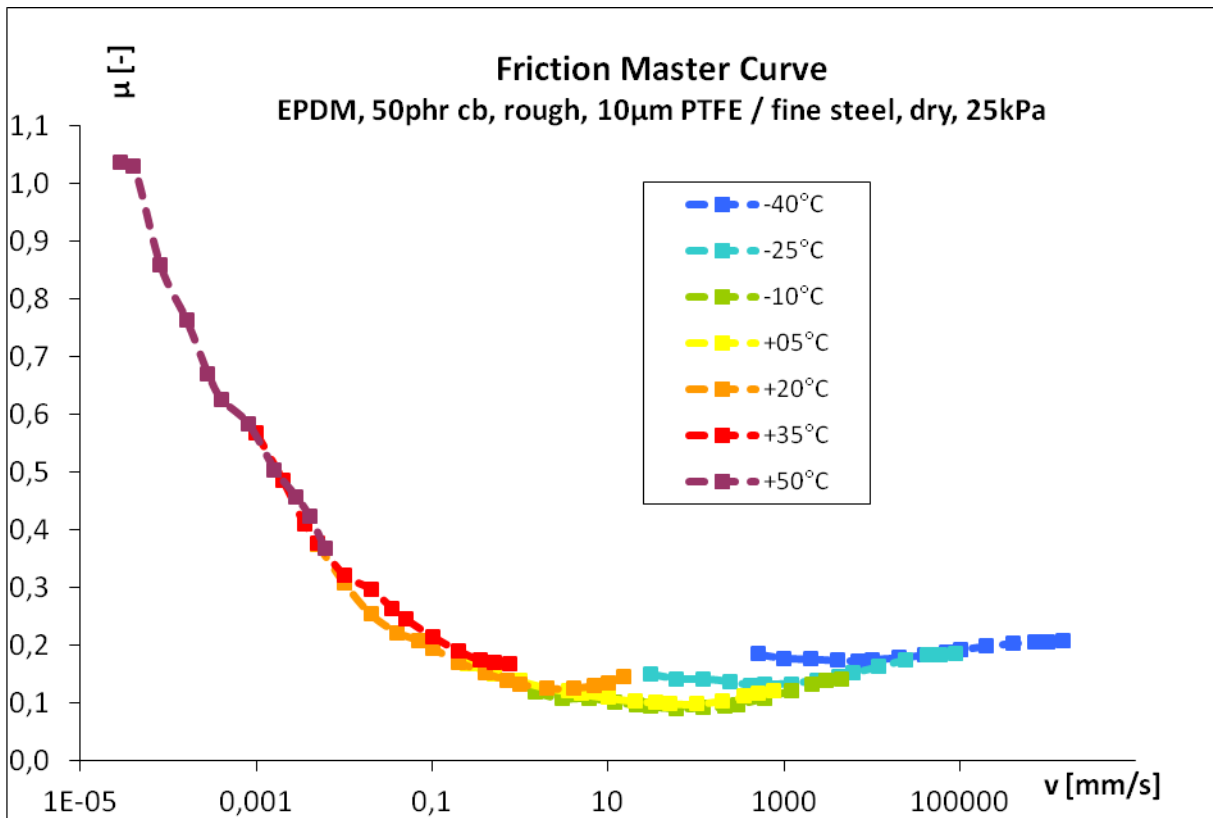

Figure 112: The temperature branches can be shifted into one single friction master curve (20°C fixed).

In chapter 4.3 the exact shift factors were gained directly from the horizontal shift factors of the viscoelastic master curves of DMA measurements. Being a superposition of elastomer bulk and PTFE coating, an exact analytical solution for this sample seems unlikely. Instead the behaviour shall be found empirically by free (i.e. best fit) horizontal shifting. Like before, 20°C is kept unshifted as reference temperature. Figure 113 plots these free shift factors (indigo) for the system just introduced.

The result very roughly resembles the course of the WLF approximations in the viscoelastic master curves of EPDM (black). Indeed the shift factors that are necessary here cover a similar range as the WLF shift factors of pure uncoated EPDM for low temperatures but differ largely above RT and, more important, display a different slope: Unlike the clearly defined course described by the WLF equation (Equation 28) the free factors form an almost linear curve on the logarithmic scale. Obviously the presence of PTFE causes an additional effect to the pure EPDM behaviour and might well appear in dependency on temperature: Probably the cold friction behaviour is dominated mainly by the EPDM bulk whereas PTFE rules the high temperature branches. The high thermal stability and glass transition temperature of PTFE can be supposed to rule this part of the curve. Chapter 4.6.3 will address this question again.
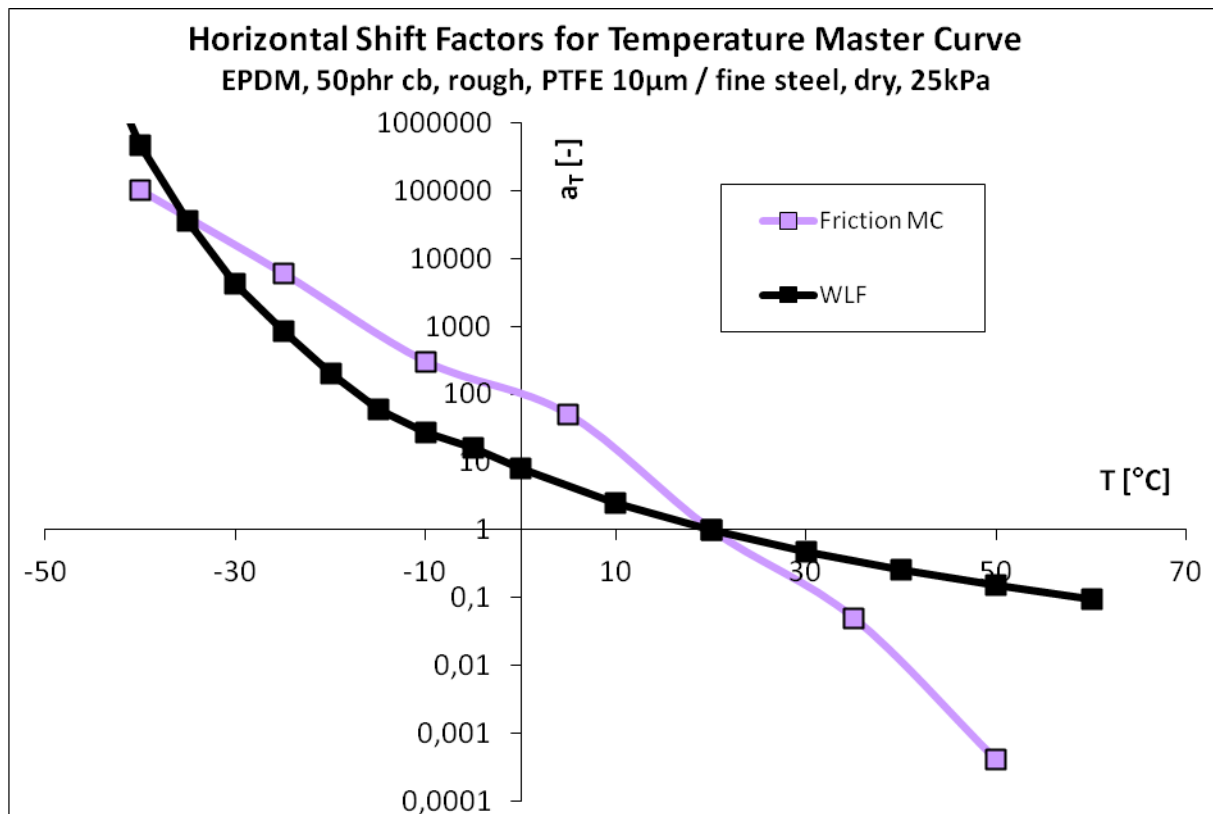

Figure 113: The shift factors of the friction master curve in Figure 112 resume to a plot that matches the WLF shift factors of EPDM only roughly for most temperatures.

As before the results for steel cannot be transferred to coated metal sheets easily. The temperature dependency of the sheet coating interacts with the sample coating and prevents the system from generating friction master curves. This does not mean that the influence of heat and cold leaves friction unchanged: Figure 114 demonstrates how a hot environment will decrease friction and how friction rises drastically when the sample is cooled. The reason for this behaviour is found in the viscoelasticity of the sample: In cold state it becomes rigid and strongly defies deformation, so hysteresis friction naturally rises. The loss of adhesion which normally accompanies the increased hardness of the rubber surface does not come to full effect because its coating rules the contact zone. On the other hand, a warm rubber will deform easily but cannot fill cavities to maximize the true contact area because it is confined by the coating. So the combination of elastomer and coating prevents hysteresis and adhesion from mitigating each other in concerns of friction. The absence of carbon black in this example even amplifies this effect because of the higher G_0/G_∞ ratio compared to filled rubbers.
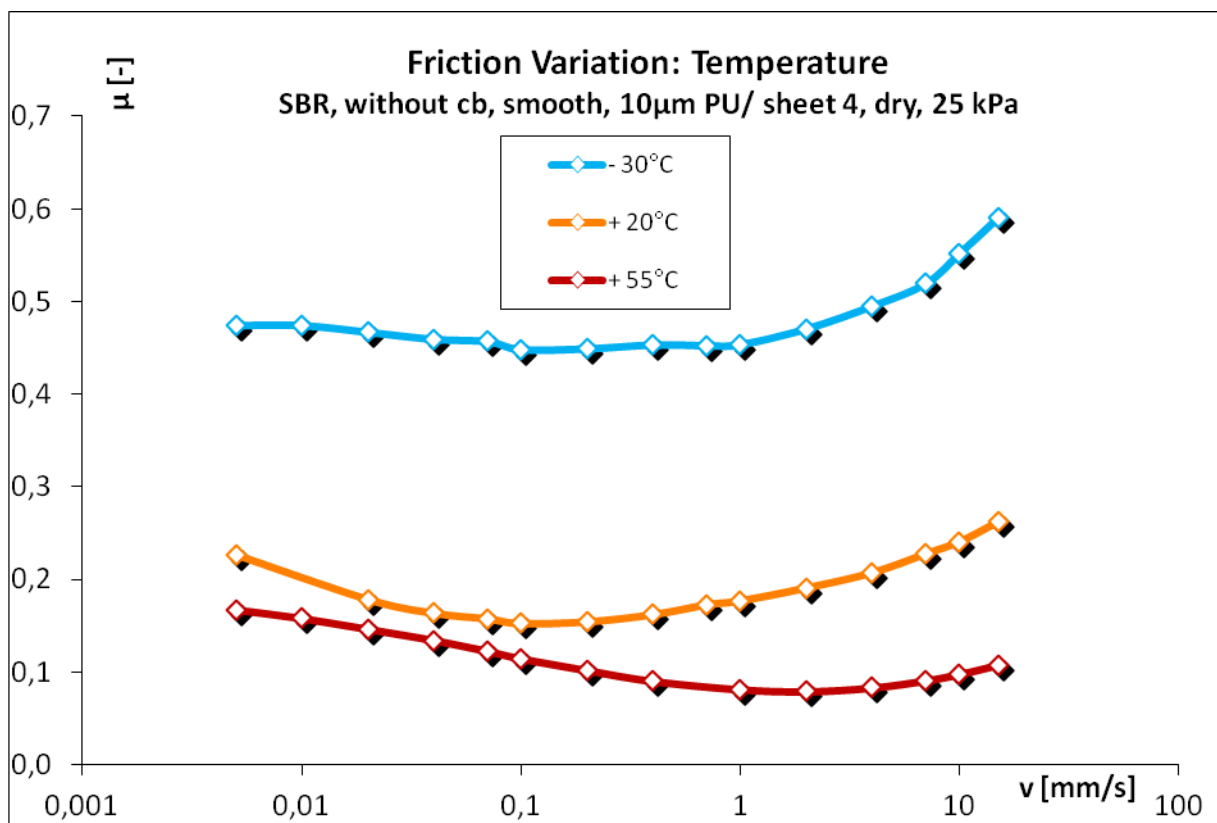

Figure 114: On coated sheets the friction drops with rising temperature, and vice versa. Colours signify temperatures in this plot, not different coatings.

4.5.5 Simulation of the Friction on Smooth Substrates

The friction modelling described in chapter 2.8 has proven successful in simulating friction effects and normally works well in correspondence with real world measurements. The validation of the friction master curves in chapter 4.3 is only one of many examples where it has been applied.

The situation is different for the coated samples. The theory is based on a rigid, fractal substrate in contact with a homogenous, elastic sample with known viscoelastic data. The coated samples in chapter 4.5.3 defy this approach in several ways:

- Two elastic materials, the rubber and the coating, combine as a composite sample
- The viscoelastic properties of a 10 µm thin layer are hardly measureable
- If the coating should not perfectly adhere to the rubber, internal shifts or even ablation may occur
- Even with perfect rubber-coating connection, the coating may act as its own liquid, like the self-lubricating ability of the siloxane
- The coating on the sheets is definitely not rigid and adds one more viscoelastic element to the system
- Glass and the two sheets are even flatter than the sample surface, so asperities on the pure sample or sample coating cannot fill microscopic substrate cavities but rather act as mesoscopic spacers, reducing the true contact area in a so far non-computable way

These constraints do not only limit a simulation of the investigated systems, they also affect the laboratory measurements: Without sample coating the extremely high dry friction can be diminished excellently by using a lubricant, as it is stated in friction theory. For coated samples, however, the wet sliding does not further decrease the already low friction of the dry contact. Due to the changed conditions in surface tension – most obvious for PTFE – the friction may even increase, as seen in Figure 115.

This abnormal behaviour is a significant evidence that a simulation in this case may produce unexpected results. Nevertheless this computational approach shall be put to the test for this special case with the best combinations of fit parameters. To minimize the obstacles, simulations will focus first on fine steel as substrate.
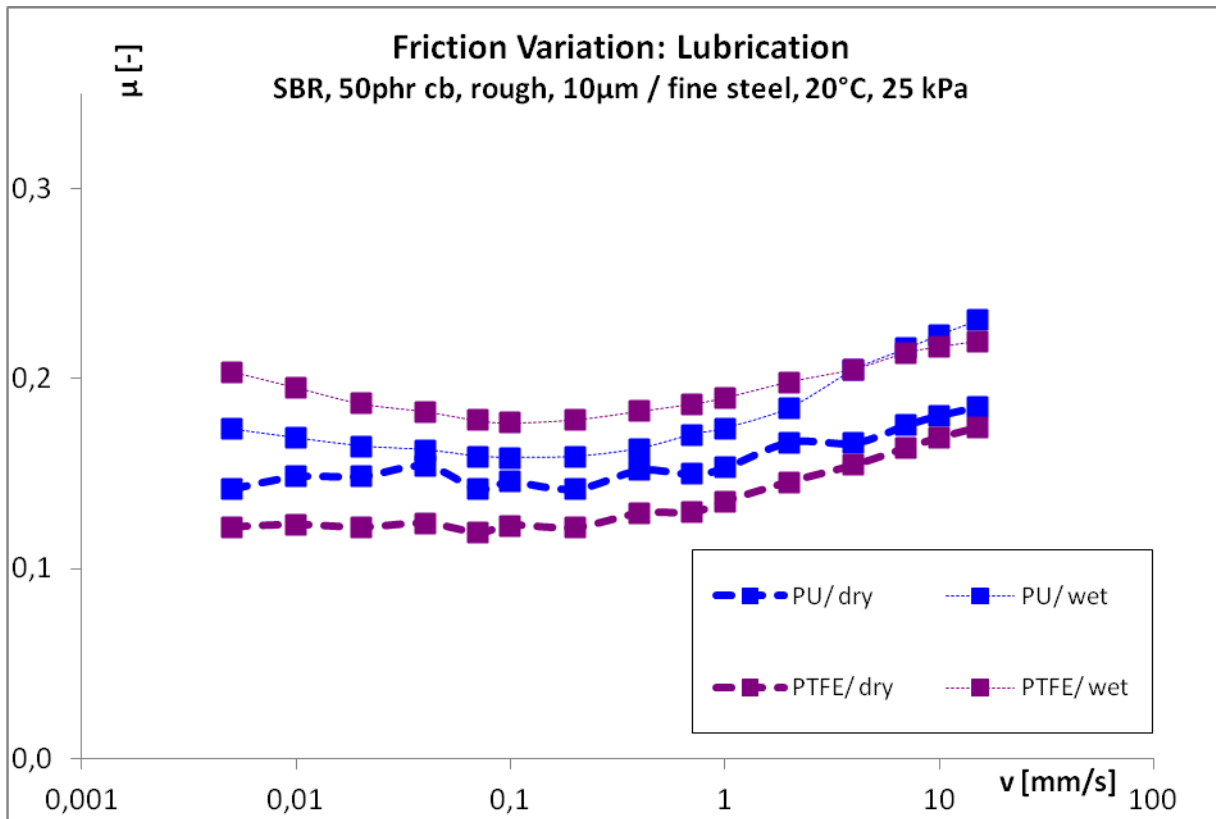
Figure 115: Lubrication does not work classically in a friction system with coated samples.
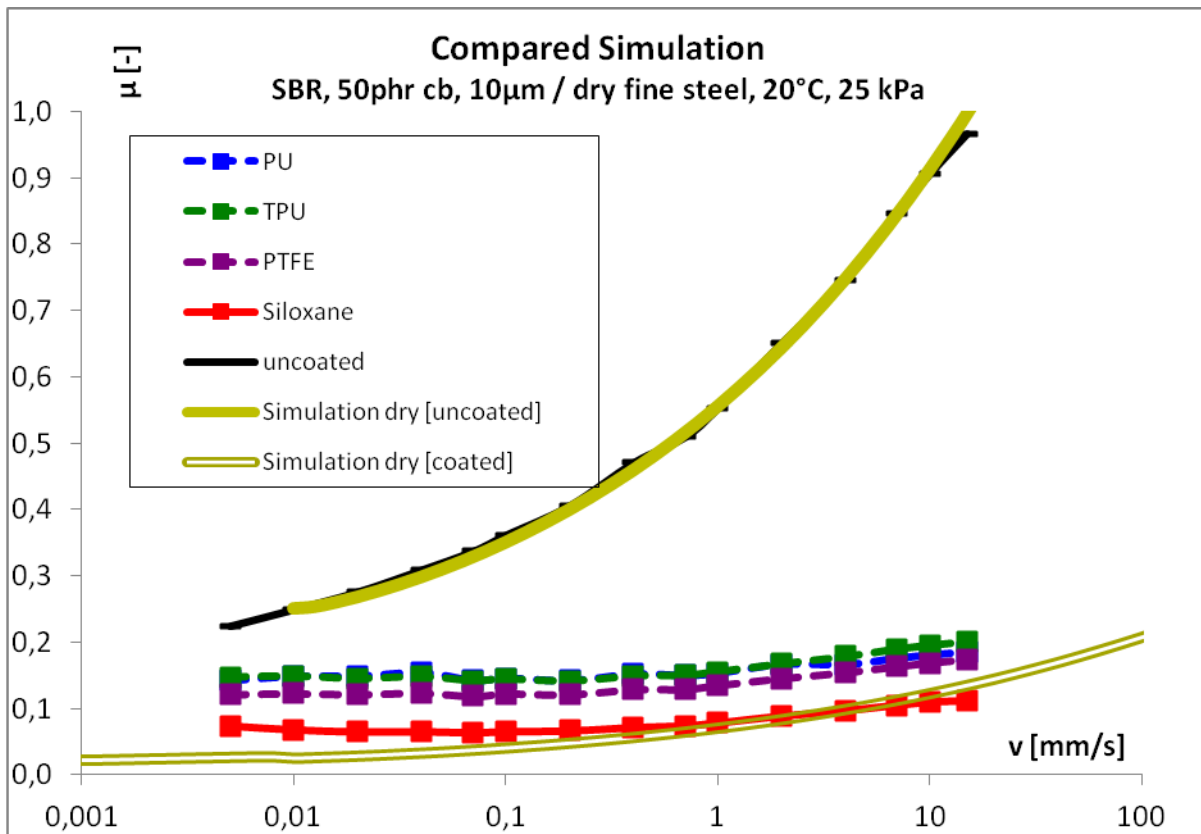

Figure 116: Simulation for uncoated filled SBR matches the experiment perfectly, whereas the much flatter friction curves of coatings fit poorly to the best parameter combination.
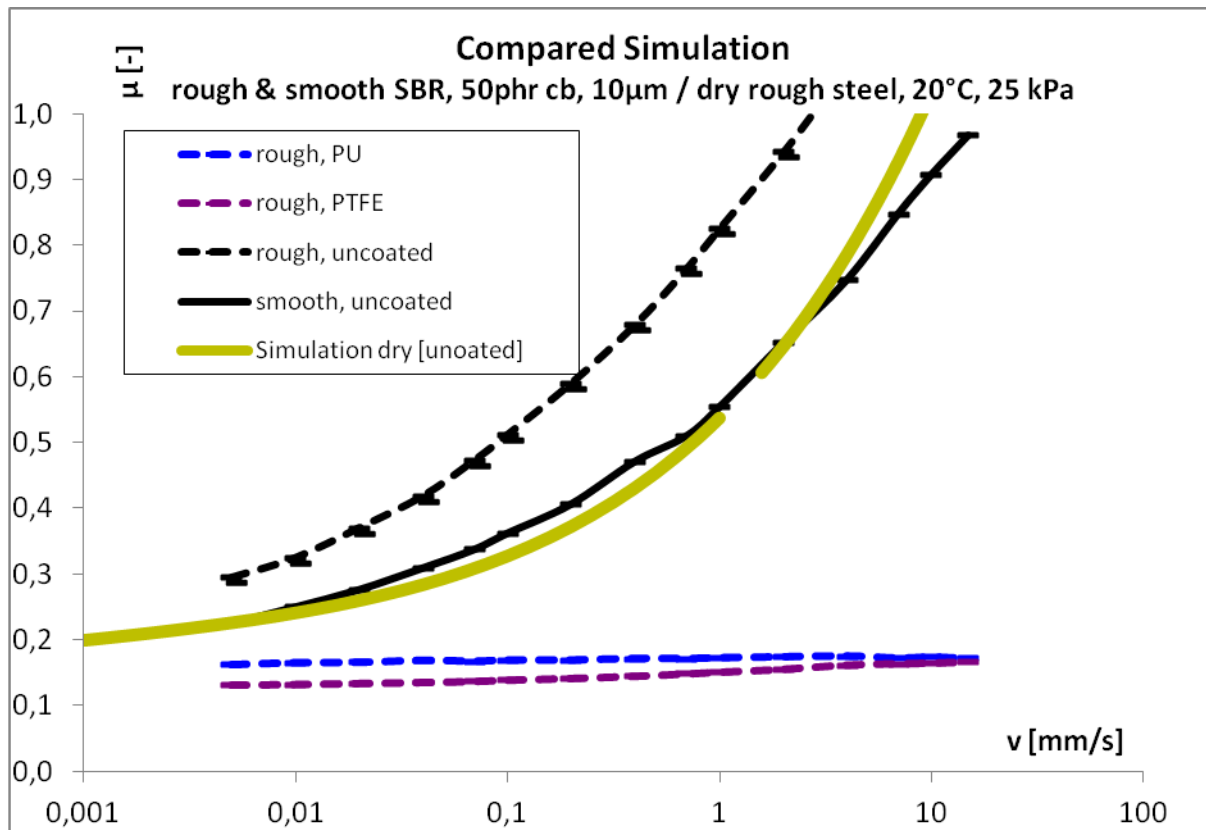
Figure 117: Rough steel is almost as suitable for simulation as fine steel, for a rough sample as well as for smooth rubber. Coating again prevents a good simulation.

Measurements on dry fine steel display an increasingly rising slope within the considered interval of velocity. This slope is reproduced with excellent accuracy by simulation, as Figure 116 shows (olive single line), as long as no coating modifies the effect. Simulations were not able to take coatings or elastomer structure into account directly and thus were fitted as closely as possible to the measurements of the given material, indicated with brackets, e.g. [PTFE]. With coating, the slope is much flatter or even negative for low velocities. As a general rule for the following considerations, a simulation will never match a negative slope in this low velocity range and thus be unable to describe the system in a state susceptible for stick-slip. On the fast sliding part of the diagram, when friction rises softly, the simulation (olive double line) can emulate this tendency but suffers a quantitative mismatch. The same situation occurs on a rough steel substrate (Figure 117): The coating friction slope is far too flat for simulation, while uncoated samples friction behaves quite similarly to simulation, either with smooth, or using a different set of fit parameters, with rough rubber surface.

On coated sheets dry friction is too high and irregular for uncoated samples, but wet sliding is possible to be measured at least for lower velocities. Figure 118 shows this strongly rising part of the curve with an adequate simulation (thin olive line). Obviously modeling is not out of question on such an exceptional substrate as long as its friction behaves comparable to

that on a hard substrate. As before a "normal" behaviour is not typically for coated samples, i.e. a positive slope often appears only for fast velocities, and even then a simulation (thick olive line) is at best mediocre and works for this part only. This might result from the extreme substrate flatness compared to the moderately rough sample substrate, or the softness of the substrate.
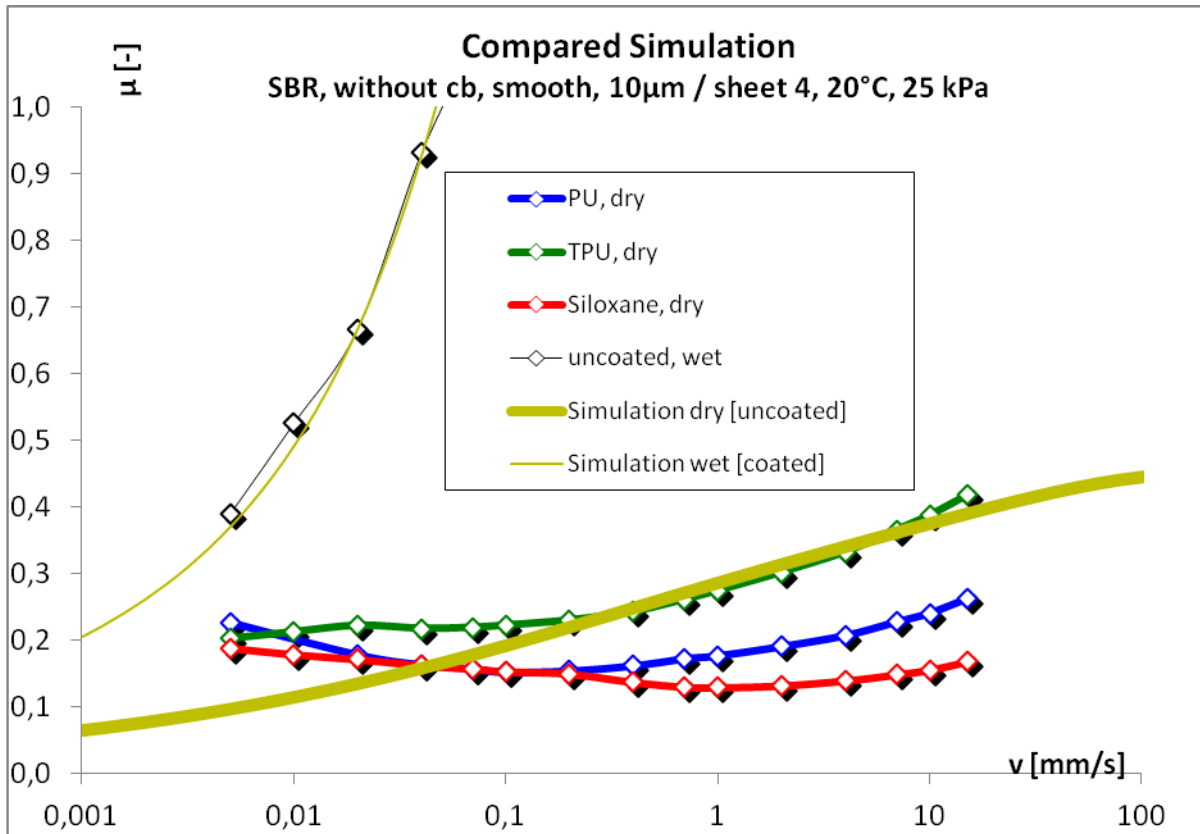
Figure 118: Simulated hysteresis on wet coated sheet is accurate for the rising slope of the curve. Higher frictions (beyond the scale) are too irregular to be simulated. Simulating dry coated samples (unfilled SBR) works moderately well for high velocities.

If the difficulties in computations for coated rubber are caused by the contact of two different coatings in combination with the elastomer bulk, the situation should be easier on a substrate of comparable smoothness without coating: glass. In fact, simulating the same coating-rubber samples on glass (Figure 119) provides a better base for fitting the simulation to the measurement – a clear hint that substrate flatness is less disturbing than softness. PU coating is obviously more suitable for this than TPU, mainly because of its bend at 2 mm/s.
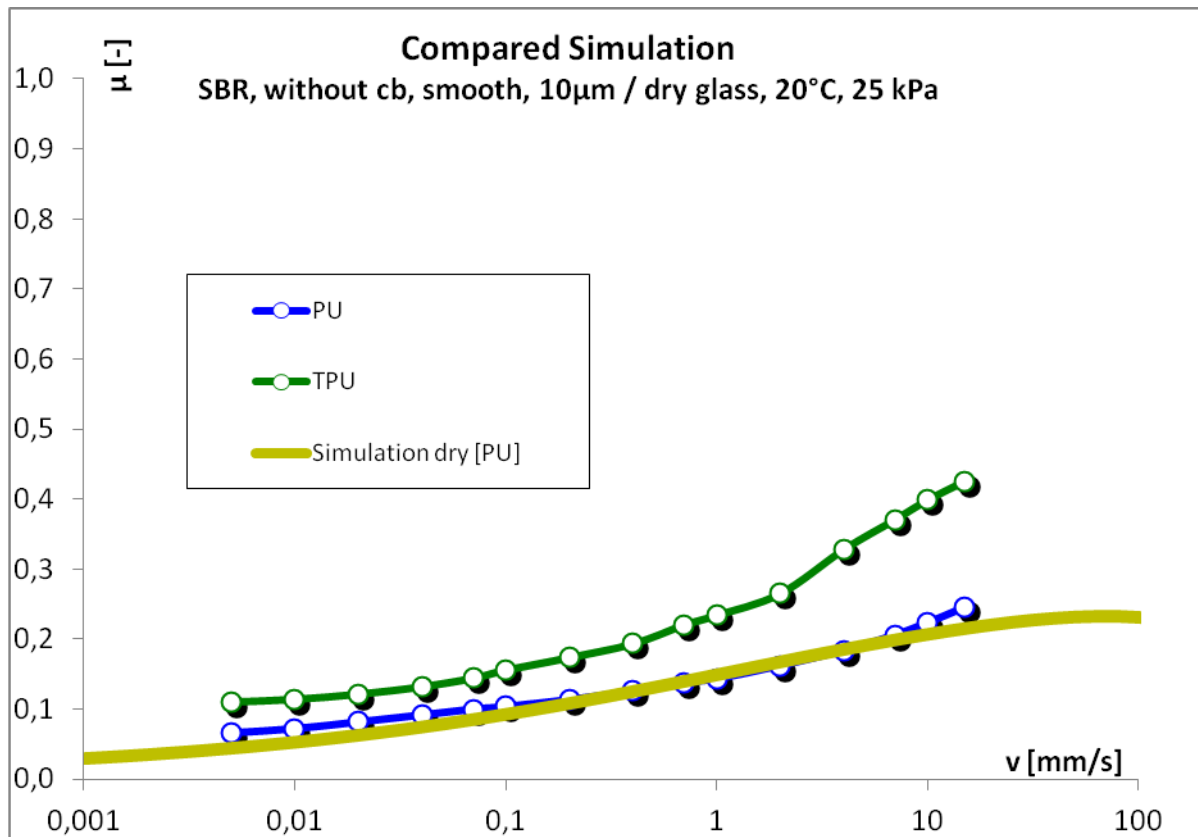
Figure 119: On glass a simulation of the same rubber becomes possible at least for PU.
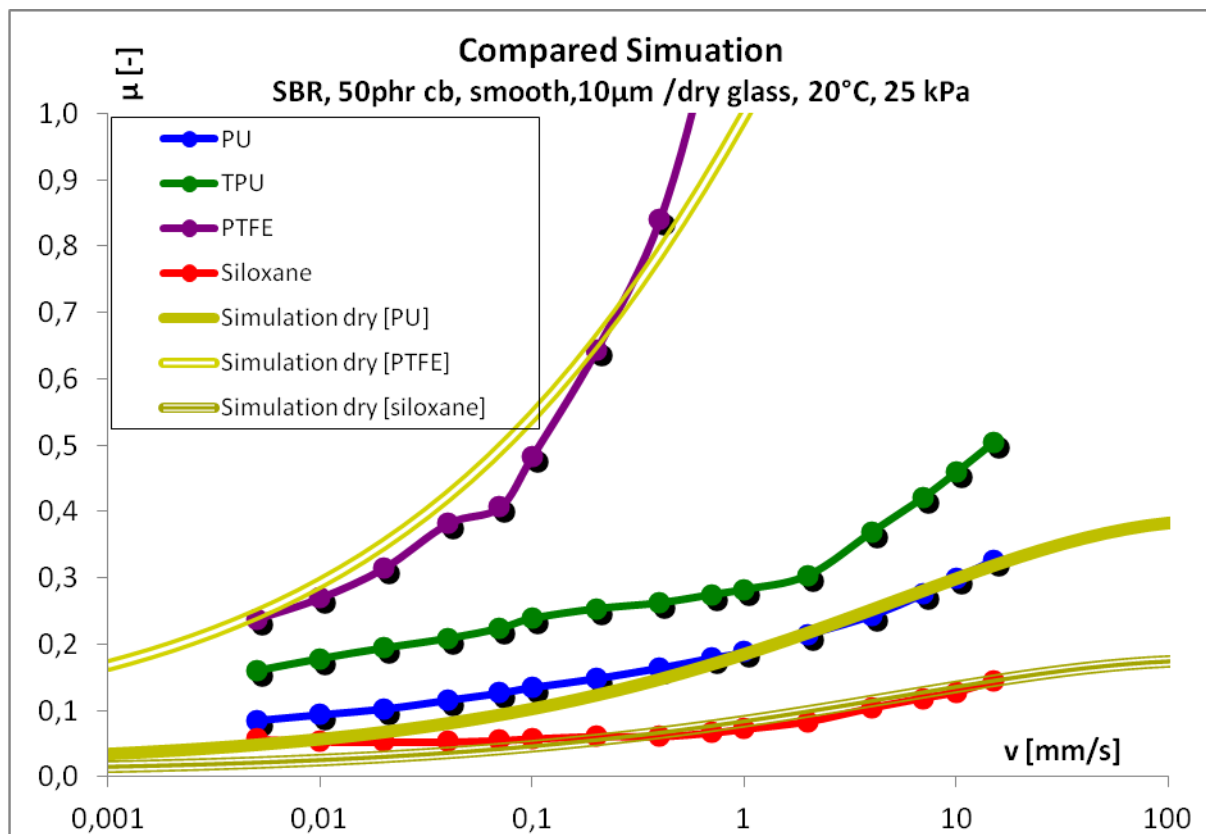
Figure 120: The same system as in Figure 119 but filled with cb displays a much better ability to be simulated (with varying sets of fit parameters) for most coatings.
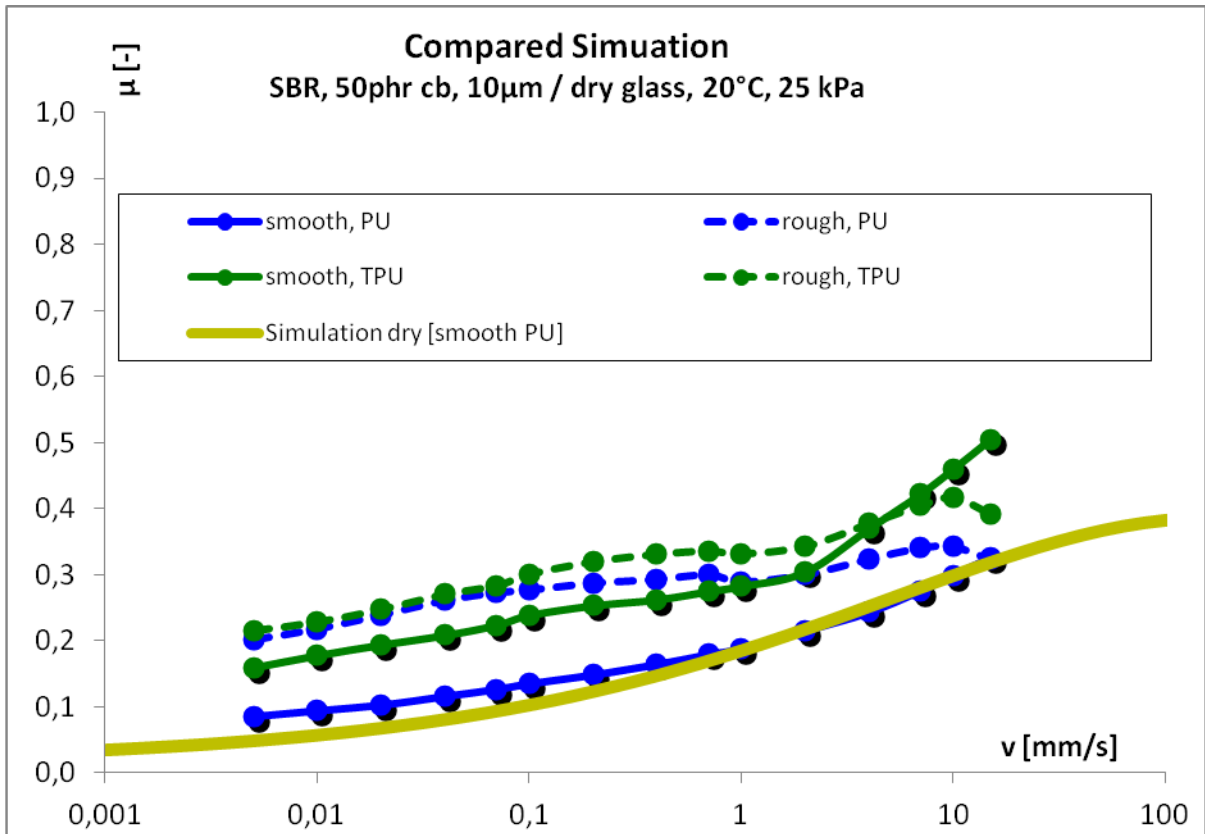
Figure 121: Sticking with the same system, the simulation describes the smooth coated samples better than the rough.
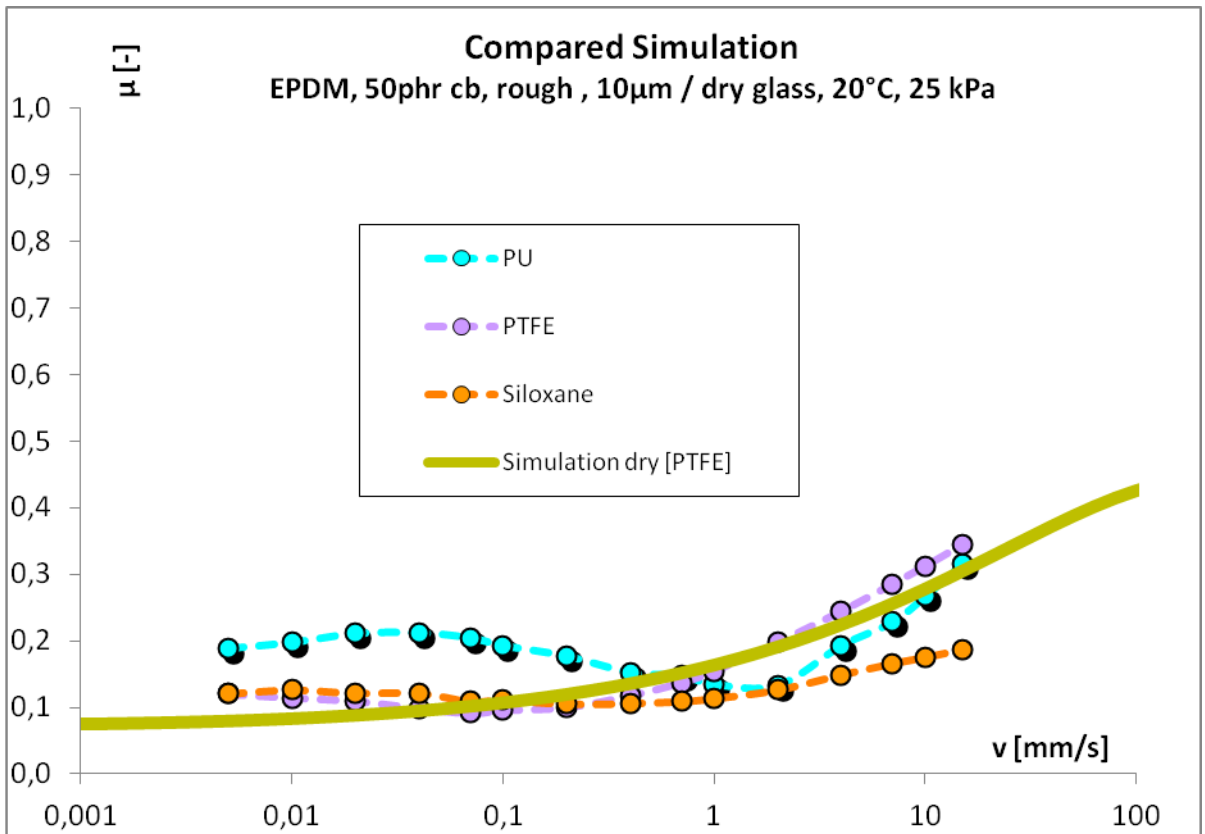
Figure 122: Switching from filled SBR to EPDM produces similar results with respect to simulations.

This feature remains also valid for cb filled rubber under otherwise same circumstances. Fillers should pronounce the influence of the rubber bulk, manifested in a quantitative change of friction. Qualitatively nothing changes with filler (Figure 120): TPU, with a pronounced bend, is hard to simulate, but PU (blue versus olive single line) is at least close, and this holds for siloxane (red and olive triple line), too. Even the PTFE measurement, considered as doubtable for its unusual strong increase, can roughly be emulated (olive double line) with a lower v_c and, of course, a higher τ_0. Simulation on smooth glass for coated smooth samples seems to be a minor problem compared to other systems with coated elastomers.

The same system (filled SBR on dry glass, Figure 121) demonstrates the meaning of sample surface structure for simulations: Modeling assumes the roughness to be higher on substrates than on rubbers. On glass this assumption is reversed, and even more so for samples treated with rough vulcanization plates. In the experiment the difference in this case is simply a rise in friction and a flattening on the high speed part, but this is enough to prevent valid simulations almost completely for rough samples, for both PU and TPU.

All simulations for SBR, just like the attached experimental curves, are part of the velocity range of monotonously rising friction – negative slopes and stick-slip at low velocities can be neglected from this point of view as not representing the "pure" elastomer behaviour. EPDM on the other hand is expected to reach its maximal friction at a significantly higher peak velocity v_p. This presumption is confirmed by these simulations, the peak being even more beyond the largest measured sliding velocity: larger than 100 mm/s for any of the simulated SBR systems, and about 1000 mm/s for most EPDM systems. The resulting effect on the slope might make a difference for friction. Comparing the same system as before with an EPDM rubber (Figure 122) reveals that simulation basically faces the same challenges than with SBR: a general similarity for rising experimental friction slopes, but deficiencies for flat or negative slopes. Only the PTFE coating simulation is fully acceptable in the comparison to the experiment. This is even more true on coated sheet, where simulating PTFE delivers poor results and all other coatings cannot be represented properly by simulation – another similarity between SBR and EPDM.

4.6 Stick-Slip and Instabilities

The previous chapters assume stable sliding conditions, so the friction coefficient can be established a measured definitely during the periods of stationary velocity. In practice, this is often not given, and the resulting instabilities of friction are subject of the following analysis. Two mechanisms must be discriminated: Irregularities in friction force that are caused by a change in material properties of the sliding partners (usually the elastomer surface), and situations that prevent the continuity of the sliding process by dynamic effects.

4.6.1 Layer Stability and Start Peaks

When friction appears, surfaces are always subject to wear and abrasion. The lowered friction of coatings on smooth samples can minimize this effect, but not completely avoid it. The reliability of coating layers must be checked to guarantee meaningful experimental results and enduring usage of coated rubber parts. But a look on the mechanical response of the coating can also give interesting hints on the physics of friction.

The first coating batches turned out to be too sensible for mechanical forces: Especially PTFE wore off easily and was furthermore not adhesive enough to the sample in wet environments, but other coatings sometimes caused similar problems like blistering (siloxane) and shrinking (PU), smooth samples being more affected than rough ones. This all was more a case of lacking adhesion to the sample than of lacking cohesion within the layer and thus affected thick layers more than thin ones. Aging and maturing effects could increase these problems.

Treating the rubber sample with gas phase fluorination caused a sufficient adhesion between coating and sample without significant effect on friction, but two questions about stability remain: How does the microscopic change of the coating surface (because of possible wear particles and self lubrication) affect friction, and how soon can a stable friction plateau be established anyway?

Nearly all experiments confirm that the samples exhibit a continuously changing friction to a measurable extent during their experimental exposure. In order to document this variation quantitatively, a long time measurement was performed with constant velocity (1 mm/s) for siloxane on coated sheet. For 72 double cycles (forward–backward) the sample was slid over 40 mm each. Unlike normal measurements, the interface was never cleaned during the 50 minutes this data acquisition took.
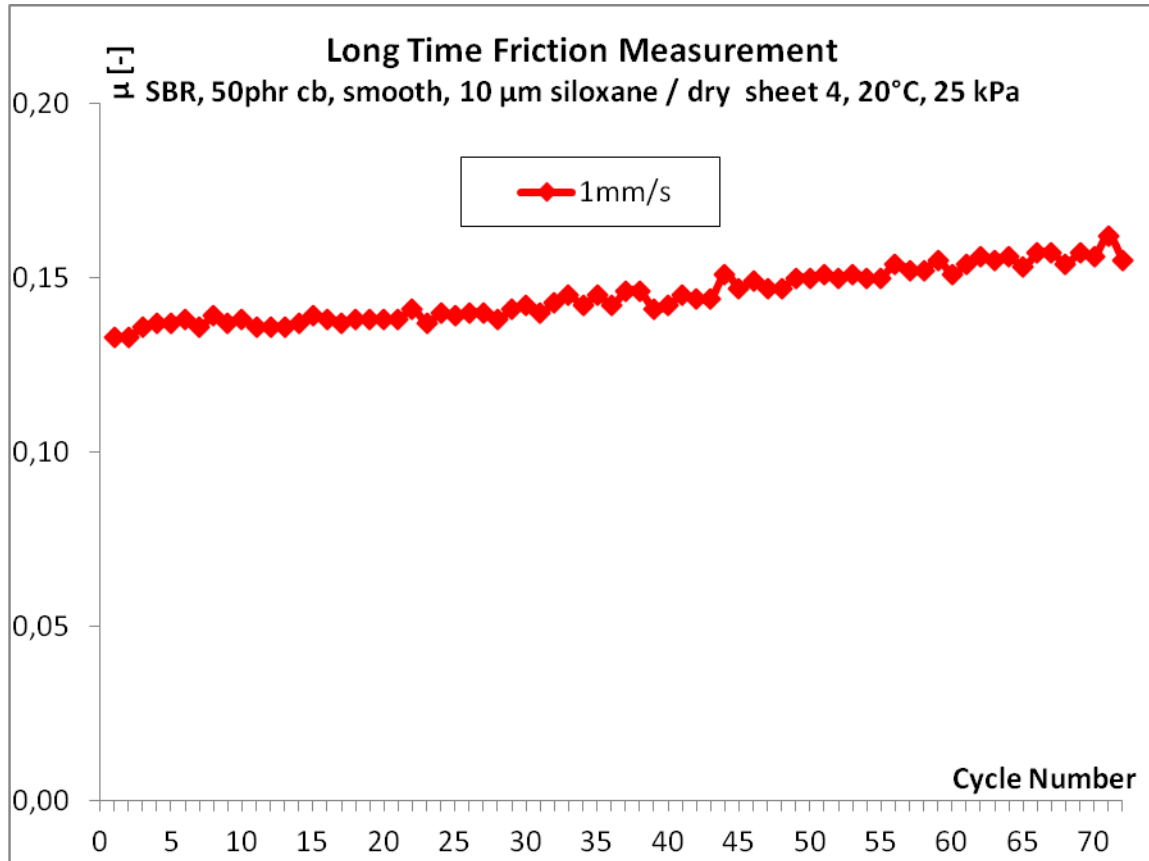
Figure 123: In long time measurement, friction stays stable for a while, then rises softly.
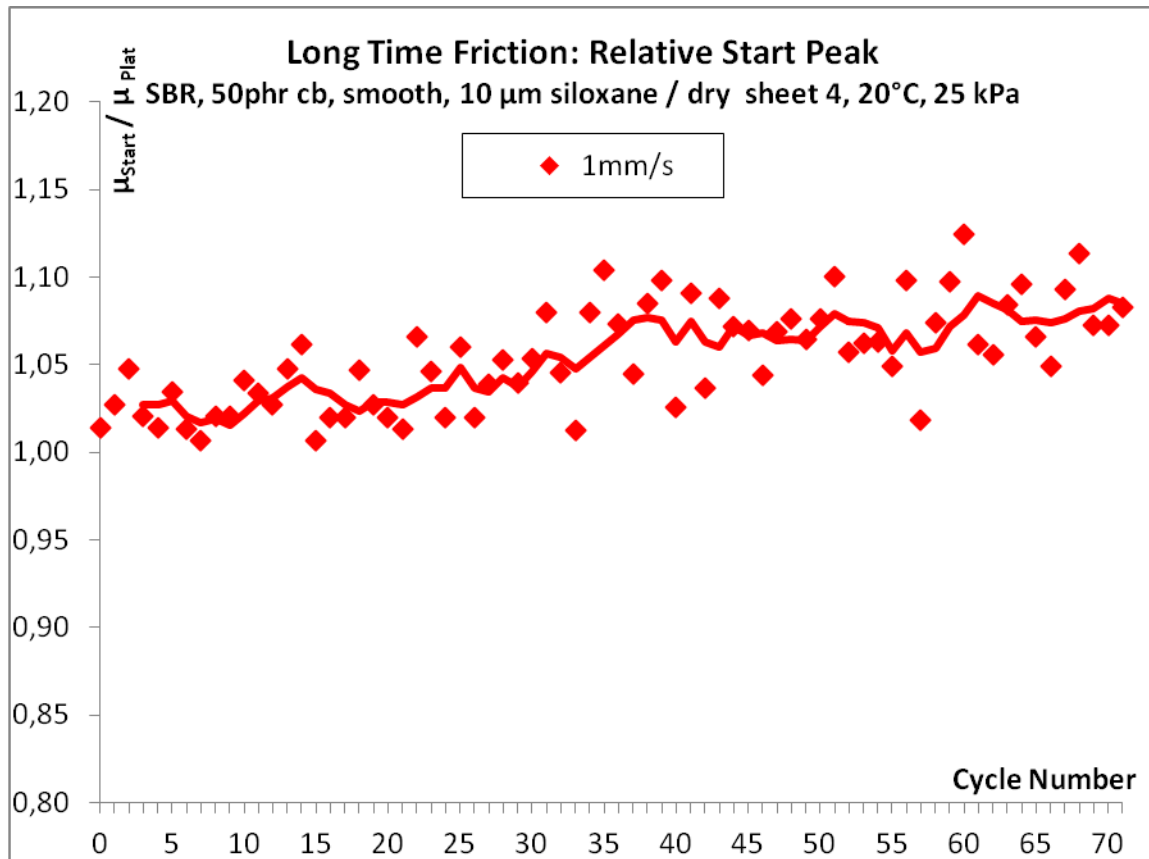

Figure 124: The relative start peaks of the same long time measurement, with a smoothed trend line

The trend of friction during the measurement is depicted in Figure 123. In the beginning, after a short running-in (for 2 cycles, compare to Figure 44), friction stays constant at $\mu \approx 0.137$ with small fluctuations ($\pm 0.7\%$) over the next 20 cycles. Until the end of measurement, friction rises more or less linearly about 13%. This result can be regarded as a proof that friction data are valid for a limited experimental time – a normal measurement consisting of fewer cycles than here, with mainly lower and thus less wearing velocities and cleaning whenever necessary – but inconsistencies do appear on the long term and must be taken into account then.

No stick-slip appeared during this experiment. However, another effect that distinguishes the "pure" friction plateau from not evaluated artefacts happens quite regularly: the start peak. It can be seen easily in the exemplary friction evaluations of Figure 32 and Figure 130. What causes start peaks is the transition from the high static friction to comparably low sliding friction. This temporary friction peak usually lasts only for a very short time, rarely more than a few acquired data points. It should largely depend on the surface tensions of the involved surface layers, and appear preferably on smooth substrates. As a static surface interaction it should not depend on the bulk features. In contrast to stationary friction, during the start phase there is no equilibrium between microscopic adhesive deformation and relaxation [67].

During acceleration, the friction coefficient drops almost instantaneously from its static peak value down to its dynamic value. The start peaks of several systems have been evaluated and related to the friction values of the plateaus. Because the plateau frictions differ for each velocity, it is not useful to compare the absolute differences of peak level and plateau level. Instead the relative start peak intensity as ratio of peak and plateau is given here. Figure 124 displays the development of this ratio during the long term measurement of the experiment described above. The averaged curve behaves very similar to the friction itself in Figure 123: Staying in a constant range for about 20 cycles and then rising slowly. This is of course even more pronounced in the absolute plot (not given here). The values become more scattered, too, with rising cycle number, possibly linked to increasing inhomogeneities on the interface.
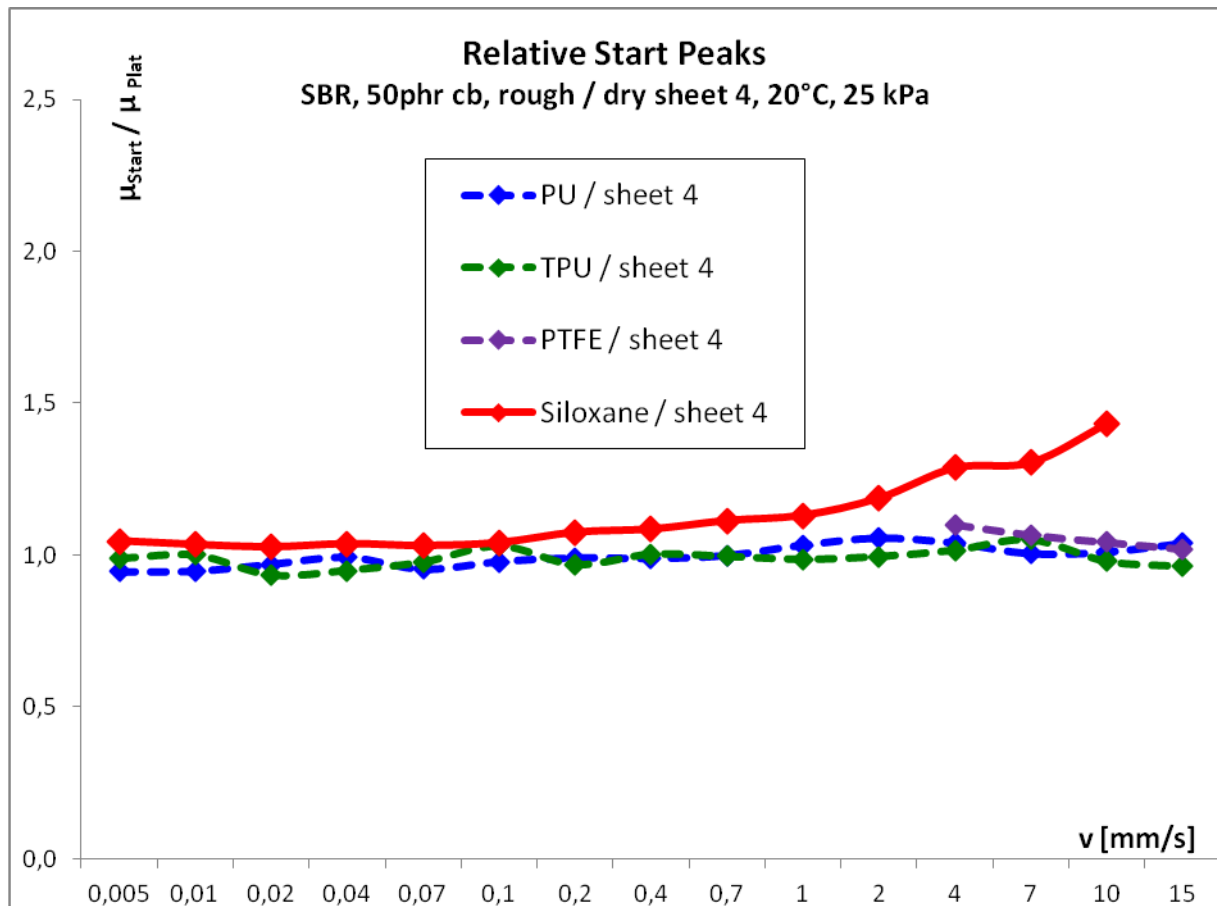
Figure 125: The relative start peaks for coated sheet 4 depend on velocity for siloxane, but are negligible for other sample coatings.

Reflecting the transition from static to dynamic surface interaction raises the question if the start peak is a function of sliding velocity. Figure 125 gives an answer: the faster the sliding, the higher the start peak in relation to the following stationary friction – at least for the system discussed up to here. All other coating types develop almost no start peaks on coated sheet 4. The data for PTFE are only partly evaluable because of extreme stick-slip. This behaviour, however, cannot be generalized: On sheet 3 (Figure 126) the start peak relation is clearly above 1 for all coatings and even reaches remarkably high values for some cases. A tendency for small peaks at slow sliding and large peaks at fast sliding is obvious, just like the extreme fluctuations at high velocities. PTFE behaves definitely more moderate than PU and TPU. Having comparable geometric surface descriptors to sheet 4, the differing behaviour of sheet 3 is caused by its surface tension and thus chemical composition.
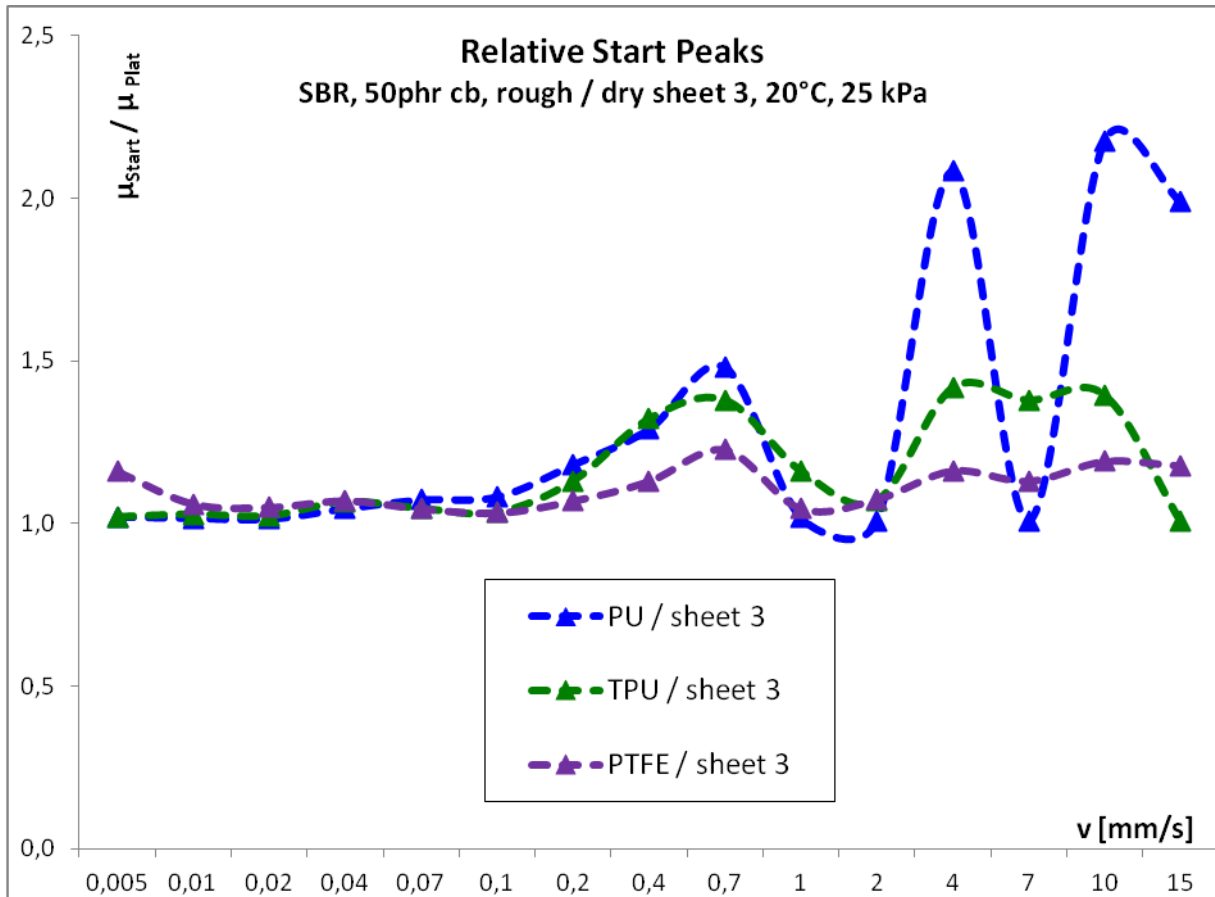
Figure 126: On sheet 3, start peaks appear, becoming stronger and more irregular for high velocities.

The roughness of the glass substrate is a bit lower than of the coated sheets. Its surface tension is clearly different. As a result (Figure 127) the start peaks are not as pronounced on glass, and the effect on each sample coating is different, too: TPU displays negligible start peaks, whereas PU and especially PTFE are prone to irregular start peaks at high velocities. The next chapter will also discuss if the start peaks are related to stick-slip effects.

Fine steel, on the other hand, is too rough to establish any start peaks for whatever coating type in this system, as Figure 128 shows.

Figure 127: On glass, coatings are more prone to start peaks than on metal sheets.

Figure 128: Start peaks are non-existent on steel.

4.6.2 Definition and Evaluation of Stick-Slip

Real sliding systems have neither perfect nor static conditions. This results in fluctuations of the involved parameters. Perturbations limit the stability of the process at least on the microscopic level but may grow under self excited vibrations to disturbing amplitudes.

Definition and Properties of Stick-Slip

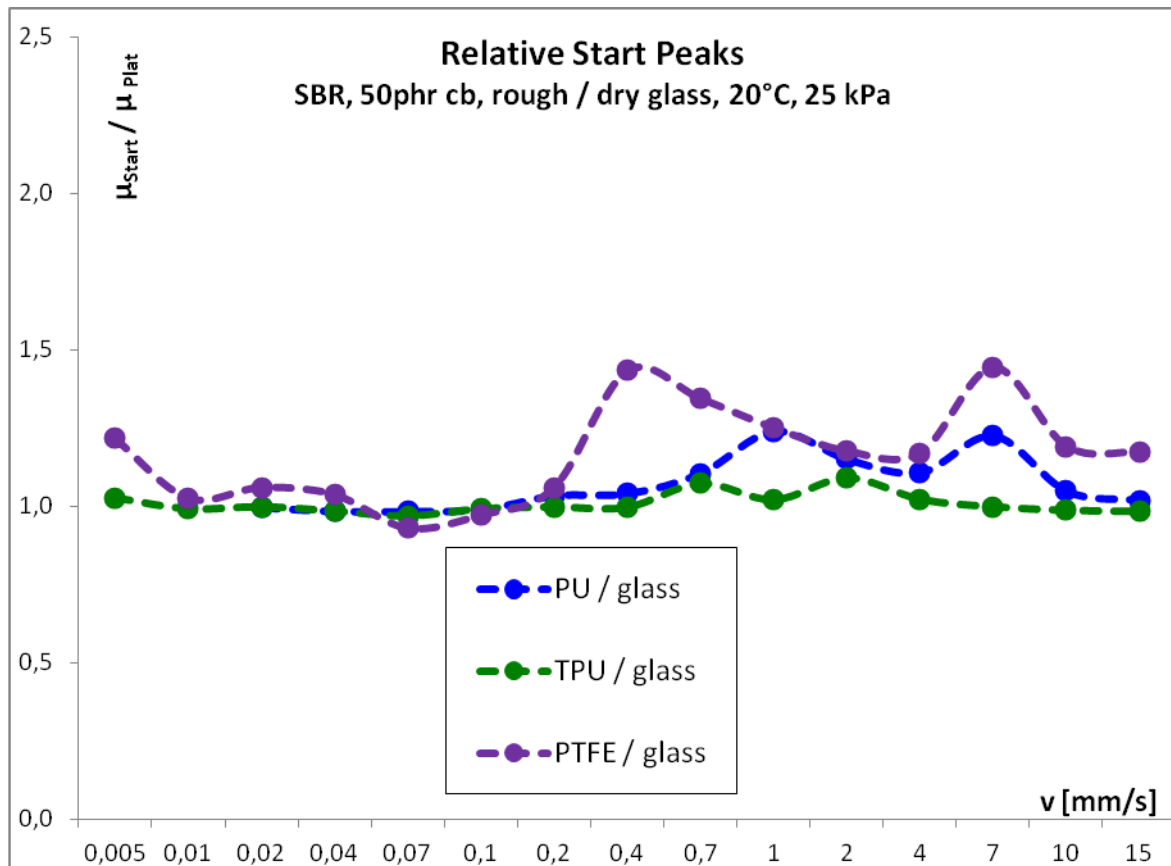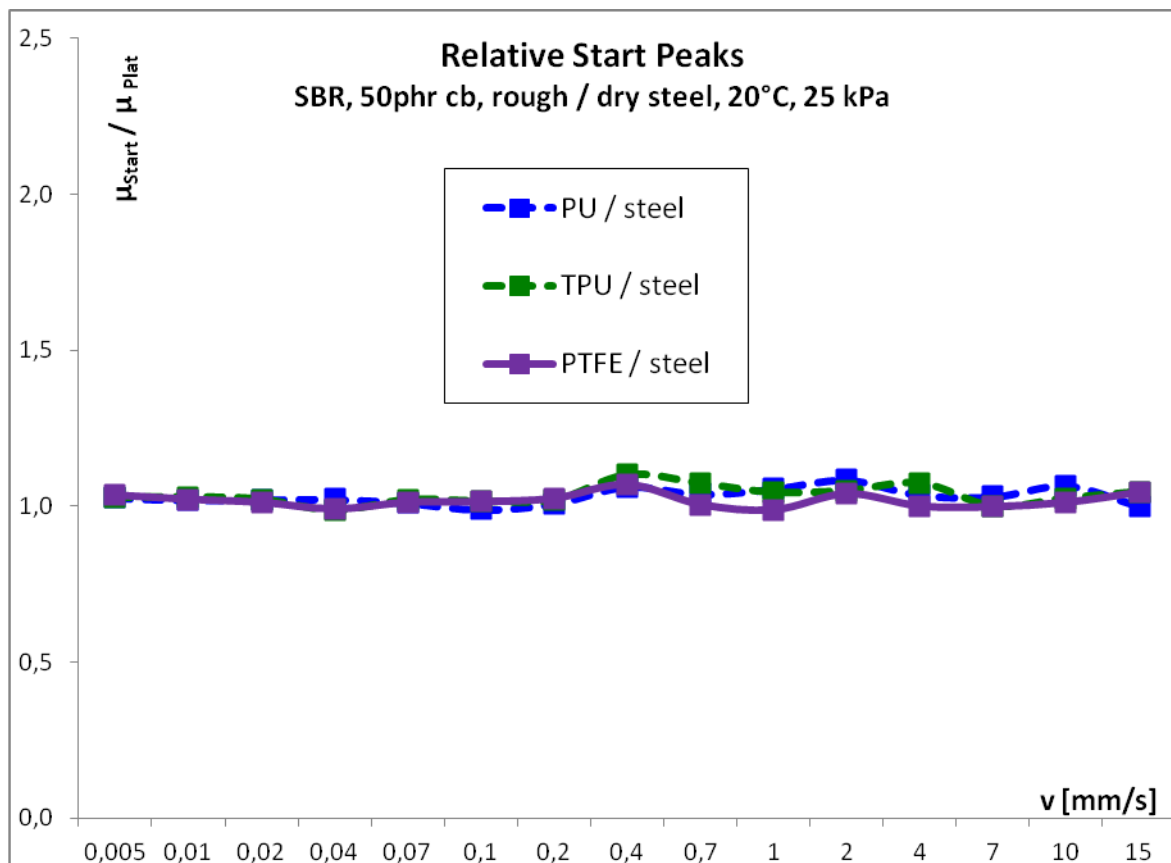Whenever two sliding partners – in this case rubber and substrate – develop a periodic change in the relative surface velocity although the rubber bulk moves at constant velocity, this is called the *stick-slip effect* (SSE). This periodicity can be split up into four phases:

1. The sample surface *sticks* to the substrate without relative movement, just like it would during static friction.

2. The movement of the elastomer bulk against the still static interface leads to a shear *deformation* of the sample. Friction remains static.

3. When the deformation becomes too much (i.e. the shear force exceeds the static friction force), the sample *detaches* (at least locally) from the substrate and follows the bulk movement – it slips. During this phase, dynamic friction occurs.

4. The normal force has remained constant and causes the sample to come into *contact* again with the substrate. When the shear force of the now relaxed rubber becomes smaller than the dynamic friction force, the sample sticks again.

Figure 129: Schematic diagram of a stick-slip cycle – sticking, deformation, detachment, re-contact

Figure 129 sketches the phases of one cycle. As a periodic mechanical oscillation, the stick-slip causes acoustic excitation in the involved materials and those in contact to it (sample, substrate, air, attached objects…) which is known as chattering, rattling, creaking, groan or squeaking, according to its frequency. This noise is most often unwanted and annoying (wheels on railway, wiper blades, hinges, chalk…), but can be desired for purposely created sounds like a vibrating string of a violin in stick-slip contact with the bow. In any case, this periodic vibration must not be confused with chaotic instabilities without cyclic steps, which would only produce white noise. Another side effect of stick-slip is an increased and often inhomogeneous abrasion including cracks and pattern building. The leading edge of a block is especially vulnerable [68].

From this point of view, stick-slip is a periodic change between static and dynamic friction. A prerequisite for samples to keep sticking instead of sliding steadily is a dynamic friction coefficient that exceeds the static friction coefficient in contrast to the normal case when the higher static friction causes a start peak before stationary sliding friction begins. Generally speaking, the appearance of stick-slip is linked to a friction coefficient that is not increasing but decreasing with rising velocity, so a negative slope in the Stribeck curve is a signal for instability. The stick-slip will vanish when velocity exceeds a critical value $v_s = v(\mu_{min})$, the stability velocity at the friction minimum.

The existence and aspects of stick-slip basically depend on the same parameters as the friction itself – viscoelasticity, surface structure, pressure [69], temperature, velocity… but with different results. Additionally, damping properties and the mass inertia of the sliding partners including the attached construction parts (the frame) play a major role for stability. The normal force is assumed to stay constant. If this is not fulfilled, due to a construction where normal force and sliding movement are not perpendicular, or because the amplitude of the stick-slip is large enough to harass the force mechanism, another effect called *sprag-slip* must be considered [2]. The presence of lubricant prevents stick-slip in most cases, as sliding friction is largely reduced by it whereas the lubricant is squeezed out of the interface during static friction. Furthermore, many systems show stick-slip only when the rubber stiffness falls below a critical value.

It is important to consider the influence of the system frame: the moveable parts attached to the rubber. In the case of the tribometer (chapter 3.5.1) there is only one degree of freedom (the lever); the universal testing machine (chapter 3.5.2) features two degrees (horizontally perpendicular to the sliding direction, and vertical). Minor vibrational potentials from device walls etc. may add to this. The physical resonance conditions employ a characteristic frequency (or a spectrum of several frequencies) for the frame of each single machine or other system. The parameters described above determine if and how strong stick-slip will appear, but its main frequencies depend on the frame. The tribometer in particular displayed quite regularly a resonance at 2 mm/s even on samples that were not prone to stick-slip. It is hence indispensable to evaluate stability of measurements performed always on the very same device in order to compare the results. The following findings all refer to the tribometer.

Evaluation, Characterization and Classification

Not all velocities display stick-slip behaviour, even if all other parameters stay the same. Normally the plateaus of stationary friction turn out to be easily discriminable between stable and unstable friction response. The friction plot as explained in Figure 32 becomes modified

like in Figure 130: Whenever stick-slip appears, the plateaus of the plots consist of wide bands as the amplitude of each SSE cycle is larger than normal fluctuations in friction. Zooming in, the fine structure becomes visible: a cyclic change between a flank rising over a long, reproducible time interval followed by an instantly falling flank. They can be associated with the phases of *deformation* (static friction) and *detachment* (dynamic friction).
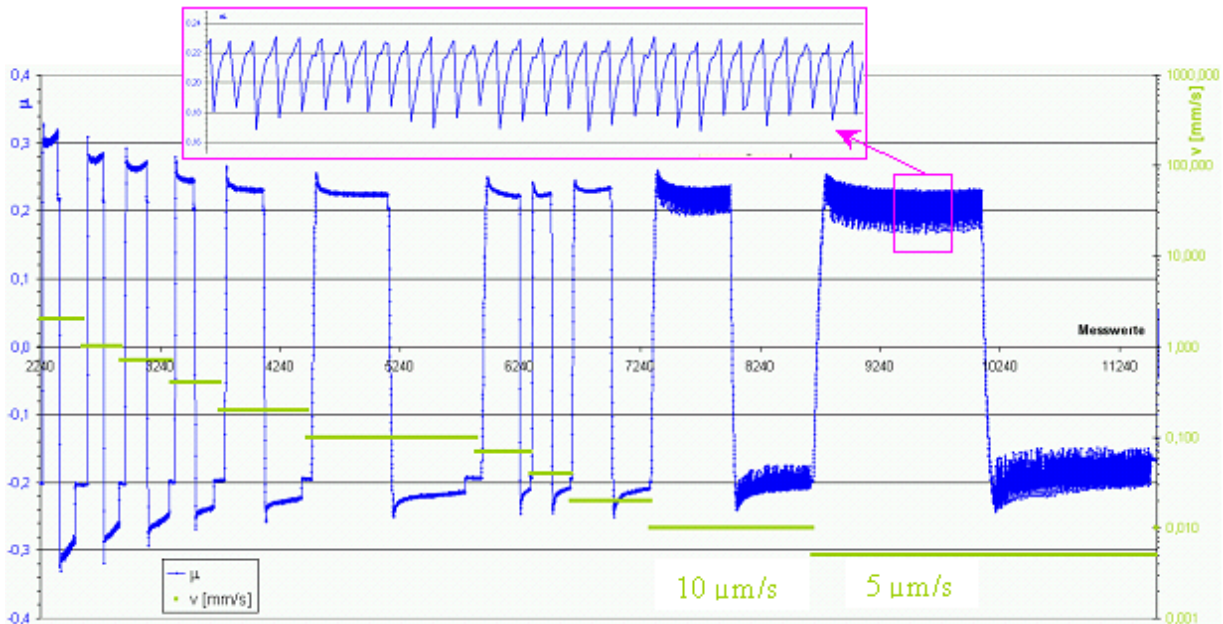

Figure 130: Friction plot with partial stick-slip at 5µm/s and 10µm/s. The zoom reveals the fine structure with slowly rising and fast falling flanks.

With appropriately adapted software, the minima and maxima of the cycles can be detected and evaluated automatically for statistical reasons. Care must be taken to capture all involved cycles and to avoid false positives. Evaluated characteristics are

- the average amplitude of the SSE as a difference between maxima and minima
- the average cycle period, either as elapsed time or traversed length
- the slopes of the rising and falling flanks

However, using one single friction coefficient as the standard parameter to describe friction phenomena is not appropriate: It is a matter of definition if friction under unstable conditions must be regarded as the average value of the analyzed interval, or its average minima or maxima.

The criteria for averaging values demand constant amplitudes and periods of a stick-slip based on a level of friction. The upper friction plot of Figure 131 is an example that conforms to this requirement within statistical deviation for all plateaus shown here. The plot in the middle proves that constant amplitudes are far from being taken as granted: The stick-slip is damped slowly until it vanishes during the forward direction, and it re-appears at the end of

the backward direction. This typically happens when the contact between the friction partners is not perfectly homogeneous, but can also have other reasons [70]. The cycle period remains unaffected nevertheless. In the lower plot, stick-slip is clearly visible but employs obvious irregularities. On a closer glance at the forward direction, the cycles consist of a period with large duration and amplitude and a superposed smaller amplitude dividing the period into smaller sections. The curve is still irregular and can hardly be evaluated satisfactorily.
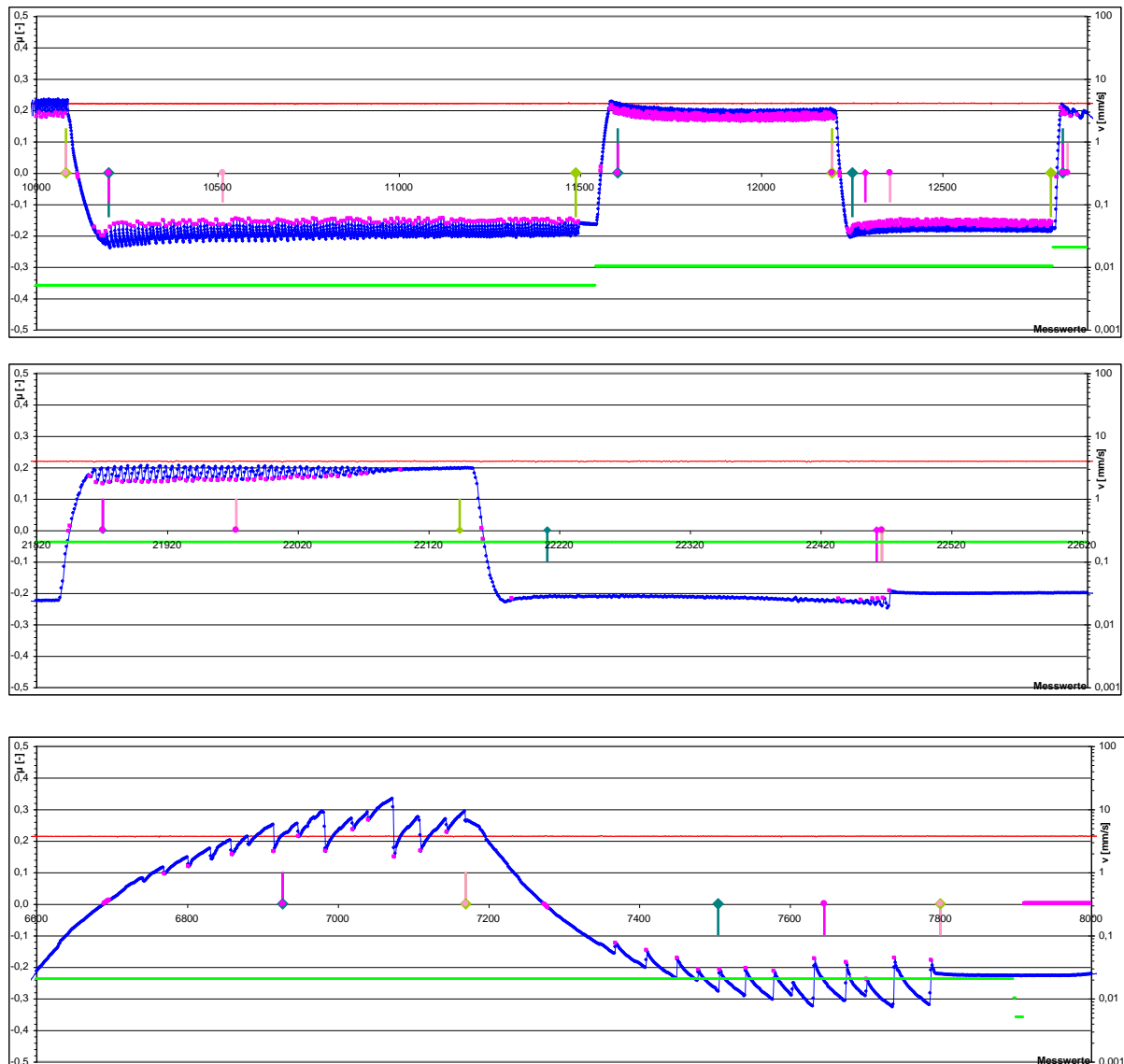
Figure 131: Different types of stick-slip characteristics. Above: stable SSE over complete stationary velocities. Middle: Decreasing and increasing SSE as result from inhomogeneous contact conditions. Below: SSE with large, irregular amplitude.

The following classification will be used to describe the **quality** of stick-slip:

- *none*: no cyclic structures are visible, sliding is continuous
- *partial*: at least some parts of the friction plot is subject to stick-slip for the regarded velocity

- *total*: complete stick-slip during this velocity

- *irregular*: anomalies like an ambiguous or even erratic period or amplitude; anything that does not fit into the other classes

To rate the **quantity**, the amplitude or height will be called *minor* if it barely exceeds background noise, *normal* if the amplitude is definitely larger, and *major* if the amplitude comes close to the friction coefficient (in extreme cases, especially with the universal testing machine, some samples have been witnessed to jump macroscopically).

To label the period **duration**, cycles will simply be denominated as *short* or *long*. If not mentioned otherwise, this relates to elapsed time, not traversed length.

4.6.3 Analysis of the Stick-Slip Effects

Influence of System Parameters on Amplitude, Period and Flank Slope

Just like the friction coefficient, the various aspects of stick-slip are illustrated best by their dependence on velocity. The diagram encoding is the same as defined in chapter 4.5.1 for coated samples.
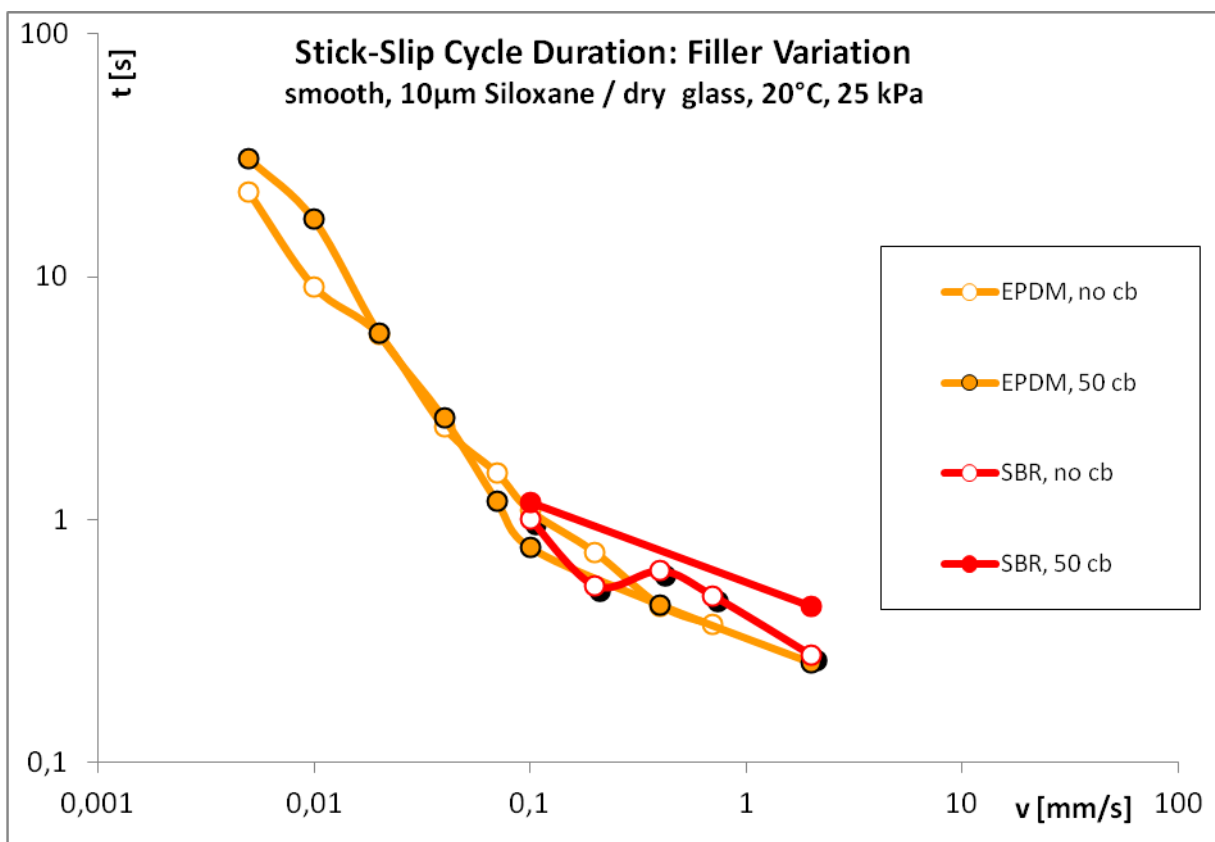

Figure 132: The influence of cb filler, like many other parameters, on the stick-slip duration is limited.

Looking at the **duration** of a single stick-slip cycle produces a remarkably characteristic course of the plot, with only marginal influence of the various system parameters. Taking different combinations of siloxane coated samples on dry glass in Figure 132 as a typical example displays an almost linear curve for low velocities up to 0.1 mm/s in a double logarithmic plot. For medium velocities below 2 mm/s the slope of these curves become flatter. For faster sliding, no stick-slip appears at all.

Variation in parameters changes this behaviour in only a few aspects: The absolute duration may increase to longer or decrease to shorter periods, especially as characteristic value for each substrate, whereas other parameters play a minor role, and the average slope remains constant in any case. The linearity may be less perfect for some combinations – sheet 4 is sometimes affected to this – and some samples may not be subjected to stick-slip at certain velocities. Apart from that, duration plots look the same, confirming that the cycle duration is ruled by the system frame as stated before. Consequently it is useful to focus on another aspect to characterize the parameter dependency of stick-slip: the **amplitude**. Naturally it is defined for the same velocities as the stick-slip duration. The amplitude height $\Delta\mu$ as average difference between maximal and minimal peaks during stick-slip occurence – also depicted best on a double logarithmic scale – is correlated to the duration by the falling slope that is typical for both aspects with rising velocity. This is not surprising as straining the rubber in the deformation phase provides a larger tension to be released. While stick-slip at high velocities tends to be dominated by the resonance frequency of the system, slow velocities couple the duration to the covered distance, which then is more or less constant (see Figure 137). The amplitudes, however, are not as strictly monotonous as the durations, and differ clearly in response to their underlying parameters. All amplitudes in any system stay considerably below $\Delta\mu = 1$, which is, on the other side, still higher than the related friction coefficient. The amplitude can well reach or exceed 100% of the underlying COF in many cases. It is noteworthy that the critical threshold to start the slip phase is modified by velocity.

Being not solely a coating related effect, the rubber bulk, and predominantly its **stiffness**, should be visible in the stick-slip amplitudes. Indeed EPDM as the softer material compared to SBR (chapter 4.1.3) can more easily be excited to stick-slip vibration, as Figure 133 shows. This is true on several substrates. Analogously, unfilled samples can be expected to react stronger when instable conditions occur. This behaviour is found best for SBR samples. Neither cb filling nor the elastomer type, on the other hand, seems to have large influence on the velocities for which stick-slip is present: A higher stiffness does not prevent stick-slip completely, but it alleviates its strength.
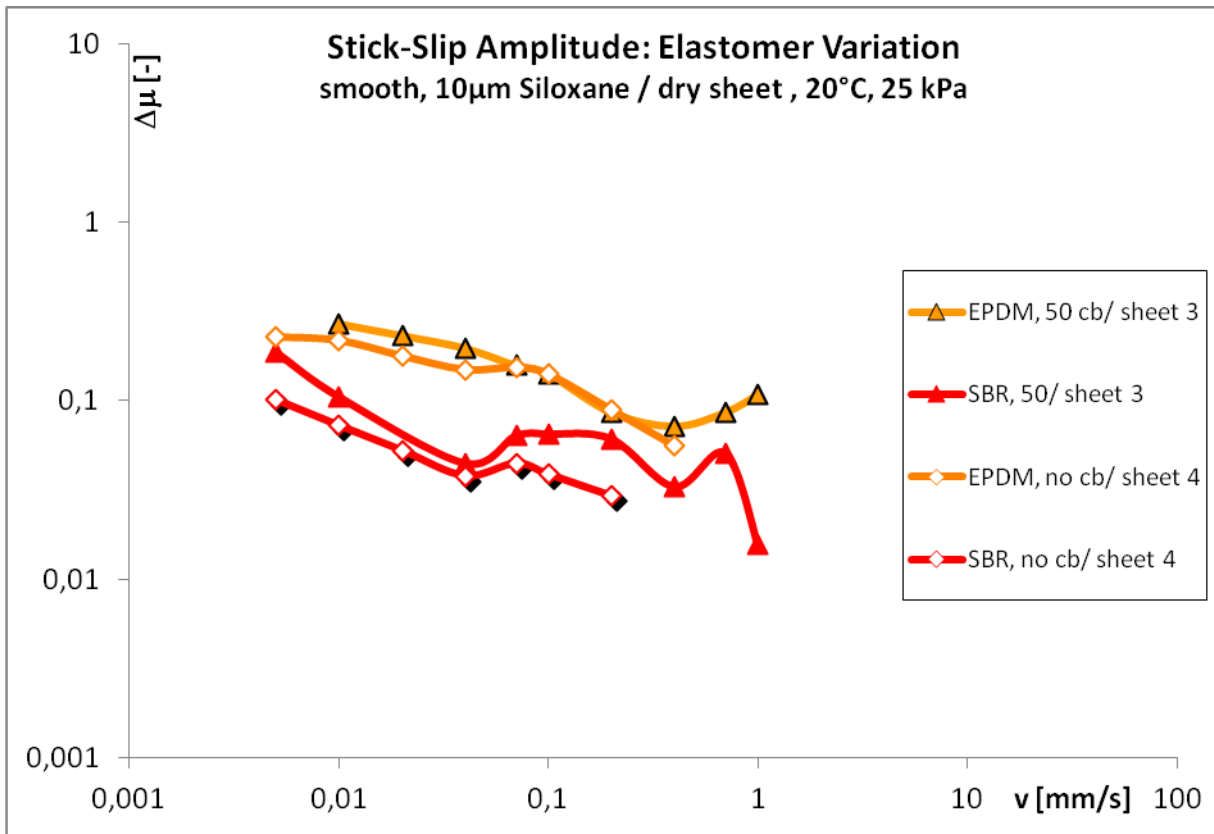
Figure 133: Stick-slip clearly exhibits higher amplitudes on EPDM than on SBR.
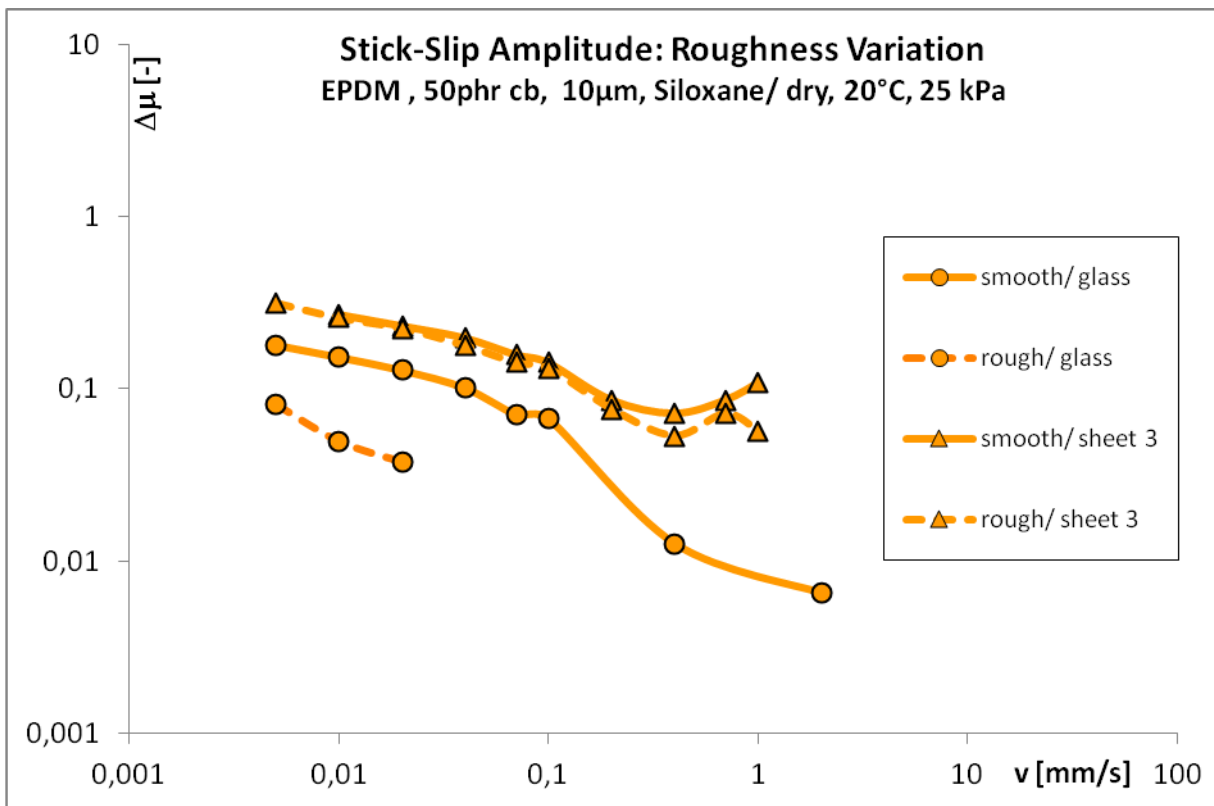

Figure 134: Whether smooth samples show larger stick-slip than rough ones depends on substrate.

Also the cycle duration is increased for soft samples (EPDM and unfilled rather than SBR and cb filled), at least on coated sheets, because they can be deformed to a larger extend before contact is released. On glass hardness is largely irrelevant. As will be discussed later, glass has significantly lower values than coated sheet in both duration and amplitude – obviously low enough to restrain the deformation in presence of this very smooth substrate mainly to the sample coating layer without ample effect into the elastomer bulk.

Quite contrarily to the bulk influence, the **roughness** of the rubber coating affects the stick-slip when the substrate is not coated sheet but glass. This holds for both sheets, and not only for siloxane like in Figure 134 but also for PTFE, and is mirrored in amplitude and duration, too.

Again, the presumingly short excitation depth on glass poses a good explanation: A rough sample surface exhibits a smaller contact area (this concerns to the microscopic *true contact area* as well as to the contact area in mesoscopic scale) and thus simply offers only a confined volume to be excited.

Another difference between the surface and the bulk has to be mentioned: A rougher coating surface does not only diminish the amplitude of the stick-slip, but can also prevent it from emerging at all, especially at medium velocities where excitation is still possible for smooth rubber.

Coatings have been applied in order to modify the surface contact of the samples and minimize friction and stick-slip. The degree of success differs in respect to which goal is highlighted: To reduce friction, PU and TPU are good, but PTFE and siloxane are better. Stick-slip, however, appears almost exclusively for the latter two coatings – and for uncoated samples, where it is rarely well measureable due to the extremely high and irregular friction.

Although similar in their friction levels, PTFE and siloxane can be separated in regard to their stick-slip amplitudes (Figure 135), siloxane being higher but slightly more regular concerning velocity. TPU, where it shows stick-slip at all, is of a comparable order. PU instabilities for normal layer thicknesses (10 µm) are virtually impossible but occur in some cases for 40 µm thick coatings. A thin layer thus may be advantageous to prevent stick-slip.
Apart from their viscoelastic properties, the coatings differ in their surface energies, and this interacts with the substrate: The amplitude of siloxane is extraordinarily high on coated sheet but drops to PTFE level on glass. When PTFE becomes physically unstable, the mechanical effects concern not only friction but the amplitude is increased analogously.
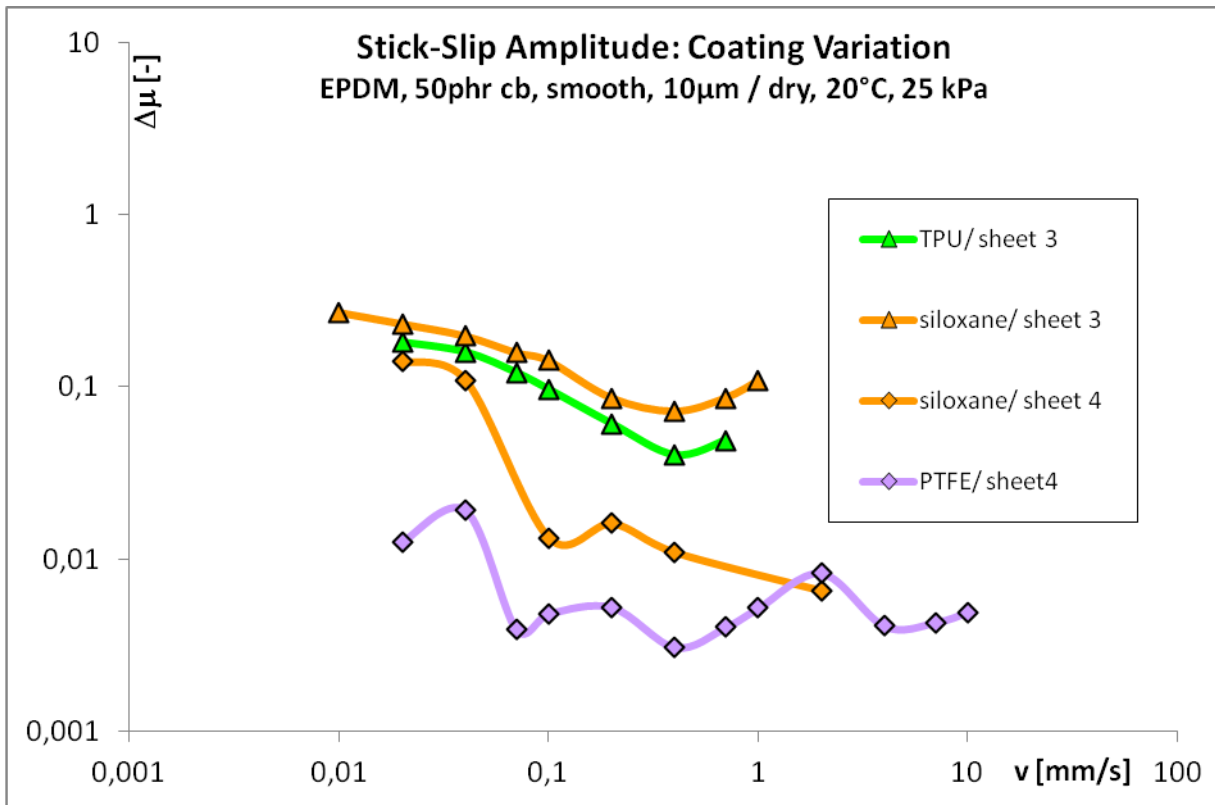
Figure 135: In most cases, stick-slip is constrained to PTFE and siloxane. If SSE does appear on PU or TPU, it reaches similar values.
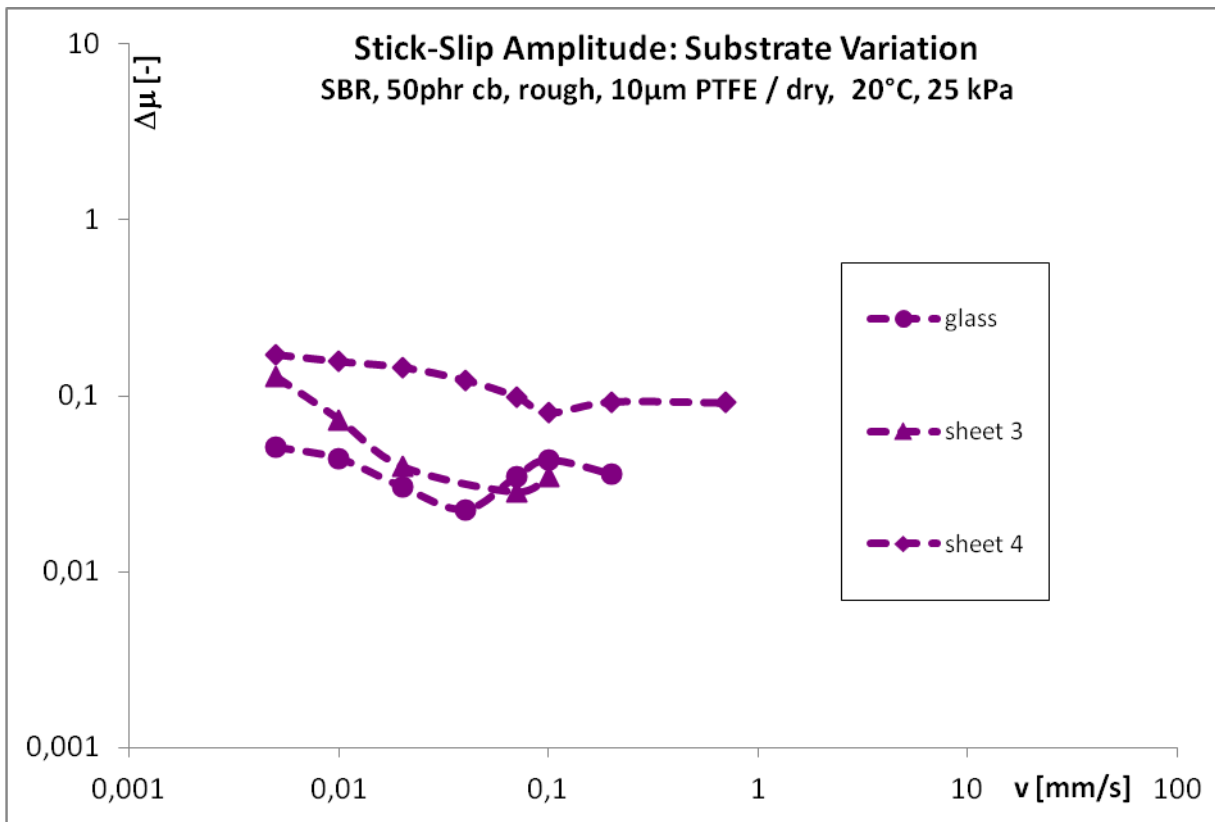

Figure 136: Substrate is one of the most important parameters for stick-slip amplitudes.

The bulk properties can be neglected in respect to the differences that coatings show. The duration is not affected by the coating type.

The most important factor on the stick-slip amplitude is the contacting **substrate**. Figure 136 demonstrates this for PTFE coated SBR. Glass is the surface that turns out to be least susceptible for high amplitudes. The two types of sheet coating can clearly be discriminated. In all other cases – see Figure 134 for an example of siloxane coated EPDM – glass exhibits the lowest values of stick-slip amplitudes, too, but the order of the sheet coatings (not shown here) is reversed, and this holds for rough surfaces as well as for smooth. Just like for the adhesion friction coefficient, the amount of stick-slip is a function not only of the substrate roughness, which is similarly tiny for all substrates prone to instabilities, but also of the surface tension, which can differ in combination with each single sample coating significantly. Considering the logarithmic nature of the plot, the amplitudes reproduce this distinction.

The horizontal split up of the various substrates in respect to their stick-slip amplitudes is retrieved in the lateral dimension, i.e. the sliding axis and thus the cycle period and cycle length. Again the short duration of cycles on glass is exceeded by coated sheets in the order known from the amplitudes, for the investigated systems. The amplitude correlates nicely to the stick-slip period for any velocity because of its influence on the stretching time and distance.

This can also be found for the **length** of each cycle in Figure 137. The durations and velocities allocate for this system to a mainly constant cycle length, for any sliding speed, of little less than 100 µm that the deformed "stick arrays" have to traverse during the slip phases. This must be assessed in relation to the total sample length of 5 mm and the sample thickness of 2 mm: Only a small volume of the sample, lateral as vertical, is excited by the deformation during the stick phase. Another dimension to judge the slip length is the coating thickness, against which the stick length is in any case much lower than the PTFE layer as found in chapter 4.1.1. This means the lateral size of the excited area is definitely larger than the coating, and excitation must be expected to penetrate deeply into the elastomer.
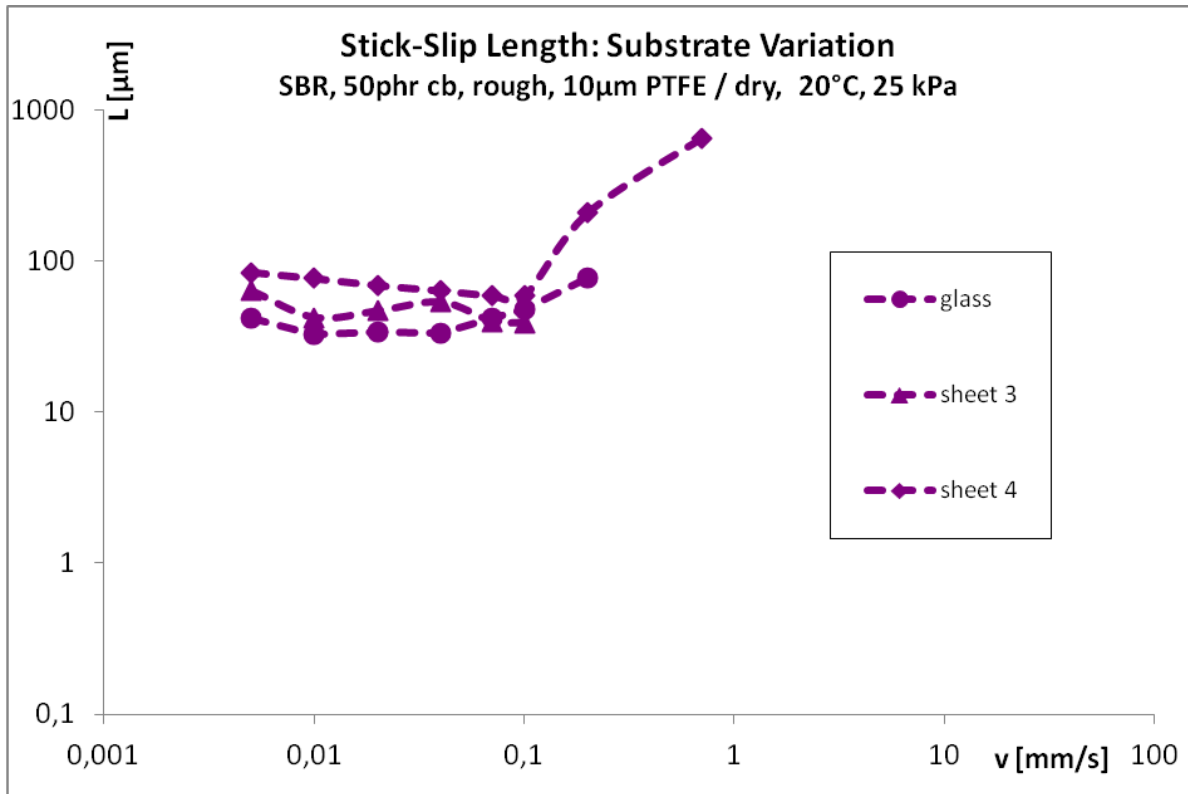
Figure 137: Although the duration falls with velocity, the cycle length compensates to constant or even rising slopes.
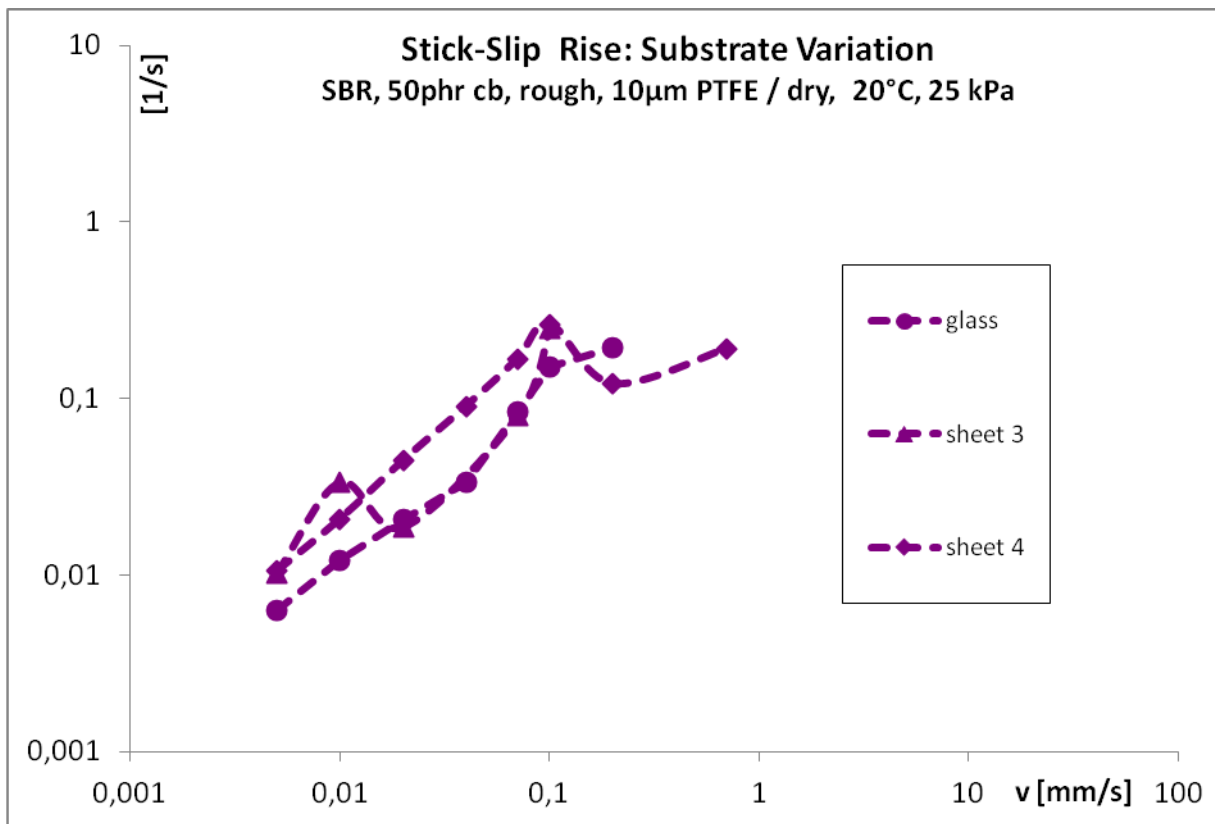

Figure 138: The faster the sliding velocity, the harsher drops the SSE during its decline.

In the consideration above, the penetration of the deformation into the elastomer is mitigated by the sample roughness that is of a similar order than the various cycle lengths. The coating, however, which levels this roughness on the one hand, and the length of a stick-slip cycle on the other hand is not in every case as constant as in this example: Values range from a few micrometers to several hundred micrometers, depending on substrate, coating, sample roughness – and sliding velocity. Rather than being independent of velocity, many systems tend to display, contrarily to duration and amplitude, rising cycle lengths for high sliding velocity if stick-slip still occurs under this condition. The rising fast end of the curve for sheet 4 in Figure 137 gives us a glimpse into this behaviour.

The amplitudes and durations of the single stick-slip cycles can directly be computed to find the slopes of the rising and declining sections of the curves. These **flanks** can be supposed to correlate with the system parameters similarly as the other aspects do. The declining flanks of the SBR curves discussed in the recent paragraphs indeed correspond nearly completely (not shown here) to the amplitudes, with the same influence of the substrates and slopes between 0.15 /s and 0.7 /s, which means the temporary friction coefficient reduces by these amounts within a second. In short: The higher the amplitude of the deformation, the faster the stuck rubber parts will resile, no matter what global velocity their bulk has compared to the substrate – a simple elastomer mechanic effect. This affinity of amplitude and declining flank is quite representative and contains little new information.

Figure 138 gives a glance on the rising flank for this system: At high sliding velocities, the rubber is deformed faster during the stick phase. The reciprocal behaviour of duration and rising flank might lead to the assumption that a constant length of SSE rise (the length that bulk and substrate are shifted against each other while deformation takes place) underlies the flanks. The duration of a rising flank indeed exceeds the duration of a declining flank by far, and the total cycle length, as already discussed, depends weakly on velocity. A closer look at the flank lengths reveals that the decline induces a longer traverse at higher velocities whereas the length of the rising flank shows the same behaviour only for its minimal values while its maximal values hardly grow with velocity. The single values for the rising length are clearly more scattered than their declining complements and also their averaged values that define the flank slope suffer from irregularities where the other aspects are straight. The general order of substrates remains unchanged anyway.

All previous graphs display aspects of stick-slip phenomena as found purely on glass and coated sheets – not on **steel**. This is not accidental: The comparably rough surface even on fine steel makes periodic instabilities improbable. Actually stick-slip appears on this substrate

solely in one single system, PTFE coated EPDM. Rough and smooth samples then behave identically in durations and very conformly in amplitudes.
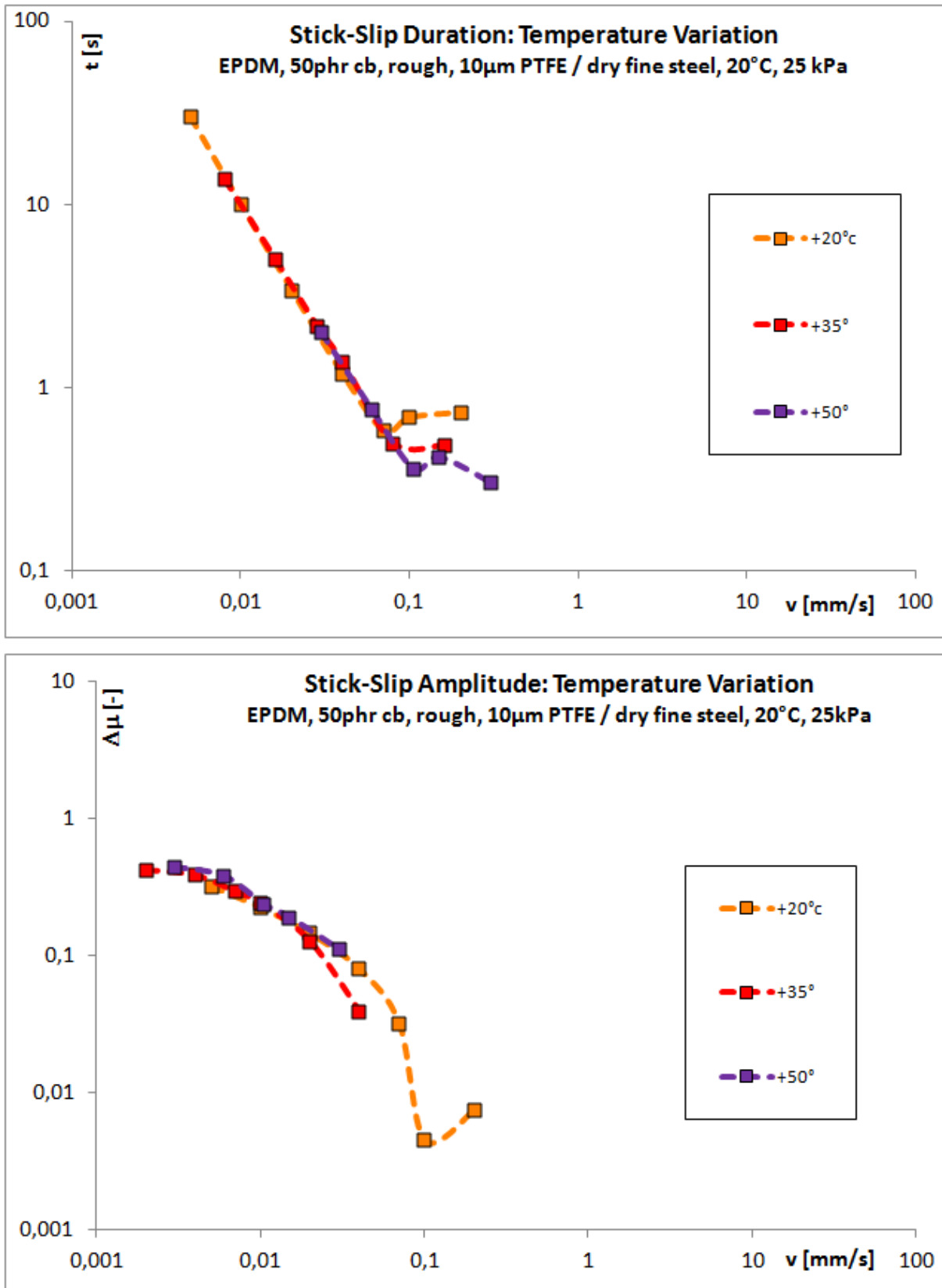

Figure 139: Not only the COF, but also duration and amplitude of SSE can be brought to an almost perfect match with appropriate fit parameters.

A **thermal variation** of this sample unveils, however, an interesting restriction on this statement: Stick-slip is possible only at or above room temperature whereas a cooler environment does not allow instabilities. This is easily imaginable after recalling Figure 111 as only branches for $T \geq 20°C$ have a clearly negative slope versus velocity. For the friction coefficient the construction of a friction master curve has been demonstrated in Figure 112, raising the question if this can be done for stick-slip aspects, too. This is really possible and shown in Figure 139 as a duration master curve and an amplitude master curve, respectively. The branches can be brought to a perfect match with the right horizontal shift factors: in the duration plot *0.400* for 35°C and *0.150* for 50°C, or in the amplitude plot *0.100* for 35°C and *0.015* for 50°C. The branches for 20°C remain of course unshifted. These factors deviate from each other as well as from the free factors that were used for building the friction master curve and that overestimate the necessary shift of the stick-slip branches. They resemble rather the shift factors extracted from the DMA measurements of Figure 113. The best factors for the duration match the viscoelastic factors (DMA 50°C as measured, 35°C interpolated) exactly. The amplitude factors are between those of duration and friction. If the high temperatures are dominated by the PTFE more than by the rubber bulk, then coating plays a maximal role in friction (viscoelastic thermal discrepancies of elastomer and coating), a lesser role for stick-slip agitation as depending less on temperature, and almost no role for the cycle duration (in concordance to the former thoughts that blame the system frame for the relation of periodicity).

It may be illuminative to investigate whether a negative friction slope and as a consequence the appearance of stick-slip instabilities is a typical sign of elevated temperatures.

The fact that all presented curves belong to dry conditions is representative and complies with the general presumption. In spite of a **lubricant**, stick-slip could exist in very few cases only – all for an unfilled, smooth SBR sample on coated sheet. Remarkably, the sample coating was neither siloxane nor PTFE in these cases, but PU, TPU or no coating, for some special combinations.

Classes of Quantity and Quality

Apart from the characteristic values of the stick-slip it might be of interest to evaluate how often instabilities appear. Excitation as a result of resonance can be expected to depend strongly on velocity. Figure 140 displays the percentage of the quantity classes defined in chapter 4.6.2, plus any irregular patterns, in which instabilities manifest themselves.

Minor excitations occur quite frequently, especially in the medium velocity range from 0.04 mm/s to 2 mm/s. These irregularities are not real stick-slip, rather a vibration softly above statistical fluctuations. They may well be produced by any kind of background noise including laboratory conditions outside the friction device. Thus this value characterizes mainly the sensibility of the particular systems towards noise amplification. For slow movement the influence of external vibration is assumingly averaged out whereas at very high velocities the reaction time is too short to reply to the impulses. However, the percentage of samples affected by minor instability rises again above 7 mm/s in combination with irregular features that are often accompanied by their own excitations. 32% of all analyzed samples experience minor instabilities, averaged over all velocities.
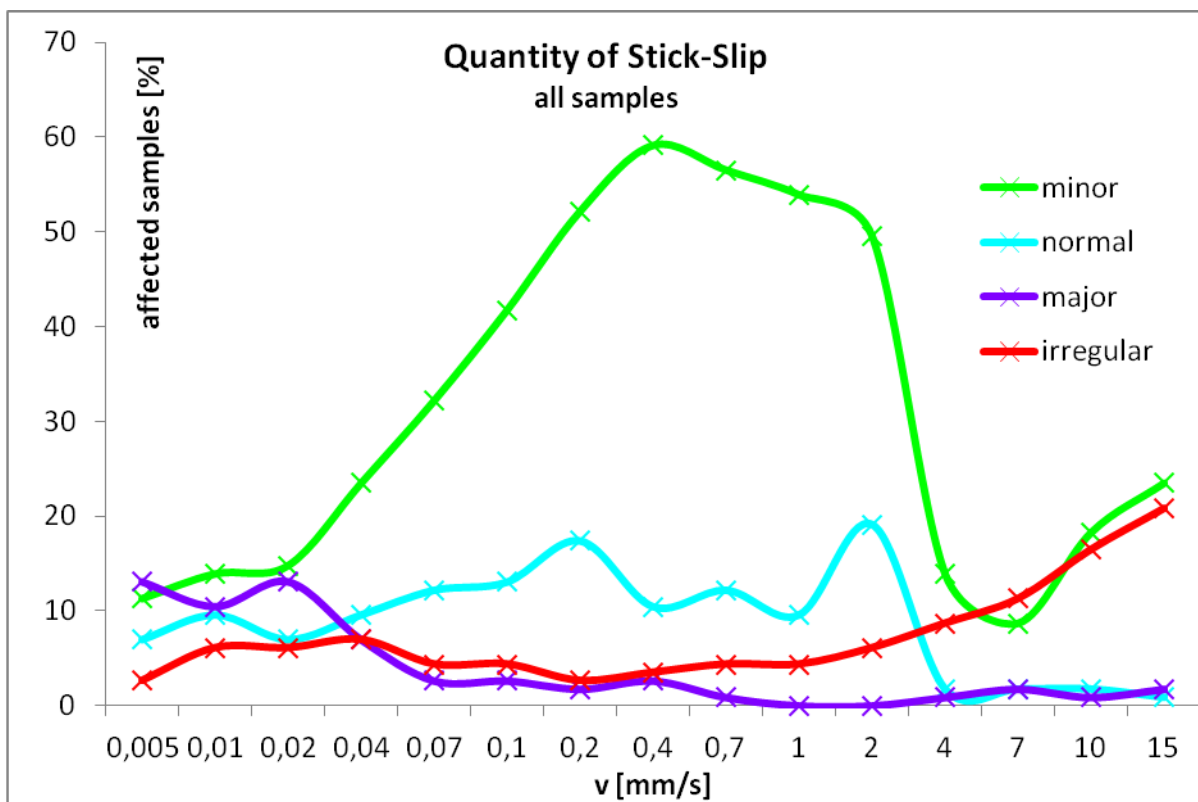
Figure 140: The amount of quantity classes for stick-slip depends on velocity.

A clearly defined **normal** stick-slip is found for 9% of the investigated combinations of sample and environment. Almost every event is confined to velocities up to 2 mm/s, a critical value depending on the system frame (a different device possessed rather 1 mm/s instead). Below this sliding speed, the appearance of any real stick-slip (the sum of normal and major counts) is distributed substantially equally.

In only 4% of all samples, the stick-slip grows to a larger extent that can be called **major**. There is definitely a correlation to velocity: Whereas appearance is marginal for speeds of 1 mm/s or more, the occurrence of major instabilities becomes significant for slow sliding and

below 40 µm/s exceeds even the effects classified as normal. A slow movement seems to foster instabilities with large amplitudes.

In some cases there are instabilities but they lack a periodic pattern. These **irregularities** arise as unstructured and at times very high peaks which makes a detailed attitude difficult to describe and the underlying friction coefficient hard to determine. Just a small part of all given circumstances, irregular behaviour affects mainly measurements at higher velocities above 2 mm/s, which sums up for 7% when averaged over all velocities.

The vast majority of evaluated plateaus shows a **total** stick-slip, if any exists. Those samples that show **partial** stick-slip do so merely at a few single velocities in a typical range from 20 µm/s to 1000 µm/s with no obvious correlation to the system parameters. Filled samples with a rough, PTFE covered surface have a slightly higher chance to be affected.

SSE class	*Elastomer*		cb filler		Roughness	
	SBR	**EPDM**	**none**	**50 phr**	**smooth**	**rough**
minor	36	26	30	32	30	33
normal	8	10	12	8	10	8
major	1	8	3	4	4	4
irregular	9	5	10	7	10	5

SSE class	*Coating Type*					Thickness	Fluor	
	none	**Siloxane**	**PTFE**	**TPU**	**PU**	**PU 40µm**	**none**	**gpf**
minor	20	37	32	24	36	38	33	30
normal	4	17	15	4	3	6	6	10
major	0	9	9	1	0	0	0	6
irregular	34	1	4	4	5	3	12	4

SSE class	*Substrate*					*Lubricant*	
	Glass	**Sheet 3**	**Sheet 4**	**fine Steel**	**rough Steel**	**dry**	**wet**
minor	29	28	22	44	42	31	48
normal	8	15	11	5	4	9	9
major	5	5	4	4	1	4	0
irregular	15	7	8	1	0	7	17

Table 13: Percental existence of the stick-slip classes under various parameter types (above: sample, middle: coating surface, below: contact conditons)

The **viscoelastic properties** seem to have little effect on instability: EPDM is only slightly less sensitive to stick-slip than the harder SBR, but if it happens the effect can become larger more easily. The rubber bulk features the peculiarity of stick-slip, not its existence.

Especially for filled uncoated samples, the universal testing machine showed stick-slip more often for smooth than rough ones, but the **roughness** has small influence on tribometer measurements. At high velocity, smooth samples tend to have major stick-slip, whereas rough surfaces constrain to normal amplitudes.

Coating is crucial for avoidance and control of instability. The pure elastomer is extremely prone to irregular friction. Classical stick-slip may superpose this but is oppressed by chaotic friction forces. Siloxane and PTFE experience stick-slip comparably often for normal and major amplitudes, whereas PU and TPU have almost none. This is exactly reciprocal to the reduction of friction. All coatings prevent irregularities well.

The effect of a **thick** layer can be compared only for PU and causes normal stick-slip more often but further lowers the chance of irregular events.

The use of **fluorination**, though necessary to provide the needed adhesion to the elastomer, seems to be counterproductive at first glance as it augments both normal and major stick-slip. But actually an unfluorinated surface will rather lose its coating integrity before periodic effects truly come into play. A drastically increased number of irregular counts is the result instead.

The choice of the **substrate** is important. Stick-slip appears on smooth interfaces: on glass and even more on coated sheet. Irregular behaviour can appear on glass especially at high velocity. Steel, on the other hand, is not likely to create real stick-slip – the rougher the steel, the more improbable it becomes. Events focus on high temperatures.

Connecting both friction partners with a **lubricant** does not automatically prevent stick-slip but rules out large amplitudes completely in the investigated cases.

Existence of Stick-Slip in Correlation to Negative COF Slope

In the vast majority of cases the relationship between a friction slope falling with velocity and the appearance of stick-slip is obvious. There is in several curves an approximate proportionality of the slope angle and the complementary stick-slip amplitude. This includes environmental parameters, in particular the temperature variation discussed above. Very few systems develop stick-slip with an astonishingly flat negative friction slope, but in no case a

clear stick-slip is established in spite of a positive slope over velocity. On the other hand, there are diverse examples of curves with a significant negative slope without attributed stick-slip or only for some of the affected velocities. On steel, this happens with higher probability. As a conclusion, a negative slope, even a flat one, is a necessary but not sufficient premise for the existence of stick-slip.

Stick-Slip and Start Peak

Finally, stick-slip effects might be related to the start peaks known from chapter 4.6.1. Both are provoked by a temporary stop of relative movement by sticking to the substrate, and both situations terminate with an abrupt break off, resulting in a sudden drop of friction. From this point of view a start peak could be a stick-slip with a single period.

However, the first peak of a stick-slip cycle may exceed the following stick maxima significantly, indicating a substantial difference in concept. Indeed stick-slip is often found only for velocities where no start peak arises and vice versa. As discussed before the start peak tends to be maximal for high velocities, contrary to stick-slip. Apart from the pure existence, also the coating dependent order of heights of the start peak is frequently complementary to those of the stick-slip as well as complementary to those of the friction coefficient.

A possible difference in the principle of the two phenomena is the spatial expansion of the deformation that leads to the peaks in both cases: The start peak affects the complete sample because its whole surface is in touch with the substrate before a new measurements starts. The comparably long time between measurements (at least 1 second) allows the adhesion to rise to an amount of only slow further increasing. When the movement starts the mass inertia of the sample causes a delay of reaction, which is largest for highest velocities. Movement is clearly non-stationary. The stick-slip on the other hand does not necessarily happen on the whole interface but can be regarded as local deformation. A slow movement may be more suitable to build up local deformations. Apart from this the global movement is stationary during this phase.

In any case a strong adhesion – a large true contact zone via smooth surfaces with appropriate tension – is important to make samples stick. Thus, on steel neither stick-slip nor start peaks are seen regularly.

5 Final Considerations

5.1 General Discussion

The previous chapter explained the details of the experimental and computational results for various aspects of tribology. Now these results shall be reviewed in an overall scope of the basic goals in order to point out coherence and interactions, and answer how successfully the objectives have been reached or where confinements exist.

One goal was the **investigation** of friction and stick-slip in a manifold of conceivable systems. The parameter space is huge and truly impossible to fathom completely. Limiting the elements for each parameter to a finite number – only few but relevant elastomers, etc. – created a large but finite number of parameter combinations. Furthermore, the focus was put on interesting and promising systems by separating the variables if necessary instead of grazing the entire mash. A digest of the most important and most meaningful results has been presented. The effect of each single aspect could be assessed clearly in most cases.

Apart from a reproducible general description of friction, some exciting common features become evident. The wet friction starts at a low level for slow sliding speeds and rises mainly monotonously with velocity whereas the maximum peak of the adhesion component in the dry friction regime causes a plateau at medium velocity. It is noteworthy that this plateau appears on "naturally" measured Stribeck curves in the same way as in synthetic friction master curves and especially when adding silica to the elastomer batch. The master curve on its part is based on the same horizontal shift factors no matter if they were applied to viscoelastic shear moduli or friction coefficients.

The investigation of dynamic effects like stick-slip, start peaks and running-in phases blends into the results for purely stationary friction. The connection between stick-slip and velocity dependence of friction is obvious with regard to strength and time scale, and reproduces the thermal influence resulting in frequency shifts.

The second goal was the **prediction** of tribological behaviour. Three different types of prediction must be discriminated here:
- the way that the parameters of bulk, surface and environment determine the friction
- the interpolation and extrapolation of sliding velocities, including master curves
- the simulation of friction according to the model

By understanding the role of the parameters in the friction mechanism it should be possible to estimate how a yet untested combination of rubber, filler material, surface structure and chemistry might slide on a certain substrate. However, predictions remain merely qualitative until measured practically. Some parameters behave not consistently in every case, and interactions between them must be taken into account, but universal trends can be spotted. Stationary friction is probably easier to gauge than dynamic effects. Predictability of dry and wet interfaces may differ.

Interpolation of blank velocities between measured values should not cause any problems, as the curves display a continuity in almost every case. Caution should be exercised for extreme sample exposures, be it due to high pressure (some applications may outrange the experimental setup by decades in pressure) or long experimental durations. Extrapolating a measured curve is doubtful for normal experimental data, but tribology enjoys the availability of the time temperature superposition principle. Via master curves an incredibly large range of velocity can be explored if measurements at variable temperatures are feasible. The results are plausible and reliable for ordinary velocities. A natural border of course exists, as the most extreme low temperature branches for SBR show impressively: The assigned sliding velocity exceeds even the speed of light – obviously no realistic interpretation and a proof that master curves are confined to "normal" velocities to remain valid. Simulation is consequently not possible for excessive velocities in this system, and for any really high velocity the influence of friction heat must be considered. The use of friction master curves at moderate and slow velocities, however, is not restricted, and extrapolating to super slow speed can be expected to work smoothly. If shift factors are unknown, like for coated samples, it is still possible to determine horizontal shift factors empirically. The non-existent need for vertical shift factors turns out very helpful then.

Simulation has proven successful in many cases and verifies the validity of the DIK friction model. Hysteresis and especially adhesion match the reality of wet and dry friction well, for standard curves as well as for master curves and silica samples. It is thus an excellent opportunity to forecast tribology when a measurement is unwanted or limited in parameters. An exact knowledge of viscoelasticity and surface descriptors is a prerequisite for a meaningful simulation. Some free fit parameters leave space for interpretation of the computed curves. An extensive analysis how the contact variables depend on external parameters has been provided. The model assumes a rigid substrate and an elastic sample with full contact at least on the macroscopic scale. It does not cover the friction of two flexible objects or a patterned sample surface. Within its frame, it is a useful tool for prediction.

Finally, there was the goal to **control** the friction coefficient and the appearance and attributes of stick-slip effects. In this work the target was a minimal friction with no or small instabilities. A reasonable choice of elastomer and its contact partner may already provide the desired effect. This is certainly not possible in many applications. Two investigated techniques promise a solution: coating the sample, and inserting hard particles into the sample surface. Which one is better?

The answer depends on the exact request. The first difference lies in the preparation: PAOS must be inserted already during the batch mixing process, coating is possible any time before usage. Adding one more component and annealing is, on the other hand, an easy step and thus cheaper and less time consuming than coating.

Both methods diminish friction and stick-slip and can be regarded successful in this perspective. The presented results should not be compared directly because measurements took place on different machines and on substrates of diverging smoothness. Coating with PTFE and siloxane gives definitely the best results in respect to low friction, but PU and TPU prevent instability much better. PAOS manages both to a certain degree if its content in the sample is high enough.

The effect vanishes when the sample surface is damaged. Gas phase fluorination before coating shows mostly good stability and allows longer usage and applying higher pressures than usual. PAOS wears off fast and is thus not dedicated to these conditions. Storing the sample for a long time or undefined environments alter the state of annealing for PAOS but leave coating untouched.

The environment itself can be another alternative to control friction and stick-slip. Sample and substrate may be arranged as fix, but for some systems the pressure, the temperature and the frame provide the key to a lower friction and less stick-slip. The temperature dependence of stick-slip in friction master curves is a formidable example.

5.2 Summary

Aim of this work was the investigation, prediction and control of friction and stick-slip for rubber sliding on rigid substrates. This included experimental testing of friction forces for a large number of tribological systems, i.e. combinations of various elastomers, surface structures and environmental conditions, on the one hand, and a comparison to simulations on the other hand.

All **computational** results of wet (hysteresis) as well as for dry (hysteresis plus adhesion) friction are based on the friction model developed at the DIK previously, which incorporates the viscoelastic properties of the rubber sample and the surface descriptors of the substrate at room temperature for variable velocities and pressures. Viscoelastic shear moduli were gained from dynamic-mechanical measurements (DMA) for the involved samples, and shear master curves were constructed using the time-temperature superposition principle of the WLF law with horizontal and for filled samples also vertical shifting. The substrates were characterized by surface techniques and analyzed due to their fractal surface parameters.

As **samples** the elastomers EPDM, NBR, NR and SBR were chosen because of their importance in not only scientific but also industrial application. Some bulks were filled with carbon black, silica or PAOS (followed by annealing) in order to enhance stabilty, hardness and surface structure. Vulcanization plates of different degrees in roughness were used to modify the sample surfaces. To analyze the effect of polymer layers, a class of samples was coated with lackers based on PU, TPU, PTFE and siloxane.

Friction **measurements** were carried out on a special tribometer sliding on one axis forward and backward with stationary velocity ranging from 5 µm/s to 15 mm/s, or on a universal tester. A tenside-water lubricant provided a wet environment for pure hysteresis friction if needed. Pressure and temperature were varied in relevant cases.

While wet friction on rough substrates like asphalt and granite rises monotonously at rising slope with the sliding velocity, dry friction reaches a **plateau** at medium velocity. This is only sparsely visible for unfilled SBR samples but becomes more pronounced and longer when **silica** filler (up to 80 phr) is added; the velocity above which the plateau begins is not affected. Under wet conditions, the silica makes the samples harder and increases friction for all velocities. Both substrates behave quite similar in experiment. Simulation reproduces the data well, and extrapolation confirms the tendency of the plateaus to become flatter and extend to higher velocites.

The plateau of many systems is barely detectable because the velocity scale does not reach far enough at room temperature. Combining the branches measured at different temperatures creates a **friction master curve**. Like the shear modulus master curves known from DMA and using the same horizontal shift factors, they form a continuous shape. After rising with velocity at high temperatures/ low velocity, a maximal dry friction is clearly visible at a velocity connected to the glass transition temperature of the material (EPDM, NR, SBR), followed by a plateau or a direct decrease. Simulation fits this course very well for all elastomers over reasonable velocities. Friction master curves for wet interfaces are also possible but limited to temperatures above freezing and thus less meaningful. Vertical shifting is not necessary. Taking temperatures form -30 to +65°C into account results in master curves that cover the huge range of 10 to more than 15 decades of velocity.

Simulating the friction process generates not only results for the friction coefficient but also for related **contact parameters**. A systematic analysis of this as function of velocity and pressure (several decades around the 23 kPa of the tribometer) for the investigated combinations of sample and substrate reveals some general insights: The true contact area, a tiny part of the nominal contact area, decreases with velocity and sample hardness but rises with pressure. The same holds true for the mean penetration depth. The gap distance displays a reciprocal reaction to these input parameters. The shear stress increases with velocity, too, but approaches a maximum asymptotically. The exact course of the functions depends on the parameter set that defines the system.

One way to reduce friction consists in minimizing the contact area on the microscopic scale. To achieve this, NBR samples have been prepared with different degrees of **PAOS** with Al_2O_3 particles that work as spacers at the sample surface. A sufficiently high concentration of PAOS (20 phr) can decrease friction up to 20%, depending on velocity, for all samples (with and without carbon black) on dry and wet granite, steel and glass. Additionally, PAOS can prevent stick-slip phenomena that appear otherwise on very flat substrates. Applications must consider the increased abrasion induced by PAOS and temporal alteration of the surface (annealing brings the sample to a defined state).

Another way to reduce friction is to uncouple the sample properties of bulk and surface. This can be done by **coating** the preferred elastomer bulk (SBR, EPDM) with a well sliding polymer. The effect is observed best on very smooth dry substrates (glass, coated sheet), which produce extremely high and irregular friction with stick-slip and chaotic instabilities otherwise. Especially siloxane and PTFE show an excellent reduction of friction, but PU and

TPU offer good results, too, without touching the ranking order of the substrates (highest friction for coated sheets, less for glass, low for fine steel and even less for rough). The typical layer thickness was 10 μm. A thicker layer could further decrease friction in some cases. Surface structures imprinted on the sample surface were mitigated by coating but not completely abolished: Smooth samples still display a higher friction than rough ones; no difference is found in case the substrate roughness exceeds the sample roughness. Normal samples filled with carbon black are subject to increased wet friction due to their hardness but dry friction is lower for unfilled ones. Coating prevents soft rubber from establishing optimal contact, so coated samples display lower friction when unfilled even on dry interfaces.

The influence of the **environmental parameters** was investigated as well. On rough substrates like steel a variation of pressure shows little effect, as for the case of uncoated samples, but on a coated sheet a rising pressure can decrease friction of coated rubber. A higher temperature lowers friction, while a cold environment increases friction. On the other hand, a modified temperature on steel does not change the height of friction but shifts the measured temperature branches analogously to mechanical shear branches to overlap as master curve. The shift factors are not identical but similar to DMA and reflect a superposition of bulk and coating layer. This additionally aggravates the difficulties of simulation.

Apart from the mechanical **stability** that can be achieved by gas phase fluorination before coating, stability of the friction coefficient is important. Static friction causes start peaks especially at high velocity on smooth substrates and may slowly increase for long friction exposure. A negative slope in the Stribeck curve is the fundament of a periodic change in friction, the **stick-slip**. A cycle consists of several phases (stick, deformation, slip, contact) that manifest in a slow rise in friction followed by a sharp drop. The duration of a cycle does little depend on the system of sample and substrate but rather on the system framework and is thus characteristic for every single device. The amplitude, however, is a function of the system parameters: Siloxane and PTFE coatings, though optimal for friction diminishment, show stick-slip regularly while PU and TPU rarely are affected. Uncoated samples on smooth substrates show large stick-slip and even larger irregular instability especially for fast sliding. Glass and coated sheet exhibit large effects, steel almost none. EPDM tends to have more stick-slip than SBR, and smooth sample surfaces more than rough. A thicker layer decreases the chance of irregular behaviour. Lubricant limits the amplitude of stick-slip. On dry interfaces, major amplitudes are found mainly for slow sliding speeds. The spatial length of a cycle is almost constant at any velocity, while the slope of the rising flank ascends with

velocity. It is possible to construct a master curve of the stick-slip parameters (duration, amplitude…) from branches of various temperatures.

5.3 Possible Applications

The results of the experiments and simulations have been described and interpreted. The final step is to judge their impact on science and technology. The scientific use of the findings and tools has already been discussed. The following thoughts debate possible applications.

The most important potential that the previous insights allow is the construction of elastomer devices with minimal susceptibility to friction – e.g. gaskets, hoses, rubberized fabrics etc. The choice of the method is determined by the conditions the sample must fulfil as discussed in chapter 5.1. PAOS induction may be a good solution for cheap, disposable devices; coating poses an enduring reduction of friction for devices with higher quality. Deciding which coating type is applied also determines if friction or stick-slip shall be minimized.

On the other hand it might even be desired to generate vibration via stick-slip for special applications. In this case it is useful to identify the typical velocity of the working device for the particular ambience temperature and then select PTFE or siloxane coated sample system with negative slope in this range. The possibility of calculating the course of the curve from master curves when knowing only either temperature or velocity exhibits as useful as the prediction by means of simulation.

A targeted reaction to temperature can be achieved by coating. The bulk behaviour is detached from the layer behaviour and thus "conserved" for its own characteristic temperature response without affecting the interface. The drastic thermal dependence shown in Figure 114 suggests devices which move easily in hot environments but block movement when the system becomes cold.

The existence of a maximal COF, often shaped as a plateau, offers another chance: The system replies with a constant friction for a range of certain velocities/ temperatures (stable, reliable conditions independent from input parameters) or maximal friction can be used to build a system with a stable equilibrium around the peak velocity. Choosing a rubber with the right glass transition temperature designs the position of the peak; coating can modify this effect and enhance sliding. Besides, the influence of coating on the start peak alters the ratio of static and dynamic friction for further application opportunities.

A modification of sample roughness induces effects which might prove helpful. This can be done by patterning during vulcanisation, or the presence of particles like PAOS may function, apart from friction reduction, as spacers to enlarge the gap between sample and substrate.

5.4 Outlook

This work has presented an extensive view on friction and stick-slip under a multitude of parameters. Still, some questions remain and some ideas are worth pursuing in future investigations.

Possible ways to continue investigations for further insight split up into tribological measurements, secondary characterizations and improvements of the software and hardware tools.

A promising advancement might be the combination of coating and surface particles. PAOS would decrease the contact between substrate and coated layer, which would prevent the particles from abrasion. Another field of investigation is the inexhaustible number of tribological systems, with focus on the interaction of temperature and pressure. The resulting master curves would allow a widespread description of friction for parameter sets and explain how common the existence of stick-slip is for high temperatures. As the available data concentrate on mainly dry interfaces, the role of lubricant could be of interest especially for high pressures that might squeeze the contact zone of flat substrates.

Rating the significance of wear is possible with a systematic characterization of the sample surfaces, with and without coating, at different degrees of load exposure. The morphology, the HDC, height profiles and distributions would document erosion and anisotropies of the sample as well as the amount of abrasion. Knowing the dynamic-mechanical properties of the pure coatings without rubber would open the simulation for two-component samples in concert of bulk and layer.

Refining the tools makes experiments not only more efficient but also improves them qualitatively. An optical survey of the interface in real-time, ideally supplemented by means of an infrared camera, or an acoustic detection to analyze the vibrations induced by stick-slip might come in handy for future generations of scientists on this subject, just like an implementation of temperature as parameter in the simulation model for direct calculation of friction in any environment.

Literature

[1]   M. Williams, J. Ferry: "Second Approximation Calculations of Mechanical and Electrical Relaxation and Retardation Distributions", *J. Polym. Sci.* **11**, 169 (1953)

[2]   V. L. Popov: "Contact Mechanics and Friction - Physical Principles and Applications", Springer-Verlag (2010)

[3]   R. Stribeck: "Die Wesentlichen Eigenschaften der Gleit- und Rollenlager", *Z. Verein. Deut. Ing.* **46**, 38, 1341-1348 (1902)

[4]   D. Moore: "The Friction and Lubrication of Elastomers", Pergamon Press, Oxford (1972)

[5]   K. Grosch: "The relation between the friction and visco-elastic properties of rubber", *Proc. R. Soc. London A* **274**, 21-39 (1963)

[6]   D. Moore, W. Geyer: "A review of Hysteresis Theories for Elastomers", *Wear* **30**, 1-34 (1974)

[7]   K. Grosch: "The Rolling Resistance, Wear and Traction Properties of Tread Compounds", *Rubber Chem. Technol.* **69**, 495 (1996)

[8]   M. Klüppel, G. Heinrich: "Rubber Friction on Self-Affine Road Tracks", *Rubber Chem. Technol.* **73,** 578, (2000)

[9]   A. Roberts: "A Guide to Estimation the Friction of Rubber", *Rubber Chem. Technol.* **65**, 673 (1992)

[10]   G. Heinrich, L. Grave, M. Stanzel: "Material- und Reifenphysikalische Aspekte bei der Kraftschlußoptimierung von Nutzfahrzeugreifen", *VDI-Berichte* **1188**, 49-67 (1995)

[11]   B. Persson: "Sliding Friction: Physical Principles and Applications", Springer Verlag, Berlin, Heidelberg, N. Y. (1998)

[12]   A. Schallamach: "The velocity and temperature dependence of rubber friction," *Proc. Phys. Soc. B* **66**, 386-392 (1953)

[13]   B. Persson: "Theory of rubber friction and contact mechanics", *J. Chem. Phys.* **115**, 3840-3861 (2001)

[14]   G. Heinrich: "Hysteresis Friction of Sliding Rubbers on Rough and Fractal Surfaces", *Rubber Chem. Technol.* **70**, 1-14 (1997)

[15]   H. Hertz: "Miscellaneous Papers", Macmillan, London, 146 (1896)

[16]   J. Greenwood, J. B. P. Williamson: "Contact of nominally flat surfaces", *Proc. R. Soc. London A* **295**, 300 (1966)

[17]   B. Mandelbrot: "The fractal geometry of nature", W.H. Freeman, N.Y. (1982)

[18]   P. de Gennes: "Soft Adhesives", *Langmuir* **12,** 4497 (1996)

[19]   M. Klüppel: „Molekulare Rheologie polymerer Schmelzen und Lösungen", *Vorlesungsscript Universität Hannover* **WS 2010/2011** (2010)

[20] C. Wrana: "Bestimmung der Glastemperatur mittels dynamisch-mechanischer Analyse", *UserCom* **2** (2002)

[21] A. Payne: "The dynamic properties of carbon black-loaded natural rubber vulcanisates" *Rubber Chem. Technol.* **36,** 432 & 444 (1963)

[22] M. Klüppel: "Evaluation of viscoelastic master curves of filled elastomers and applications to fracture mechanics", *J. Phys. Condens. Matter* **21**, 035104, (2009)

[23] A. Le Gal, M. Klüppel: "Investigation and Modelling of Rubber Stationary Friction on Rough Surfaces", *J. Phys. Condens. Matter* **20**, 015007 (2008)

[24] H. Hertz: "Ueber die Berührung elastischer Körper" (1881)

[25] T. Geike: "Theoretische Grundlagen eines schnellen Berechnungsverfahrens für den Kontakt rauer Oberflächen" *(Dissertation)* TU Berlin (2008)

[26] J. Schramm: "Reibung von Elastomeren auf rauen Oberflächen und Beschreibung von Nassbremseigenschaften von PKW-Reifen", *(Dissertation)* Universität Regensburg (2002)

[27] A. Le Gal, L. Guy, G. Orange, Y. Bomal, M. Klüppel: " Modelling of sliding friction for carbon black and silica filled elastomers on road tracks", *Wear* **264**, 606 (2007)

[28] B. Persson: "Rubber friction: role of the flash temperature", *J. Phys. Condens. Matter* **18,** 7789 (2006)

[29] G. Heinrich, M. Klüppel: "Rubber Friction, Tread Deformation and Tire Traction", *Wear* **265**, 1052-1060 (2008)

[30] A. Le Gal, X. Yang, M. Klüppel: "Sliding friction and contact mechanics of elastomers on rough surfaces", *(P. Wriggers & U. Nackenhorst: Analysis and Simulation of Contact Problems)*, Lecture Notes in Applied and Computational Mechanics Vol. **27**, Springer, 253-260 (2006)

[31] T. Meyer, L. Busse, A. Le Gal, M. Klüppel: "Simulations of hysteresis friction and temperature effects between elastomers and rough or microscopically smooth interfaces", *(Boukamel, Laiarinandrasana, Meo, Verron: Constitutive Models for Rubber V)*, 351-355, Taylor & Francis Group, London (2008)

[32] A. Le Gal: "Investigation and Modelling of Rubber Stationary Friction on Rough Surfaces" *(PhD Thesis)* University of Hannover (2007)

[33] A. Müller, J. Schramm, M. Klüppel: "Ein neues Modell der Hysteresereibung von Elastomeren auf fraktalen Oberflächen", *Kautschuk Gummi Kunstst.* **55,** 432 (2002)

[34] H. Kummer: "Lubricated Friction of Rubber Discussion", *Rubber Chem. Technol.* **41,** 895 (1968)

[35] A. Le Gal, M. Klüppel: "Modelling of rubber friction: A quantitative description of the hysteresis and adhesion contribution", *(P.E. Austrell & L. Kari: Constitutive Models for Rubber IV)*, Taylor & Francis Group, London, 509 (2005)

[36] A. Le Gal, X. Yang, M. Klüppel: "Evaluation of sliding friction and contact mechanics of elastomers based on dynamic mechanical analysis", *J. Chem. Phys.* **123,** 014704 (2005)

[37] B. Persson, E. Brener: "Crack propagation in viscoelastic solids", *Phys. Rev. E* **71**; 036123 (2005)

[38] A. Le Gal, M. Klüppel: "Investigation and Modelling of Adhesion Friction on Rough Surfaces", *Kautschuk Gummi Kunstst.* **59,** 308 (2006)

[39] R. Good, L. Girifalco: "A Theory for Estimation of Surface and Interfacial Energies 3: Estimation of Surface Energies of Solids From Contact Angle Data", *J. Phys. Chem.* **64**, 561-565 (1960)

[40] A. Savkoor, A. Briggs: "The effect of a tangential force on the contact of elastic solids in adhesion", *Proc. R. Soc. Lond A*, **356**, 103-114 (1977)

[41] D. Owens, R.J. Wendt: "Estimation of the surface free energy of polymers", J. Appl. Polym. Sci. 13, 1741-1747 (1969)

[42] H. Busscher et al: "The Effect of Surface Roughness of Polymers on Measured Contact Angles of Liquids", *Colloids and Surfaces* **9**, 319-331 (1984)

[43] H. Batzer: "Polymere Werkstoffe III: Technologie 2", Georg Thieme Verlag Stuttgart, New York (1984)

[44] T. Kempermann: "Handbuch für die Gummi-Industrie", Bayer AG (1991)

[45] M. Klüppel: "The Role of Disorder in Filler Reinforcement of Elastomers on Various Length Scales", *Adv. Polym. Sci.* **164**, 1-86 (2003)

[46] G. Heinrich, M. Klüppel: "Role of Polymer-Filler-Interphase in Reinforcement of Elastomers" *Kautschuk Gummi Kunstst.* **57**, 452 (2004)

[47] M. Klüppel, J. Schramm: "A generalized tube model of rubber elasticity and stress softening of filler reinforced elastomer systems", *Macromol. Theory Simul.* **9**, 742 (2000)

[48] M. Klüppel, G. Heinrich: "Physics and Engineering of Reinforced Elastomers", *Kautschuk Gummi Kunstst.* **58**, 217 (2005)

[49] M. Qu, F. Deng, S. Kalkhoran, A. Gouldstone, A. Robisson, K. Van Vliet : "Nanoscale visualization and multiscale mechanical implications of bound rubber interphases in rubber-carbon black nanocomposites", *Soft Matter* **7**, 1066-1077 (2011)

[50] X. Zhu, M. Jaumann, K. Peter, M. Möller, C. Melian, A. Adams-Buda, D.E. Demco, B. Blümich: "One-Pot Synthesis of Hyperbranched Polyethoxysoloxanes", Macromol. **39**, 1701 - 1708. (2006)

[51] Q. Dou, X. Zhu, K. Peter, D.E. Demco, M. Möller: "Preparation of polypropylene/ silica composites by in-situ sol-gel processing using hyperbranched polyethoxysiloxane", *J.Sol-Gel Sci Technol* **48**, 51-60 (2008)

[52] L. Busse, K. Peter, C.W. Karl, H. Geisler, M. Klüppel: "Reducing Friction with Al$_2$O$_3$/SiO$_2$-Nanoparticles in NBR", Wear **271**, 1066-1071 (2011)

[53] C. Karl, L. Busse, M. Klüppel, U. Giese: „ Varnish Coating of Elastomers: Morphology, Friction and Surface Energies", *9. Kautschuk Herbst Kolloquium*, Hannover (2010)

[54] C. Karl, A. Lang, A. Stoll, A. Weiße, M. Stoll, M. Klüppel: „Tribologische Eigenschaften beschichteter Elastomere - Teil 1: Charakterisierung der Oberflächen mittels modifizierter Wilhelmy-Methode", *Kautschuk Gummi Kunstst.* **75**, 44-49 (April 2012)

[55] C. Karl, A. Lang, L. Busse, A. Stoll, A. Weiße, M. Stoll, M. Klüppel: „Tribologische Eigenschaften beschichteter Elastomere - Teil 2: Charakterisierung der stationären Reibung gegenüber glatten Substraten", *Kautschuk Gummi Kunstst.* **76**, 33-36 (May 2012)

[56] C. Karl, L. Busse, A. Stoll, M. Klüppel: „AIF-Abschlussbericht: Vermeidung von Stick-Slip Reibinstabilitäten beschichteter Elastomere auf mikroskopisch rauen und glatten Oberflächen" (2011)

[57] C. Karl, M. Klüppel: „Characterization of Elastomers by Wetting: Roughness and Chemical Heterogeneiy", *Chem. Listy* **105**, 233-234 (2011)

[58] J. Fritzsche, M. Klüppel: "Filler networking and reinforcement of carbon black filled styrene butadiene rubber", *Kautschuk Herbst Kolloquium*, Hannover (2008)

[59] L. Busse, M. Klüppel: "Wet and Dry Friction of Elastomers in Advanced Simulation Compared to Experiment", *(Heinrich, Kalliske, Lion, Reese: Constitutive Models for Rubber VI)* Taylor & Francis Group, London, 295-300 (2010)

[60] L. Busse, A. Le Gal, M. Klüppel: "Modelling of Dry and Wet Friction of Silica Filled Elastomers on Self-Affine Road Surfaces", Lecture Notes in Applied and Computational Mechanics Vol. **51** (Besdo, Heimann, Klüppel, Kröger, Wriggers, Nackenhorst), Springer, 1-26 (2010)

[61] L. Busse, I. Boubakri, M. Klüppel: "Friction Master Curves for Rubber on Dry and Wet Granite: Experiments and Simulations", *Kautschuk Gummi Kunstst.* **64**, 35-39 (May 2011)

[62] L. Busse, C. W. Karl, I. Boubakri, M. Klüppel: „Praxis and Theory of rubber Friction on rough and smooth surfaces", *9. Kautschuk Herbst Kolloquium*, 31-34 Hannover (2010)

[63] T. Papatheodorou: "Weniger Reibung", *Kautschuk Gummi Kunstst.* **60**, 586, (2007)

[64] G. Carbone, F. Bottiglione: "Asperity contact theories: Do they predict linearity between contact area and load?", *J. Mech. Phys. Solids* **56**, 2555-2572 (2008)

[65] G. Carbone, F. Bottiglione: "Contact mechanics of rough surfaces: a comparison between theories", *Meccanica* (2010)

[66] Q. Bui, J. Ponthot: "Estimation of rubber sliding friction from asperity interaction modeling", *Wear* **252**, 150-160 (2002)

[67] M. Barquins: "Adherence, friction and wear of rubber-like materials", *Wear* **158**, 87-117 (1992)

[68] M. Lindner: "Experimentelle und theoretische Untersuchungen an Profilklötzen und Dichtungen" *(PhD Thesis)* Universität Hannover (2005)

[69] B. Lorenz, B. Persson: "Interfacial separation between elastic solids with randomly rough surface - comparison of experiment with theory", *J. Phys. Condens. Matter* **21**, 015003 (2009)

[70] M. Kröger, P. Moldenhauer: "Modellierung von Elastomerkontakten", *Kautschuk Gummi Kunstst.* **63**, 30-35 (2010)

List of Tables

Acknowledgement

I thank **Paul Rutledge** for proofreading this text in respect to the English language and Dr. **Christian Weichmann** for general hints about dissertations.

I appreciate the internet for the pivotal last information I needed to programme my custom-made spreadsheet for a more efficient friction evaluation.

Very cordially I would like to thank **my parents** for letting spark my joy for science, giving me the opportunity to study and for my existence… and theirs.

Finally, my gratitude holds for my girlfriend **Evelyn Rzymelka**, who always believed in me, for her support and love.

Curriculum Vitae

Personal Data

Name:	Leif Busse
Date of birth:	1968-10-26
Place of birth:	Reinbek
Nationality:	German
Marital status:	unmarried

Education & Professional Experience

2007 - 2010	PhD student and scientific associate at the **Deutsches Kautschukinstitut** (DIK) in Hannover *Topics:* friction and stick-slip of elastomers in experiment and simulation, dynamic-mechanical measurements
2001 - 2006	scientific associate at the **Research Center Caesar** in Bonn *Topics:* nano-optics, electron beam lithography, surface characterization and material testing
2000	associate in the IT department of the **Allergopharma** in Reinbek
1990 - 2000	studies of physics at the **University of Hamburg** *diploma topic:* „STM / STS on binary layers of iron and gadolinium on W(110)"
1988 - 1990	**civilian service**
1979 - 1988	gymnasium, abitur at the **Sachsenwaldschule Reinbek**
1976 - 1979	**primary school** in Reinbek